ISSN 2525-2461

Vietnam Journal of Science, Technology and Engineering

SEPTEMBER 2018 • VOL.60 NUMBER 3

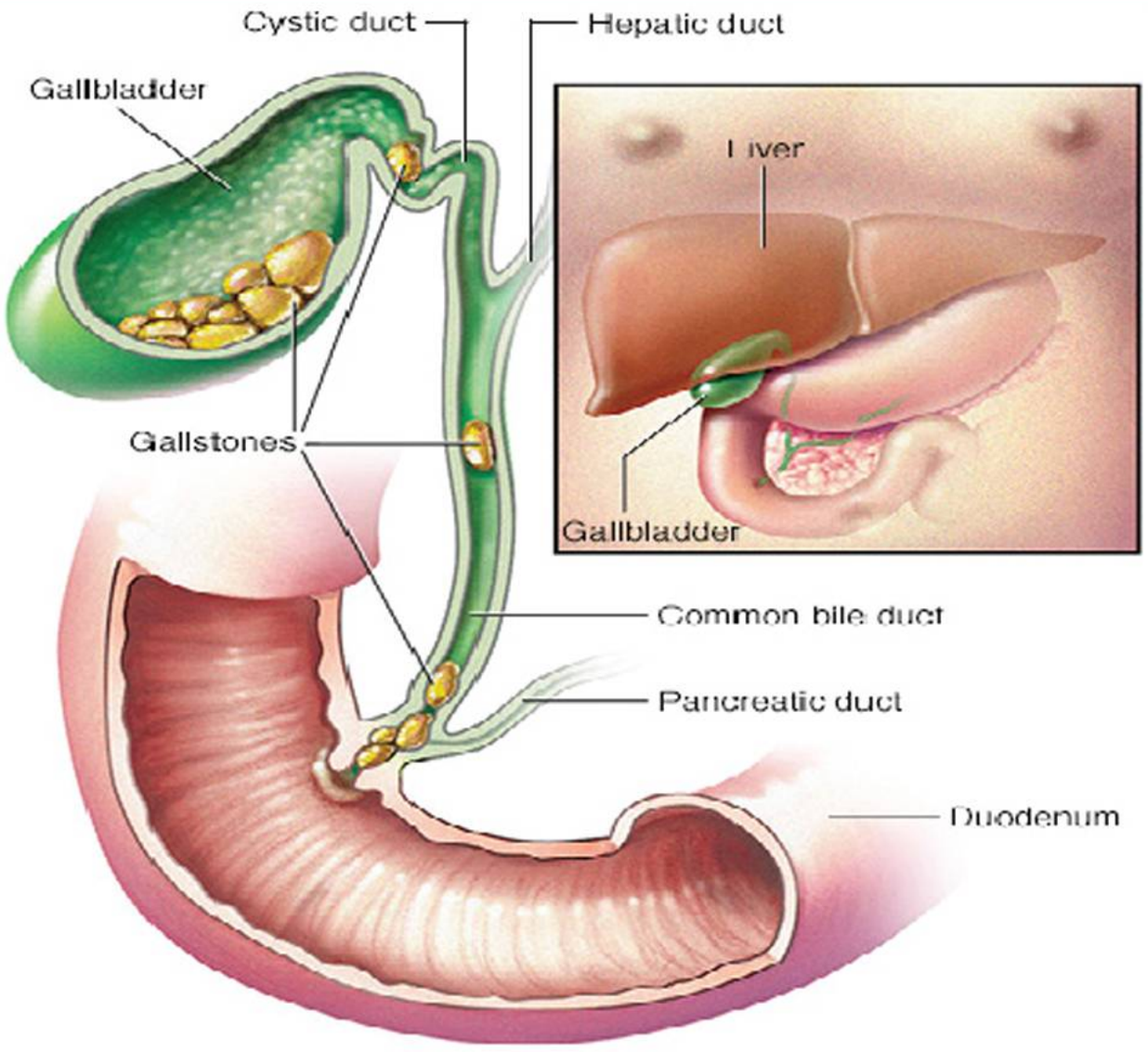

Gallstones and common bile duct stones: single or separated-step endoscopic retrograde cholangiopancreatography and laparoscopic cholecystectomy?

VIETNAM JOURNAL OF SCIENCE, TECHNOLOGY AND ENGINEERING • SEPTEMBER 2018 • VOL.60 NUMBER 3
vietnamscience.vn

Vietnam Journal of Science, Technology and Engineering (VJSTE) **is a quarterly double-blind peer-reviewed academic journal. VJSTE publishes research articles and review articles in all areas of science, technology and engineering with the focus on the life sciences and environmental sciences including the following topics:**

- **Agriculture**
- **Medicine**
- **Pharmacology**
- **Biology**
- **Biotechnology**
- **Ecology**
- **Climatology.**

CLASSIFICATION SCHEME

1. **Mathematics and Computer Science**
   - 1.1. Mathematics
   - 1.2. Computer Science
   - 1.3. Computational Science
2. **Physical Sciences**
   - 2.1. Physics
   - 2.2. Chemistry
   - 2.3. Engineering
3. **Life Sciences**
   - 3.1. Agriculture
   - 3.2. Medicine
   - 3.3. Pharmacology
   - 3.4. Biology
   - 3.5. Biotechnology
4. **Geosciences**
   - 4.1. Geography
   - 4.2. Geology
   - 4.3. Geophysics
   - 4.4. Oceanography
5. **Nanoscience and Nanotechnology**
   - 5.1. Nanophysics
   - 5.2. Nanochemistry
   - 5.3. Nanobiotechnology
   - 5.4. Nanomedicine
   - 5.5. Nanoengineering
6. **Environmental Sciences**
   - 6.1. Ecology
   - 6.2. Climatology

CONTENTS

SEPTEMBER 2018 • VOL.60 NUMBER 3

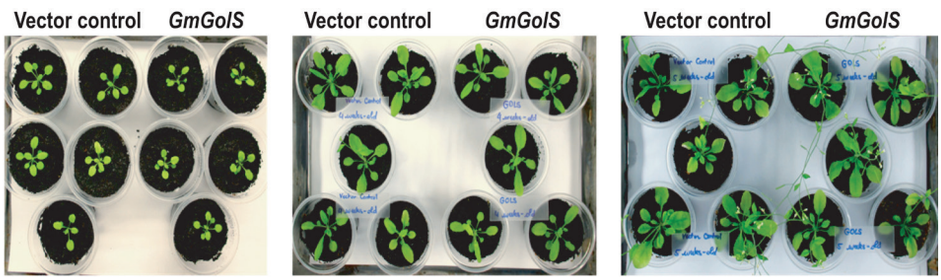

PHYSICAL SCIENCES

LIFE SCIENCES

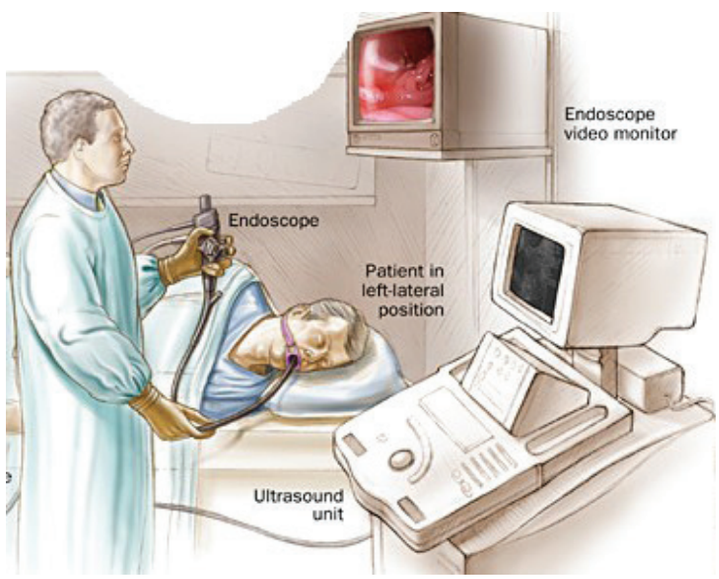

CONTENTS

SEPTEMBER 2018 • VOL.60 NUMBER 3

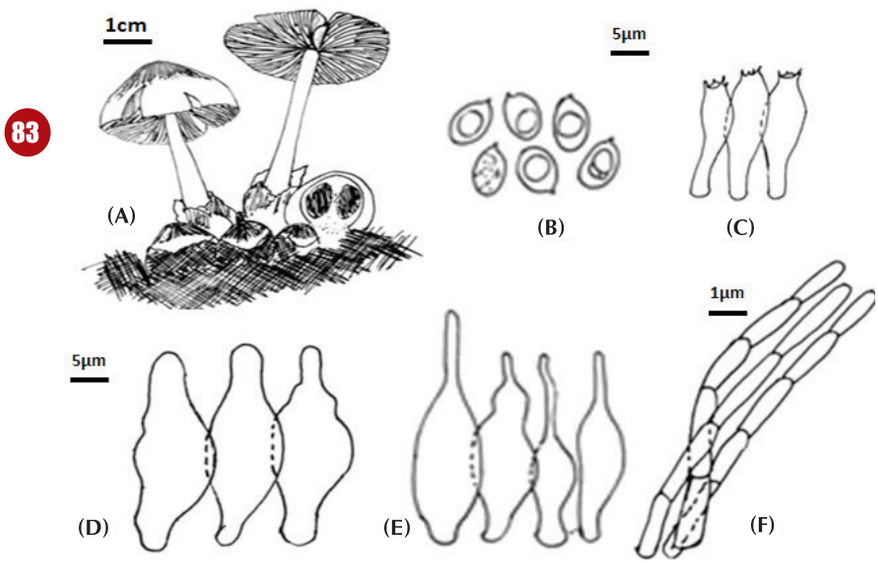

NANOSCIENCE AND NANOTECHNOLOGY

ENVIRONMENTAL SCIENCES

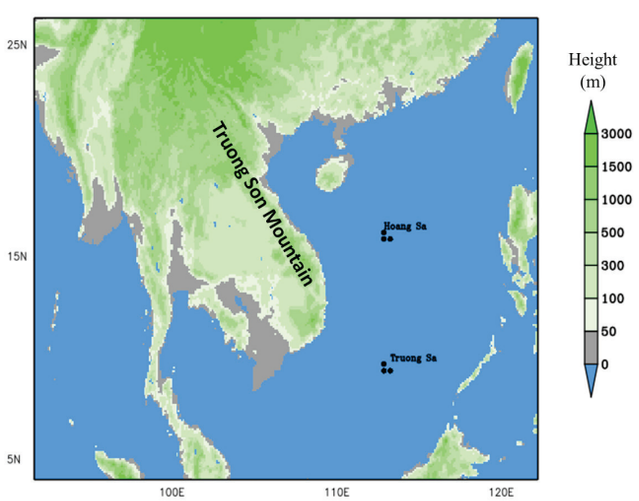

Synthesis and modification of maleic anhydride-vinyl acetate copolymer by a long alkyl chain alcohol for cold flow impovers of biodiesel

Thi Thu Huong Tran, Thi Tuyet Mai Phan*, Van Boi Luu, Ngoc Lan Pham

University of Science, Vietnam National University, Hanoi

Received 26 February 2018; accepted 29 June 2018

Abstract:

This research illustrates the results of a study on the synthesis of maleic anhydride-vinyl acetate copolymers (MAVA) with the monomer molar ratio of 1:1 by the radical polymerisation method in which benzoyl peroxide was used as a catalyst. The structure and composition of MAVA were characterised by FTIR, ^{1}H-NMR and ^{13}C-NMR spectra. The molecular weight of the copolymers was determined by the viscosity method. The copolymers were then modified by the esterification reaction with hexadecanol - a long alkyl chain alcohol. The modified copolymer products (MAVAC) were used as additives to improve the cold flow properties of palm oil-based biodiesel through pour point temperature measurement according to standard ASTM-D97 and dynamic viscosity according to ASTM D445-97. The results showed that the MAVAC additives with the comb-shape structure at the concentration of 1000 ppm could decrease the pour point temperature of palm oil-based biodiesel by 5.5^{o}C and dynamic viscosity by 0.17 cPs.

Keywords: **additive, cold flow property, maleic anhydride-vinyl acetate copolymer, palm oil-based biodiesel.**

Classification number: **2.2**

Introduction

The study of producing biodiesel from non-edible oils, such as palm oil, rubber seed oil, waste cooking oil, animal fats, is a strategy of development in most countries in the world, including Vietnam. This biodiesel has the disavantage of having poor flow properties at low temperatures. When the temperature drops, the monomethyl esters of fatty acids are separated in the form of either crystals or wax thus preventing the flow of oil which causes clogging of the fuel nozzle. This ultimately leads to a stop in the working of the engine [1, 2]. Numerous methods have been assessed for improving the cold flow property of biodiesel [3], including winterisation [4, 5], ozonisation [6], addition of cold flow improvers (CFIs) [7] and modification of the fatty ester composition [8]. Among these, the use of polymeric CFIs provides an effective and feasible approach that has been investigated in many studies [9-11]. Recent studies reported that copolymeric CFIs can remarkably improve the low temperature performance of biodiesel. These CFIs have chemical structures consisting of a hydrocarbon chain that is able to co-crystallise with the hydrocarbon chain of the fatty acids in biodiesel fuels and thereby affect the growth and nucleation of the wax crystals [12-14]. Using polymer additives to reduce the pour point temperature of biodiesel is the useful solution to this problem. In particular, copolymers with comb-shape structures prove most active [3, 9-11]. Copolymerisation is of great interest while synthesising polymers to obtain the desired physical and chemical properties by controlling monomer ratios, their concentrations and the polymerisation procedure [1]. However, the synthesis of copolymers with comb-shape structures, that consist of long and short branch chains which are arranged regular alternatively, is still a challenge for scientists [11, 15-17]. It is very important to be able to generate copolymers with regular alternative structures by choosing the pairs of monomers that contain

*Corresponding author: Email: maimophong@gmail.com

a small copolymerisation constant (~ 0) [18]. Maleic anhydride (MA) is a unique comonomer because it does not readily undergo homopolymerisation, but forms copolymers without difficulty [14]. So, maleic anhydride (MA) and vinyl acetate (VA) have been selected [1, 14]. They have the copolymerisation constant r_1 = 0.072 and r_2 = 0.01, respectively ($r_1.r_2$ = 0.00072 ~ 0) [16, 18, 19], and so are able to generate copolymers with alternative structures, as desired.

Cold flow properties of biodiesel generally depend on fatty acid composition. The relative concentration proportion of saturated and unsaturated fatty acid methyl ester species in biodiesel may have a significant effect on the thermodynamics of nucleation and crystallisation under cold weather. Biodiesel derived from palm oil has a relatively high saturated fatty acid residue content, most of which is palmitic acid (C16), leading to pour point value in the range of 13-17°C [2, 14, 20]. So, it is essential to design suitable copolymeric CFIs that would be most effective in improving the cold flow for specific biodiesel.

In this research, combshape poly–(maleic anhydride –co-vinyl acetate) copolymers esterified with hexadecanol were synthesised. The effect of various of alkyl group/carboxyl group as well as the side chain length of CFIs on the wax crystallisation and the flowability of biodiesel was studied by measuring the pour point temperature and dynamic viscosity. Solubility of the synthesised copolymers in different solvents was investigated to identify whether there is an increase intheir efficiency on palm oil biodiesel.

Experiment

Chemicals

The main chemicals used in this study include: Maleic Anhydride-MA (Merck), Vinyl Acetate-VA, Benzoyl Peroxide-BPO, p-Sulfonic Acid-PTSA (Wako, Japan), Cetyl Alcohol (Sigma Aldrich). The solvents include Methanol, Ethanol, Acetone, Toluene, Dimethyl Formamide-DMF (Merck). Monomethyl Ethyl Ketone-MEK (Prolabo), Palm oil Biodiesel from Palm oil of Vietnam [21].

Preparation methods

Synthesis of MAVA copolymer: MA and VA with molar ratio 1:1 [16, 18, 22] and MEK solvent (ratio of monomeric mass to volume of solvent is 30%, g/ml) were poured into a four-neck round-bottom flask, equipped with a reverse condenser, a thermometer and a N_2 gas pipe. N_2 gas was supplied for thirty minutes. Then, a solution of BPO (0.6% mass of monomers) in MEK (0.02 mmol) was prepared separately and added to the above mixture. The mixture was heated with vigorous stirring. The reaction temperature remained at 80°C for six hours. When the reaction ended, the copolymer was precipitated three times with an excess volume of cold diethyl ether, then dried at a temperature of 50°C under vacuum pressure for six hours. The end product was solid with light pink-white colour.

The molecular weight of copolymers was determined by viscometry [18]. The reaction yield (H), molecular weight (M, g/mol), % mol of MA in copolymer unit and vibration wavenumbers of the copolymer are given in Table 1.

Table 1. Parameters and vibration wavenumbers of copolymer samples.

Sample	Mol ratio MA:VA	H (%)	M (g/mol)	% mol MA	Vibration wavenumbers (cm^{-1})
MAVA	1:1	75	22410	55	ν_{C-H} 2924-2853, $\nu_{C=O}$ 1730, ν_{C-O} 1244, ν_{C-O-C} 1033, ν_{C-H} 954
MA			98		ν_{C-H} 3125, $\nu_{C=O}$ 1853, $\nu_{C=O}$ 1777, $\nu_{C=C}$ 1627, ν_{C-O-C} 1059
VA			86		γ_{C-H} ($-CH_3$) 1375, ν_{C-H} ($-CH_2$) 1442, ν_{C-H} 2924-2854, $\nu_{C=C}$ 1646, $\nu_{C=O}$ 1772 ν_{C-O} 1222, ν_{C-H} 720

Esterification of MAVA copolymer: MAVA copolymer was esterified by hexadecanol with the mol ratio 1:1 based on molar portion of anhydride in copolymers [21]. Hexadecanol was dissolved in toluene to keep dry from water by azeotropic method. Solution of MAVA copolymers was added to the reaction flask. Finally, PTSA catalyst (1% mass of reactants) was introduced. The reaction was performed in 6h. The water formed during the reaction was separated by using the Dean-Stark trap. The reaction product was gained by precipitation with an excess volume of cold methanol. Next, the precipitate was dissolved two times with excess cold methanol. The pure modified MAVAC product was dried overnight at 50°C under vacuum pressure. The final product is a pale-yellow powder.

The yield, some physico-chemical parameters, the average molecular weight and the spectral data of the modified copolymers are given in Table 2.

The reaction yield (H), molecular weight (M, g/mol), % mol of MA in copolymer unit, and vibration wavenumbers of modified copolymer are given in Table 2.

Table 2. Parameters and vibration wavenumbers of modified copolymer samples.

Sample	H (%)	M	FTIR (cm^{-1})
MAVAC	83	39830	ν_{C-H} 2922-2851, $\nu_{C=O}$1857, $\nu_{C=O}$1780-1734, ν_{C-O} 1074, ν_{C-H}929, ν_{C-H} 720

Determination of solidifying temperature for biodiesels: the pour point temperature with and without copolymer additives was measured according to standard ASTM D97 [23]. The modified copolymer was dissolved in a mixture of toluene and acetone with volume ratio 1:1. This additive solution was then added to the biodiesel at a certain mass fraction before it was poured into a test tube. The temperature of the test tube was slowly decreased by using a mixture of salt and ice. When the temperature of the sample was 9^0C above pour point, we started to monitor it every 3^0C. The determinant of pour point ends when laying the test tube horizontally in 5s but there is no emotions of biodiesel. The pour point is that temperature plus 3^0C. The pour point of biodiesel without additives is got similarly to determining activity of the additive.

Determination of dynamic viscosity (μ) by using Gilmont viscometer: the dynamic viscosity (μ) of biodiesel with and without copolymer CFIs was measured by using Gilmont viscometer of Thermo Scientific Company (Faculty of Chemistry, HUS). It was measured at 40^oC according to standard ASTM D445-97.

Research methods

Infrared spectroscopy (FTIR): FTIR spectra were recorded on FT/IR-6300 type spectrometer (Faculty of Chemistry, HUS). The spectra were scanned 32 times, with a resolution of 4 cm^{-1}, in the wave range of 600-4000 cm^{-1}.

Proton Nuclear Magnetic Spectroscopy (^{1}H-NMR): ^{1}H-NMR spectra were recorded on Bruker Avance 400MHz FT-NMR spectrometer (Faculty of Chemistry, HUS). The solvents used were $CDCl_3$ and DMSO-d6. TMS was used as the internal standard.

Viscosity measurement method: the average molecular weight (M) of copolymers was determined by viscometry according to the Mark and Houwink-Sakurada equation [17]:

$[\eta] = K.M^{\alpha}$.

Where $[\eta]$ ($dl.g^{-1}$) is the intrinsic viscosity; M is the average molecular weight of polymers; K and α are characteristic constants for the used polymer-solvent systems. $K = 9{,}32.10^{-6}$dl/g và $\alpha = 0{,}94$ [22].

Intrinsic viscosity measurements were carried out using an Ubbelohde capillary viscometer having an internal diameter of 0.5 mm and a length of 10 cm. The flow times were recorded using a stopwatch.

Results and discussion

Synthesis of MAVA copolymer

The copolymerisation reaction scheme is described as follows:

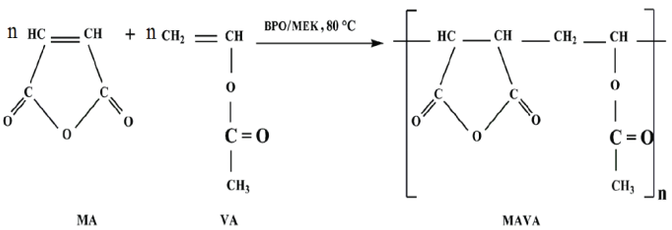

Schem 1. Synthesis routine for the preparation of MAVA copolymer.

The structure of synthesised copolymers was confirmed by FTIR, ^{1}H-NMR and ^{13}C-NMR spectra.

FTIR Spectra: FTIR spectrum of MAVA copolymer is given in Fig. 1, the spectral data are presented in Table 1.

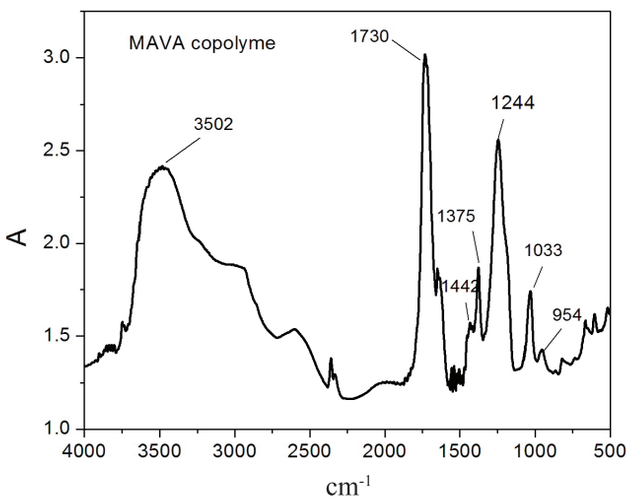

Fig. 1. FITR spectrum of MAVA copolymer.

As shown in Fig. 1, the deformation vibration in the plane of the C-H (in CH_3) of VA appears at 1375 cm^{-1} [16], while the deformation vibration of C-H (in CH_2) appears at 1442 cm^{-1}. Carbonyl groups of both MA and VA have absorption peaks close to each other, thus forming a large and strong overlap peak at 1730 cm^{-1}. However, there was a shift of C=O peak to the lower frequency (compared to the C=O peak in the acid and esters). This could be due to the C=O of acetate group attracting electrons. This makes the H atoms

in the methyl groups more electron deficient and thus have the ability to create hydrogen bonds with oxygen atoms of the adjacent MA. The formation of hydrogen bonds did shift the peak to the lower frequency [24]. Besides, the presence of VA is also characterised by the appearance of vibrations of C-H at 954 cm^{-1}; the peak at 1244 cm^{-1} is attributed to the vibrations of the C-O linkage [16]. The peak at 1033 cm^{-1} corresponds to the vibrations of the C-O-C linkage in MA [16].

At the same time, it can be seen that the absence of characteristic spectral bands for scissing vibrations of linkage C=C of the monomers at 1646 cm^{-1} (VA) and 1627 cm^{-1} (MA) [16, 18, 19, 25] showed that the copolymerisation had taken place completely. It also showed that the copolymer product had high purity and contained no traces of residual monomers. So, the FTIR spectra confirmed the formation of MAVA copolymers.

^{1}H-NMR Spectra: the structure of MAVA copolymer was also confirmed by proton nuclear magnetic resonance spectroscopy. The ^{1}H-NMR spectrum of MAVA copolymer is indicated in Fig. 2.

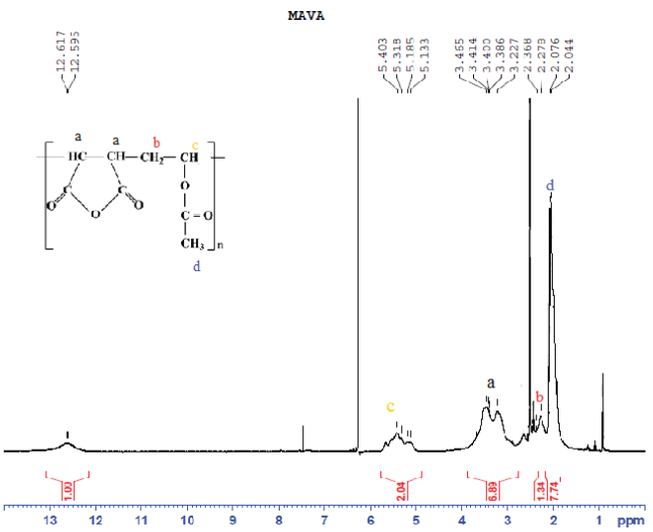

Fig. 2. ^{1}H-NMR spectrum of MAVA copolymer.

It can be seen that the peak at 5.1-5.4 ppm corresponds to the proton in CH, the peak at 2.04-2.07 ppm - to the protons of the CH_3, the peak at 2.27-2.36 ppm - to the protons of the CH_2 in VA, and the peak at 3.2-3.5 ppm - to the protons of the MA. So, as in the case of infrared spectroscopy, the ^{1}H-NMR spectra could also explain in full the chemical structure of MAVA copolymers. The MA monomer content in the MAVA copolymer was determined based on the ^{1}H-NMR spectral data according to the following equation [18]:

$$\%MA = \frac{\frac{S_a}{2}}{\frac{S_a}{2} + \frac{S_d}{3}}.100\% \approx 57\% \quad (1)$$

Where S_a, S_d are peak areas at 3.4 ppm and 2.07 ppm corresponding to the protons in -CH of MA and -CH_3 of VA, respectively.

It can be seen that by using the technique of slow drip of catalyst solution into the reaction mixture for 30 minutes, one can acquire MAVA copolymers with constituent monomer molar ratio that almost equals 1.

^{13}C-NMR Spectra: ^{13}C-NMR spectroscopy has been used to assert the alternative structure of the obtained copolymers (Fig. 3).

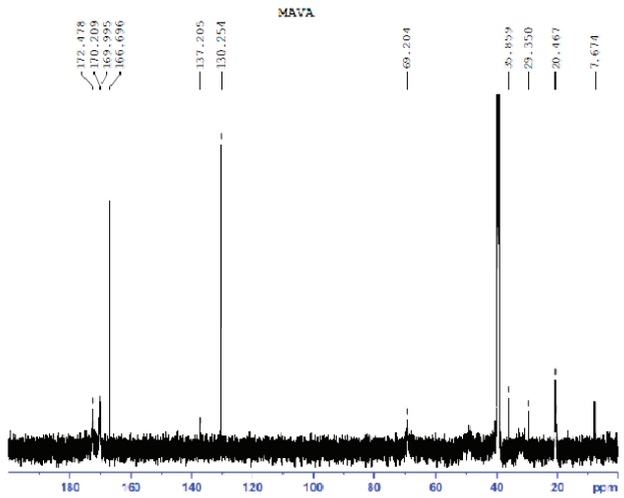

Fig. 3. ^{13}C-NMR spectrum of MAVA copolymer.

From Fig. 3, the appearance of a peak at 172 ppm that belongs to carbon in the group C=O of VA and the dual peak at 170 ppm and 166 ppm for the two C=O groups of MA has asserted that the obtained MAVA copolymers had a regular alternative structure. Similar results were also announced in the work of Gabrielle, et al. [22]. The molecular weight of the MAVA copolymers determined by viscosity methods are presented in Table 1.

Study on the solubility of MAVA copolymer: the solubility of the synthesised MAVA copolymers influence the scope of the polymer's application, especially the ability to purify the product. Hence, the study on solubility of the reaction products is essential. A survey on the solubility of MAVA copolymers in different solvents has been conducted. Results are presented in Table 3.

Table 3. Solubility of MAVA copolymers in solvents.

Solvent		Soluble	Insoluble
Aprotic	Acetone	✓	
	DMF	✓	
	MEK	✓	
Protic	Methanol	✓	
	Ethanol	✓	
	Water	✓	
Non-polar	Toluene		✓

From Table 3, it is understood that the MAVA copolymers have the ability to dissolve in polar solvents. This is understandable, because the C=O in MA has a free electron pair, and due to the difference in electronegativity C=O can be polarising. Moreover, in the MAVA copolymers, CH_3COO-acetate groups also have polar C=O. Therefore, MAVA copolymer can dissolve in polar solvents and are insoluble in non-polar solvents such as toluene.

Based on the above results, acetone was chosen as a solvent to dissolve the MAVA copolymers in subsequent experiments.

Modification of MAVA copolymers with hexadecanol

The structure and molecular weight of polymer additives have a great influence on the ability to improve cold flow properties of biodiesel. Additives having the comb-shape structure [1, 14, 18, 20], with long alkyl side chains and short chains alternative to each other embedded in the polymer main chains, demonstrated the ability to reduce the solidifying temperature of biodiesel.

The long alkyl side chains interact with long alkyl chains of methyl esters of fatty acids (FAME) in biodiesel, inhibits or slows the crystallisation process, thus prevents the formation of wax plates in biodiesel at low temperatures. According to this approach, the ring-opening reaction of MA in the MAVA copolymers has been conducted using hexadecanol, as shown in Scheme 2:

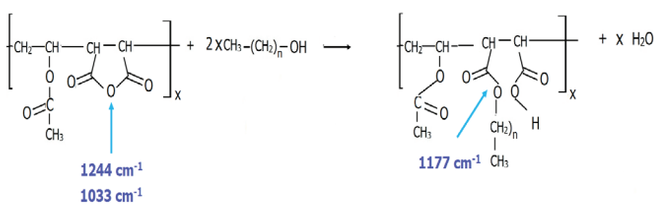

Scheme 2. Synthesis routine for the preparation of MAVAC.

The opening of the anhydride ring was confirmed by the decrease in IR peak intensity of the absorption bands at 1244 cm^{-1} and 1033 cm^{-1}, characterising the vibration of the C-O-C linkage in the anhydride ring and the increase in intensity of peak at 1177 cm^{-1} of the formed C-O- ester linkage (Fig. 4).

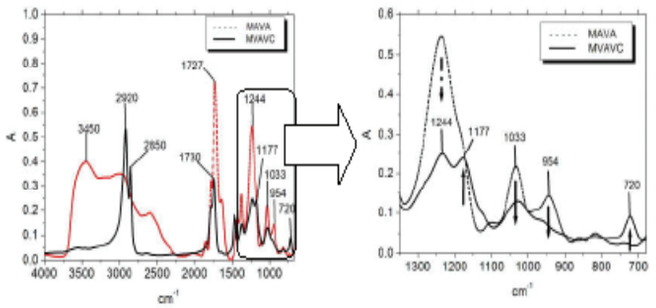

Fig. 4. FTIR spectra of MAVA and MAVAC.

Moreover, the presence of long alkyl chains (C16) of hexadecanol in the product was confirmed by the appearance of a new peak at 720 cm^{-1} characterizing the vibration of the C-H in $(CH_2)_n$ when $n \geq 4$. The yield of esterification is relatively high about 83. The molecular weights of MAVAC copolymers determined by viscosity method are presented in Table 2.

Study on solubility of MAVAC copolymer: in order to find a suitable solvent that disperses additives into the biodiesel efficiently, the solubility of additives in different solvents was investigated. The results obtained are presented in Table 4.

Table 4. Solubility of MAVAC in solvents.

Solvent	Soluble	Insoluble
Toluene		✓
Acetone		✓
Toluene + acetone	✓	
Methanol		✓

From Table 4, it is understood that the MAVAC copolymer can be dissolved in a mixture of toluene and acetone (ratio of volume is 1:1), so this solvent mixture will be chosen to dissolve the polymer additives for biodiesel.

Test on flow property improvement of biodiesel: a test was conducted on the ability of the polymer additives to improve cold flow properties of palm oil biodiesel via the determination of pour point temperature and dynamic viscosity. The results are given in Table 5.

Table 5. Solidifying temperature (T) and dynamic viscosity (μ) of palm oil biodiesel with and without polymer additives at a concentration of 1000 ppm.

Samples	T(°C)	μ (cPs)
Palm oil biodiesel (BDF)	13.5	4.16
BDF + MAVA	14.0	4.20
BDF + MAVAC	8.0	3.99

The MAVAC copolymers can help to improve the cold flow property of palm oil biodiesel. For instance, the solidifying temperature of BDF containing MAVAC reduced by 5.5°C and dynamic viscosity by 0.17 cPs in comparision with the original BDF (see Table 5). At the same time, it showed that the MAVA copolymers did not have this ability; their presence barely increased both pour point temperatures and dynamic viscosity. As such, the results have proved that copolymers that have comb-shape structures, with long and short side alkyl chains arranged alternatively to one another, mainly determined the activity of the additives.

From this opens a prospect that one can design copolymer additives having regularly alternative structures from MA and VA. One can also adjust the number and the length of the branch chains for a specific biodiesel in order to achieve the best cold flow property improvement.

Conclusions

- The polymerisation of vinyl acetate with maleic anhydride was conducted with a monomer molar ratio of 1:1. The structure and compositions of the synthesised MAVA copolymers were characterised by FTIR, ^{1}H-NMR and ^{13}C-NMR spectra. The molecular weight was determined by the viscosity method.

- The esterification of MAVA copolymers with hexadecanol was conducted. The modified MAVAC product was used as an additive for cold flow property improvement of palm oil biodiesel. It was able to reduce the pour point temperature of the obtained biodiesel by 5.5°C, and the dynamic viscosity by 0.17 cPs at 1000 ppm concentration.

ACKNOWLEDGEMENTS

The work was financially supported by the Scientific Research Project of the National University of Hanoi, code: QG.14.18.

REFERENCES

[1] A.M. Ayman, G.E. Rasha, M.A. Fatma, H.S. AliM, E. Abdullah (2015), "Adsorption of polymeric additives based on vinyl acetate copolymers as wax dispersant and its relevance to polymer crystallization mechanisms", *Journal of Chemistry,* **2015,** 8pp.

[2] S.F. Cheng, C.L. Yung, L.H. Noor, Y.M. Choo, C.H. Chuah, A.N. Ma (2006), "Crystallisation and melting behavior of methyl esters of palm oil", *American Journal of Applied Sciences,* **3(5)**, pp.1859-1863.

[3] P.C. Smith, Y. Ngothai, Q.D. Nguyen, B.K.O. Neill (2010), "Improving the low-temperature properties of biodiesel: Methods and consequences", *Renewable Energy,* **35**, pp.1145-1151.

[4] A. Perez, A. Casas, C.M. Fernadez, M.J. Ramos, L. Rodriguez (2010), "Winterization of peanut biodiesel to improve the cold flow properties", *Biosource Technology,* **101**, pp.7375-7381.

[5] I. Lee, A.A. Johnson, E.G. Hammond (1996), "Reducing the crystallization temperature off biodiesel by winterizing methyl soyate", *Journal of the American Oil Chemists' Society,* **73**, pp.631-636.

[6] J.N.U. Soriano, V.P. Migo, M. Matsumura (2006), "Ozonized vegetable oil as pour point depressant for neat biodiesel", *Fuel,* **85**, pp.25-31.

[7] B.S. Chen, Y.Q. Sun, J.H. Fang, J. Wang, J. Wu (2010), "Effect of cold flow improvers on flow properties of soybean biodiesel", *Biomass and Bioenergy,* **34**, pp.1309-1313.

[8] G. Knothe (2009), "Improving biodiesel fuel properties by modifying fatty ester composition", *Energy Environmental Science,* **2**, pp.759-766.

[9] G. Pranab, D. Tapan, D. Moumita (2011), "Evaluation of poly(acrylates) and their copolymer as viscosity modiffiers", *Res. J. Chem. Sci.,* **1(3)**, pp.18-25.

[10] I.M. Gamal, A.M. Sabbagh (1996), "Polymeric additives for improving the flow properties of waxy distillate fuels and crude", *Fuel,* **75**, pp.743-750.

[11] I.M. Gamal, A.M. Sabbagh (1997), "Polymeric structures as cold flow improvers for waxy residual fuel oil", *Fuel,* **76**, pp.1471-1478.

[12] L. Xiang, X. Yuan, X. Guangwen, Z. Zhicheng, S. Han, L. Hualin (2016), "Effect of methyl acetoacetate as a potential cold flow improver for biodiesel", *Energy Soucers,* **39(1)**, pp.97-102.

[13] L. Reng, Z. Zhang, F. Wang, T. Wang, S. Yang (2014), "Synthesis and evaluation of alkyl acrylate-vinyl acetate-maleic anhydride terpolymers as cold flow improvers for diesel fuel", *Fuel Processing Technology,* **118**, pp.42-48.

[14] T.C. Ming, N. Ramli, O.T. Lye, M. Said, Z. Kasima (2005), "Strategies for decreasing the pour point and cloud point of palm oil products", *Eur. J. Lipid Sci. Technol.,* **107**, pp.505-512.

[15] J. Wang, L. Cao, S. Han, (2014), "Effect of polymeric cold flow improvers on flow properties of biodiesel from waste cooking oil", *Fuel,* **117**, pp.876-881.

[16] K. Gülderen, M. Erdoğan, Z. Haci Bayram, D. Serpil (2013), "In vitro amoebicidal activity of poly(maleic anhydrideco-vinyl acetate) copolymer on acanthamoeba spp. trophozoites and cysts", *Basic Clin. Sci.,* **2**, pp.1-14.

[17] M.A. Masuelli (2012), "Mark-Houwink parameters for aqueous-soluble polymers and biopolymer at various temperatures", *Journal of Polymer and Biopolymer Physics Chemistry,* **2(2)**, pp.37-43.

[18] N. Gheorghe, B. Camelia, T. Carmen, P. Iuliana, C. Igor, H. Ionel, H. Doina (2001), "Behaviour of the poly(maleic anhydride-co-vinyl acetate) copolymer in aqueous solutions", *European Polymer Journal,* **37**, pp.729-735.

[19] L. Cao, J. Wang, C. Liu, Y. Chen, K. Liu, S. Han (2014), "Ethyelene vinyl acetate copolymer: a bio-based cold flow improver for waste cooking oil derived biodiesel fuel", *Applied Energy,* **132**, pp.163-167.

[20] P.V. Pengmei, C. Yufeng, Y. Lingmei, Y. Zhenhong, L. Huiwen, L. Wen (2009), "Improving the low temperature flow properties of palm oil biodiesel: addition of cold flow improver", *Fuel Process Technol.,* **110**, pp.61-64.

[21] Phan Thi Tuyet Mai, Tran Thu Huong, Pham Ngoc Lan, Luu Van Boi (2017), "Synthesis and characterization of comb-shape (maleic acid alkyl ester-vinyl aceatate) copolymers for cold flow impovers of biodiesel", *The 6th Asian Symposium on Advanced Materials*, September 27-30th, pp.728-733.

[22] C.C. Gabrielle, P. Irina, C. Adrian (2006), "Synthesis and characterization of maleic anhydride copolymer and their derivatives. 2. New data on the copolymerization of maleic anhydride with vinyl acetate", *Revue Roumaine de Chimie,* **51(9)**, pp.923-929.

[23] ASTM Standard D97-12 (2012), *Test method for pour point of petroleum products*.

[24] D.T Nguyen (2007), "Methods in organic chemistry and biochemistry", *Vietnam National University Press*, Hanoi.

[25] X. Jun, X. Shili, Q. Hauiqin, C. Sheng, W. Xiaoming (2013), "Effect of polar/nonpolar groups in comb-type copolymers on cold flowability and paraffin crystallization of waxy oils", *Fuel,* **103**, pp.600-605.

Solution structure of the reduced active site of a starch-active polysaccharide monooxygenase from *Neurospora crassa*

Chinh N. Le[1], Han Phan[2], Duy P. Tran-Le[1], Diem H. Tran[1], Erik R. Farquhar[3], Van V. Vu[1*]

[1]*NTT Hi-Tech Institute, Nguyen Tat Thanh University, Ho Chi Minh city, Vietnam*
[2]*Department of Chemistry, University of Science, Vietnam National University, Hanoi, Vietnam*
[3]*Case Center for Synchrotron Biosciences, National Synchrotron Light Source, Brookhaven National Laboratory, Upton, New York, USA*

Received 12 March 2018; accepted 19 June 2018

Abstract:

X-ray absorption spectroscopy (XAS) was utilized to gain insights into the structure and electronic properties of the reduced copper active site in NCU08746, a polysaccharide monooxygenase (PMO) from *Neurospora crassa* that activates O_2 to cleave glycosidic linkages in starch. The reaction of NCU08746 likely starts with binding of O_2 to the copper(I) center. However, the solution structure of the reduced active site in NCU08746 has not been properly elucidated. In this study, we prepared Cu(I)-NCU08746 in solution, which was snap-frozen to preserve the solution structure of the copper(I) active site prior to XAS analysis. Results show that the copper(I) center in Cu(I)-NCU08746 exhibits a 4-coordinate geometry, which is different from the 3-coordinate geometry observed for some other PMOs. This difference likely arises from the coordination of the active site tyrosine residue and could contribute to the difference in activity between NCU08746 and other PMOs.

Keywords: **oxygen activation, polysaccharide monooxygenase, X-ray absorption spectroscopy.**

Classification number: **2.2**

Introduction

Enzymes that contain a copper active site capable of activating O_2 for C-H bond cleavage are of great fundamental and practical interests. Around 2010, a new superfamily of oxygen-activating mono-copper enzymes called polysaccharide monooxygenases (PMOs) were discovered [1]. It is generally accepted that PMOs degrade polysaccharide via hydroxylating either C-H bond of the glycosidic linkages (Fig. 1). PMOs can act directly on the surface of their polysaccharide substrates in an "endo" fashion, which enables them to work synergistically with currently available industrial hydrolytic enzymes in converting recalcitrant polysaccharides to fermentable sugars [1]. Currently there are 6 families of PMOs listed in the carbohydrate active enzymes (CAZy) database [2]. The starch-active PMO family was discovered in 2014, which is classified as AA13 family in the CAZy database [3]. While other PMOs act on β(1→4) glycosidic linkages found in chitin, cellulose, and xylans, AA13 PMOs only cleave α(1→4) linkages found in starch, which has expanded the perspectives in starch metabolism.

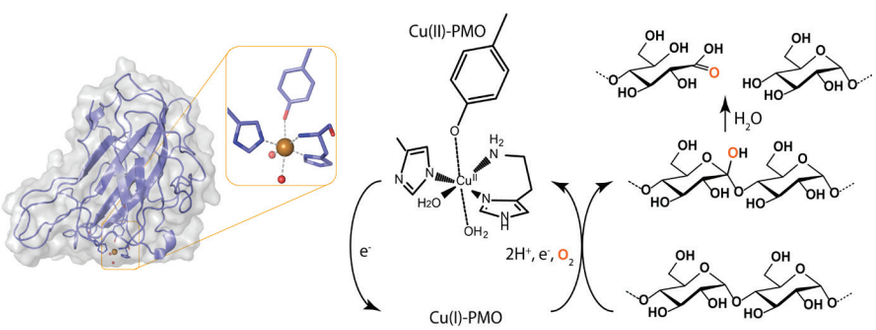

Fig. 1. Structure of Cu(II)-PMO (left) and the PMO reaction (right).

**Corresponding author: Email: vanvu@ntt.edu.vn*

The structures of PMOs have been characterized extensively with single crystal X-ray crystallography (XRD), which revealed an absolutely conserved Type 2 mono-copper active site coordinated by two histidine residues in all PMOs in a motif termed as *histidine brace* [4] (Fig. 1). The *N*-terminal histidine residue coordinates in a bidentate mode using the N atom of its amine group and the $N_{\delta 1}$ atom of the imidazole group (Fig. 1). The other histidine residue coordinates via its $N_{\varepsilon 2}$ atom. The reaction of PMOs likely starts from the reduced state, in which the copper(I) center readily binds O_2 to generate a reactive copper-oxygen species. The structure and electronic properties of the copper(I) center thus play an important role in the mechanism of PMOs. Nevertheless, the structure of PMOs in the copper(I) state (Cu(I)-PMO) have not been well characterized by single crystal XRD. The available structures of Cu(I)-PMO are obtained either from the photo-reduction of the copper(II) center during XRD data collection or from *in crystallo* chemical reduction, which may not represent the true structure of Cu(I)-PMO in solution [4].

In this work, we attempted to obtained insights into the structure and electronic properties of the copper(I) active site in the starch-active PMO NCU08746 of *Neurospora crassa* using X-ray absorption spectroscopy (XAS). The X-ray Absorption Near Edge Structure (XANES) of the XAS spectrum could provide insights into the geometry and electronic properties of the copper center. The extended X-ray absorption fine structure (EXAFS) region contains the important local structural information up to ca 4.5 Å from the copper center. The reduced sample for XAS analysis was prepared under inert gas atmosphere and snap-frozen in a sealed sample holder, which closely represents the solution state of Cu(I)-NCU08746.

Materials and methods

Cu(II)-NUC08746 was prepared as previously described [3]. The enzyme was buffer exchanged to 700 mM MES buffer pH 5.0 and degassed under a stream of argon for 30 minutes and stored in a refrigerator inside an anaerobic Mbraun glove box. Buffer solution and glycerol were degassed by bubbling with argon for 2 hours and left open in the glove box overnight. Ascorbic acid solution was prepared by mixing ascorbic acid powder with anaerobic MES buffer inside the glove box. Cu(I)-NCU08746 sample was prepared by incubating anaerobic Cu(II)-NCU08746 with 15 fold excess anaerobic ascorbic acid at room temperature in the glove box for 30 minutes. Anaerobic glycerol (20% final concentration) was subsequently added to the sample to prevent ice crystal formation when the sample was frozen. The concentration of the enzyme in the final reduced sample was 1.14 mM. The reduced sample was transferred to an XAS sample holder, which was put in a reaction vial sealed with septum screw cap. The vial was taken out of the glove box, immediately frozen in liquid isopentane, and stored in liquid nitrogen until the data was collected. Data collection was carried out at Beamline X3B of the National Synchrotron Radiation Light Source (NSLS) of Brookhaven National Laboratory in Long Island, New York, USA. Data reduction and processing were carried out using Athena [5]. Fitting of the EXAFS data was carried out using Artemis [5] and FEFF6.0 [6]. The FEFF model was built based on a PMO crystal structure (Fig. 2).

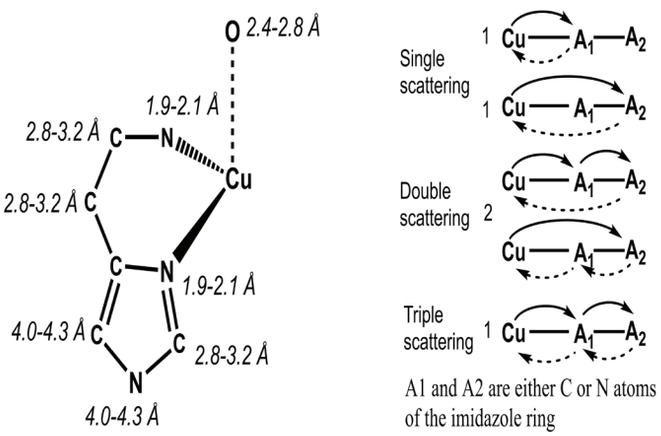

Fig. 2. FEFF input model used for EXAFS fitting and representation of single and multiple scattering paths of the imidazole ring.

Results and discussion

The XANES spectrum of Cu(I)-NCU08746 is shown in Fig. 3, which is significantly different from that of Cu(II)-NCU08746 previously reported [3]. The XANES spectrum of Cu(I)-NUC08746 exhibits a clear shoulder at 8983 eV, which is absent in the spectrum of Cu(II)-NCU08746. The featureless edge of Cu(II)-NCU08746 is consistent with a 5- or 6-coordinate copper center as previously described [3]. In contrast, the shoulder in Cu(I)-NCU08746 is indicative of a coordination number of 3 or 4, which arises from the 1s→4p electron transition of the copper(I) center [7]. This result indicates that the structure of the copper center is

significantly altered upon reduction from Cu(II) to Cu(I).

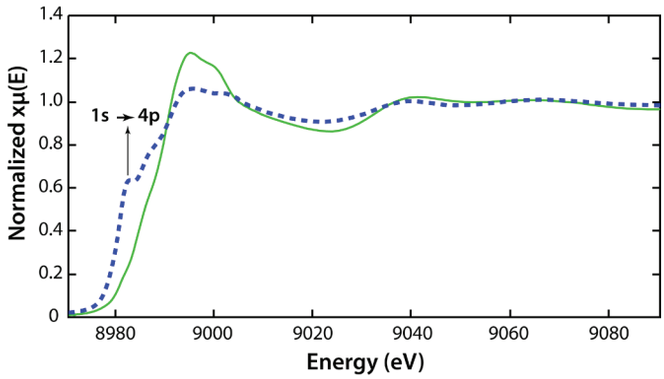

Fig. 3. XANES spectrum of Cu(I)-NCU08746 (dashed blue) obtained in this work in comparison with that of Cu(II)-NCU08746 (solid green) reproduced from ref. [3] with permission.

EXAFS data of Cu(I)-NCU08746 is shown in Fig. 4, which is exhibits a typical double-humped feature of histidine coordinated metal species near 4-4.5 $Å^{-1}$ [4, 8, 9]. The Fourier transform of Cu(I)-NCU08746 exhibits an inner shell at 1.5-2.0 Å, a second shell at 2.0-3.0 Å, and a third shell at 3.0-4.0 Å. The inner sphere can be fitted with several Cu-N/O paths at 1.9-2.5 Å, which is typical for copper enzymes including PMOs. The second shell can be fitted with several Cu•••C paths at ~ 2.9 Å and 3.2 Å, which can be attributed to the C atoms of the histidine ligands as depicted in Fig. 2.

The third shell corresponds to the double-humped feature in the EXAFS spectrum. As shown for many metal-imidazole species, the double-humped feature can be simulated with significant single and multiple scattering paths due to the imidazole ring (Fig. 2). By floating the coordination number of the imidazole ring in the fitting process, Vu, et al. were previously able to closely predict the number of histidine ligands in iron [9] and copper [3] enzymes. Here we used the same approach by fixing the number of histidine ligands at 2 according to the crystal structure of a starch-active PMO in *Aspergillus oryzae* [10]. The double-humped feature of Cu(I)-NCU08746 is reasonably well simulated with two imidazole rings, which were included in all the fits.

Table 1. Fitting results to unfiltered k^3-weighted EXAFS data of Cu(I)-NCU08746.

Fit #	First shell						Second shell			Third shell			R-factor
	Cu-N/O			*Cu-N/O*			*Cu•••C*			*Cu•••Im*			
	N	*R*	σ^2	*N*	*R*	σ^2	*N*	*R*	σ^2	*N*	*R*	σ^2	
1	2	1.90	6.6	1	2.52	3.53	3	2.91	6.0	2	n/a	n/a	0.04835
	1	2.25	5.7				1	3.18	2.8				
2	2	1.88	6.0				3	2.89	0.4	2	n/a	n/a	0.13689
	2	2.60	12.4				2	3.13	6.0				
3	2	1.99	5.1				3	2.94	1.9	2	n/a	n/a	0.18967
	1	2.19	8.0				2	3.19	2.8				

k range = 2-11 $Å^1$; number of independent points is 17; resolution = 0.174 Å; scale factor S_0^2 = 1.0; N = coordination number; R = distance (Å); σ^2 = respective Debye-Waller factor (10^{-3} $Å^{-2}$). Cu•••Im represents the significant single and multiple scattering paths of an imidazole ring.

Notably, the best fit requires a Cu-N/O path at ~ 2.5 Å (Fit #1, Table 1). Removing this path severely lowers the fit quality (Fits # 2 and 3). This path likely arises from the O atom of the active site tyrosine residue (Fig. 1), which is also observed in the crystal structure of photoreduced starch-active PMO from *Aspergillus oryzae* [10]. We thus propose the structure of Cu(I)-NCU08746 as shown in Fig. 5. The coordination of tyrosine to the reduced copper active site has only observed in starch-active PMOs but not on other PMO families [4]. Thus, this difference may contribute to the difference in activity between the starch-active PMO family and other PMO families.

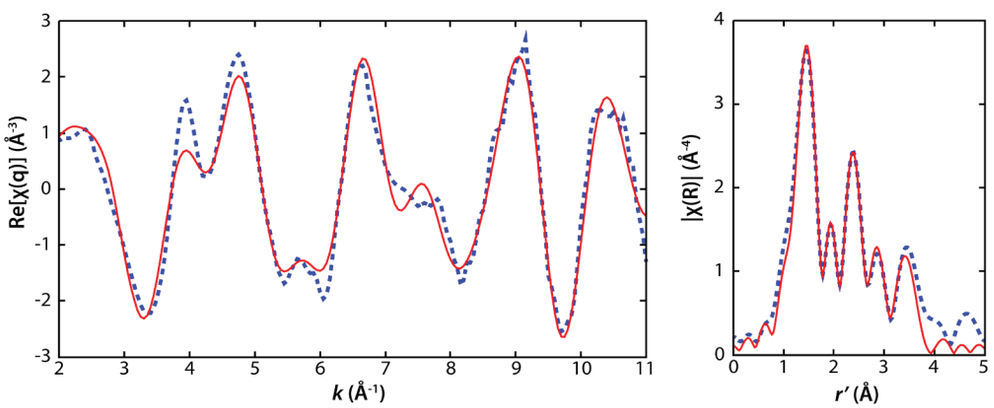

Fig. 4. k^3-weighted EXAFS spectrum (left) and its Fourier transform (right) of Cu(I)-NCU08746. Data is shown as dashed blue line and fit as solid red line. The best fit parameters are provided in Table 1 (Fit # 1).

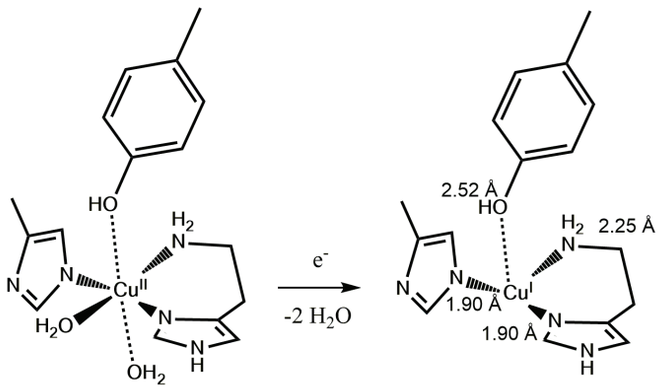

Fig. 5. Proposed structural change upon reduction of Cu(II)-NCU08746 to Cu(I)-NCU08746.

ACKNOWLEDGEMENTS

This research is funded by Vietnam National Foundation for Science and Technology Development (NAFOSTED) grant # 106-NN.02-2016.33.

REFERENCES

[1] W.T. Beeson, V.V. Vu, E.A. Span, C.M. Phillips, M.A. Marletta (2015) "Cellulose Degradation by PMOs", *Annu. Rev. Biochem.*, **84**, pp.923-946.

[2] Carbohydrate-active Enzymes database, http://www.cazy.org/, accessed on February 10, 2018.

[3] V.V. Vu, W.T. Beeson, E.A. Span, E.R. Farquhar, M.A. Marletta (2014), "A family of starch-active polysacchride monooxygenases", *Proc. Natl. Acad. Sci. USA*, **111(38)**, pp.13822-13827.

[4] V.V. Vu, S.T. Ngo (2018), "Copper active site in polysaccharide monooxygenases", *Coord. Chem. Rev.*, **368**, pp.134-157.

[5] B. Ravel, M. Newville (2005), "Athena, artemis, hephaestus: data analysis for X-ray absorption spectroscopy using IFEFFIT", *J. Synchrotron Rad.*, **12(4)**, pp.537-541.

[6] J.J. Rehr, J. Mustre de Leon, S.I. Zabinsky, R.C. Albers (1991), "Theoretical x-ray absorption fine structure standards", *J. Am. Chem. Soc.*, **113(14)**, pp.5135-5140.

[7] R. Sarangi (2013), "X-ray absorption near-edge spectroscopy in bioinorganic chemistry: Application to M-O_2 systems", *Coord. Chem. Rev.*, **257**, pp.459-472.

[8] M. Pellei, et al. (2011), "Nitroimidazole and glucosamine conjugated heteroscorpionate ligands and related copper(II) complexes. Syntheses, biological activity and XAS studies", *Dalton Trans.*, **40(38)**, pp.9877-9888.

[9] V.V. Vu, T.M. Makris, J.D. Lipscomb, L. Que (2011), "Active-site structure of a b-hydroxylase in antibiotic biosynthesis", *J. Am. Chem. Soc.*, **133(18)**, pp.6938-6941.

[10] L.L. Leggio, et al. (2015), "Structure and boosting activity of a starch-degrading lytic polysaccharide monooxygenase", *Nat. Commun.*, **6**, pp.5961-5970.

High-temperature production of acerola vinegar using thermotolerant *Acetobacter senegalensis* A28

Trinh Nguyet Tran, Huynh Xuan Phong, Bui Thi Thao Anh, Bui Hoang Dang Long, Nguyen Ngoc Thanh, and Ngo Thi Phuong Dung*

Biotechnology Research and Development Institute, Can Tho University

Received 11 May 2018; accepted 4 September 2018

Abstract:

Acerola (*Malpighia emarginata*) vinegar is one kind of fruit vinegar produced using acetic acid fermented by acetic acid bacteria. In this study, *Acetobacter senegalensis* A28 was applied in acerola vinegar production at a high temperature. With 1.0% (v/v) of *A. senegalensis* A28 inoculum, the suitable conditions for production of acerola vinegar were determined to be pH 6.5, 20°Brix, 10^6 cells/ml, as well as 4.0% (v/v) of ethanol added to acerola juice. Moreover, a temperature of 35°C was found to be suitable for fermentation in both 100 ml and 2 litre working volumes. Total acid concentrations of 5.45% (w/v) and 4.90% (w/v), respectively, were achieved after 4 days of fermentation. Acid concentrations of 5.40% (w/v) and 4.70% (w/v) were obtained at 37°C after 5 days of fermentation in volumes of 100 ml and 2 litres, respectively. At pilot-scale fermentation of 20 litres at 37°C, acid concentration of 3.68% (w/v) was achieved after 5 days of fermentation.

Keywords: **acerola, acetic acid bacteria, *Acetobacter senegalensis,* fruit vinegar, thermotolerance.**

Classification number: **2.2**

Introduction

Fermentation products have been studied to improve their quality, productivity, scale, and diversity to meet consumers' increasing demands. Today, such research brings the possibility of the application of the results to industrial production [1]. One of these products is vinegar, a condiment that is indispensable in our daily diet; in addition, it plays an important role in supporting and maintaining human health. At present, many new types of vinegar are being studied and put into trial production at low cost. These are based on inexpensive and readily available raw materials, compared to traditional rice vinegar, in order to meet the current market's demands. Among the variety of methods of fermentation, sink methods are most commonly used. Much research has been conducted to explore the possibility of producing fruit vinegar from many sources, such as pineapple peel [2]. Acetic acid bacteria (AAB), one of the essential bacteria in vinegar fermentation, are being studied by scientists (e.g. oxidation mechanisms of ethanol to produce acetic acid, methods for identification, etc.), and achieve a variety of applications in practice. Thus, the process of vinegar fermentation is being optimised day by day. They are very diverse in nature (appearing more in fruits, grains, herbs, etc.) and are important in the food industry for oxidizing sugar and wine into acetic acid [3, 4]. Therefore, AAB play an important role in the industrial production of vinegar. In addition, they can be used in the production of cellulose and sorbose [5]. Temperature is a factor that plays an important role - it is the deciding factor in vinegar fermentation. However, climate change which is increasing global temperatures, is significant challenge for the fermentation ability of AAB. The optimal temperature for the fermentation of AAB is 28-30°C, and increased temperature has a strong influence on the production of vinegar [1, 6]. Therefore, today, the study of thermotolerant

*Corresponding author: Email: ntpdung@ctu.edu.vn

strains of AAB is an important consideration, not only for scientists but also for producers. In addition, the application of heat-resistant strains of AAB in large-scale industrial manufacturing is widely studied at present.

The goal of this paper is twofold: to determine the suitable proportion of ethanol to be added, and the favorable pH value, °Brix, and cell density; and to study high-temperature vinegar fermentation from acerola at working volumes of 2 litres and 20 litres.

Materials and methods

Culture and materials

Thermotolerant *A. senegalensis* A28 was isolated from a rice wine starter, identified, and stored at the Food Biotechnology Laboratory, Biotechnology Research and Development Institute, Can Tho University. Acerola which had ripened to a red colour was selected and purchased at An Nghiep market, Ninh Kieu district, Can Tho, Vietnam.

Examination of the characteristics of A. senegalensis A28

A. senegalensis A28 was cultured in yeast extract-peptone-glycerol-D_glucose (YPGD, yeast extract 5 g/l, peptone 5 g/l, glycerol 5 g/l, D-glucose 5 g/l) agar and broth for 24-48 hours at 35°C to observe the bacterial shape and cells under the microscope. Gram stain, catalase, and oxidase tests were conducted

Study of the suitable proportion of ethanol to be added to the acerola juice

The experiment was designed according to completely random design (CRD), with one factor, five levels (proportion of ethanol added (4, 5, 6, 7, 8% v/v)) and three replications. °Brix, pH, and cell density of the acerola juice were adjusted based on the suitable conditions selected from the previous section, and were supplied with a percentage of ethanol as experimental design. The amount of acid, pH value, and amount of total sugar were determined during 7 days of fermentation in aerobic conditions at 35°C.

Study of the suitable levels of °Brix, pH, and cell concentration for vinegar fermentation

The experiment was designed according to CRD, with 3 factors, 3 levels, and 3 replications: °Brix (15, 20, 25); pH (3.5, 5, 6.5); cell concentration (10^3, 10^5, 10^7 cell/ml). *A. senegalensis* A28 was cultured in a YPGD medium for 48 hours at 30°C, and the acerola juice was diluted with distillated water at a ratio of 1:4. °Brix, pH, and cell density were adjusted according to the experimental design, sterilised with $NaHSO_3$ (140 mg/l), and supplied with 4% (v/v) ethanol. The amount of acid amount, pH value, and amount of total sugar were determined during 7 days of fermentation in aerobic conditions at 35°C.

Study of vinegar fermentation with a working volume of 100 ml

The experiment was designed according to CRD with 3 levels of temperature: 35°C, 37°C and 39°C, and 3 replications. °Brix, pH, cell density, and the percentage of ethanol in the acerola juice were adjusted based on the suitable conditions selected from the previous sections. The prepared acerola juice with a volume of 100 ml was incubated at 35°C, 37°C, and 39°C. The amount of acid, pH value, and amount of total sugar were determined during 7 days of fermentation in aerobic conditions.

Study of vinegar fermentation with a working volume of 2 litres

The experiment was designed according to CRD with 3 levels of temperature: 35°C, 37°C and 39°C, and 3 replications. °Brix, pH, cell density, and the percentage of ethanol in the acerola juice were adjusted based on the suitable conditions selected from the previous sections. The prepared acerola juice with a volume of 2 litres was incubated at 35°C, 37°C, and 39°C. The amount of acid, pH value, and amount of total sugar were determined during 7 days of fermentation in aerobic conditions.

Study of vinegar fermentation with working volume of 20 litres

The experiment was designed according to CRD with 2 levels of temperature (37°C and 39°C) and 3 replications. °Brix, pH, cell density, and the percentage of ethanol in the acerola juice were adjusted based on the suitable conditions selected from the previous sections. The prepared acerola juice with a volume of 20 litres was incubated at 37°C and 39°C. The amount of acid, pH value, and amount of total sugar were determined during 7 days of fermentation in aerobic conditions.

Acerola vinegar products with the working volumes of 2 litres and 20 litres underwent preliminary analysis using quality indicators following Vietnam's standard No. 3215:79. This included: sensory evaluation (colour, odour, and clarity) by 10 people, as well as pH, amount of retentive ethanol, and amount of total acid amount.

Data analysis

The results of these experiments were calculated using Microsoft Excel 2013 (Microsoft Inc., USA) software and statistically analyzed using Statgraphic Centurion XV (Statgraphics Technologies Inc., USA).

Results and discussion

Morphological and biochemical characteristics of A. senegalensis A28

The colonies of bacteria were circular, convex, opaque, and beige, and the cells were coccoid when observed under the microscope. The results of the Gram stain, oxidase, and catalase tests showed that *A. senegalensis* A28 is Gram negative, oxidase negative, and catalase positive. In summary, the morphological and some of the biochemical characteristics of *A. senegalensis* A28 are completely suitable with previous studies of such colonies: circular, convex, opaque, beige, coccoid cells; Gram negative, oxidase negative, and catalase positive [7].

The suitable proportion of ethanol to be added for vinegar fermentation

The initial acerola juice was acidic so it had a lower amount of total acid (3.6% (w/v) and 0.3% (w/v), in turn) and a higher pH value after we adjusted to pH 6.5. Moreover, the amount of total sugar in the juice after we adjusted 20°Brix doubled in comparison to what it had been initially (62.1 g/l and 116.5 g/l). The results of the experiments with 4, 5, 6, 7, and 8% (v/v) ethanol added to the prepared acerola juice are presented in Fig. 1.

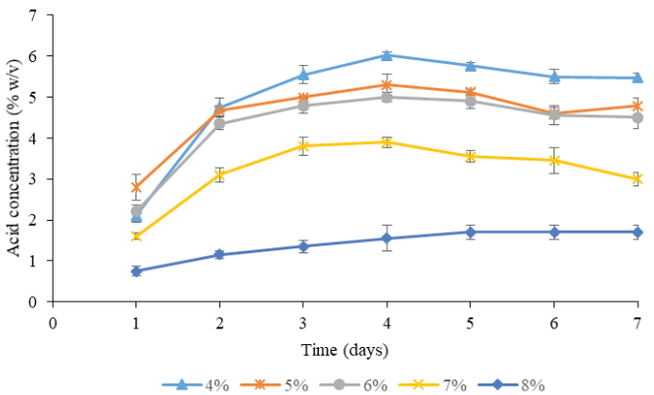

Fig. 1. Total acid production by *A. senegalensis* A28 at different ethanol concentrations.

In almost all the treatments, the amount of acid produced increased from the 1st day to the 4th day and decreased in the last 3 days, especially, the treatment that had 4% ethanol added. Following 7 days of fermentation, *A. senegalensis* A28 in the acerola juice containing 4% (v/v) ethanol produced a larger amount of acid than the other treatments; the highest amount of acid produced was 6.02% (w/v) on the 4th day. The pH value dropped dramatically compared to the initial value (ranging from 4.18 to 3.59 on the final day). The total amount of sugar used in all these treatments was not particularly high (from 13.09 g/l to 11.03 g/l). These results were also suitable with studies of the supplemented the YPGD medium with 4% ethanol [3]. However, the treatment that added 2% and 3% ethanol (v/v) will need to be studied in order to understand more clearly the suitable percentage of ethanol for this strain to grow in acerola juice. In summary, the research supports the finding that the treatment that adds 4% ethanol (v/v) is the suitable concentration (with the acid produced amounting to 6.02% w/v).

The suitable conditions for vinegar fermentation

The results of testing different conditions over 7 days of fermentation are shown in Fig. 2. The surface plotting was constructed using Statgraphics software.

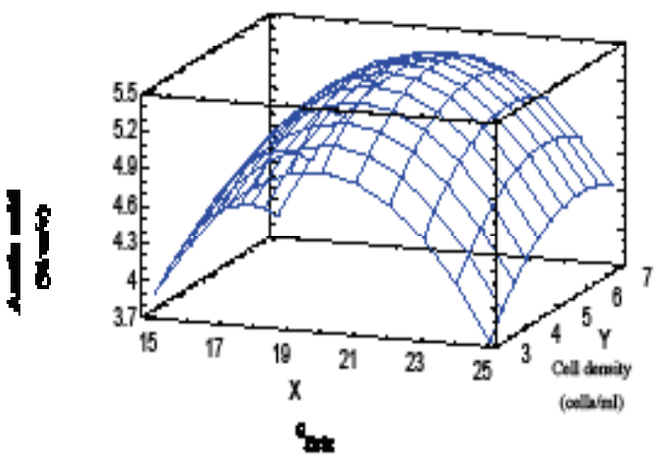

Fig. 2. Surface plotting of acetic acid production.

The final equation in terms of coded factors: Acid content = -19.4669+1.997×X+ 0.798333×Y+0.449444×6.5-0.0468×X×X+0.019×X×Y-0.0288333×X×6.5-0.0825×Y×Y-0.0316667×Y×6.5+0.0488889×6.5×6.5-0.0005×X×Y×6.5

Here, X is the concentration of sugars and Y is cell density. The results were obtained after solving the equation X=20.26°Brix, Y=10^6 cells/ml. As a result, the optimal condition for fermentation was determined as 20.26°Brix (concentration of sugars), initial pH 6.5, and 10^6 cells/ml (cell density). The highest amount of acid produced was 5.88% (w/v). After fermentation, the pH values were reduced. However, thermotolerant bacteria can grow in pH conditions ranging from 3.0 to 7.7. In addition, the

optimal fermentation conditions for acerola vinegar in this experiment were similar to the conditions for the fermentation of banana vinegar: the highest acetic acid level obtained was 4% (v/v) after 6 weeks of fermentation at 37-38°C in a medium containing 5% ethanol (v/v), 20.62 g/l used sugars, and 10^5 cells/ml [8].

Vinegar fermentation at 35°C, 37°C, and 39°C with a working volume of 100 ml

The results of fermentation with *A. senegalensis* A28 in 100 ml of prepared acerola juice are presented in Fig. 3. The amount of total acid of treatments incubated at 35°C and 37°C was much higher than others. Indeed, *A. senegalensis* A28 incubated at 35°C produced the largest amount of acid on the 4th day of fermentation (5.45% w/v); while for the incubation of bacteria at 37°C, the highest amount of acid produced 5.4% (w/v) on the 5th day because when incubating at 37°C, bacteria need more time for their development and growth. In order to save both time for fermentation costs of production for treatment at 35°C, day 4 was selected, as the amount of acid produced then was greater than on the other days. Moreover, the pH value after 7 days of fermentation decreased considerably compared to the initial values (3.19 for the 37°C treatment, and 3.68 for the 35°C treatment). The amount of sugar used for treatments incubated at 35°C and 39°C was very low (11.37 g/l and 14.31 g/l, respectively). In comparison, 2.52% (w/v) of acid was achieved from *A. tropicalis* DK4 after 7 days of fermentation in YPGD containing 4% (v/v) ethanol at 39°C. That is, the amount of acid produced in this study was much higher [9]. This research shows that the fermentation capacity of *A. senegalensis* at three levels of temperatures, 35°C, 37°C, and 39°C. 35°C was the most suitable temperature for the fermentation of acerola juice.

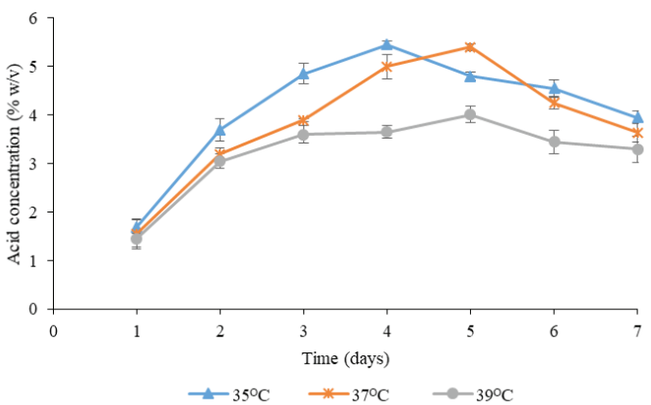

Fig. 3. Total acid production by *A. senegalensis* A28 at a working volume of 100 ml.

Vinegar fermentation at 35°C, 37°C, and 39°C at a working volume of 2 litres

The fermentation results of *A. senegalensis* A28 in 2 litres at 35°C, 37°C, and 39°C over 7 days are presented in Fig. 4. The amount of acid for treatment at 35°C was always higher than two other treatments during fermentation, and, at 35°C, the highest amount of acid was produced on the 4th day (4.9% w/v). However, the amount acid produced in the two treatments at 37°C and 39°C increased from day 1 to day 5 and decreased over the last two days because the bacteria needed time for development and growth. Thus, as with the above experiment, the amount of acid on the 4th day was selected. Moreover, on the 5th day of fermentation, the amount of acid produced was 4.7% (w/v). Subsequently, the range of pH values at the three levels of temperature was 3.58 to 4.01 over 7 days of fermentation. With treatment at 35°C, the amount of sugar used by the bacteria was the lowest (9.9 g/l). In addition, the most suitable temperature for *A. senegalensis* A28 was 28°C [7]. Previous works show that when the temperature increases, the amount of acid produced decreases [1, 10]. Thus, we see that at 35°C, the amount of acid produced was the largest; it decreased when temperature was increased to 37°C and 39°C. In conclusion, experiment shows the fermentation capacity of bacteria at temperatures of 35°C, 37°C, and 39°C at the working volume of two litres.

According to the experiments at the working volume of 100 ml and 2 litres, 35°C was the suitable temperature level for fermentating with acerola juice and *A. senegalensis* A28. However, at 37°C and 39°C, this strain also demonstrated good fermentation capacity and good ability for growth. The purpose of these experiments was to test the fermentation ability of *A. senegalensis* A28 at high temperatures; hence, these two temperatures were selected for fermentation at a larger scale.

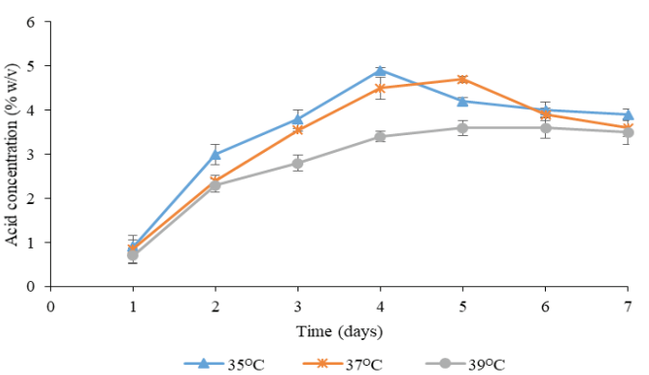

Fig. 4. Total acid production by *A. senegalensis* A28 at a working volume of 2 litres.

Vinegar fermentation at 37°C and 39°C at a working volume of 20 litres

A. senegalensis A28 was fermented with 20 litres of prepared acerola juice, and incubated at 37°C and 39°C in aerobic conditions for 7 days. The results are presented in Fig. 5. Over 7 days of fermentation, *A. senegalensis* A28 produced a higher amount of acid when incubated at a working volume of 20 litres at 37°C (3.68% (w/v) on day 5) in comparison to incubation at 39°C. The amount of acid increased from the 1st day to the 5th day, and decreased over the last 2 days; thus, on days 6 and 7, the amounts of ethanol and sugar were not enough for the bacteria to use for growth and to produce acid.

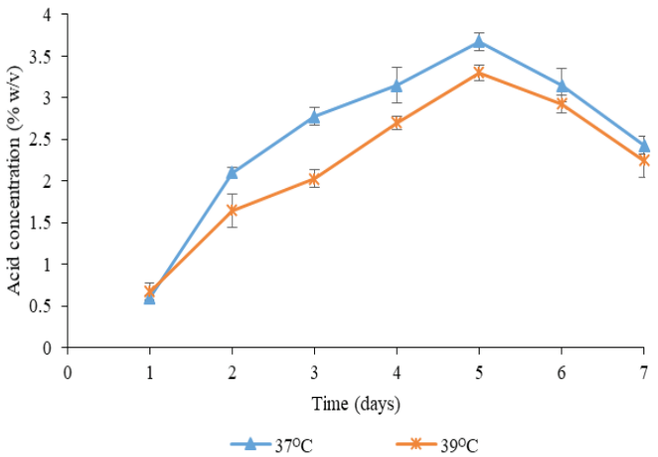

Fig. 5. Total acid production by *A. senegalensis* A28 at a working volume of 20 litres.

At the two levels of temperature, the highest amount of acid was produced on the 5th day of fermentation, so day 5 was selected. The pH value of acerola juice declined dramatically compared to what it had been initially (both 3.52 for the two treatments on the final day). as the amount of sugar used by the bacteria with treatment at 37°C was lower (7.79 g/l). This experiment illustrates that at 37°C, *A. senegalensis* A28 has better fermentation capacity. In comparison with the working volume of 100 ml and 2 litres, the amount of acid produced with the working volume of 20 liters was continuously lower because of the aerobic condition for the fermentation of acetic acid bacteria [11]. Indeed, when bacteria were incubated at larger scale, the surface that was in contact with the atmosphere was decreased, leading to a decline in the amount of acid.

In addition, for acerola vinegar products at a working volume of 2 litres and 20 litres, sensory evaluation by 10 people was undertaken, as was analysis of pH, the amount of acid, and the amount of retentive ethanol. The results of physical and chemical indicators show that the pH and the amount of acid produced correlate with each other. The highest amount of acid produced in five treatments was 5.9% (w/v). The amount of acid in the vinegar was equivalent to that of some vinegar products in supermarkets, such as apple vinegar, rice fermented vinegar, and the like (approximately 4-7% acid, depending on the products). In addition, the amount of retentive ethanol in the acerola vinegar products was very low (the largest was 0.032%); thus, it would not affect consumers' health. The results of the sensory evaluation following TCVN 3215:79 in almost all treatments showed a general score that was higher than 15.2. This means that acerola vinegar products were evaluated as being of 'moderately good' quality. However, treatment at 39°C at a working volume of 2 litres obtained a score of 13.0, that is, a 'medium' standard of quality. Moreover, acerola vinegar products that were incubated at 37°C at working volumes of 2 litres and 20 litres attained higher scores than the others.

Conclusions

The addition of 4% (v/v) ethanol to acerola juice (pH 6.5, 20°Brix), initial bacterial cell density of 10^6 cells/ml, and a fermentation temperature of 35°C are suitable conditions for acerola vinegar fermentation using *A. senegalensis* A28. The amounts of acid at 5.45% (w/v) and 4.90% (w/v) were achieved at working volumes of 100 ml and 2 litres, respectively, after 4 days of fermentation. The amount of acid at a working volume of 100 ml was 5.4% (w/v) and at a working volume of 2 litres was 4.7% (w/v). The acerola juice was fermented for 5 days at 37°C. At a working volume of 20 litres, the highest amount of acid was 3.68% (w/v) when incubated for 5 days at 37°C. In addition, evaluation of organoleptic, physical, and chemical indicators illustrate that treatment at 37°C produced a delicious product that is suitable for the tastes of consumers.

ACKNOWLEDGEMENTS

This research was jointly supported by the Ministry of Science and Technology of Vietnam (contract Nr. 09/2014/HĐ-NĐT); the Advanced Programme in Biotechnology, Can Tho University; and the New Core-to-Core Programme (2014-2019). We would like to thank Prof. Dr Kazunobu Matsushita and Assoc. Prof. Dr Toshiharu Yakushi (Department of Biological Chemistry, Yamaguchi University) for their support and guidance with acetic acid bacteria identification under the JSPS and SSSV exchange research at Yamaguchi University, Japan.

REFERENCES

[1] A. Saeki, G. Theeragool, K. Matsushita, H. Toyama, N. Lotong, and O. Adachi (1997), "Development of thermotolerant acetic acid bacteria useful for vinegar fermentation at high temperatures", *Biosci. Biotechnol. Biochem.*, **61(1)**, pp.138-145.

[2] O.R. Yusuf, M. Jibril, I.M. Misau, and Y.D. Baba (2012), "Production of vinegar from pineapple peel", *Int. J. Adv. Sci. Res. Tech.*, **2(3)**, pp.4-11.

[3] A. Moryadee and P. Wasu (2008), "Isolation of thermotolerant acetic acid bacteria from fruits for vinegar production", *Res. J. Microbiol.*, **3(3)**, pp.209-212.

[4] W. Pathom-aree (2009), "Isolation of acetic acid bacteria from honey", *Maejo Int. J. Sci. Tech.*, **3(1)**, pp.71-76.

[5] I.Y. Sengun and S. Karabiyikli (2011), "Importance of acetic acid bacteria in food industry", *Food Control*, **22(5)**, pp.647-656.

[6] D. Moonmangmee, O. Adachi, Y. Ano, E. Shinagawa, H. Toyama, G. Theeragool, N. Lotong, and K. Matsushita (2000), "Isolation and characterization of thermotolerant *Gluconobacter* strains catalyzing oxidative fermentation at higher temperatures", *Biosci. Biotechnol. Biochem.*, **64(11)**, pp.2306-2315.

[7] B. Ndoye, I. Cleenwerck, K. Engelbeen, R. Dubois-Dauphin, A.T. Guiro, S. Van Trappen, A. Willems, and P. Thonart (2007), "*Acetobacter senegalensis* sp. nov., a thermotolerant acetic acid bacterium isolated in Senegal (sub-Saharan Africa) from mango fruit (*Mangifera indica* L.)", *Int. J. Syst. Evol. Microbiol.*, **57(7)**, pp.1576-1581.

[8] N.T.M. Hien and N.M. Thuy (2014), "Correlation between the amount of produced acid, ethanol, sugar and *Acetobacter aceti* concentration in the production of banana vinegar", *Can Tho Univ. J. Sci.*, **1**, pp.76-83.

[9] H. X. Phong (2011), *Isolation and characterization of thermotolerant acetic acid bacteria*, Master thesis, Can Tho University, Vietnam.

[10] W. Kanchanarach, G. Theeragool, T. Yakushi, H. Toyama, A. Adachi, and K. Matsushita (2010), "Characterization of thermotolerant *Acetobacter pasteurianus* strains and quinoprotein alcohol dehydrogenases", *Appl. Microbiol. Biotechnol.*, **85(3)**, pp.741-751.

[11] D. Mamlouk and M. Gullo (2013), "Acetic acid bacteria: physiology and carbon sources oxidation", *Indian J. Microbiol.,* **53(4)**, pp.377-384.

Brain tumour segmentation using U-Net based fully convolutional networks and extremely randomized trees

Hai Thanh Le[1*], Hien Thi-Thu Pham[2]

[1]Faculty of Mechanical Engineering, Ho Chi Minh city University of Technology, VNU Ho Chi Minh city
[2]Department of Biomedical Engineering, International University, VNU Ho Chi Minh city

Received 12 April 2018; accepted 27 July 2018

Abstract:

In this paper, we present a model-based learning for brain tumour segmentation from multimodal MRI protocols. The model uses U-Net-based fully convolutional networks to extract features from a multimodal MRI training dataset and then applies them to Extremely randomized trees (ExtraTrees) classifier for segmenting the abnormal tissues associated with brain tumour. The morphological filters are then utilized to remove the misclassified labels. Our method was evaluated on the Brain Tumour Segmentation Challenge 2013 (BRATS 2013) dataset, achieving the Dice metric of 0.85, 0.81 and 0.72 for whole tumour, tumour core and enhancing tumour core, respectively. The segmentation results obtained have been compared to the most recent methods, providing a competitive performance.

Keywords: **brain tumour, convolutional neural network, extremely randomized trees, segmentation, U-Net.**

Classification number: **2.3**

Introduction

Accurate brain tumour segmentation plays a key role in cancer diagnosis, treatment planning, and treatment evaluation. Since the manual segmentation of brain tumours is laborious, the development of semi-automatic or automatic brain tumour segmentation methods makes enormous demands on researchers [1]. Ultrasound, computed tomography (CT) and magnetic resonance imaging (MRI) acquisition protocols are standard image modalities that are used clinically. Many previous studies have shown that the multimodal MRI protocols can be used to identify brain tumours for treatment strategy, as the different image contrasts of these MRI protocols can be used to extract important complementary information. The multimodal MRI protocols include T2-weighted fluid-attenuated inversion recovery (FLAIR), T1-weighted (T1), T1-weighted contrast-enhanced (T1c) and T2-weighted (T2).

In recent years, an annual workshop and challenge, called Multimodal Brain Tumour Image Segmentation (BRATS), is held to different benchmark methods that have been developed to segment the brain tumour [2]. The previous studies on brain tumour segmentation can be categorised into unsupervised learning [3] and supervised learning [4, 5] methods. We only reviewed some of the most recent and closely relevant studies to our method.

Unsupervised learning-based clustering has been successfully applied for the brain tumour segmentation.

*Corresponding author: Email: lthai@hcmut.edu.vn

In [3], the Szilagyi group proposed a multi-stage c-means framework for segmenting brain tumours using multimodal MRI scans and received promising results, although limited by the considered scope of the data.

On the other hand, supervised learning-based methods demand a pair of training data and its label to train a classifier that can then be segmented new data without training. Pinto, et al. [4] proposed an algorithm based on a random decision forest (RDF), using a k-fold cross-validation approach. They extracted features for RDF which is intensity complemented and context based features for every voxel represented. Morphological filters were used for post-processing to reduce misclassification errors. Recently, Soltaninejad, et al. [5] applied extremely randomized trees (ExtraTrees) [6] classification with superpixel based segmentation using a single FLAIR scan in four modalities of MRI dataset. Their results achieved an overall 0.88 Dice score of the complete tumor segmentation for both high-grade glioma (HGG) and low-grade glioma (LGG) cases. However, the final segmentation of this method could be influenced by the final delineation caused by the tuning of superpixel size. Additionally, the Soltaninejad group [7] presented a different method by using random forests classifier to segment the brain tumour. This method is based on the features extracted from a fully convolutional neural network (FCN), namely FCN-8s architecture.

Besides, our previous method [8] trained ExtraTrees classifier for brain tumour segmentation based on a region of interest (ROI) of tumour in FLAIR sequence. This method obtained a 0.9 Dice score of the complete tumour but received a low score of enhancing and core tumour with the BRATS 2013 dataset [2].

In the recent years, a lot of researchers have used the convolutional neural networks (CNNs) to classify images, specifically deep CNNs, which makes it possible to train extremely deep neural networks from the random initialised weights with complex and big data. The deep CNNs are constructed by combining many convolutional layers, which convolve an image with kernels to extract features that are more robust and adaptive for discriminative models. Currently, various deep learning methods have achieved the high score in BRATS challenges [9-11]. A detailed review of various medical image classification, segmentation, and registration methods can be found in [12]. Biomedical images have many patterns of the object such as the tumours, and their intensities are usually variable. Ronneberger, et al. [13] developed the U-Net-based fully convolutional networks (FCNs), which consist of a down-sampling (encoding) pathway and an up-sampling (encoding) pathway with residual connections between the two that concatenate feature maps at different spatial scales in order to segment the cell cancer. Based on the original U-Net architecture, some groups [14, 15] proposed a method for brain tumour segmentation and achieved the competitive performance of those built models with BRATS datasets.

However, there are still several challenges: (1) most methods obtain the promising results for HGG cases, but the performance of LGG cases is still poor; (2) especially, the segmentation of enhancing and core tumor always has a low score compared to complete tumor score; (3) finally, the demand for reducing computation time and memory is still unsatisfied.

In this study, we propose a novel segmentation method that uses the U-Net architecture [13] to extract features and then inputs these to train ExtraTrees classifier [8]. Furthermore, we apply a simple filter in a postprocessing step to eliminate misclassified labels.

Methods

Discriminative models create a decision function that describes the input vectors and assigns each vector to a class. The decision function aims to make the needful informational relation based on the training samples. Additionally, the performance of segmentation depends on the quality of the input data and the extraction of effective features. The models for segmentation tasks create the relational space based on the intensity information of input images to ground truth images.

The general structure of our model is shown in Fig. 1. In the following part, we will describe the role of each part of brain tumour segmentation.

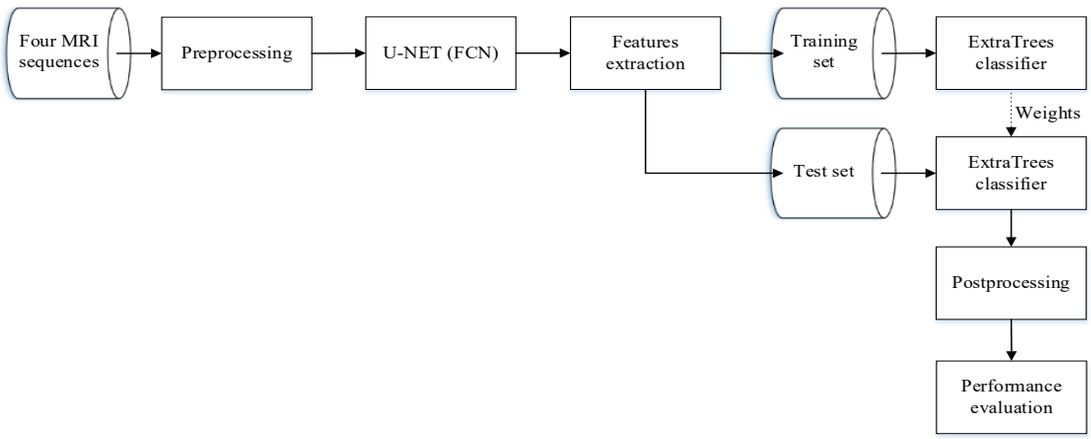

Fig. 1. The proposed discriminative model.

Dataset

The proposed method is trained and validated on the BRATS 2013 dataset [2], which consists of 30 patient MRI scans, of which 20 are HGG and 10 are LGG. Each patient has four MRI sequences including FLAIR, T1c, T2 and T1. This dataset with multimodal MRI data has already been skull-stripped, registered into the T1c scan and interpolated into 1×1×1 mm^3 with a sequence size of 240×240×155. Moreover, the ground truth images of dataset were manually labeled into four types of intra-tumoral classes (labels): 1-necrosis (red), 2-edema (green), 3-non-enhancing (blue) and 4-enhancing tumour (yellow) and the others are 0-normal (healthy) tissue (black) as shown in Fig. 2 (GT). The ground truth data have been used in two steps: model training and performance evaluation for final segmentation.

Pre-processing

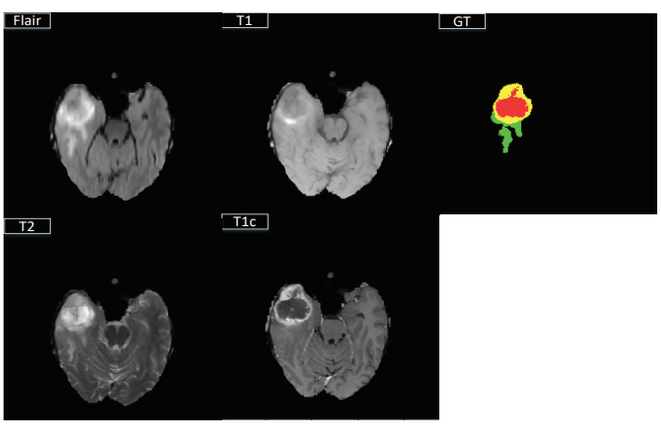

Fig. 2. Four MRI modalities and their ground truth from HGG patient.

In this study, we applied the N4ITK method [16] to reduce inhomogeneity in MR images. A histogram normalisation method [17] was then employed to ensure that addresses data heterogeneity caused by multi-scanners acquisitions of MR images. Finally, the intensities of each MRI sequence were normalised by subtracting the average of intensities of each sequence and then dividing them by its standard deviation. Fig. 2 shows the sample of four MRI modalities and their ground truth from HGG patient 0001 after pre-processing.

U-Net based deep convolutional neural networks

Our network is similar in spirit to the U-Net [14], which is different from the original U-Net [11]. The U-Net [14] described in Fig. 3 uses the deconvolution operator instead of an up-sampling operator in the decoding pathway and applies zero padding to keep the same resolution of output images as the input images. Therefore, the network does not need a cropping operator of the border regions. Every block in the encoding pathway has two convolutional layers with a 3×3 filter, a stride of 1 and rectified linear unit (ReLU) activation, which increases the number of feature maps from 1 to 1024. For the down-sampling, max pooling with stride 2×2 is used to the end of every block except the last block. Therefore, the size of feature maps decrease from 240×240 to 15×15. In the decoding pathway, every block starts with a deconvolutional layer with same size filter in the decoding pathway and a stride of 2×2, which doubles the size of feature maps in both directions but decreases the number of feature maps by two. Thus, the size of feature maps increases from 15×15 to 240×240. In every up-

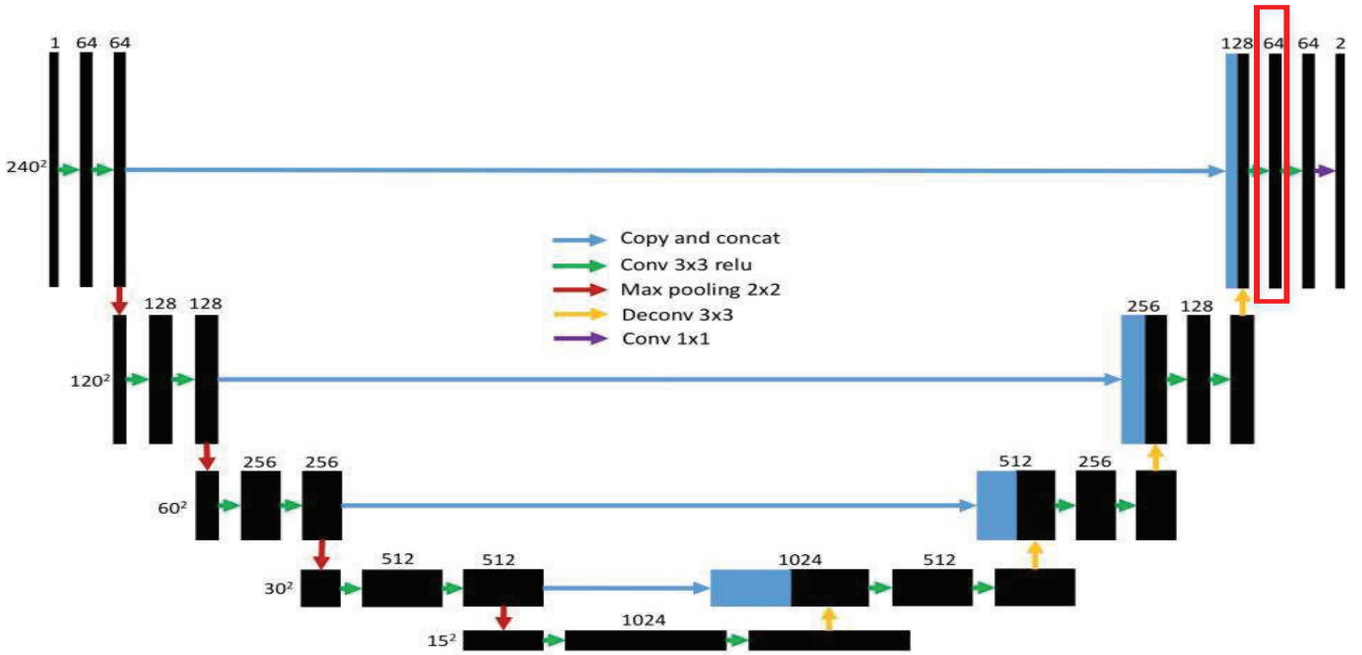

Fig. 3. The U-Net architecture [14].

sampling block, two convolutional layers reduce a half of the feature maps after concatenating the deconvolutional feature maps and the feature maps from the encoding path.

Our proposed network is then added to the batch normalization [18] layer after each convolutional layer for regularization purposes.

Feature extraction

Image processing provides many algorithms for the extraction of characteristics from images. In the field of biomedical image analysis, many studies are trying to find the tumour characteristics with a high correlation to the appearance of the brain images. Nonetheless, no proper feature sets have been extracted yet, which is why various groups need to use a large feature set based on many feature extraction methods such as texture features, spatial context features and higher order operators.

The U-Net model uses the powerful CNN to filter the useful features from input data in encoding pathway and then embeds these features in the output map with the same position in the decoding pathway. It makes the collected features easier to calculate for the next step or compare with the desired output. In this study, we extracted the features in all MRI protocols from the U-Net model, but we did not obtain the output of the model from a top layer, as it was only two values. We collected the features from the convolutional layer next to the concatenated layer in the final block of the decoding pathway as shown a red rectangle in Fig. 3. This

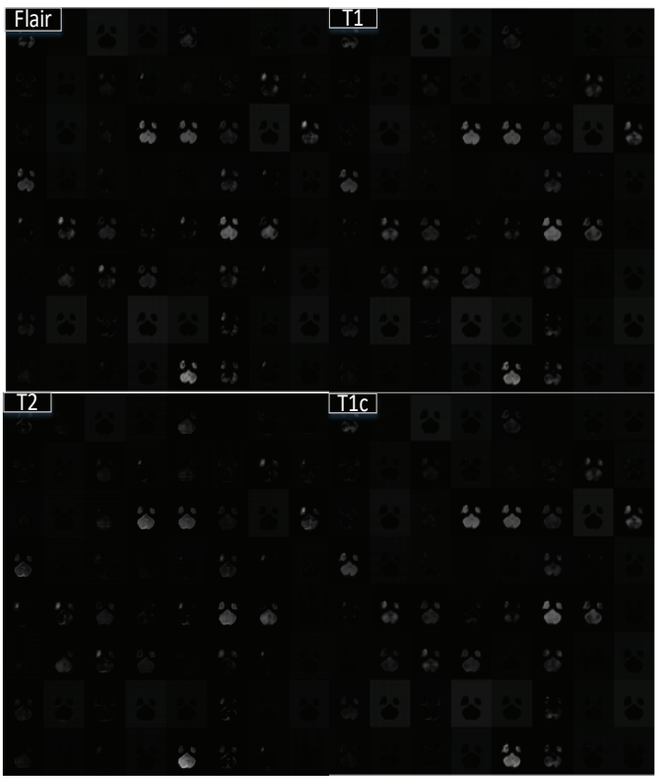

Fig. 4. Feature maps from four MRI multimodalities.

output has 64 feature maps with the size of 240×240 and total parameters of 73792 for each image of MRI scans. Fig. 4 shows the feature maps of each image of FLAIR, T1c, T2 and T1 sequences extracted from the U-Net model.

Training set and test set

From the BRATS 2013 dataset, we used the first half of HGG and LGG cases with all MRI modalities for the training set and the second half of dataset including 10 HGG and 5 LGG cases to evaluate the performance of our method. In this study, the HGG and LGG training sets are combined, trained and cross-validated together.

Classifier

In our method, the Extremely Randomized Trees (ExtraTrees) [6] classifier is the main part of the brain tumour segmentation system. In our previous work [8], we had described the reason for choosing this classifier with the following advantages:

- High accuracy
- Easy handling of large datasets
- Estimating feature importance.

In the ExtraTrees classifier, the splitting rule differs from the Random Decision Forests in how the randomness is applied to choose the cut-points for each candidate feature during the training. It means that a single threshold is chosen at random instead of searching the best threshold for each feature. This classifier usually allows to reduce the variance of the model a bit more. Thus, it can provide slightly better results than the Random Decision Forests.

The main parameters of the ExtraTrees classifier are the number of trees, depth of tree and the set of attributes (K) that performs the random split. For the classification tasks, the optimum value of K is $K=\sqrt{n}$, with n being the total number of features; in our study, K=16. After that calculation, we tuned the other parameters with different number of trees and depths of the tree on the training set and evaluated the accuracy of classification. The highest accuracy was achieved with the number of trees $N_{tree}=50$ and depth $D_{tree}=15$ as in [7]. Finally, the ExtraTrees classifier was trained by combining the features extraction described above to a 256-dimensional feature vector.

Postprocessing

Our model is applied without a priori information about the classified objects; hence, the obtained results have to be refined by postprocessing. In this step, we employ simple morphological filters including dilation and erosion with a structuring element of a 3×3 square to remove small false positives (the misclassified labels or 'salt' noises) in the segmented image while keeping the large tumorous regions unaffected.

Performance evaluation

The final step of segmentation is an evaluation of the obtained results. In this study, we evaluate the tumour segmentation on three sub-tumoral regions, following [2], which are the enhancing tumour, the core (necrosis + non-enhancing tumour + enhancing tumour) and the complete tumour (all classes combined), by using the measurements in Dice coefficient and Sensitivity [19]. The Dice score provides the overlap measurement between the ground truth images from the BRATS 2013 dataset and the segmentation results of our proposed method:

$$Dice = \frac{2TP}{FP+2TP+FN} \quad (1)$$

in which, TP, FP and FN denote the true positive, false positive and false negative measurements, respectively.

Additionally, sensitivity is used to determine the number of TP and FN:

$$Sensitivity = \frac{TP}{TP+FN} \quad (2)$$

Results and discussion

In this study, we proposed using the ExtraTrees classifier with features learned from U-Net-based fully convolutional neural networks for solving the brain tumour segmentation challenge. For HGG and LGG training sets, the images were selected from each MRI sequence that depends on their ground truth's energy with a threshold value of HGG greater than LGG. Therefore, this step helped in reducing the number of images that are put into the U-Net model to extract features for training data.

Our U-Net model and ExtraTrees classifier were implemented in Keras [20] with a TensorFlow [21] backend and open source library provided by [22]. The best advantage of our proposed method is that the training

Table 1. Dice and sensitivity scores of our proposed method compared to the results from other groups recently published random forests, ExtraTrees and U-Net based methods for the BRATS 2013 dataset.

Method	Dice score			Sensitivity		
	Complete	*Core*	*Enhancing*	*Complete*	*Core*	*Enhancing*
Proposed	0.85	0.81	0.72	0.87	0.85	0.82
Pinto [4]	0.86	0.71	0.74	0.82	0.66	0.72
Soltaninejad [7]	0.88	0.80	0.73	0.89	0.77	0.70
Our previous [8]	0.90	0.63	0.61	0.87	0.72	0.65
Dong [14]	0.86	0.86	0.65	0.88	0.90	0.78

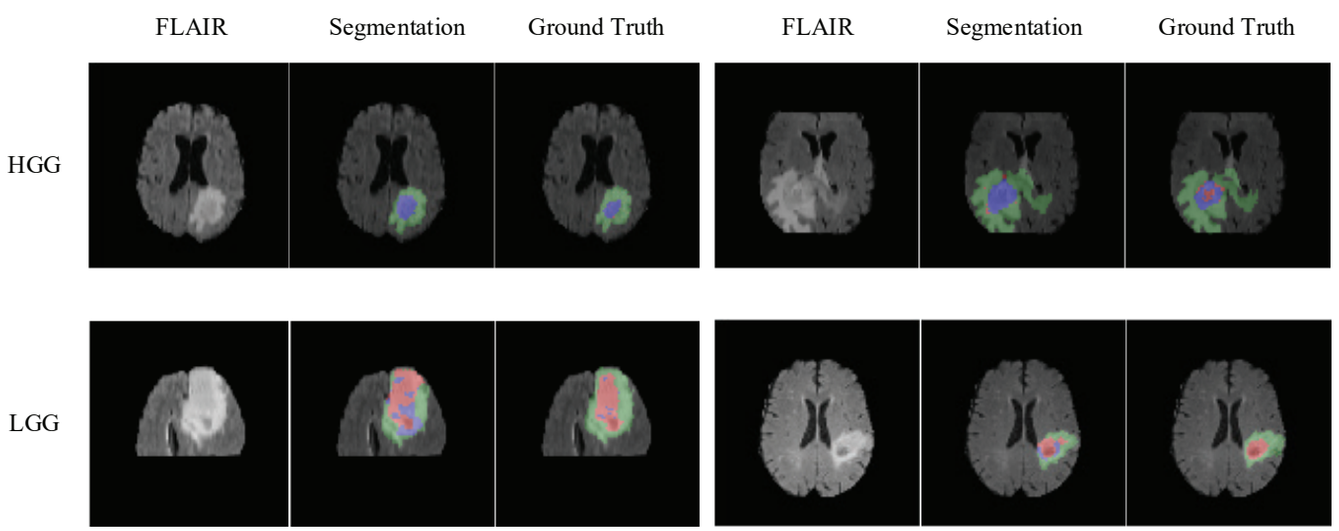

Fig. 5. Segmentation results for the HGG and LGG cases compared to their ground truth.

time is only around one hour, but for the prediction, the computation time is about 3–4 minutes per case. Compared to some studies, our computational time is more efficient than [7-8] and less efficient than [14].

The results of our proposed model and the recent state-of-the-art methods validated on the BRATS 2013 dataset is shown in Table 1. These results are uploaded on the BRATS 2015 server, which evaluates the segmentation and provides measurements in Dice and sensitivity scores of whole tumour, tumour core and enhancing tumour core. Table 1 shows that our method achieves competitive results in the Dice score and performs slightly better in sensitivity measurement for all types of brain tumour with the smaller data for learning.

Figure 5 shows some examples of our qualitative overlaid segmentation results for both HGG and LGG cases on FLAIR MR images compared to the ground truth images. The segmented results are coloured as described in the Dataset section.

Due to the limitation of computational resource, our proposed model is only trained and evaluated on the BRATS 2013 dataset, which contains much less HGG and LGG patient cases than the BRATS 2015 dataset. Furthermore, our model segmenting the enhancing tumour for LGG cases is less successful than for HGG cases because there are fewer LGG cases than HGG cases and because most of the LGG cases rarely have regions of enhancing tumour.

Conclusions

In this paper, we developed a learning-based automatic method for brain tumour segmentation in MR images.

This method used the features extracted from the U-Net-based deep convolutional networks and applied them to the ExtraTrees classifier as the input data. Additionally, we refined the segmentation results by removing the false labels using the simple morphological filters. Based on the BRATS 2013 dataset, in comparing to other state-of-the-art methods, we demonstrated that our approach can achieve comparable results with average Dice scores of 0.85, 0.81 and 0.72 for whole tumour, tumour core and enhancing tumour core, respectively.

ACKNOWLEDGEMENT

This research was carried out in part at the Saijo Laboratory of Professor Yoshifumi Saijo, Department of Biomedical Engineering, Tohoku University. This research is funded by Vietnam National Foundation for Science and Technology Development (NAFOSTED) under grant number 103.03-2016.86.

REFERENCES

[1] S. Bauer, R. Wiest, L.P. Nolte, and M. Reyes (2013), "A survey of MRI-based medical image analysis for brain tumor studies", *Physics in Medicine and Biology*, **58**, pp.97-129.

[2] B.H. Menze, et al. (2015), "The multimodal brain tumor image segmentation benchmark (BRATS)", *IEEE Transitions on Medical Imaging*, **34(10)**, pp.1993-2024.

[3] L. Szilagyi, L. Lefkovits, and B. Benyo (2015), "Automatic Brain Tumor Segmentation in multispectral MRI volumes using a fuzzy c-means cascade algorithm", *The 12th International Conference on Fuzzy Systems and Knowledge Discovery (FSKD)*, pp.285-291.

[4] A. Pinto, S. Pereira, H. Dinis, C.A. Silva, and D.L.M.D Rasteiro (2015), "Random decision forests for automatic brain tumor segmentation on multi-modal MRI images", *Bioengineering (ENBENG) IEEE 4th Portuguese Meeting on IEEE*, pp.1-5.

[5] M. Soltaninejad, G. Yang, T. Lambrou, N. Allinson, T.L. Jones, T.R. Barrick, F.A. Howe, and X. Ye (2017), "Automated brain tumor detection and segmentation using superpixel-based extremely randomized trees in FLAIR MRI", *International Journal of Computer Assisted Radiology and Surgery*, **12(2)**, pp.183-203.

[6] P. Geurts, D. Ernst, and L. Wehenkel (2006), "Extremely randomized trees", *Machine Learning*, **63(1)**, pp.3-42.

[7] M. Soltaninejad, L. Zhang, T. Lambrou, N. Allinson, and X. Ye (2017), "Multimodal MRI brain tumor segmentation using random forests with features learned from fully convolutional neural network", *arXiv preprint arXiv:1704.08134v1*.

[8] H.T. Le, H.T.T. Pham and H.H Tran (2018), "Automatic brain tumor segmentation using extremely randomized trees", *Journal of Science and Technology (Technical Universities)* (accepted).

[9] S. Pereira, A. Pinto, V. Alves, and C.A. Silva (2016), "Brain Tumor Segmentation using Convolutional Neural Networks in MRI Images", *IEEE Transactions Medical Imaging*, **35(5)**, pp.1240-1251.

[10] M. Havaei, A. Davy, D. Warde-Farley, A. Biard, A. Courville, Y. Bengio, C. Pal, P.M. Jodoin, and H. Larochelle (2017), "Brain tumor segmentation with Deep Neural Networks", *Medical Image Analysis*, **35**, pp.18-31.

[11] K. Kamnitsas, C. Ledig, V.F.J. Newcombe, J.P. Simpson, A.D. Kane, D.K. Menon, D. Rueckert, and B. Glocker (2017), "Efficient multi-scale 3D CNN with fully connected CRF for accurate brain lesion segmentation", *Medical Image Analysis*, **36**, pp.61-78.

[12] G. Litjens, T. Kooi, B.E. Bejnordi, A.A. Setio, F. Ciompi, M. Ghafoorian, J.A.W.M. van der Laak, B.V Ginneken, and C.I. Sanchez (2017), "A survey on deep learning in medical image analysis", *Medical Image Analysis*, **42**, pp.60-88.

[13] O. Ronneberger, P. Fischer, and T. Brox (2015), "U-Net: Convolutional networks for biomedical image segmentation", *Medical Image Computing and Computer-Assisted Intervention*, **9351**, pp.234-241.

[14] H. Dong, G. Yang, F. Liu, Y. Mo, and Y. Guo (2017), "Automatic brain tumor detection and segmentation using U-Net based fully convolutional networks", *arXiv preprint arXiv:1705.03820v3*.

[15] A. Beers, K. Chang, J. Brown, E. Sartor, C.P. Mammen, E. Gerstner, B. Rosen, and J.K. Cramer (2017), "Sequential 3D U-Nets for biologically-informed brain tumor segmentation", *arXiv preprint arXiv:1709.02967v1*.

[16] N.J. Tustison, B.B. Avants, P.A. Cook, Y. Zheng, A. Egan, P.A. Yushkevich, and J.C. Gee (2010), "N4ITK: Improved N3 bias correction", *IEEE Transactions Medical Imaging*, **29(6)**, pp.1310-1320.

[17] C.P. Loizou, M. Pantziaris, C.S. Pattichis, and I. Seimenis (2013), "Brain MR image normalization in texture analysis of multiple sclerosis", *Journal of Biomedical Graphics and Computing*, **3(1)**, pp.20-34.

[18] S. Ioffe, and C. Szegedy (2015), "Batch normalization: Accelerating deep network training by reducing internal covariate shift", *The 32nd International Conference on Machine Learning*, **37**, pp.448-456.

[19] D.M. Powers (2011), "Evaluation: from precision, recall and F-measure to ROC, informedness, markedness and correlation", *Journal of Machine Learning Technologies*, **2(1)**, pp.37-63.

[20] F. Chollet, and others (2015), "Keras", *GitHub*, https://github.com/keras-team.

[21] https://www.tensorflow.org/

[22] F. Pedregosa, G. Varoquaux, A. Gramfort, V. Michel, B. Thirion, O. Grisel, M. Blondel, P. Prettenhofer, R. Weiss, V. Dubourg, J. Vanderplas, A. Passos, D. Cournapeau, M. Brucher, M. Perrot, and E. Duchesnay (2011), "Scikit-learn: Machine learning in Python", *Journal of Machine Learning Research*, **12**, pp.2825-2830.

Experimental and numerical analysis of the unreinforced and reinforced notched timber beam by a screw

Van Dang Tran[1*], Dong Tran[2], Marc Oudjene[3]

[1]Division of Transportation, Faculty of Civil Engineering, Thuyloi University, Vietnam
[2]Division of Engineering Geology, Faculty of Bridge and Road Engineering, National University of Civil Engineering, Vietnam
[3]LERMAB, Lorraine University, France

Received 15 May 2018; accepted 1 August 2018

Abstract:

Timber is highly anisotropic. It behaves differently in diverse directions. Tension and compression perpendicular to the grain present a low strength with respect to the ones parallel to the grain. To compensate for the lack, the self-tapping screw is an excellent choice for reinforcing the timber. This paper focuses on the notched timber beam with the experimental and numerical results. In the first part, the experimental results of the unreinforced notched beams and the screw reinforced notched beams under bending load will be presented. The second part describes a numerical study in which a 3D finite element (FE) model and a fast FE model of the notched beam reinforced by a self-tapping screw are realised. In particular, the fast FE model is simplified with the use of the screw's model as a beam element having one translational degree of freedom. This model not only presents a good result in comparison with the experiment as well as the 3D FE model but also requires six times less computational times as compared to the 3D FE model.

Keywords: **cohesive zone, finite element method, self-tapping screw, timber behaviour.**

Classification number: **2.3**

Introduction

Timber structure is mainly used in construction due to its outstanding properties such as high resistance and stability, aesthetic and, in particular, environment-friendly. However, timber behaves weakly in the direction perpendicular to the grain. Hence, its performance in the direction should be optimised to obtain a good global resistance of the timber structure. Various techniques with the aim of increasing the strength of timber structures have been used. These include the use of elements made from timber, iron, steel, aluminium, concrete and the more recent laminated timber, epoxy resins fibber reinforced polymers (FRP). The performance of timber can be extended by adding the steel elements at zones where the timber is weak or the timber can be reinforced by the manufactured technique of gluing several timber lamellas such as the glued laminated timber and the cross-laminated timber. On the other hand, FRP is used because it has several advantages, such as being easily applicable and suitable for the strengthening of timber elements under bending, connections between different elements, local bridging where defects are present, confining local rupture and preventing crack opening. The other solution is the use of epoxy resins as adhesives for the strengthening of extremities of the beam, the filling of hollow sections due to biotic attack and the in situ strengthening of floor beams. However, all these methods require materials with high cost, which are not common, especially in Vietnam. Self-tapping screws become the first choice because of their economic advantages and comparatively easy handling. The European Standard EN 1995-1-1 [1] presents the requirements for self-tapping screws. The literature review shows that the

*Corresponding author: Email: tranvandang@tlu.edu.vn.

research works about reinforcement are mostly focused on testing reinforcement materials and the development of alternative methods [2-10]. Extremely less attention was paid to the calculation methods predicting the load-carrying capacity of reinforced structures and joints [11]. Therefore, the need for the development of design methods arises, as it is a key point to assess the strength and deformation properties of reinforced structures and joints.

The present paper describes the experimental results related to the reinforcement of a notched beam by screws and a simplified finite element model to simulate the global behaviour of self-tapping screw reinforcements in timber structural elements and joints. The numerical methodology has been applied successfully to simulate the load-slip behaviour of timber connections [12-14]. Here, it is presented and applied in the context of reinforcement of the notched spruce beams. The obtained results are compared with the experimental tests, showing good agreement.

Experimental results

Methodology

The beam specimens have been made from a spruce timber, which has an average density of 420 kg/m^3 at the moisture constant that fluctuated between 10% and 12%. The experimental tests consist of two sets of notched beams: unreinforced notched beams (Fig. 1A) and reinforced notched beams (Fig. 1B).

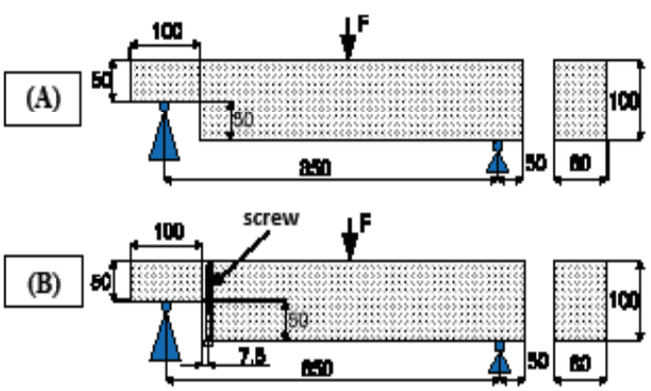

Fig. 1. Schematic illustration of the tested notched beams: (A) unreinforced beams, **(B)** reinforced beams.

The reinforced notched beam is reinforced by one screw at the perpendicular middle of the beam. As the reinforcement of the screw should impact as soon as the failure of the beam at the notch appears, the screw should be as near to the notch as possible (Fig. 2A).

The beams have a total length of 900 mm and a cross section of 100 mm x 80 mm. For the reinforcement of notches, a single threaded-screw of 100 mm length and 5 mm diameter was used (Fig. 2B).

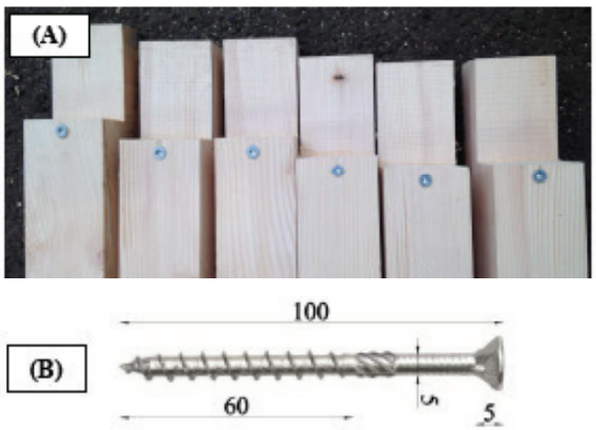

Fig. 2. Reinforced notched beams with one screw.

The specimens were tested under the three-point bending in a standard Instron machine (Fig. 3) with 150 kN load cell capacity at the crosshead speed of 2 mm/min.

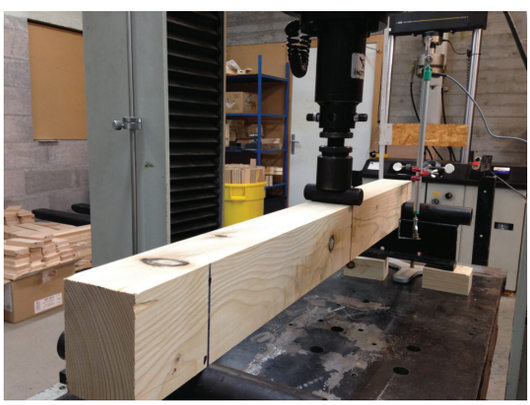

Fig. 3. Three-point bending test set-up.

Results

Fig. 4 and 5 display the experimental load-deflection curves from the unreinforced and the reinforced beams, respectively. Fig. 4 presents a brittle behaviour caused by the damage of timber in transversal tension at the notch. However, the curves from the reinforced beams in Fig.5 show a plastic behaviour after an initial elastic stage. The beams' performance in transversal tension is extended by the reinforcement of the screw. That causes the appearance of the elasto-plastic behaviour of the beams, and the damage initiates at a later stage. From these figures, it can be observed that the reinforced notches noticeably enhanced the load-carrying capacity of the entire beams.

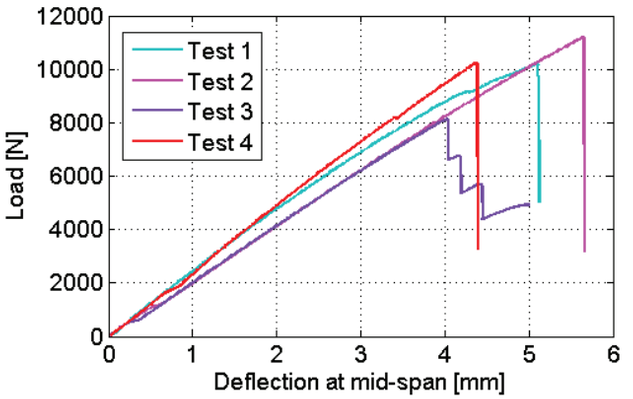

Fig. 4. Experimental load-deflection curves from the unreinforced beams.

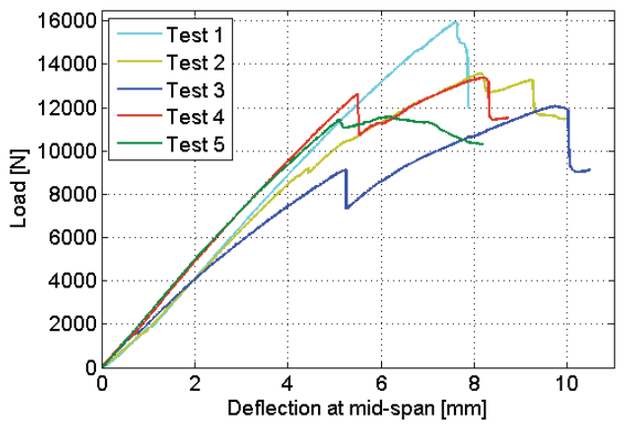

Fig. 5. Experimental load-deflection curves from the reinforced beams.

Additionally, the failure of the reinforced specimens shows less brittleness as compared to that of the unreinforced specimens. The load carrying capacity values recorded from all the beam specimens are summarised in Table 1, where it can be seen that the one-screw reinforcement has delayed the fracture of the notch details leading to the strengthening of the timber beams by about 34%.

Table 1. Experimental results of the reinforced notched beam and the unreinforced notched beam.

Tests N°	F_{max}(kN) Reinforced	F_{max}(kN) Unreinforced
1	15.97	10.17
2	13.57	11.21
3	12.07	08.13
4	13.37	10.22
5	11.58	/
Mean	**13.31**	**09.93**
C.o.V (%)	11.7	6.72

Modelling of the screw reinforcement

Mechanical behaviour of materials

Timber is a natural material. In the ideal model, timber can be considered as a homogeneous anisotropic material in three main directions: the longitudinal direction L (z), following the grain direction, the tangential direction T, corresponding with the tangent of the medullary ray, and the radial direction R, which is the centripetal direction (Fig. 6A, 6B).

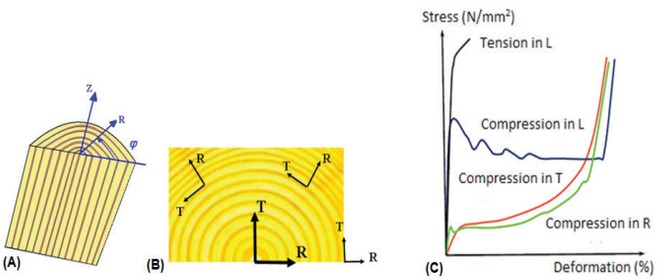

Fig. 6. (A) Longitudinal and radial direction; **(B)** Orthogonal direction: T and R; **(C)** Stress-deformation curve of timber in different directions.

The mechanical behaviour of timber in different directions is quite different. In tension according to the grain, the timber is crushed. In contrast, when it is compressed, the stress-strain curves appear as a flexible term to the endurance point. However, the strength of the wood subjected to the grain is significantly greater than that of compression in different directions (Fig. 6C).

The elastic behaviour is estimated by the Hooke's law, as follows:

$$\begin{pmatrix} \varepsilon_L \\ \varepsilon_R \\ \varepsilon_T \\ \gamma_{RT} \\ \gamma_{LT} \\ \gamma_{LR} \end{pmatrix} = \begin{bmatrix} 1/E_L & -\nu_{RL}/E_R & -\nu_{TL}/E_R & 0 & 0 & 0 \\ -\nu_{LR}/E_L & 1/E_R & -\nu_{TR}/E_T & 0 & 0 & 0 \\ -\nu_{LT}/E_L & -\nu_{RT}/E_R & 1/E_T & 0 & 0 & 0 \\ 0 & 0 & 0 & 1/2G_{RT} & 0 & 0 \\ 0 & 0 & 0 & 0 & 1/2G_{LT} & 0 \\ 0 & 0 & 0 & 0 & 0 & 1/2G_{LR} \end{bmatrix} \begin{pmatrix} \sigma_L \\ \sigma_R \\ \sigma_T \\ \tau_{RT} \\ \tau_{LT} \\ \tau_{LR} \end{pmatrix} \quad (1)$$

where, ε_I: deformations in the main directions (I = L, T, R); γ_{IJ}: angular deformations in the plans IJ (I, J = L, T, R); σ_I: nominal stresses following the direction I; τ_{IJ}: shear stresses in the plan IJ; E_I: Young's modulus according to the direction I; G_{IJ}: Coulomb's modulus according to the plan IJ; υ_{IJ}: Poisson's ratio according to the plan IJ.

The behaviour of plasticity initiates as soon as the stress reaches a threshold σ_e, called elastic limit and is expressed by a plastic criterion f_p.

The plastic criterion can be written by [15, 16]:

$$f_p = \|\underline{\sigma}\| - (R + \sigma_e) = 0; \quad R = \frac{Q}{b}\left(1 - e^{-b\Delta\lambda}\right) \tag{2}$$

where, $\|\underline{\sigma}\|$ is the standard of stress tensor; R is the stress of isotropic hardening; $\Delta\lambda$ is the cumulative deformation of plasticity; Q and b are the parameters of isotropic hardening.

The anisotropic plasticity is estimated by the Hill quadratic criterion [17]. The criterion assumes that the stress of isotropic hardening R is given by 0, so the equation (2) becomes as follows:

$$f_p = \|\underline{\sigma}\| - \sigma_e = 0 \Leftrightarrow \sqrt{\underline{\sigma} : \underline{\underline{H}} : \underline{\sigma}} - \sigma_e = 0$$

$$\Leftrightarrow \sqrt{F(\sigma_{22} - \sigma_{33})^2 + G(\sigma_{33} - \sigma_{11})^2 + H(\sigma_{11} - \sigma_{22})^2 + 2L\sigma_{23}^2 + 2M\sigma_{31}^2 + 2N\sigma_{12}^2} = \sigma_e \tag{3}$$

F, G, H, L, M, N are the Hill's constants, estimated as follows:

$$\sigma_L = \frac{\sigma_e}{\sqrt{G+H}}; \sigma_R = \frac{\sigma_e}{\sqrt{F+H}}; \sigma_T = \frac{\sigma_e}{\sqrt{G+F}}$$

$$L = \frac{\sigma_e^2}{2\tau_{RT}^2}; M = \frac{\sigma_e^2}{2\tau_{LT}^2}; N = \frac{\sigma_e^2}{2\tau_{LR}^2}$$

where, σ_L, σ_R, σ_T, are the threshold stress in compression according to the longitudinal, radial, tangential direction of the grain, respectively, as estimated by the experiment.
τ_{RT}, τ_{LT}, τ_{LR}, are the threshold stress in shear according to the plans RT, LT and LR, respectively, as estimated by the experiment.

During the bending test, the cracking initiates within the notch detail of the beams and propagates along the grain direction under the mode I crack growth. The bi-linear traction-separation law was adequately used for the mode I crack growth [18]. The parameters of the traction-separation law to simulate cracking of timber under mode I have been determined with an appropriate experimental procedure based on the modified DCB test similar to that used in [19, 20].

The linear traction-separation law is assumed to compose of three states: the first is the linear elastic behaviour, the second is the initiation of the damage and then, the last is the evolution of the damage (Fig. 7).

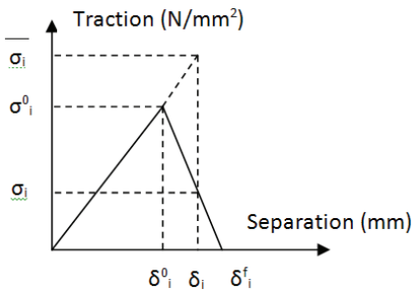

Fig. 7. Traction-separation behaviour.

The elastic behaviour can be estimated as follows:

$$\begin{pmatrix} \sigma_n \\ \sigma_s \\ \sigma_t \end{pmatrix} = \begin{bmatrix} K_{nn} & K_{ns} & K_{nt} \\ K_{sn} & K_{ss} & K_{st} \\ K_{tn} & K_{ts} & K_{tt} \end{bmatrix} \begin{pmatrix} \delta_n \\ \delta_s \\ \delta_t \end{pmatrix} \tag{4}$$

where, σ_n, σ_s and σ_t represent the stresses in the normal and tangential directions, respectively. δ_n, δ_s and δ_t are the relative displacements (separations) in the normal and tangential directions, respectively. K_{ij} is the rigidities in the plan ij (i, j = n, s, t).

The quadratic maximum stress is selected to evaluate the initiation of damage, as follows:

$$\left(\frac{\sigma_n}{\sigma_n^c}\right)^2 + \left(\frac{\sigma_s}{\sigma_s^c}\right)^2 + \left(\frac{\sigma_t}{\sigma_t^c}\right)^2 = 1 \tag{5}$$

where, σ_n^c, σ_s^c and σ_t^c are the maximum stresses according to the nominal and transversal directions.

The evolution of the damage is assumed to be a linear displacement-based softening:

$$\sigma_n = \begin{cases} (1-D)\overline{\sigma_n} \Leftrightarrow \overline{\sigma_n} \geq 0 \\ \overline{\sigma_n} \Leftrightarrow \overline{\sigma_n} < 0 \end{cases}$$
$$\sigma_n = (1-D)\overline{\sigma_s} \tag{6}$$
$$\sigma_n = (1-D)\overline{\sigma_t}$$

where, D is a scalar damage variable, which allows the simulation of the degradation of the cohesive stiffness. It is evaluated by a function of the effective separation as follows:

$$D = \frac{\delta_m^f\left(\delta_m^{\max} - \delta_m^0\right)}{\delta_m^{\max}\left(\delta_m^f - \delta_m^0\right)}$$
$$\delta_m = \sqrt{(\delta_m)^2 + (\delta_s)^2 + (\delta_t)^2} \tag{7}$$

where, δ_m^0 and δ_m^f is the effective displacement at the initiation and ending moment of the damage, respectively; δ_m^{max} is the maximum effective displacement during charging history.

Numerical approach and Finite element models

The behavior of the contact between the screw and the timber is described by three internal forces: tension, shearing and bending (Fig. 8). In this, the shearing and the bending are due to the contact between two bodies of timber. The tension is caused by the contact between the screw and the timber such as the screw-head embedment and the friction between the screw and the timber. In relation to the tension, if the friction between the screw and timber is neglected, the remaining force will be due to the screw-head embedment.

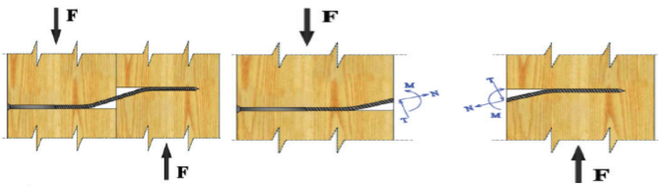

Fig. 8. Internal forces of the reinforced screw.

The basic idea is to build a model with the beam element for the screw's part and the 3D solid element for the timber's part (Fig. 9). However, the problem is the incompatibility of the degree of freedom (dof) between the beam element and the solid element. Therefore, the 2-node beam element has to modified to obtain a modified element beam with only translational dof, which is compatible with the solid element [14]. In this model, the element beam is coupled to the mesh of the solid timber element. The approach has been earlier validated in the context of timber-to-timber and timber-to-concrete connections [12, 13]. Here, it is applied in the context of timber reinforcement based on full continuity between screw and timber similar to steel reinforcement in concrete structures.

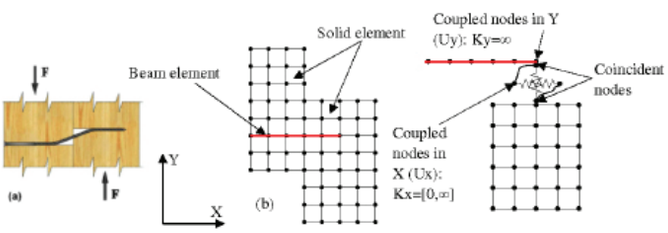

Fig. 9. Beam-to-solid element approach of the reinforced timber by screw.

In order to demonstrate the main advantages of the proposed approach, the simulation of the reinforced beams was undertaken in two ways:

- Model 1: both the screws and the timber beams have been modelled using 3D constitutive laws involving brick-solid element meshes (Fig. 10A).

- Model 2: the timber beam was simulated using 3D constitutive law, whereas the screw was modelled using a one-dimensional beam element (Fig. 10B), leading to a beam-to-solid coupling (proposed approach).

Note that the first model (Model 1) is not efficient in the case of large number of screws. In order to reduce the computational time, only one half of the model was simulated, sine the symmetry of the model (Fig. 10).

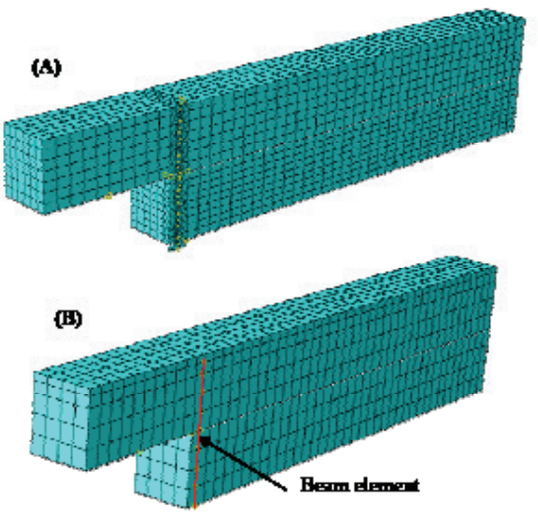

Fig. 10. Finite element meshes (one half) of the notched beams: (A) Model 1; **(B)** Model 2.

For the timber, the 8-node solid element was used. Orthotropic-anisotropic non-linear material model [15, 16, 20-23] has been assumed for the timber behaviour. The mechanical properties of timber are shown in Table 2.

Table 2. Elasto-plastic properties of timber.

Elasticity	Plasticity
E_L = 10000 MPa	f_L = 25 MPa
$E_R = E_T$ = 490 MPa	$f_R = f_T$ = 2.9 MPa
$\upsilon_{LR} = \upsilon_{LT}$ = 0.41	f_{RT} = 5.5 MPa
Y_{RT} = 0.33	σ_e = 25 MPa
$G_{LR} = G_{LT}$ = 650 MPa G_{RT} = 100 MPa	Q = 10 MPa; b = 2.5 F = 73,8; G = H = 0.5 N = M = L = 10.3

To simulate the mode I crack growth in timber, the cohesive zone model (CZM), exhibited in ABQAUS, is used, with the optimal damage parameters summarised in Table 3.

Table 3. The optimal damage parameters of the mode I crack growth.

Stiffness (N/mm^3)	Failure stress (N/mm^2)	Total failure displacement (mm)
$K_{nn} = 2$	$\sigma_n^c = 0.9$	$\delta_m^f = 0.02$

The isotropic elasto-plastic behaviour is used for the screw material and modelled using the modified one-dimensional beam element. The elastic modulus of the screw is selected as $E_s = 210$ GPa and its yield strength is $\sigma_y = 400$ N/mm^2. The nodes of the element beam of the screw and the corresponding nodes of the solid element of the timber were coupled with the constraint condition.

Results and discussion

The numerical simulation of the unreinforced notched beams has been undertaken, and the results were compared with the experiment. It can be seen that the numerical load-deflection curve fits well with the experimental curve (Fig. 11). Thus, it can be concluded that the CZM can adequately simulate the progressive cracking of the timber under opening fracture mode. Fig. 12 displays the comparison between the numerical and the experimental failure modes, which shows a good correlation.

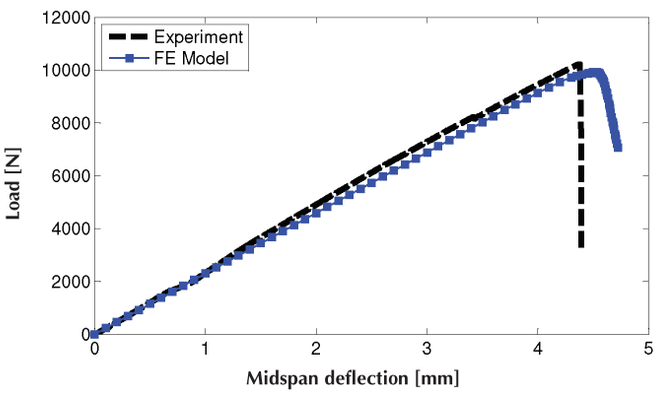

Fig. 11. Comparison between numerically predicted load-deflection curve and experimental curves from unreinforced beams.

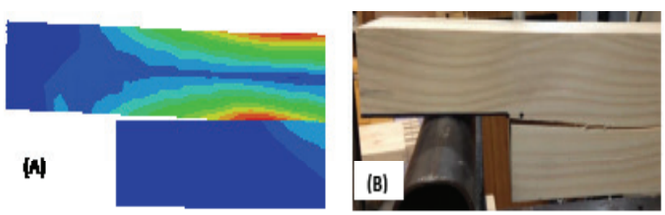

Fig. 12. Failure of the notch detail: (A) FE model, **(B)** experiment.

Figure 13 shows the numerically predicted load-deflection curves against experimental ones. It can be seen that both Model 1 and Model 2 perfectly predict the global response of the reinforced specimens including the progressive failure of the notches.

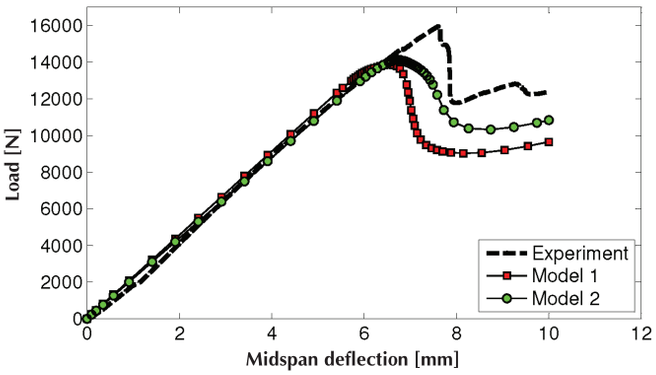

Fig. 13. Comparison between numerically and experimentally predicted load-deflection curves.

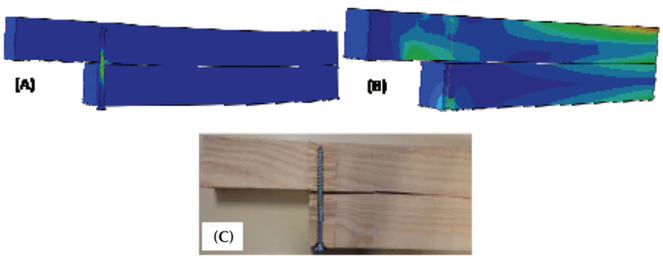

Fig. 14. Comparison between numerically and experimentally predicted failure modes: (A) Model 1, **(B)** Model 2, **(C)** Experiment.

Figure 14 illustrates the experimental mode of failure as well as those predicted by the numerical simulations, where a good correlation can be observed. Both the models show good and similar quality results; however, Model 2 has shown a higher amount of simplicity and quickness, as it requires six times less computational time as compared to Model 1.

Conclusions

This paper presents a simple method for reinforcing the timber structure in using the screws. The research is focused on the notched beam. Two sets of unreinforced and reinforced notched beams have been carried out, in order to find out the mechanism of this structure. Effectively, the notched beam reinforced by a screw shows 34% gain when compared with the unreinforced beam. Through the experiment, it seems that the failure mode of the notched beam is similar to the mode I crack growth. Therefore, in the numerical part, the finite element models were realised, using the cohesive behavior, to simulate the behavior of

the unreinforced notched beam and the reinforced notched beam by a screw. The results present a good correlation in comparison with the experiment. In particular, a fast finite element model has been established, using a beam element with one translational degree of freedom for the screw's model, which allows the reduction of the computational time by six times as compared to the full 3D model.

REFERENCES

[1] European Committee for Standardization EN 1995-1-1:2004+A1 (2008), *Eurocode 5: Design of timber structures - part 1.1: General - common rules and rules for buildings.*

[2] A. Kevarinmäki (2002), "Joints with inclined screws", *Proceeding CIB-W18/35-7-5,* Kyoto, Japan.

[3] F. Prat-Vincent, C. Rogers, et al. (2010), "Evaluation of the performance of joist-to header selftapping screw connections", *World Conference on Timber Engineering*, Trentino, Italy.

[4] P. Ellingsbø, K.A. Malo (2012), "Withdrawal Capacity of Long Self-Tapping Screws Parallel to Grain Direction", *World Conference on Timber Engineering*, Auckland.

[5] P. Mestek, H. Kreuzinger, S. Winter (2011), "Design concept for CLT - reinforced with Self-tapping screws", *Proceeding of CIB-W18/*44-7-6, Alghero, Italy.

[6] S. Franke, B. Franke, A.M. Harte (2015), "Failure modes and reinforcement techniques for timber beams - state of the art", *Construction and Building Materials*, **97**, pp.2-13.

[7] P. Dietsch, R. Brandner (2015), "Self-tapping screws and threaded rods as reinforcement for structural timber elements - A state of the art", *Construction and Building Materials*, **97**, pp.78-89.

[8] H.J. Blaß, M. Frese (2012), "Failure analysis on timber structures in Germany", *Lehrstuhl für Ingenieurholzbau und Baukonstruktionen*, Universität Karlsruhe, Germany, doi:10.1016/j.engstruct.2011.02.030.

[9] H.J. Blaß, P. Schädle (2011), "Ductility aspects of reinforced and non-reinforced timber joints", *Engineering Structures*, **33**, pp.3018-3026.

[10] A.M. Harte, K. Crews (2015), "Special issue: Reinforcement of timber structures", *Construction and Building Materials*, **97,** pp.1-130.

[11] R. Tomasi, A. Crosatti, et al. (2010), "Theoretical and experimental analysis of timber-to-timber joints connected with inclined screws", *Construction and Building Materials,* **24**, pp.1560-1571.

[12] E.M. Meghlat, M. Oudjene, H. Ait-Aider, J.L. Batoz (2013), "A new approach to model nailed and screwed timber joints using the finite element method", *Construction and Building Materials,* **41**, pp.263-269.

[13] M. Oudjene, E.M. Meghlat, H. Ait-Aider, J.L. Batoz (2013), "Non-linear finite element modelling of the structural behavior of screwed timber-to-concrete composite connections", *Composite Structures,* **102**, pp.20-28.

[14] Meghlat, E.M. Oudjene, M. Ait-Aider, H. Batoz, J.L. Batoz (2012), "A one-dimentional 4-node shear-flexible beam element for beam-to-solid modelling in mechanically jointed connections made with screws or nails", *ECCOMAS 2012 - European Congress on Computational Methods in Applied Sciences and Engineering*, e-Book Full Papers.

[15] M. Oudjene, M. Khelifa (2009), "Finite element modelling of wooden structures at large deformations and brittle failure prediction", *Materials and Design*, **30**, pp.4081-4087.

[16] M. Oudjene, M. Khelifa (2009), "Elasto-plastic constitutive law for wood behavior under compressive loadings", *Construction Building Materials*, **23**, pp.3359-3366.

[17] R. Hill (1948), *A theory of yielding and plastic flow of anisotropic metals*, Royal Soc. Lond. Proc., p.281.

[18] Abaqus theory manual (2008), *Dassault Systemes Simulia Corp. Providence: Rhode Island*, U.S.A.

[19] S. Fortino, G. Zagari, A.L. Mendicino, G. Dill-Langer (2012), "A simplified approach for FEM simulation of mode I cohesive crack growth in glued laminated timber under short-term loading", *J. Struct. Mech.*, **45**, pp.1-20

[20] Van-Dang Tran, Marc Oudjene, Pierre-Jean Méausoone (2014), "FE analysis and geometrical optimization of timber beech finger-joint under bending test", *International Journal of Adhesion and Adhesives*, **52**, pp.40-47.

[21] M. Oudjene, M. Khelifa (2010), "Experimental and numerical analyses of single double shear dowel-type timber joints", *Proceedings of the 11th World Conference on Timber Engineering.*

[22] C. O'Loinsigh, M. Oudjene, E. Shotton, A. Pizzi, P. Fanning (2012), "Mechanical behavior and 3D stress analysis of multi-layered wooden beams made with welded-through wood dowels", *Composite Structures*, **94**, pp.313-321.

[23] M. Oudjene, M. Khelifa, C. Segovia, A. Pizzi (2010), "Application of numerical modelling to dowel-welded wood joints", *J. Adhes.Sci.Technol.*, **24**, pp.359-70.

Functional characterisation of a soybean galactinol synthase gene under various stress conditions

Duc Ha Chu[1*], Buffel Melanie[2], Tien Dung Le[1]

[1]*Agricultural Genetics Institute, Vietnam Academy of Agricultural Sciences*
[2]*University of Science and Technology of Hanoi*

Received 28 November 2017; accepted 30 March 2018

Abstract:

Galactinol synthase (GolS) has been known to play a key role in raffinose biosynthesis by catalysing the formation of galactinol. The *GolS* gene family has been recently identified in various plant species. Among them, many individual *GolS* genes have been reported to function in plant stress tolerance. In this study, we reported the construction of transgenic *Arabidopsis* overexpressing a soybean *GolS* gene, *GolS2*. There were no significant differences in the phenotypes of the transgenic and control plants during normal physiological conditions. We evaluated the performance of the transgenic plants under various stress conditions in relation to that of the control plants. The result evidenced that the overexpression of *GmGolS2* gene in *Arabidopsis* improved the plant's tolerance to salt stress but did not protect the plants against heavy metals and paraquat. Our study suggested that soybean *GolS* genes could be a potential candidate for genetic engineering to improve abiotic stress tolerance of plants.

Keywords: ***Arabidopsis thaliana,*** **galactinol synthase, overexpression, phenotypic analysis, stress tolerance.**

Classification number: **3.1**

Introduction

Plant growth and development are greatly affected by adverse environmental conditions. To respond to these stresses, regulatory compounds - including mannitol, proline, and various soluble oligosaccharides - are produced to function in cell protection and maintenance. Among them, the raffinose family of oligosaccharides is evidentially believed to perform a critical role in desiccation tolerance. As a direct precursor of raffinose, galactinol is known as a critical compound in raffinose biosynthesis. In the synthesis of galactinol, galactinol synthase (GolS) is an enzyme catalysing the formation of galactinol from UDP-D-galactose and myo-inositol. Therefore, the study on *GolS* genes may help us expand our understanding of how plants respond to stress conditions.

Up till now, *GolS* genes have been identified in many higher plant species, such as coffee (*Coffea canephora*) [1], wheat (*Triticum aestivum*) [2] and chickpea (*Cicer arietinum*) [3]. Among them, several *GolS* genes were well-established to respond to various stress conditions. For example, transgenic rice lines overexpressing *TaGolS1* and *TaGolS2* contain higher concentrations of galactinol and raffinose and exhibit enhanced cold-stress tolerance [2]. Overexpression of chickpea *CaGolS1* and *CaGolS2* in Arabidopsis conferred improved seed vigour and seed longevity to the transgenic plants [3]. More recently, *Arabidopsis thaliana AtGolS2* gene was reported to strengthen drought tolerance and increase grain yield in rice under dry field conditions [4]. In the past, overexpression of *AtGolS2* caused an increase in the galactinol and raffinose contents in leaves and exhibited improved drought tolerance of transgenic *Arabidopsis* plants [5]. The previous studies clearly indicated that genetic modification of the biosynthesis of raffinose by transformation with *GolS* genes could be an effective method for enhancing stress tolerance in plants. In this study, we generated transgenic lines of *Arabidopsis* overexpressing a soybean *GolS* gene, specifically *GolS2*. Then, transgenic plants were analysed for their abiotic stress tolerance.

Materials and methods

Materials

A. thaliana (Columbia-0 ecotype) and soybean (*Glycine max* L.) Williams 82 cultivar were used in this study.

Methods

Plant transformation: the coding sequence of *GmGolS2* (*Glyma03G38080*) from 'Williams 82' soybean genome

**Corresponding author: Email: hachuamser@yahoo.com*

was cloned into pGreen plasmid in between a cassette containing a 35S promoter and NOS terminator, which also harbours the kanamycin resistance gene. Then, this plasmid was transformed into *Agrobacterium tumefaciens* strain GV3101. Agrobacterium carrying the pGreen-35S::*GmGolS2* plasmid was used for transformation into *Arabidopsis* by following the floral dip technique [6]. Transgenic plants were selected on the kanamycin-containing medium.

Detections of GmGolS2 gene in transgenic plants: to detect the *GmGoLS2* in transgenic plants, we used PCR. The total DNA was isolated from four-week-old plants using the Exgene Plant kit (GeneAll, Korea). PCR primer sequences were aligned to 35S promoter, 5'-CCCACTATCCTTCGCAA-3' and NOS terminator, 5'-GTTGTAAAACGACGGCCAGT-3'. PCR reaction contained 0.2 µM primers, 200 µM dNTP, 1.25 U Taq DNA polymerase in 50 mM KCl, 1.5 mM $MgCl_2$ and 10 mM Tris-HCl pH 8.3. The PCR program comprised 35 amplification cycles at 95°C for 30 seconds and at 54°C and 68°C for 45 seconds each.

Morphological evaluation of transgenic Arabidopsis plants under normal condition: the sterilised *Arabidopsis* seeds were germinated in the Murashige and Skoog (MS) medium agar plates containing 30 mg/l of kanamycin. Two-week-old seedlings were transplanted into 20 cm soil-filled pots and allowed to grow at 24±2°C, relative humidity of 60-70%, under long day conditions (16-hour light/8-hour dark). The growth and development of *Arabidopsis* plants were observed and recorded at indicated times (three-, four- and five-week-old).

Performance of the transgenic plants under various stress treatments: the seeds of transgenic plants overexpressing *GmGolS2* were surface sterilised, placed in the dark at 4°C for two days, and then sown on selective half-strength MS medium agar plates. The seedlings were transferred onto half-strength MS medium supplemented with various concentrations of NaCl (for high salinity condition) and $CdCl_2$ (for heavy metal condition). The survival rates were visually observed and recorded after two days of treatments. For paraquat leaf disc assay, the procedures described in the previous study were followed [7].

Results and discussion

Development of transgenic plants overexpressing GmGolS2 gene

To examine the function of *GmGolS2* gene in plants, we transformed *A. thaliana* plants with *Agrobacterium* carrying the plasmid 35S::*GmGolS2*. The individual kanamycin-resistant plants were finally selected.

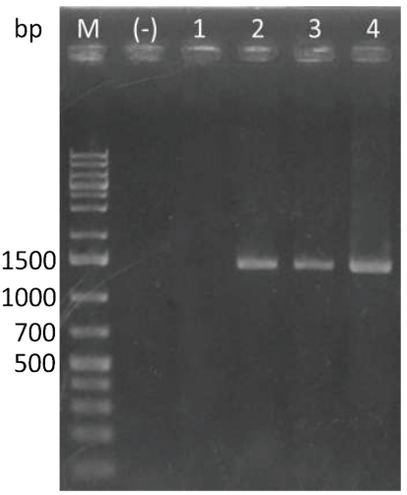

Fig. 1. Verification of the presence of *GmGolS2* gene in *Arabidopsis* transgenic lines. M: 1 kb DNA ladder; lane (-): negative control; lane 1: wild-type control; lane 2-4: transgenic lines.

The transgenic lines were confirmed by PCR. The total DNA extracted from young leaves of each transgenic lines was used as templates. Then, PCR products were visualised on 1.3% agarose gel with 1 kb DNA markers. As shown in Fig. 1, no band was found in the wild-type plant. The presences of a target band (~ 1.5 kb) in lane 2, 3 and 4 clearly confirmed the insertion of *GmGolS2* gene in 3 transgenic lines. In this work, one transgenic line was selected for further studies.

Phenotype evaluation of transgenic Arabidopsis overexpressing GmGolS2

Evaluation of the growth and development of the transgenic plants under normal condition is an important step to functionally characterise these plants in various stress conditions. Sterilised homozygous transgenic *Arabidopsis* seeds were germinated in selective MS medium agar plates, two-week-old seedlings were transplanted into pots. The growth conditions in the greenhouse included a 16h photoperiod, a day/night thermo period of 24±2°C, and a day/night relative humidity of 60-70%. The observations were recorded after 3 weeks.

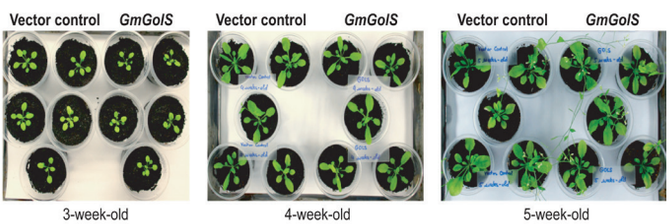

Fig. 2. The evaluation of the morphology of the 35S::GmGolS2 transgenic plants.

As shown in Fig. 2, no significant difference in morphology was visible between the transgenic lines and the control. This observation confirmed that the overexpression of *GmGolS2* gene in *Arabidopsis* did not affect the growth and development of transgenic plants under normal conditions.

Performance of 35S::GmGolS2 Arabidopsis under various stress treatments

In the past, the *GolS* gene family was identified in many plant species [1-3], and most *GolS* genes were reported to be highly expressed under various abiotic stress treatments. For instance, it has been reported that the overexpression of *AtGolS2* caused high accumulation of galactinol and raffinose in leaves and exhibited enhanced drought tolerance of transgenic *Arabidopsis* plants [5]. The previous authors clearly demonstrated that the overexpression of *GolS* genes increased the galactinol and raffinose contents with enhanced abiotic stress tolerance in transgenic plants. Thus, to test whether 35S::*GmGolS2* plants altered their responses to abiotic stress, the transgenic plants were treated under high-salinity, heavy metal, or paraquat conditions.

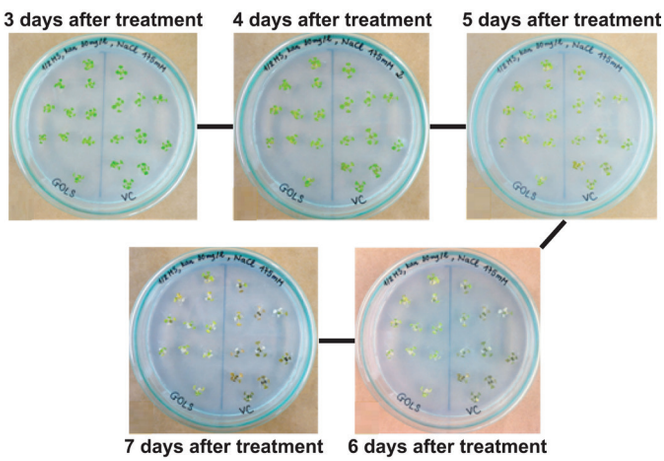

Fig. 3. Survival rates of transgenic plant under high salinity condition.

Previously, transgenic *Arabidopsis* plants overexpressing *TsGolS2* were treated with 0, 50, 100, 150, and 200 mM NaCl. Among them, with 200 mM NaCl, the germination rates of transgenic lines were recorded to be significantly higher than the control plants [8]. Here, we reported the survival rates of our transgenic plants under 175 mM NaCl. Seven days after cultivation on half-strength MS medium with 175 mM NaCl, the transgenic plants still maintained growth, whereas the vector control plants exhibited growth inhibition or died; even the high salt medium inhibited the growth of both transgenic and control plants (Fig. 3). These observations revealed that the overexpression of *GmGolS2* gene conferred salt resistance to transgenic *Arabidopsis* during their growth on the MS plates. Thus, our results indicate that the *GmGolS2* gene functions on improving salt stress tolerance in plants.

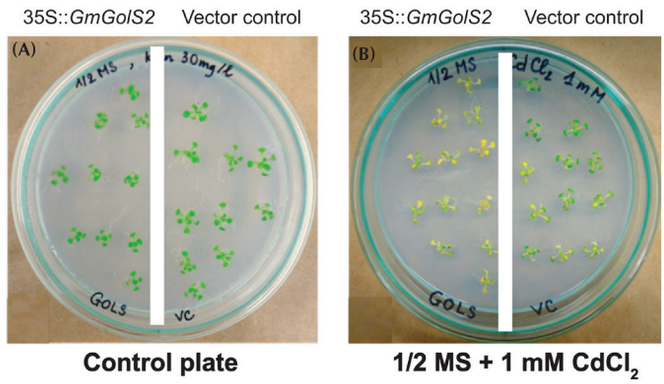

Fig. 4. Survival rates of 12-day-old transgenic plants under (A) normal condition and (B) heavy metal treatment.

Next, to examine the function of *GmGolS2* in heavy metal resistance, transgenic seeds were germinated, grown on selective half-strength MS agar plates and then transferred onto half-strength MS containing 1 mM $CdCl_2$. The result, as shown in Fig. 4, indicates that most transgenic seedlings were yellowing, but a majority of control plants were still green. It seemed that the over-expression of *GmGolS2* did not have a protective role in the plants against heavy metal (Cd) stress.

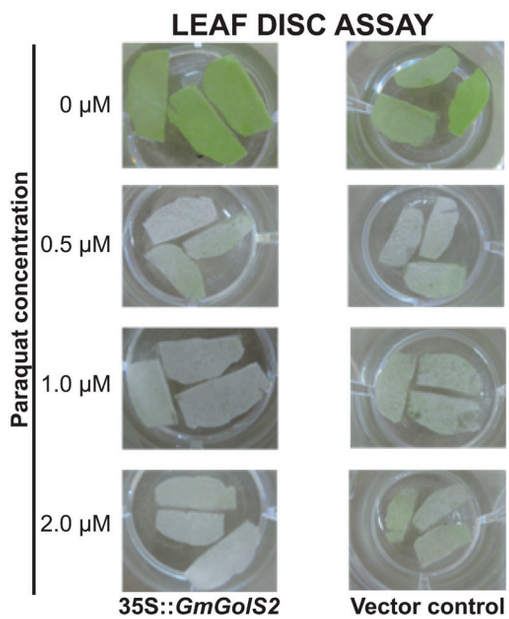

Fig. 5. Paraquat leaf disc assay of transgenic plants.

Finally, we also examined the sensitivity of transgenic plants to paraquat by using leaf disc assay. Paraquat is a recognised compound that generates reactive oxygen species (ROS) in the cell, causing cell injury and cell death [9]. As shown in Fig. 5, paraquat caused loss of the regular green

coloration of transgenic leaves; the leaf discs of the control plants lost their green colour a little bit slower under the same treatment, suggesting that *GmGolS2* did not provide protection against paraquat-induced ROS.

Conclusions

The transgenic *Arabidopsis* plants overexpressing the *GmGolS2* gene have been successfully created by the floral dip method. The presence of *GmGolS2* gene was verified by the PCR test with designed primers.

During normal growth conditions, no morphological differences were observed between the transgenic lines and the control plants. We found that the overexpression of *GmGolS2* gene in *Arabidopsis* did not affect the growth and development of transgenic plants.

The overexpression of *GmGolS2* gene improved tolerance to salt stress but not to heavy metal and paraquat stress in the Arabidopsis plants. This study suggested that soybean *GolS2* gene could be a potential candidate for molecular breeding and genetic engineering to improve abiotic stress tolerance of plants.

REFERENCES

[1] T.B.D. Santos, et al. (2015), "Galactinol synthase transcriptional profile in two genotypes of *Coffea canephora* with contrasting tolerance to drought", *Genet. Mol. Biol.*, **38(2)**, pp.182-190.

[2] E. Shimosaka, K. Ozawa (2015), "Overexpression of cold-inducible wheat galactinol synthase confers tolerance to chilling stress in transgenic rice", *Breed Sci.*, **65(5)**, pp.363-371.

[3] P. Salvi, et al. (2016), "Differentially expressed galactinol synthase(s) in chickpea are implicated in seed vigor and longevity by limiting the age induced ROS accumulation", *Sci. Rep.*, **6(35088)**, doi: 10.1038/srep350881.

[4] M.G. Selvaraj, et al. (2017), "Overexpression of an *A. thaliana* galactinol synthase gene improves drought tolerance in transgenic rice and increased grain yield in the field", *Plant Biotechnol. J.*, **15(11)**, pp.1465-1477.

[5] T. Taji, et al. (2002), "Important roles of drought- and cold-inducible genes for galactinol synthase in stress tolerance in *A. thaliana*", *Plant J.*, **29(4)**, pp.417-426.

[6] S.J. Clough, A.F. Bent (1998), "Floral dip: A simplified method for *Agrobacterium*-mediated transformation of *A. thaliana*", *Plant J.*, **16(6)**, pp.735-743.

[7] Ha Duc Chu, Quynh Ngoc Le, Huy Quang Nguyen, Dung Tien Le (2016), "Genome-wide analysis of genes encoding methionine-rich proteins in *Arabidopsis* and soybean suggesting their roles in the adaptation of plants to abiotic stress", *Int. J. of Genomics*, 8p, doi: 10.1155/2016/5427062.

[8] Z. Sun, et al. (2013), "Overexpression of *TsGOLS2*, a galactinol synthase, in *A. thaliana* enhances tolerance to high salinity and osmotic stresses", *Plant Physiol. Biochem.*, **69**, pp.82-89, doi: 10.1016/j.plaphy.2013.04.009.

[9] E.W. Tsang, et al. (1991), "Differential regulation of superoxide dismutases in plants exposed to environmental stress", *Plant Cell*, **3(8)**, pp.783-792.

Effects of anaerobic fermentation in a nitrogen atmosphere on bioactive compound content in Vietnamese GABA tea

Quoc Sinh Nguyen[1*], Chi Bao Nguyen[2], Thanh Long Le[1], Sy Vuong Ho[1], Thi Diem Huong Nguyen[1], Van Quoc Bao Vo[1], Van Toan Nguyen[1]

[1]Hue University of Agriculture and Forestry
[2]Hue University

Received 6 May 2018; accepted 31 July 2018

Abstract:

Gamma(γ)-Aminobutyric acid (GABA), which provides a variety of health benefits, is an important bioactive component of tea (*Camellia sinensis*). A special tea product, GABA tea, contains high levels of γ-Aminobutyric acid which is produced by anaerobic fermentation. Tea fermentation is affected by a number of factors, including anaerobic conditions (vacuum, and the kind of gas used), temperature, and the duration of anaerobic fermentation.

In this study, the levels of bioactive compounds in tea leaves produced by fermenting fresh tea leaves in nitrogen gas are investigated. The fermentation was conducted at different temperatures: room temperature (28±2), 35, and 40°C; and for each temperature setting, the fermentation times were 6, 9, 12, and 15 hours. The results show that the GABA content increased significantly with fermentation temperature. The most appropriate temperature and time for the anaerobic fermentation to produce GABA and other bioactive compounds were, respectively, 40°C and 9 hours. Under these conditions, GABA content reached the maximum value (202.77 mg/100 g of dry tea); that of total polyphenols was 22.30% of dry matter (DM); caffeine was 2.39% DM; and soluble solids were 36.25% DM.

Keywords: **anaerobic fermentation, gamma-aminobutyric acid, nitrogen gas, tea.**

Classification number: **3.1**

Background

γ-Aminobutyric acid - GABA, $C_4H_9NO_2$, a non-proteinaceous amino acid, is one of three bioactive compounds in tea (the other two are caffeine and L-Theanine). GABA is one of the major inhibitory neurotransmitters in the sympathetic nervous system, exerting antihypertensive and antidiabetic effects in humans. GABA can act effectively as a natural relaxant to induce relaxation and diminish anxiety, and its administration can enhance immunity in stressful conditions [1]. Furthermore, GABA has a physiological role in many bodily systems outside the central somatic system, such as regulating cardiovascular functions, inhibiting metastasis of cancer cells, and modulating renal function. Kanehira, et al. [2] suggest that intake of GABA-containing beverages, especially those containing 50 mg of GABA, may help reduce both psychological and physical fatigue and improve task-solving ability.

Tea is a beverage that is widely appreciated and consumed in vast quantities worldwide. Tea products have been studied as functional foods for many years. A special tea product, GABA tea, which contains a large amount of GABA was discovered Japan in 1987 by Tsushida and Murai, and has been reported to have some medical functions [3-6]. The key difference between GABA tea and other tea products is the complicated anaerobic fermentation during withering operations [7]. The quality of a commercialised GABA tea is determined by the GABA content (at least 150 mg GABA/100 g dried tea) and its flavour [8]. Recently, GABA tea has been successfully produced in Taiwan. Tea farmers

*Corresponding author: Email: nguyensinh@huaf.edu.vn

in Taiwan combine the technique of making Olong tea and green tea to produce the Taiwanese GABA tea which has a uniquely characteristic taste and flavour. GABA tea is becoming increasingly popular in Taiwan.

The information necessary for producing GABA tea in Vietnam remains unknown [5]. GABA content increases with the use of anaerobic fermentation. Recently, research on anaerobic fermentation in a vacuum has been published [9]. The fermentation in the current study was undertaken in nitrogen atmosphere to ensure a completely anaerobic medium [4, 10]. This study aims to improve the flavour and GABA content of GABA tea. The results will be provided to tea producers to improve GABA tea production technology. The purpose of this study is to determine the levels of certain bioactive compounds - caffeine, soluble solids, polyphenols, and GABA - in tea leaves under conditions of continuous anaerobic fermentation in a nitrogen atmosphere.

Materials and methods

Materials

Tea shoots consisting of a bud and 2-3 leaves of the LDP2 cultivar (*C. sinensis* x *C. sinensis* var. *assamica*) were used as raw material. These were collected from the Anh Son district (Nghe An province, Vietnam) in April 2017. Folin-Ciocalteau's phenol reagent, GABA (Sigma-Aldrich, USA), gallic acid (Sigma-Aldrich, USA), and other analytical-grade chemicals were used for biochemical compound analysis.

Methods

Experimental method:

After picking, tea shoots were spread on bamboo tray with a diameter of 1.1 m and placed in a cool room to wither for 4 hours before fermentation. Next, half of the plucked tea shoots were packed into a nitrogen-filled chamber and then incubated continuously at room temperature (28±2ºC), at 35ºC, and at 40ºC. For each temperature, fermentation times of 6 hours, 9 hours, 12 hours, and 15 hours were applied. The other half of the tea shoots were not subjected to anaerobic treatment and were used as the control.

The GABA tea production process can be summarily described as follows: fresh tea shoots → withering (25-30ºC) → anaerobic fermentation → panning (5 minutes) → rolling (45 minutes) → drying (95ºC for 60 minutes) → final products.

The samples were collected at the end of each fermentation period and were kept in hermetic packaging and stored in dry, cool place before analysis. The soluble solid, polyphenol, caffeine, and GABA content were used as observation parameters.

Methods of analysis of biochemical components:

Soluble solid content was determined by Voronsov's method. Caffeine content was determined using the method of Bertrand [11]. Determination of total polyphenol content was conducted by means of a colorimetric method using Folin-Ciocalteau's reagent [12]; and GABA content was also determined by a colorimetric method [13, 14].

Statistical analysis:

Statistical analysis was performed using SAS software 9.1. A significance level of 0.05 was applied.

Results and discussion

Effect of anaerobic fermentation time and temperature on soluble solid content

The results in Table 1 show that the content of dissolved substances decreases when anaerobic fermentation time increases. However, after 15 hours of fermentation, the concentration of solutes seemed to be stable; the value for

Table 1. Soluble solid content (% DM) in tea obtained by anaerobic fermentation in a nitrogen gas environment.

Temperature	Anaerobic fermentation time				
	Control	*6 hours*	*9 hours*	*12 hours*	*15 hours*
28°C	40.27^{a}	36.52^{b}	35.11^{bc}	33.62^{c}	31.70^{d}
35°C	40.27^{a}	38.39^{b}	37.58^{b}	35.20^{c}	33.29^{d}
40°C	40.27^{a}	37.60^{b}	36.25^{c}	35.46^{c}	31.98^{d}

Values with different superscripts in a row are significantly different ($p<0.05$).

fermentation at 28°C was 31.70% DM. The same trend was observed for temperatures of 35°C and 40°C. Soluble dry-matter reduction in tea may be due to the anaerobic metabolism of micro-organisms during fermentation, and degradation through enzymatic and non-enzymatic reactions that contribute to the taste and colour of the tea blocks [15-18]. It can be deduced that a short anaerobic period leads to less soluble matter loss. Thus, the duration of anaerobic fermentation needs to be limited to minimise soluble matter loss.

Effect of anaerobic fermentation time and temperature on total polyphenol content

Green tea contains polyphenol compounds, which include flavanols, flavandiols, flavonoids, and phenolic acids. Most of the polyphenols in green tea are flavanols, commonly known as catechins. Table 2 shows the total polyphenol content of tea leaves under different anaerobic conditions. The total polyphenol content of fermented tea leaves was significantly lower than that control sample ($p<0.05$). After 6 hours of anaerobic fermentation at room temperature, polyphenol content decreased significantly compared to that of the untreated sample ($p<0.05$). This trend was similar to that of the anaerobic fermentation conducted at 35°C and 40°C. Specifically, the total polyphenol content decreased from 22.30% to 20.42% DM after 9 hours of anaerobic fermentation at 40°C and continued to decline significantly after 12 hours and 15 hours of fermentation. This suggests that the polyphenols were used for the biosynthesis of other chemical components during the anaerobic fermentation. Thus, it is necessary to control fermentation time in order to minimise the loss of these antioxidants which are beneficial to human health.

Effect of anaerobic fermentation time and temperature on caffeine content

Caffeine is also found in tea leaves. The proportion varies from 2.5% to 5.5% in dry leaves, depending on their origin, age, and processing. Caffeine continues to be one of the most popular products used as an energy stimulant and as an antioxidant. Table 3 shows the caffeine content of the tea leaves when different anaerobic treatment temperatures and times are used. For all fermentation temperatures, caffeine content decreased slightly after 6 hours ($p>0.05$) and then significantly after 12 hours ($p<0.05$). The caffeine content of the leaves depends on the fermentation conditions. In a carbon dioxide atmosphere, caffeine content decreases; in a nitrogen atmosphere, it increases; and it seems unchanged in an oxygen atmosphere [4]. Microorganisms can cause caffeine degradation through demethylation. The major metabolite formed in fungi is theophylline (1,3-dimethylxanthine), whereas theobromine (3,7-dimethylxanthine) is the major metabolite in bacteria [17, 18].

Table 2. Total polyphenol content (% DM) in tea obtained by anaerobic fermentation in a nitrogen gas environment.

Temperature	Anaerobic fermentation time				
	Control	*6 hours*	*9 hours*	*12 hours*	*15 hours*
28°C	24.66^{a}	23.27^{b}	22.58^{b}	21.32^{c}	20.03^{d}
35°C	24.66^{a}	23.10^{b}	22.88^{bc}	21.65^{c}	19.87^{d}
40°C	24.66^{a}	23.46^{b}	22.30^{c}	20.42^{d}	19.58^{d}

Values with different superscripts in a row are significantly different ($p<0.05$).

Table 3. Caffeine content (% DM) in tea obtained by anaerobic fermentation in a nitrogen gas environment.

Temperature	Anaerobic fermentation time				
	Control	*6 hours*	*9 hours*	*12 hours*	*15 hours*
28°C	2.74^{a}	2.28^{b}	2.15^{b}	2.03^{c}	1.84^{d}
35°C	2.74^{a}	2.34^{b}	2.18^{b}	2.13^{b}	1.92^{c}
40°C	2.74^{a}	2.50^{b}	2.39^{bc}	2.23^{c}	2.05^{d}

Values with different superscripts in a row are significantly different ($p<0.05$).

Table 4. GABA content (mg/100 g dry tea) in tea obtained by anaerobic fermentation.

Temperature	Anaerobic fermentation time				
	Control	*6 hours*	*9 hours*	*12 hours*	*15 hours*
28°C	66.07^{c}	137.74^{b}	167.04^{a}	169.03^{a}	170.95^{a}
35°C	66.07^{d}	139.35^{c}	182.61^{a}	183.95^{a}	178.03^{b}
40°C	66.07^{d}	142.2^{c}	202.77^{ab}	211.31^{a}	200.97^{b}

Values with different superscripts in a row are significantly different ($p<0.05$).

Effect of anaerobic fermentation time and temperature on GABA content

GABA tea is one kind of functional tea manufactured by special methods in anaerobic conditions. It is referred to as GABA tea because it is rich in GABA, the acronym for the special amino acid it contains. The results show wide variation in most of the GABA content (Table 4). As shown in Table 4, the GABA content range depends on the temperature and fermentation time. The present study accords with those of Park [19] and Tsushida [4]. The GABA content was highest at a fermentation temperature of 40°C and a fermentation time of 9 to 15 hours (200.97-211.31 mg/100 g dry tea). It is at this temperature that the GAD enzyme works best [20]. However, after 12 hours of fermentation, the content of biologically active ingredients such as caffeine and polyphenols decreased significantly. Therefore, an anaerobic fermentation time of 9 hours at 40°C is the most suitable as it ensures the greatest quantities of GABA and other biologically active ingredients [6-8]. The highest GABA content obtained was 202.77 mg/100 g, from the treatment of 9 hours at 40°C [7, 9, 10]. The levels of biologically active compounds in GABA tea are ensured by Vietnamese national standards for commercial tea products (TCVN 1454-1993).

Conclusions

Results showed that GABA content in GABA tea had increased significantly after anaerobic fermentation in a nitrogen gas environment, reaching the standard of GABA tea. Changes in the quantities of tea polyphenols, caffeine, and soluble matter tended to gradually decrease as the fermentation time was extended. The most appropriate temperature and time for anaerobic fermentation in nitrogen gas were, respectively, 40ºC and 9 hours. Under these conditions, the GABA tea analysed possessed a high GABA content (202.77 mg/100 g of dry tea), and the quantities of other components met commercial product requirements (total polyphenol content was 22.30% DM; caffeine was 2.39% DM; and soluble solids were 36.25% DM). The presence of these active components is beneficial to the quality of the tea.

REFERENCES

[1] A.M. Abdou, S. Higashiguchi, K. Horie, M. Kim, H. Hatta, H. Yokogoshi (2006), "Relaxation and immunity enhancement effects of gamma-aminobutyric acid administration in humans", *Biofactors*, **26**, pp.201-208.

[2] T. Kanehira, Y. Nakamura, K. Nakamura, et al. (2011), "Relieving occupational fatigue by consumption of a beverage containing γ-aminobutyric acid", *J. Nutr. Sci. Vitaminol.*, **57**, pp. 9-15.

[3] Y. Abe, S. Umemura, K. Sugimoto, N. Hirawa, Y. Kato, N. Yokoyama (1995), "Effect of green tea rich in gamma-aminobutyric acid on blood pressure of Dah1salt-sensitive rats", *American Journal of Hypertension*, **8**, pp.74-79.

[4] T. Tsushida, T. Murai, M. Omori, J. Okamoto (1987), "Production of a new type tea containing a high level of γ-aminobutyric acid", *Nippon Nogeikagaku Kaishi*, **6**, pp.817-822.

[5] H.F. Wang, Y.S. Tsai, M.L. Lin, A.S.M. Ou (2006), "Comparison of bioactive components in GABA tea and green tea produced in Taiwan", *Food Chemistry*, **96**, pp.648-653.

[6] Zhen Zeng, Chunlan Wu, Yahui Huang, W. Juan (2012), "Study on flavour volatiles of γ-aminobutyric acid (GABA) green tea", *African Journal of Biotechnology*, **11(51)**, pp.11333-11341.

[7] Y. Sawai, Y. Yamaguchi, D. Miyama, H. Yoshitomi (2001), "Cycling treatment of anaerobic and aerobic incubation increases the content of γ-aminobutyric acid in tea shoots", *Amino Acids*, **20**, pp.331-334.

[8] A.S.M. Ou, S.F. Wang, C.Y. Wu, Y.S. Tsai (2005), "Investigation of optimum manufacturing condition and biological functions", *NSC project report*.

[9] Nguyen Quoc Sinh, Nguyen Van Toan, Do Thi Bich Thuy, Le Thanh Long, Ho Sy Vuong, Nguyen Thi Diem Huong, Nguyen

Cao Cuong, Vo Van Quoc Bao (2016), "Effects of anaerobic fermentation in vacuum conditions on bioactive compound content of GABA tea", *Journal of Agricultural Sciences and Technology*, Nong Lam University Ho Chi Minh city, **6**, pp.50-54.

[10] Mingyuan Lee, Jinchyau Peng (2010), "Effects of fermentation time and seasons on the γ-aminobutyric acid and glutamic acid contents of TTES-12 GABA tea producing", *International Symposium on Machinery and Mechatronics for Agriculture and Biosystems Engineering, Fukuoka, Japan*, pp.614-620.

[11] V.T. Thu, D.H. Tien, D.T. Gam, G.T. Khoa (2001), *Chemical compounds in tea and some popular analysis methods in tea production in Vietnam*, Hanoi Agricultural Publisher.

[12] The Ministry of Science and Technology of Vietnam (2005), *National standards for determining the quality characteristics of green tea and black tea - Part 1: total polyphenol content in tea - Colorimetric method using Folin's reagent-ciocalteu (ISO 14502-1:2005)*.

[13] Truong Nhat Trung, Dong Thi Anh Dao (2016), "Study of boosting gamma-Aminobutyric acid (GABA) content in germinated mung bean under hypoxia-anaerobic condition and evaluating the loss of GABA after boiling", *Science & Technology Development Journal (University of Technology, VNU-HCM)*, **7(19)**, pp.1-9.

[14] Qian Zhang, Jun Xiang, Lizhen Zhang, Xiaofeng Zhu, Jochem Evers, Wopke van der Werf, Liusheng Duan (2014), "Optimizing soaking and germination conditions to improve gamma-aminobutyric acid content in japonica and indica germinated brown rice", *Journal of Functional Foods*, **10**, pp.283-291.

[15] Katsuhiro Hakamata, Norio Nakada, Toshihiro Mukai, Hirokazu Fukushima, Ryo Yamaguchi, Tomofumi Nakada (1988), "Improvements of manufacturing process of anaerobically treated tea (Gabaron tea)", *Chagyo Kenkyu Hokoku*, **68,** pp.8-13.

[16] J.H. Kim, M.Y. Kim (2012), "Enhancement of bioactive components content and the antioxidant activity of green tea after continuous anaerobic incubation", *J. Agr. Sci. Tech.*, **14**, pp.837-844.

[17] S. Dash, S. Gummadi (2006), "Catabolic pathways and biotechnological applications of microbial caffeine degradation", *Biotechnol. Lett.*, **28,** pp.1993-2002.

[18] S. Ibrahim, M.Y. Shukor, M.A. Syed, N.A. Ab Rahman, K.A. Khalil. A. Khalid, S.A. Ahmad (2014), "Bacterial degradation of caffeine: a review", *Asian J. Plant Biol.*, **1**, pp.18-27.

[19] Jang Hyun Park (2001), "Change in the main constituents by a treatment condition of anaerobically treated green tea leaves", *Korean J. Medicinal Crop Sci*., **9**, pp.275-279.

[20] Nguyen Thi Hong Hanh, Trieu Ngoc Han, Le Nguyen Doan Duy and Nguyen Cong Ha (2016), "Changes of glutamic acid content and glutamate decacboxylase during the soaking and germination of pre-germinated brown rice", *Scientific Magazine of Can Tho University (Agriculture)*, **1**, pp.66-74.

Genetic parameters for reproductive traits of VCN03 breed

Sang Van Le*, Pham Duy Pham, Hong Son Trinh

Thuy Phuong Pig Research Center, National Institute of Animal Science, Vietnam

Received 7 February 2018; accepted 30 May 2018

Abstract:

This study was conducted in Thuy Phuong Pig Research Center (TPPRC), Vietnam to determine the genetic parameters of four reproductive traits including numbers born alive (NBA), litter birth weight (LBW), number of weaned pigs (NW) and litter weaning weight (LWW). The reproductive performance of 254 sows of VCN03 breed from four generations between 2010 and 2017 was collected and used in this study. Data from NBA, LBW, NW and LWW were subjected to repeated-measures of ANOVA in PROC MIXED in SAS with four reproductive traits and generations as fixed factors. Data from heritabilities and genetics and phenotypic correlations were plotted using the ASReml. It was concluded that the heritabilities of the four traits ranged from low to moderate, resulting from 0.134 to 0.267. The heritabilities of NBA, LWW, LBW and NW were 0.264, 0.267, 0.137 and 0.134, respectively. The genetic and phenotypic correlations among the four traits were moderate to high positive. The genetic correlations ranged from 0.467 to 0.991, with the highest estimate for the genetic correlation being between LBW and NW and the lowest estimate for the genetic correlation being between NBA and LWW. The genetic correlation between NBA and NW was 0.67, between NBA and LBW was 0.774, between LBW and LWW was 0.69 and between LWW and NW 0.51.

Keywords: **genetic parameters, litter birth weight, litter weaning weight, number born alive, number weaned pigs.**

Classification number: **3.1**

Introduction

Reproductive traits are the major component in pig production, and genetic improvement is important in swines' breeding objective. Genetic improvement of sow productivity was mainly focused on NBA and NW [1]. However, an increase in NBA was associated with a decrease in LBW and survival [2]. In addition, low average piglet weight at birth led to an increase in mortality [3]. Therefore, to increase pig production via genetic improvement, the reproductive traits of sows such as LBW and LWW should be taken as main objectives in breeding programs. Furthermore, it is necessary to comprehend the knowledge of genetic parameters to accurately estimate breeding values, optimise breeding programs and predict genetic responses to economic selection [4].

Synthetic Duroc breed, namely VCN03, have been imported from PIC (Pig Improvement Company) in the United Kingdom to Vietnam since 1997. This breed has played an important role in a breeding structure in TPPRC as a final sire line in breeding with the objective of creating commercial crossbred pigs containing five different breeds. However, the potential use of the VCN03 breed to increase pig productivity in Vietnam has received little attention.

This study aims to obtain genetic parameters such as heritabilities and genetic as well as phenotypic correlations between reproductive traits including NBA, LBW, NW and LWW in the VCN03 breed.

Materials and methods

Data and animals

A total of 254 sows from the VCN03 breed in TPPRC's program were used to study genetic parameters for reproductive traits of sows including NBA, LBW, NW and LWW.

The data was recorded between 2010 and 2017, and each year was divided into two seasons (Spring-Summer season

*Corresponding author: Email: lesang86@gmail.com.

from February to July and Autumn-Winter season from August to January). All animals were raised in the same units and sows were farrowed by artificial insemination. The summary statistics for four traits and covariates used in this model are shown in Table 1.

Table 1. Factors included (✓) in the repeated animal models.

Factors	Type of factor	NBA	LBW	NW	LWW
Generation	F	✓	✓	✓	✓
Parity	F	✓	✓	✓	✓
Age of farrowing	F	✓			
Season	F	✓	✓	✓	✓
Year	F	✓	✓	✓	✓
Season * Year	F	✓	✓	✓	✓
Date of weaning	F				✓
Boar genotype	F		✓		✓
Animal	A	✓	✓	✓	✓
Permanent environment effect of sow	R	✓	✓	✓	✓
Residual effect	R	✓	✓	✓	✓

A = random animal additive genetic effect, R = random, F = fixed effect.

Analysis

Data from NBA, LBW, NW and LWW were subjected to repeated-measures of ANOVA in PROC MIXED in SAS, version 9.2 with four reproductive traits and generations as fixed factors. Data from heritabilities and genetics and phenotypic correlations were plotted using the ASReml procedure at the School of Rural and Environmental Science, UNE, Armidale, Australia.

The statistical models in the data analysis can be written as a repeated model:

$$Y = Xb + Z_1a + Z_2p + e$$

where, Y is the vector of observations, b is the vector of fixed effects that includes year, parity for NBA and herd and parity for NW, X is the incidence matrix of fixed effects, a is the vector of random additive genetic effects, Z_1 is the incidence matrix of random genetic effects, p is the vector of random permanent environmental effects, Z_2 is the incidence matrix of random permanent environmental effect and e is the vector of random residual effects.

Results and discussion

Reproductive performance traits

The descriptive statistics of this study with the least squares means and standard errors for traits are presented in Table 2.

Table 2. Estimated least squares means and standard errors of NBA, NW, LBW and LWW of VCN03 across parities.

Parity	NBA	NW	LBW	LWW
	LSM±SE	*LSM±SE*	*LSM±SE*	*LSM±SE*
1	8.81^{b}±0.17	8.72^{c}±0.16	13.39^{c}±0.28	55.10^{cd}±1.19
2	8.95^{b}±0.18	8.82^{bc}±0.18	13.70^{c}±0.28	57.01^{bc}±1.22
3	10.20^{a}±0.2	9.86^{a}±0.19	14.07^{ab}±0.29	58.65^{ab}±1.23
4	10.08^{a}±0.22	9.59^{a}±0.21	13.65^{c}±0.32	60.30^{a}±1.39
5	9.96^{a}±0.24	9.04^{ab}±0.22	14.37^{a}±0.34	57.60^{bc}±1.47
6	9.57^{a}±0.26	8.65^{cd}±0.25	14.12^{a}±0.38	56.49^{c}±1.61
7	8.32^{b}±0.3	8.23^{d}±0.28	13.54^{c}±0.43	59.22^{ab}±1.83
8	8.17^{b}±0.38	8.05^{d}±0.36	13.89^{bc}±0.56	53.36^{d}±2.39
9	6.33^{c}±1.58	6.33^{c}±1.49	-	-

The different letters such as a, b, c, d and e in the same column show the difference of value with the statistical significance $p<0.05$.

The average NBA of VCN03 was 8.9 piglets per litter, ranging from 6.33 to 10.2 piglets per litter across the first nine parities. This result was similar to the study by [5], but it was higher than the reports by Luan and Linh (1988) [6], with 7.9 piglets per litter, and Doanh (1979) [7], with 7.8 piglets per litter. However, the NBA of VCN03 in this report was lower than the reports by Hung and Binh (2008) [8], with 10.61 piglets per litter, and Tholen, et al. (1996) [9], with 10.78 piglets per litter.

The NBA increased from the lowest at the first parity to the highest at the third parity, from 8.8 to 10.2 piglets per litter, varying from 9.57 to 10.2 piglets per litter from the third parity to the sixth parity and then, it decreased from the seventh to ninth parities from 8.32 to 6.33 piglets per litter. This changing pattern was in agreement with [4, 10]. The NBA from the third to sixth parities was significantly higher than in the first, second, seventh, eighth and ninth parities. These results agreed with the findings by [11, 12].

The NW ranged from 6.33 piglets per litter at the ninth parity to 9.59 piglets per litter at the third parity, and the average was 8.15 piglets per litter. This result was lower than the report by [8], with 9.72 piglets per litter, and [13], with 10.46 piglets per litter, but it was higher than the report

of 7.98 piglets per litter by [14]. Additionally, the effect of parities on NW was similar to the NBA with an increase from 8.72 piglets per litter at the first parity to 9.86 piglets per litter at the third parity. This significant effect of parity on NW in this study agreed with the report by [15].

The lower values in the NBA and NW of VCN03 could be explained by a number of factors such as high air temperatures, relative humidity and diseases. The high proportion of piglets that died during the nursing period was a result of being starved and overlain by the sows. Furthermore, the influence of heat and humidity and low lactational nutrition contributed to a direct effect on milk production of lactating sows. Another reason is that VCN03 was a sire line in the breeding program in which more selection was emphasised on growth traits.

The LBW and LWW per litter were 14.1 kg and 58.56 kg, respectively. The LBW per piglet was 1.56 kg, which is similar with LBW of other breeds in Vietnam [8, 11, 13, 14]. However, an average of 6.72 kg per piglets LBW of VCN03 on average of 22.6 weaning days was significantly higher than the reports by [8, 13].

The estimate of heritability for reproductive traits

The heritabilities with standard errors and variance components for reproductive traits of the VCN03 sows are presented in Table 3. The heritability of NBA was moderate, being 0.264. Previous studies have reported a large range in heritability for NBA (0.04 to 0.66). The result of this study is in agreement with previous studies [16-19]. This result was higher than the reports of [20-24]. In contrast, the heritability of NBA in this study was lower than the report of 0.66 by [25]. The moderate heritability of NBA in this study could be explained by a better control experimental population when compared to the use of filed data in the previous studies.

Table 3. Heritabilities with standard errors and variance components for NBA, NW, LBW, and LWW of VCN03 breed.

	σ_A^2	σ_E^2	σ_P^2	h^2±SE
NBA	2.192	6.098	8.290	0.264±0.056
LBW	0.002	0.012	0.014	0.137±0.044
NW	0.926	5.999	6.926	0.134±0.037
LWW	0.216	0.591	0.807	0.267±0.051

The estimated heritability for LBW was 0.137. This estimate is in agreement with that reported by [11, 26-28]. In contrast, Hermesch, et al. (2000) [23], Kerr and Cameron (1995) [29] and Ferraz and Johnson (1993) [30] found the heritability of LBW to be 0.08, 0.09 and 0.06, respectively. However, a high estimate of heritabilities with a range of 0.47-0.54 were reported by [16-18], which were higher than the estimated heritability of LBW in this study. Rydhmer, et al. (1992) [3] reported that an early weighing of the litter after birth is important, and delay in recording litter birth weight in field data might be the reason for lower heritabilities.

The estimate of heritability for NW was 0.134. This heritability is in agreement with that reported by [29, 31]. Higher mean estimates for NW found by [9, 17, 25] were 0.48, 0.25, and 0.3, respectively. In contrast, the result of this study is greater than the estimates reported by [4, 20, 21, 29], ranging from 0.03 to 0.1. The differences of heritability for NW among studies could be explained by the varied swine breeds and the research data.

The LWW recorded in this study was moderate heritability (0.267), which was in agreement with the estimates reported by [11, 18, 32, 33]. However, the result of this research's finding is smaller than the estimates reported by [34] for LWW (0.34), as well as the prediction of 0.38 reported by [25]. Additionally, a higher estimate for this trait (0.38) was found by [35]. The LWW in this study had a higher heritability in comparison with the estimates presented by previous studies [9, 14, 22, 24, 27].

Heritability is the proportion of phenotypic variance due to additive genetic effects. The more heritable a trait is, the more the observed variation is due to genetic rather than environmental effects. The heritabilities of NBA, NW, LBW and LWW in this study ranged from 13.5% to 26.5%. These results mean that the major difference between animals is due to environmental effects. Therefore, increasing the NBA and NW can be done through crossbreeding, especially crossbred dam, due to the benefit of heterosis. In addition, the creation of a good environment may be another solution to increase NBA and NW.

Although the effect of parities on heritability was not examined in this study, previous studies [23, 31] found that the heritabilities of reproductive traits were influenced by parities. The heritability for NBA in the first three parities was lower than these estimates in the fourth and fifth parities [14]. Hermesch, et al. (2000) [23] reported that heritability for LBW in the first parity of Large White and Landrace was smaller than that in the second and third parities (0.08 as opposed to 0.22 and 0.20, respectively). Gilts' uterine capacity are smaller than those of multiparous sow. Therefore, this may have a restriction on the expression of their genetic potential in LBW [36]. The heritability

increased with parity number in some reports [9, 22], but not in other research [2, 22].

Genetic and phenotypic correlations for reproductive traits

Genetic and phenotypic correlations between reproductive traits of the VCN03 sows are shown in Table 4. The estimated values of genetic and phenotypic correlations between NBA and NW were positive at 0.627 and 0.45, respectively, indicating that survival is not a heritable trait. These estimates of correlations between NBA and NW were lower than the range of 0.8 to 0.96 reported by [11, 25, 27, 31, 33]. However, the correlations in this study were higher than 0.59 found in the Mong Cai breed [14], 0.48 in the Duroc breed [27] and 0.38 in the Yorkshire breed [33]. Furthermore, Bushman (2007) [34] reported that the genetic correlation between NBA and NW was negative (-0.38). The difference in genetic correlations among studies was the result of the use of field data and different breeds. Another reason for the differences between this study and the previous ones is that cross-fostering was not practiced in the previous populations but was a common management practice in this study.

Table 4. Genetic correlations with standard errors (above diagonal) and phenotypic correlations with standard errors (below diagonal) between reproduction traits.

	NBA	NW	LBW	LWW
NBA		0.627±0.134	0.774±0.090	0.467±0.165
NW	0.450±0.034		0.991±0.062	0.510±0.137
LBW	0.912±0.021	0.596±0.026		0.690±0.118
LWW	0.338±0.049	0.796±0.018	0.386±0.037	

The genetic correlation between NBA and LBW was high and positive (0.774). This genetic correlation is in agreement with that reported by [27] in the Large White breed. The larger and stronger correlation between NBA and LBW were found by [11] with 0.95 and by [25] with 0.92. However, these results contradicted the negative relationship between NBA and LBW at -0.38, -0.2 and -0.34 in reports of [23, 34, 37], respectively. The differences of genetic correlation between these two traits could be caused by the recording procedure of litter birth weight as well as the cross-fostering procedures.

The genetic correlation between NBA and LWW in this study is in agreement with [25, 27], who found a moderate positive correlation between the two traits. Negative genetic correlations between NBA and LWW with -0.43, -0.14 and -0.18 in reports by [9, 23, 34], respectively, were much lower than those seen in this study (0.467). However, the genetic correlations between these two traits in reports by [17] with 1.13, [33] with 0.9 and [31] with 0.87 were higher than the result of this study. The difference could be attributed, in part, to the pooled estimates of the three breeds in the study of [17], two breeds in [33] and Mong Cai crosses in the study of [31] compared to purebred VCN03 in this study.

The estimated genetic correlation between NW and LBW in this study (0.99) was similar to those reported by previous studies [17, 27]. The positive genetic correlations between NW and LBW were also found in reports by [18] with 0.55, [27] with 0.48, and [25] with 0.64, but it was lower in comparison with the result of this study. The high positive genetic correlation between these two traits indicates that the higher LBW led to the higher number of piglets weaning.

The positive genetic correlation between LBW and LWW was revealed in this study and in other researches. The estimate of the genetic correlation between these two traits in this study was the same as the studies by [27, 38] in Large White at 0.69. Young, et al. (1978) [25] and Bereskin (1984) [33] showed much greater genetic correlations between LBW and LWW, ranging from 0.92 to 0.95, in comparison to the result of this study. However, this result was higher than the reports by [16, 23, 34]. The moderate to high genetic correlation between LBW and LWW indicate that the heavier litter weight at birth is associated with a higher litter weight at weaning.

The high positive genetic correlation was found between NW and LWW. The result of this study is as large as the genetic correlation between NW and LWW in the report of [25] at 0.51. However, the estimate of genetic correlations between these two traits were greater, ranging from 0.8 to 0.87 in the reports of previous studies by [18, 21, 34, 39, 40] in comparison with the result of this study. In addition, Siewerdt, et al. (1995) [27], Irvin and Swiger (1984) [17] and Bereskin (1987) [41] found a high genetic correlation between LWW and NW, ranging from 0.95 to 0.97. The magnitude of the genetic correlation between these two traits gives rise to the expectation that more piglets weaning per sow per year would result in a heavier LWW.

The genetic and phenotypic correlations of average piglet weight at birth (APWB) with other reproductive traits were not examined in this study, but Rydhmer, et al. (1992) [3] and Hermesch, et al. (2000) [23] reported that

APWB had an unfavorable relationship with NBA; their genetic correlation ranged from -0.86 to -0.27. In addition, APWB had a favourable relationship with piglet mortality [3]. Therefore, increasing NBA by selection would lead to decreasing weight of piglet at birth and consequently, lead to low weaning rate.

Conclusions

The results of this study showed low heritabilities for LBW and NW, at 13.7% and 13.4%, respectively, while the heritabilities for NBA and LWW were moderate, at 26.4% and 26.7%, respectively. These low and moderate heritabilities showed potential for subsequent selection such as improvement of environment and crossbreeding program to increase the NBA and NW.

The genetic and phenotypic correlations among the four reproductive traits were moderate to high positive. The genetic correlations between NW and LBW account for 0.99, whilst the genetic correlations between NBA and LWW and between NW and LWW were the lowest with 0.467 and 0.51, respectively. The genetic correlation between NBA and NW and between LBW and LWW were 0.627 and 0.69, respectively. Moderate to high positive genetic associations between these reproductive traits suggest that increasing one trait by selection would lead to the improvement of other traits.

REFERENCES

[1] A.G. de Vries and E. Kanis (1994), "Selection for efficiency of lean tissue deposition in pigs", *Principles of Pig Science*, *Nottingham University Press*, pp.23-42.

[2] C.S. Haley, E. Avalos, and C. Smith (1988), "Selection for litter size in the pig", *Animal Breeding Abstracts*, **56**, pp.317-332.

[3] L. Rydhmer, K. Johansson and L. Eliasson-Selling (1992), "A Genetic Study of Pubertal Age, Litter Traits, Weight Loss during Lactation and Relations to Growth and Leanness in Gilts", *Acta Agriculturae Scandinavica, Section A - Animal Science*, **42(4)**, pp.211-219.

[4] R. Roehe and B.W. Kennedy (1995), "Estimation of genetic parameters for litter size in Canadian Yorkshire and Landrace swine with each parity of farrowing treated as a different trait", *J. Anim. Sci.*, **73(10)**, pp.2959-2970.

[5] N. Thien, P.H. Doanh, and P.T. Van (1990), "Reproductive capacity of Landrace, Large White, DBI-81 and their acrosses", *The Scientific result of technology in Animal livestock from 1995 to 1990*, pp.17-25.

[6] D.H. Luan and T.V. Linh (1988), "Productivity of Cuban Swine reared in Vietnam", *Journal of Agricultural Science and Technology*, **8**, pp.364-369.

[7] P.H. Doanh (1979), "Results on surveying, investigation and evaluation for Southern pig breeds", *Reports of Animal Husbandry Insitute (1969-1979)*, pp.7-11.

[8] V.P. Hung, and D.V. Binh (2008), "The productive performance of boar Duroc (L19) with sows F1 (LxY) and F1 (YxL) in Vinh Phuc province", *Journal of Science and Development*, **6(6)**, pp.537-541.

[9] E. Tholen, K. Bunter, S. Hermesch and H.U. Graser (1996), "The genetic foundation of fitness and reproduction traits in Australian pig populations. 1. Genetic parameters for weaning to conception interval, farrowing interval, and stayability", *Australian Journal of Agricultural Research*, **47(8)**, pp.1261-1274.

[10] R.B.M. Huirne, A.A. Dijkhuizen, and J.A. Renkema (1991), "Economic optimization of sow replacement decisions on the personal computer by method of stochastic dynamic programming", *Livestock Production Science*, **28(4)**, pp.331-347.

[11] D.V. Binh (1993), *Heritability and selection indeces of reproductive performance of Mong Cai Pig breed*, PhD Dissertation in Hanoi University of Agriculture.

[12] W.L. Flowers and H.D. Alhusen (1992), "Reproductive performance and estimates of labor requirements associated with combinations of artificial insemination and natural service in swine", *J. Anim. Sci.*, **70(3)**, pp.615-621.

[13] V.D. Soan and D.V. Binh (2011), "The productive performance of sows F1 (LxY) and F1 (YxL) mating with boar Duorc in Hanoi", *Journal of Science and Development*, **9(4)**, pp.614-621.

[14] N.V. Duc (1997), *Genetic characterization of indigenous and exotic pig breeds and crossess in Vietnam*, PhD Dissertation in The school of rural and environmetal science, University of New England, Australia.

[15] C.M. Dwyer, N.C. Stickland, and J.M. Fletcher (1994), "The influence of maternal nutrition on muscle fiber number development in the porcine fetus and on subsequent postnatal growth", *J. Anim. Sci.*, **72(4)**, pp.911-917.

[16] N.V. Luc (1984), "The performances and heritabilities of pig breed in Nghia Binh farm", *The Scientific result of technology in Animal livestock from 1979 to 1984*, pp.4-10.

[17] K.M. Irvin, and L.A. Swiger (1984), "Genetic and phenotypic parameters for sow productivity", *J. Anim. Sci.*, **58(5)**, pp.1144-1150.

[18] P.W. Ferguson, W.R. Harvey, and K.M. Irvin (1985), "Genetic, phenotypic and environmental relationships between sow body weight and sow productivity traits", *J. Anim. Sci.*, **60(2)**, pp.375-384.

[19] D. Kaufmann, A. Hofer, J.P. Bindane and N. Kinzi (2008), "Genetic parameters for individual birth and weaning weight and for litter size of Large White pigs", *J. Anim. Breed. Genet.*, **117(3)**, pp.121-128.

[20] O.I. Southwood and B.W. Kennedy (1990), "Estimation of direct and maternal genetic variance for litter size in Canadian Yorkshire and Landrace swine using an animal model", *J. Anim. Sci.*, **68**(7), pp.1841-1847.

[21] M.J. Kaplon, M.F. Rothschild, J.P. Berger and M. Healey (1991), "Population parameter estimates for performance and reproductive traits in Polish Large White nucleus herds", *J. Anim. Sci.*, **69(1)**, pp.91-98.

[22] R. Irgang, J.A. Favero, and B.W. Kennedy (1994), "Genetic parameters for litter size of different parities in Duroc, Landrace, and large white sows", *J. Anim. Sci.*, **72(9)**, pp.2237-2246.

[23] S. Hermesch, B.G. Luxford, and H.U. Graser (2000), "Genetic parameters for lean meat yield, meat quality, reproduction and feed efficiency traits for Australian pigs", *Livestock Production Science*, **65(3)**, pp.249-259.

[24] P. Chen, T. Baas, J. Mary and K.J. Koehler (2003), "Genetic correlations between lean growth and litter traits in U.S. Yorkshire, Duroc, Hampshire, and Landrace pigs", *J. Anim. Sci.*, **81(7)**, pp.1700-1705.

[25] L.D. Young, R.A. Pumfrey, J.P. Cunningham and R.D. Zimmerman (1978), "Heritabilities and genetic and phenotypic correlations for prebreeding traits, reproductive traits and principal components [Swine]", *J. Anim. Sci.*, **46(4)**, pp. 937-949.

[26] R.E. Crump, C.S. Haley, R. Thompson and J. Mercer (1997), "Individual animal model estimates of genetic parameters for performance test traits of male and female landrace pigs tested in a commercial nucleus herd", *Animal Science*, **65(2)**, pp.285-290.

[27] F. Siewerdt, R.A. Cardellino, and V. Costa Da Rosa (1995), "Genetic parameters of litter traits in three pig breeds in southern Brazil", *Braz. J. Genet.,* **18**, pp.199-205.

[28] J.S. Wu and W.C. Zhang (1982), "Genetic analysis of some Chinese breeds as a resource for world hog improvement", *Proc. 2nd World Congress on Genetics Applied to Livestock Production*, pp. 593-600.

[29] J.C. Kerr and N.D. Cameron (1995), "Reproductive performance of pigs selected for components of efficient lean growth", *Animal Science*, **60(2)**, pp.281-290.

[30] J.B. Ferraz and R.K. Johnson (1993), "Animal model estimation of genetic parameters and response to selection for litter size and weight, growth, and backfat in closed seedstock populations of large white and Landrace swine", *J. Anim. Sci.*, **71(4)**, pp.850-858.

[31] N.V. Duc, B.P. Kinghorn, and H.U. Graser (1997), "Genetic evaluation of number born alive in Mong Cai and their crosses in North Vietnam", *Proc. Assoc. Advmt. Anim. Breed. Genet.*, **12**, pp.189-193.

[32] R.K. Johnson, M.K. Nielsen, and D.S. Casey (1999), "Responses in ovulation rate, embryonal survival, and litter traits in swine to 14 generations of selection to increase litter size", *J. Anim. Sci.*, **77(3)**, pp.541-557.

[33] B. Bereskin (1984), "A genetic analysis of sow productivity traits", *J. Anim. Sci.,* **59(5)**, pp.1149-1163.

[34] A.L. Bushman (2007), *Correlated response in litter traits to selection for intramuscular fat in Duroc swine*, Master of Science Thesis in Iowa State University, United States.

[35] J.F. Schneider, L.A. Remple, G.A. Rohner and T.M Brown-Brandl (2011), "Genetic parameter estimates among scale activity score and farrowing disposition with reproductive traits in swine", *J. Anim. Sci.*, **89(11)**, pp. 3514-3521.

[36] S. Hermesch (1996), *Genetic parameters for lean meat yield, meat quality, reproduction and feed efficiency traits for Australian pigs, in AGBU*, PhD Dessertation, University of New England, Australia.

[37] L. Rydhmer, N. Lundeheim, and K. Johansson (1995), "Genetic parameters for reproduction traits in sows and relations to performance-test measurements", *Journal of Animal Breeding and Genetics*, **112(1-6)**, pp.33-42.

[38] L.K. Hutchens, R.L. Hintz, and R.K. Johnson (1981), "Genetic and Phenotypic Relationships between Pubertal and Growth Characteristics of Gilts", *J. Anim. Sci.*, **53(4)**, pp.946-951.

[39] M.F. Rothschild, and J.P. Bidanel (1998), "Biology and genetics of reproduction", *The genetics of the pig*, *CAB International*, pp.313-343.

[40] N.V. Duc, N. Thien, and N.V. Vinh (1991), "Genetic evaluation of Landrace, Large White, Mong Cai and their crosses raised in Quang Ninh", *Pro. Animal Science, National Institude of Animal Science, Vietnam.*

[41] B. Bereskin (1987), "Genetic and phenotypic parameters for pig growth and body composition estimated by intraclass correlation and parent-offspring regression", *J. Anim. Sci.*, **64(6)**, pp.1619-1629.

Characterization and identification of nitrogen-fixing bacteria isolated from agricultural soil

Tran Thi Thuy Ha[1], Thai Thi Lam[2], Nguyen Thanh Huyen[2], Nguyen Xuan Canh[2*]

[1]Centre of Aquaculture Biotechnology, Research Institute for Aquaculture No 1
[2]Faculty of Biotechnology, Vietnam National University of Agriculture

Received 4 May 2018; accepted 30 August 2018

Abstract:

To isolate and characterise free nitrogen-fixing bacteria, we collected randomly soil samples from different areas of Ha Noi. Nitrogen-fixing bacteria were isolated using Burk's medium without nitrogen mineral supplement. The ammonia (NH_4^+) synthesis of these bacterial strains after biomass production was determined by means of Nessler reagent. Based on the results of isolation, we observed and evaluated colony and cellular morphology, pigment production, and metabolic activities of twenty-five isolates. Among the isolated bacteria, two bacterial strains (6.2 and 8.2) with high NH_4^+ concentration in the cultural medium were selected as the best strains for nitrogen-fixing ability. The optimal pH and temperature for their growth and nitrogen fixation are 7.0 and 30°C, respectively. Growth is best favored in the presence of sucrose. We sequenced the 16S rRNA gene of selected strains and compared the homology of them in GenBank using BLAST search. The result of the comparison shows that the 6.2 and 8.2 strains have 99% and 100% 16S rRNA-sequence similarity with *Pseudomonas* sp. and *Bacillus* sp., respectively.

Keywords: **biological nitrogen fixation, nitrogen-fixing bacteria, 16S rRNA.**

Classification numbers: **3.1, 3.4**

Introduction

Nitrogen is an important element of all organisms because it is an essential constituent of proteins, nucleic acids, amino acids, chlorophyll, and other organic substances. In addition, nitrogen is one of the most important nutrients for plant growth and the plant metabolic system. Consequently, nitrogen plays a key role in agriculture by increasing of crop yield. The element is present in the soil in small amounts, in both inorganic and organic forms. Most of nitrogen in the soil exists in organic form, and inorganic nitrogen constitutes only a small fraction of total soil nitrogen. The total amount of nitrogen in the mineral soil surface normally ranges between 0.05 and 0.2% and is directly available to plants, principally as nitrate (NO_3^-) and NH_4^+. The organic nitrogen slowly becomes available through mineralisation [1].

Although nitrogen gas (N_2) accounts for approximately 78% of the atmosphere, it cannot be directly used by plants; therefore, N_2 must be transformed into a form such as ammonia before being consumed through biological nitrogen fixation (BNF), chemical nitrogen fixation, and atmospheric addition. Of these methods, BNF by micro-organisms is the best way to make nitrogen fertiliser. In addition, the contribution of the BNF method leads to reduced use of chemical nitrogen fertiliser, thereby preventing soil erosion and reducing environmental pollution. Nitrogen-fixing micro-organisms are commonly found in the plant rhizosphere. By releasing exudates, plants can exhibit higher nitrogen-fixation activity in the soil [2]. Free-living nitrogen-fixing microorganisms have generally been reported to be plant growth promoters [3, 4]. The primary objective of this study is to isolate and characterise nitrogen-fixing bacteria from different agricultural soils, and, hence, to identify the strains with the greatest nitrogen-fixing ability by means of

*Corresponding author: Email: nxcanh@vnua.edu.vn

16S rRNA gene-sequence analysis.

Materials and methods

Soil sampling

Soil samples were collected from agricultural lands in Ha Noi. A 2 mm sieve was used to remove stones and plant debris from the samples.

Isolation of nitrogen-fixing bacteria

Individual samples of 1 g each were dissolved in 10 ml sterile distilled water and its 0.1 ml soil suspension was inoculated on Burk's solid medium (sucrose 20.0 g, K_2HPO_4 0.64 g, KH_2PO_4 0.16 g, $MgSO_4.7H_2O$ 0.20 g, NaCl 0.20 g, $CaSO_4.2H_2O$ 0.05 g, $Na_2MoO_4.2H_2O$ (0.05%) 5.0 ml, $FeSO_4.7H_2O$ (0.3%) 5.0 ml, 15 g agar 1,000 ml, pH=7) at 30˚C for 2 days.

Determination of nitrogen-fixation capacity of isolated bacteria using Nessler's reagent

The bacteria were cultured in Burk's liquid medium, shaken at 180 rpm, at 30°C. After 48 hours of incubation, the broth was centrifuged at 10,000 rpm for 2 min at 4°C, and the supernatant was reserved. NH_4^+ concentration was determined by the Nessler method. The reaction between Nessler's reagent and NH_3 can be shown as:

$2K_2[HgI_4] + NH_3 + 3KOH \rightarrow I\text{-}Hg\text{-}O\text{-}Hg\text{-}NH_2 + 7KI + 2H_2O$

After treatment with Nessler's reagent, amount of the sample develops a yellowish-brown colour. The colour intensity of solution corresponds to the amount of ammonia originally present. The standard curve was generated to determine the concentration of ammonia produced in the reaction.

Biological characterisation of selected bacteria

The isolates showing high nitrogen fixation, namely 6.2 and 8.2, were selected for further study. The morphology, colour, and size of the colonies on Burk's solid medium were recorded.

The effects of temperature, pH, carbon sources, and incubation time on the growth and development of the two selected strains were determined.

The bacteria were grown in Burk's broth, shaken at 180 rpm at temperatures ranging from 25-45˚C to study the effect of temperature on the growth and nitrogen-fixing capability of the soil isolates. The concentration of ammonia was determined colorimetrically with Nessler's reagent at the wavelength of 420 nm.

The influence of pH on the nitrogen-fixing activity of bacteria was studied by inoculating the bacteria in Burk's broth, shaking at 180 rpm, with pH ranging from 4.0 to 10.0. The concentration of ammonia was calculated by colourimetry with Nessler reagent at 420 nm.

The bacteria were cultured in liquid Burk's medium, shaking at 180 rpm, with different carbon sources (20 g/l): glucose, sucrose, maltose, and mannitol in order to study the effect of these on the growth and nitrogen-fixation of soil isolates. The concentration of ammonia was determined colorimetrically with Nessler's reagent at the wavelength of 420 nm.

To test the effect of incubation time on the nitrogen-fixation capacity of bacteria, the bacteria were cultured in liquid Burk's medium, shaking at 180 rpm, with the optimal temperature, pH, and carbon source conditions. Samples were taken at intervals of every 24 hours. The concentration of ammonia was calculated by colorimetry with Nessler's reagent at 420 nm.

Identification of selected bacteria

Primers 27F (5'-AGAGTTTGATCCTGGCTCAG-3') and 1492R (5'-ACGGCTACCTTGTTACGACTT-3') are used to amplify the 16S rRNA sequences from the DNA of the two selected bacterial strains. Aliquots (5 µl) of PCR products were electrophoresed in 1% agarose gel using standard electrophoresis procedures. 16S rRNA gene of selected isolates was sequenced by 1st BASE company (Malaysia). Finally, sequences of the bacteria with the highest ability to fix nitrogen were compared to sequences from GenBank based on the 16S rRNA sequences to ascertain the relationships between the endophytic strains [5] and phylogenetic trees were thereby constructed by the neighbour-joining method using MEGA software version 6.06 based on 1,000 bootstraps.

Results and discussion

Isolation of nitrogen-fixing bacteria

Nitrogen-fixing micro-organisms were isolated on Burk's medium. These isolates use atmospheric N_2 to synthesise their cell proteins. The cell proteins are then mineralised in soil after tcell death, thereby contributing towards nitrogen availability for plant growth. Burk's

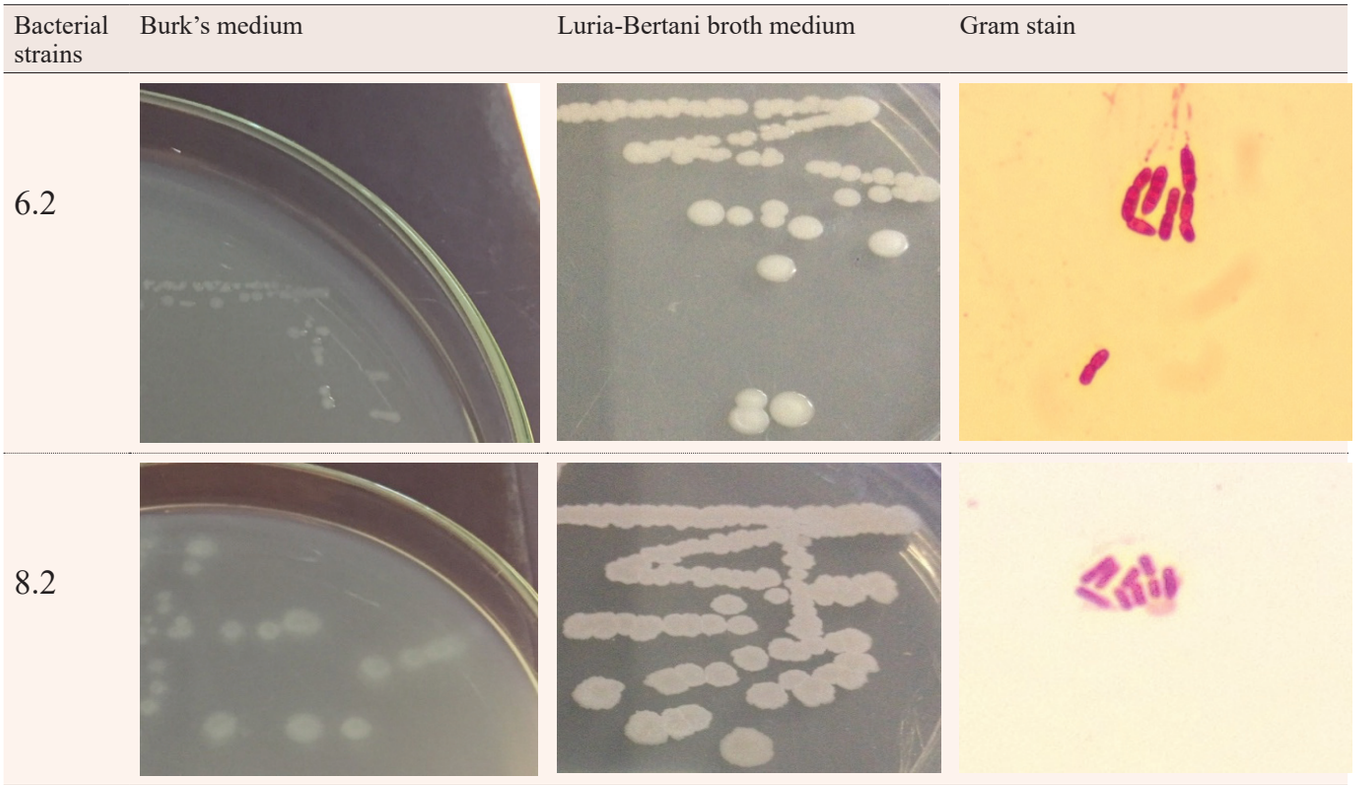

Fig. 1. Morphology and gram stain of the two isolated strains.

medium contains inorganic salts and carbohydrate sources but lacks a nitrogen source. Nitrogen-fixing bacteria can fix atmospheric nitrogen, thus they can live and grow in this nitrogen-free medium. Twenty-six isolates were obtained after two days of incubation on Burk's medium. Morphologically, most isolated bacterial colonies are a whitish cream colour, smooth, irregular, and shiny. Almost all the isolates were gram-positive and gram-negative by gram stain. Of the twenty-six isolated bacterial strains, 65.38% were rod-shaped and 34.62% spherical (Fig. 1).

Determination of nitrogen-fixing capacity of isolated bacteria

Construction of calibration curve: a standard curve was generated specifically to determine the concentration of ammonia in samples by means of colourimetry with Nessler's reagent at 420 nm. Using this method, we can evaluate the nitrogen-fixation capacity of the isolated bacteria.

We used the absolute values of blank and standards measured at a wavelength of 420 nm to generate a calibration curve, and measured absolute as a function of the ammona concentration (Fig. 2).

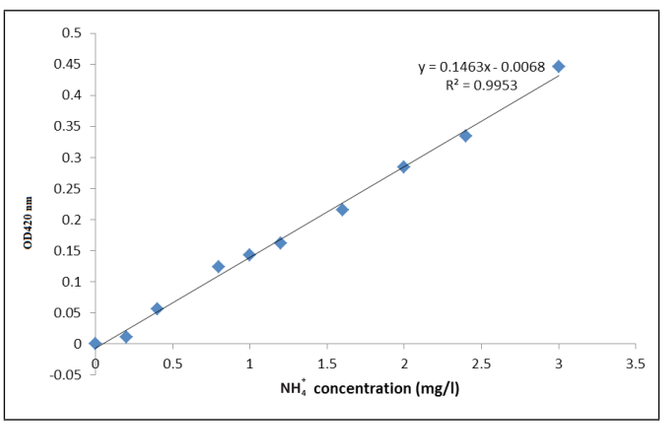

Fig. 2. Calibration curve for ammonia analysis of samples.

Sample analysis: the nitrogen-fixation ability of the twenty-six isolates was measured by Nessler's reagent, allowing us to understand any effective application of this organism by means of studying other attributes in the near future. The bacteria were cultured in Burk's liquid medium. After 2 days of incubation, aliquoted 5 ml of the broth was centrifuged at 10,000 rpm for 5 min at 4°C, and the supernatant was reserved. The concentration of ammonia was determined colorimetrically with Nessler's reagent and the optical density was measured at 420 nm (Fig. 3).

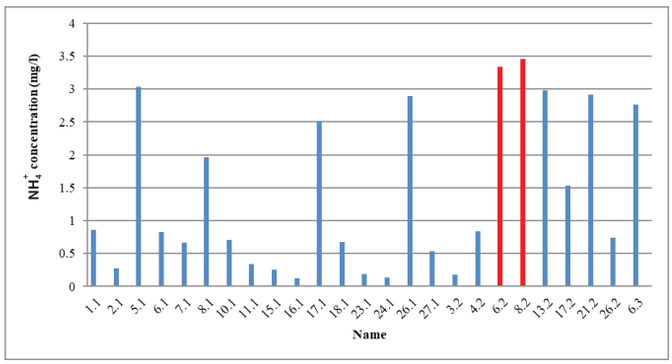

Fig. 3. Ammonium concentration in the medium released by isolates from Trau Quy soil samples.

All twenty-six isolates were able to fix nitrogen. The range of nitrogen-fixation ability ranged from 0.12 to 3.46 mg/l. The 8.2 strain could fix the highest amount of nitrogen (3.46 mg/l); the 16.1 strain fixed the least (0.12 mg/l). Of the twenty-five isolates, two fixed the highest amount of nitrogen, namely 8.2 (3.46 mg/l) and 6.2 (3.34 mg/l). This study shows that the isolates recovered from the soybean fields are of average standard in terms of their nitrogen-fixing potential in the laboratory condition.

Investigating the effect of the cultural conditions on selected bacteria

Investigation of the medium's cultural factors based on the growth and development of two selected strains provided useful information about cultural conditions for further research. The two selected strains (6.2 and 8.2) were cultured in Burk's liquid medium at different temperatures, pH, and with different carbon sources. Observation of the growth and development of these strains is summarised in Table 1.

Table 1. The influence of some environmental conditions on the nitrogen-fixing ability of the two selected strains.

Factor	Optimal Value	
	6.2	*8.2*
Temperature	30˚C	35˚C
pH	7.0	7.0
Carbon source	Sucrose	Sucrose
Incubation time	3 days	3 days

The results show that the 6.2 and 8.2 strains can fix nitrogen at temperatures of between 20 and 45°C. These strains have the optimal nitrogen capacity at 30-35°C. Both strains can use mantose, mannitol, sucrose, and glucose for growth. However, the maximum ammonia secretion of the two strains was obtained in the presence of sucrose. The maximum nitrogen-fixing ability of the two strains was obtained at pH 7 and after 3 days of incubation.

Physiological studies of the selected strains

The physiological activities of the strains were tested by means of Indole-3-acetic acid (IAA) production, methyl red (MR), acetoin production (Voges-Proskauer, V-P), citrate utilisation, catalase, cellulose hydrolysis, starch hydrolysis, and mobility. The biochemical characteristics of the two selected bacterial strains are shown in Table 2.

Table 2. The physiological activities of the 6.2 and 8.2 strains.

Name of the test	Response of strains	
	6.2	*8.2*
IAA production	+	-
MR reaction	+	+
V-P reaction	-	-
Citrate utilisation	-	+
Catalase	+	+
Cellulose hydrolysis	-	-
Starch hydrolysis	+	+
Mobility	+	+

+: positive result; -: negative result.

The two strains were mobility positive, catalase positive, starch hydrolysis positive, and MR positive, but V-P negative and cellulose hydrolysis negative. Strain 6.2 had the property of IAA production, but did not use citrate. In contrast, strain 8.2 can use citrate but cannot produce IAA.

Identification and phylogenetic analysis of selected strains

Molecular tools for the identification of soil bacteria and 16S rRNA gene analysis were used to understand the phylogenetic relationships. The phylogenetic tree was constructed by the neighbour-joining method using MEGA software version 6.06 based on 1,000 bootstraps. According to the genetic analysis, the amplified 16S rRNA sequence of the two selected strains produced 1.5 kb fragments. Homological searches of the 16S rRNA gene sequence of the selected strains in GenBank by means of BLAST revealed that strain 6.2 had sequence similar to *Pseudomonas* sp. and that strain 8.2 belongs to *Bacillus* sp. The phylogenetic trees were constructed as shown in Figs. 4 and 5, respectively. The position of the two selected strains and their relatedness to other bacteria were determined (Figs. 4 and 5).

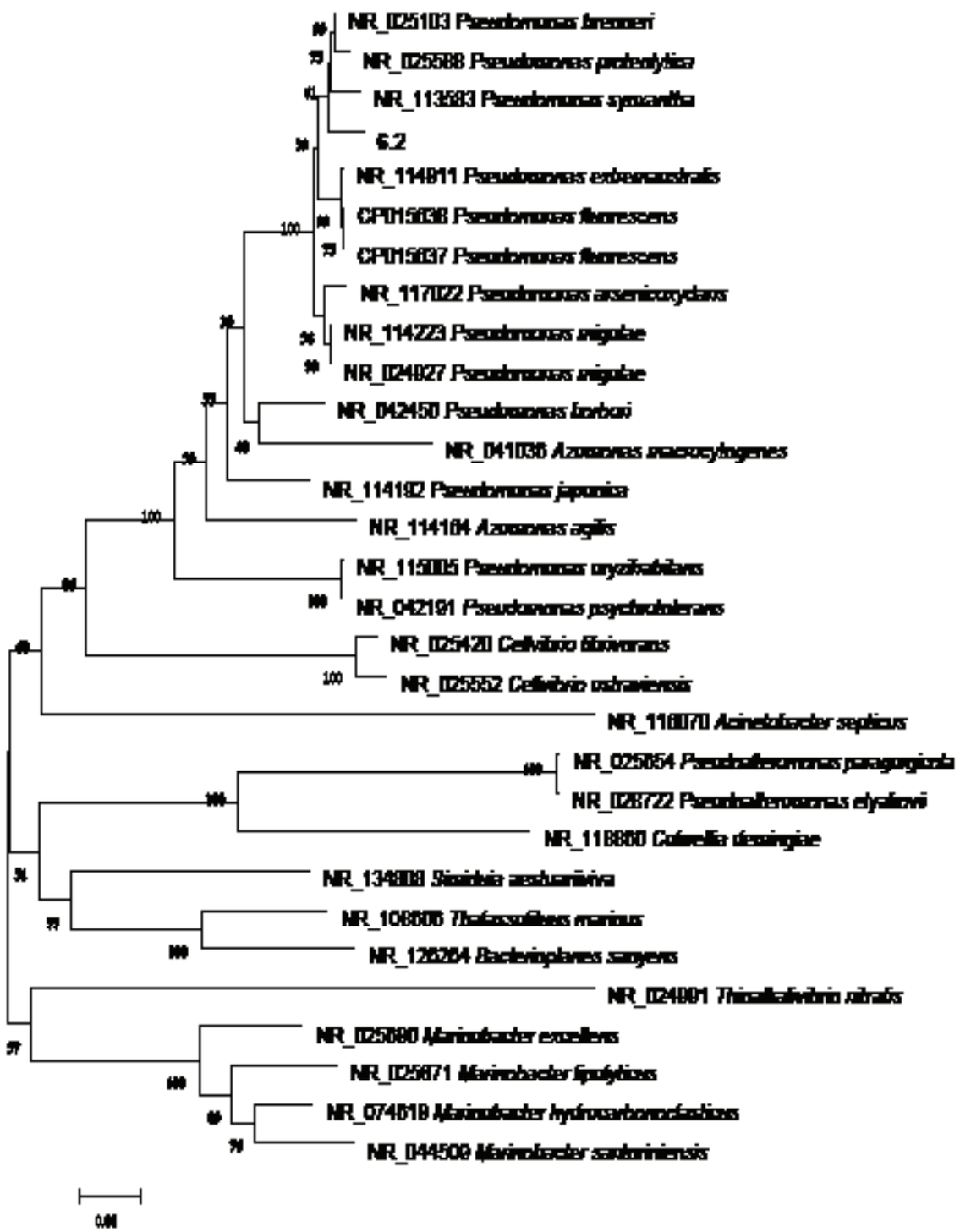

Fig. 4. Phylogenetic tree showing the relative position of the 6.2 strain using the neighbour-joining method of the complete 16S rRNA sequence.

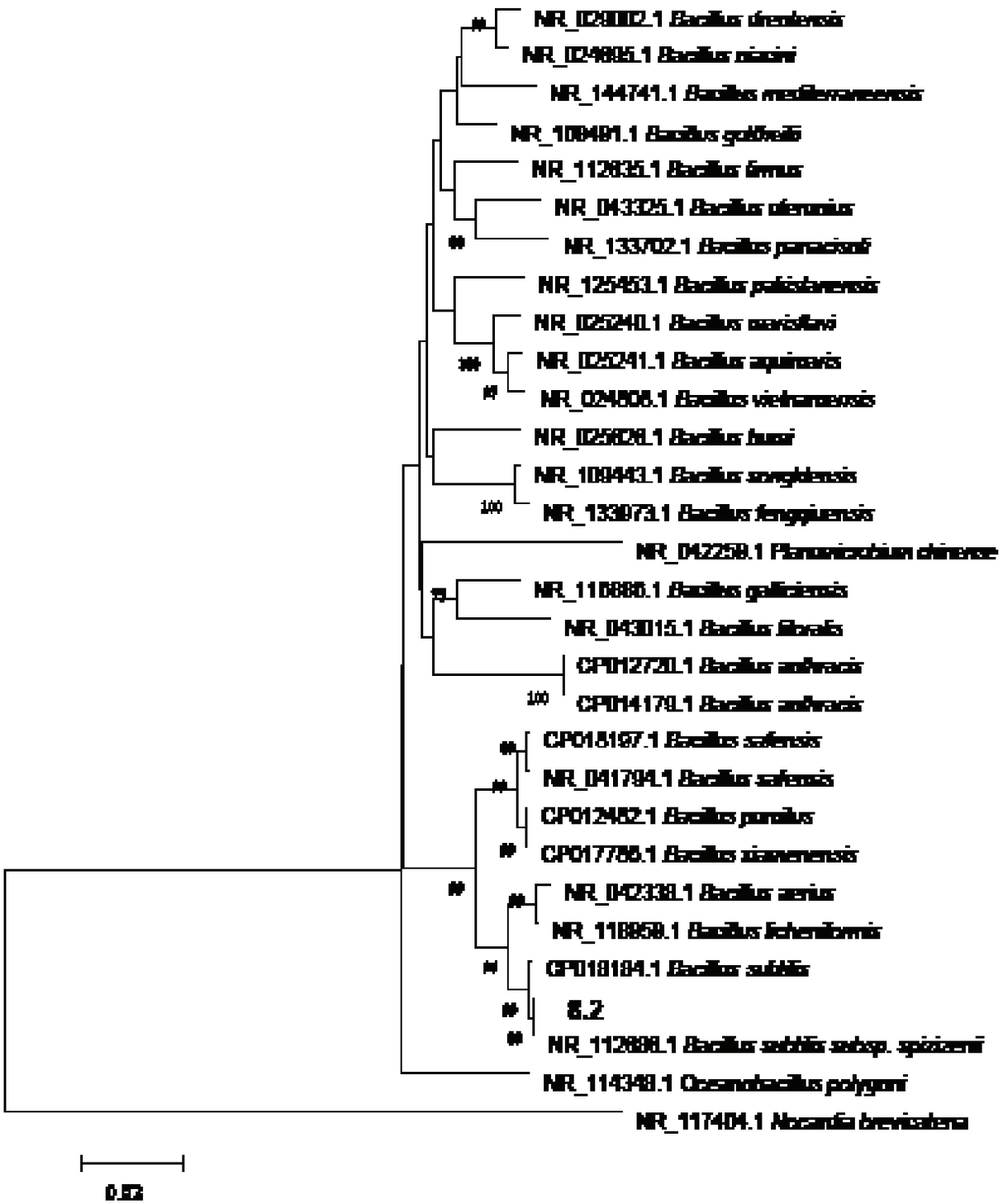

Fig. 5. Phylogenetic tree showing the relative position of the 8.2 strain using the neighbour-joining method of the complete 16S rRNA sequence.

According to *Bargey's Manual of Systemic Bacterilogy*, the biochemical test indicated that the characteristics presented by strains 6.2 and 8.2 are similar to *Pseudomonas* sp. and *Bacillus* sp., respectively. *Bacillus subtilis* sp. and *Pseudomonas* sp. are excellent rhizosphere-colonising bacteria [6]. Strains of *Pseudomonas* and *Bacillus* are among the most efficient plant growth-promoting bacteria and promote growth and yield of a variety of plants [4]. This result is consistent with the results of previous research that indicates that *Bacillus* sp. (*Bacillus subtilis* sp.) and *Pseudomonas* sp. fix nitrogen effectively. *Bacillus subtilis* strains AS-4, OSU-142, UPMB10, and *B. Pumilus* S1r1 [7] have high nitrogen-fixing ability. *Bacillus subtilis* AS-4 could be exploited as a soil inoculant and can be used for nitrogen fixation in soil with a high concentration of salt, which is eco-friendly and cost ineffective in the long run [8]. *B. subtilis* OSU-142 may be used as a substitute for costly N-fertilisers in chickpea production even in cold highland areas such as in Erzurum [9]. Inoculation with *B. pumilus* S1r1 and *B. subtilis* UPMB10 could significantly increase plant N uptake, dry biomass and ear yield of maize. *B. pumilus* S1r1 is able to fix up to 304 mg of fixed plant N_2 [7]. Recent studies have confirmed that some strains belonging to the genus *Pseudomonas sensu stricto*, such as *P. stutzeri* A1501, *P. stutzeri* DSM4166, *P. azotifigens* 6HT33bT, and *Pseudomonas* sp. K1 have the capability to fix nitrogen [10]. The strains CY4 (*P. koreensis*) and CN11 (*P. entomophila*) show *nif*H gene expression in sugarcane (the *nif*H gene has to do with nitrogen fixation). Inoculation of the strains may be an imminent development for biofertiliser application, for sustainable crop production, in reducing environmental pollution, and in biological agri-business [11]. The inoculation of red beets with the nitrogen-fixing bacteria *Pseudomonas putida* 23 increased the activity of nitrogen fixation in the rhizosphere of plants grown in meadow soil in the central part of the Oka River floodplain [12].

Conclusions

Twenty-five bacteria strains capable of nitrogen fixation were isolated. Of these, two strains (6.2 and 8.2) have the best capacity for nitrogen fixation.

The optimal pH and temperature for the growth and nitrogen fixation of the 6.2 and 8.2 strains are 7.0 and 30°C. Growth is best favoured in the presence of sucrose.

Homological searches of 16S rRNA gene sequence of the selected strains in GenBank by BLAST revealed that the 6.2 strain is similar to sequences of *Pseudomonas* sp., and that the 8.2 strain belongs to *Bacillus* sp.

REFERENCES

[1] G. Hofman, O. van Cleemput (2004). "Soil and plant nitrogen", **1**, *International Fertilizer Industry Association*.

[2] D. Egamberdieva, Z. Kucharova (2008), "Cropping effects on microbial population and nitrogenase activity in saline arid soil", *Turk. J. Biol.*, **32**, pp.85-90.

[3] A.C. Das, D. Saha (2007), "Effect of diazotrophs on mineralization of organic nitrogen in the rhizosphere soils of rice (*Oryza sativa* L.)", *J. Crop and Weed*, **3(1)**, pp.47-51.

[4] R. Hayat, et al. (2010), "Soil beneficial bacteria and their role in plant growth promotion: a review", *Annals of Microbiology*, **60(4)**, pp.579-598.

[5] K. Tamura, et al. (2011), "MEGA5: molecular evolutionary genetics analysis using maximum likelihood, evolutionary distance, and maximum parsimony methods", *Mol. Biol. Evol.*, **28(10)**, pp.2731-2739.

[6] B.B. McSpadden Gardener (2004), "Ecology *Bacillus* and *Paenibacillus* spp. In agricultural systems", *Phytopathology*, **94(11)**, pp.1252-1258.

[7] B.K. Khing, et al. (2016), "Plant growth-promoting Rhizobacteria inoculation to enhance vegetative growth, nitrogen fixation and nitrogen remobilization of maize under greenhouse conditions", *PLOS ONE*, **11(3)**, doi.org/10.1371/journal.pone.0152478.

[8] P.P. Satapute, et al. (2012), "Isolation and characterization of nitrogen fixing bacillus subtilis strain AS-4 from agricultural soil", *International J. of Recent Scientific Research*, **3(9)**, pp.762-765.

[9] E. Erdal, K. Faik, S. Fikrettin (2007), "Influence of nitrogen fixing and phosphorus solubilizing bacteria on the nodulation, plant growth, and yield of chickpea", *Journal of Plant Nutrition*, **31(1)**, pp.157-171.

[10] S. Mehnaz (2011), "Plant growth-promoting bacteria associated with sugarcane from book Bacteria in Agrobiology: crop Ecosystems", *Bacteria in Agrobiology: crop Ecosystems*, pp.165-187, Springer-Verlag Berlin Heidelberg.

[11] H.B. Li, et al. (2017), "Genetic diversity of nitrogen-fixing and plant growth promoting *Pseudomonas* species isolated from sugarcane rhizosphere", *Front. Microbiol.*, **8**, article 1268, doi: 10.3389/fmicb.2017.01268.

[12] V.P. Shabayev (2010), "Effect of the introduction of the nitrogen-fixing bacteria *Pseudomonas putida* 23 on the nitrogen balance in soil", *Eurasian Soil Science*, **43(4)**, pp.436-441.

Gallstones and common bile duct stones: single or separated-step endoscopic retrograde cholangiopancreatography and laparoscopic cholecystectomy?

Nhu Hiep Pham[1*], Trung Vy Pham[1], Huu Thien Ho[1], Hai Thanh Phan[1], Anh Vu Pham[2], Nhu Nguyen Phuong Tran[1], Ngoc Sang Ho[1], Thanh Xuan Nguyen[1], Tien Nhan Van[1], Nghiem Trung Tran[1], Xuan Dong Pham[1], Trung Hieu Mai[1]

[1]Hue Central Hospital
[2]Hue University of Medicine and Pharmacy

Received 26 January 2018; accepted 9 May 2018

Abstract:

Purpose: **the treatment of concomitant gallstones and common bile duct (CBD) stones by endoscopic retrograde cholangiopancreatography (ERCP) following laparoscopic cholecystectomy (LC). The analysis of single-step or separated-step characteristics.** ***Object:*** **during the three years (2015-2017), 68 patients having CBD stones concomitant gallstones suitable criteria for inclusion at Hue Central Hospital. Retrospective clinical description study.** ***Results:*** **the average age is 52.2±12.5 years (24-90) and the male/female ratio is 0.7/1 (27/41). Abdominal pain was the most common symptom 91.2%, which was followed by jaundice 51.5%; direct bilirubin increased by 27.3±15.6 µmol/l (2.2-165). The size of CBD stones is 12.4±3.2 mm (6-20), the size of gallstones is 11.3±6.2 mm (5-36). The first time CBD stones 95.6%, recurrent CBD stones 4.4%. Single-step ERCP and LC 34 patients, separated-step group: ERCP 1.4±2.5 times and secondary LC. Single-step ductal clearance 76.5%, separated-step ductal clearance 94.1% (p=0.041). Length of hospital stay 6.5±4.3 days and 13.6±2.2 days (p<0.0001).** ***Conclusions:*** **the rate of ductal clearance in the separated-step group was significantly higher than the single-step group with p=0.041. The indication of laparoscopic cholecystectomy immediately ERCP should be based on the patient's morbidity, the ductal clearance as well as the prognostic complications of ERCP.**

Keywords: **gallstones, common bile duct stones, endoscopic retrograde cholangiopancreatography.**

Classification number: **3.2**

Introduction

Biliary stone is a common disease in gastrointestinal surgery and often causes serious complications. Diagnosis is usually not difficult, but the treatment of clearance and prevention of recurrence, especially with intrahepatic stones, is often difficult [1, 2].

According to the studies of many authors, at the time of diagnosis, gallstones are about 10-18% concomitant CBD stones.

With gallstones, LC has become the gold standard and the first choice. However, for concomitant gallstones and CBD stones, laparoscopy alone is not enough, and thus, we need other methods such as open choledochotomy and particular ERCP with or without Oddi sphincterotomy [3, 4].

With the development of science-technology and the cooperation between gastrointestinal surgeons and interventive endoscopists, ERCP has been widely applied. By cleaning the CBD stones through ERCP, patients avoid a long incision from open surgery, avoid Kehr drainage with its complications, as well as decreasing length of hospital stay, the cost of treatment and early working.

Based on the treatment of concomitant gallstones and CBD stones in Hue Central Hospital, we conducted this study to evaluate the results of applying ERCP technique and the effects of single-step LC at the same time anaesthesia or separated-step LC.

Materials and methods

Materials: during the three years (2015-2017), 285 patients having CBD stones concomitant or not gallstones underwent ERCP. This included 68 patients who underwent ERCP following laparoscopic cholecystectomy (34 patients

*Corresponding author: Email: nhuhieppham@yahoo.com.vn

single-step LC, 34 patients separated-step LC) and were suitable for this research.

Methods:

- Retrospective clinical description study at Hue Central Hospital.

- The duration was three years (from January 2015 to December 2017).

- Inclusion: patients with concomitant gallstones and CBD stones (Fig. 1).

+ Symptomatic gallstones or size ≥1 cm.

+ The first time CBD stones or recurrence size ≤2 cm suitable for ERCP [3].

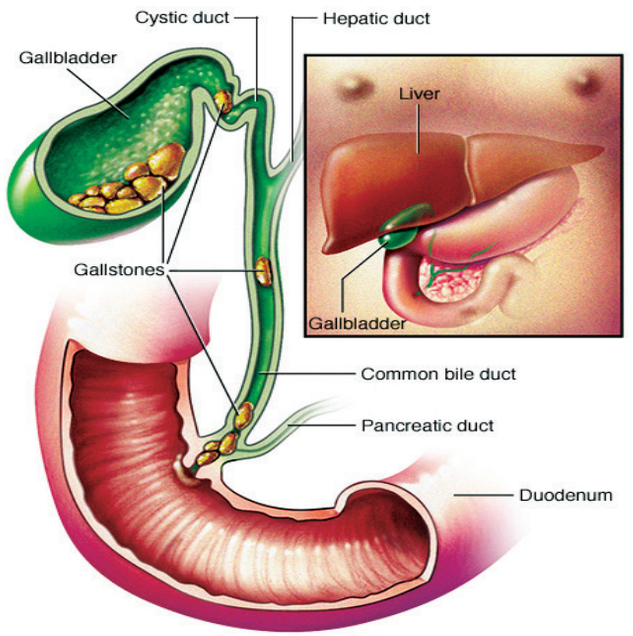

Fig. 1. Concomitant gallstones and common bile duct stones.

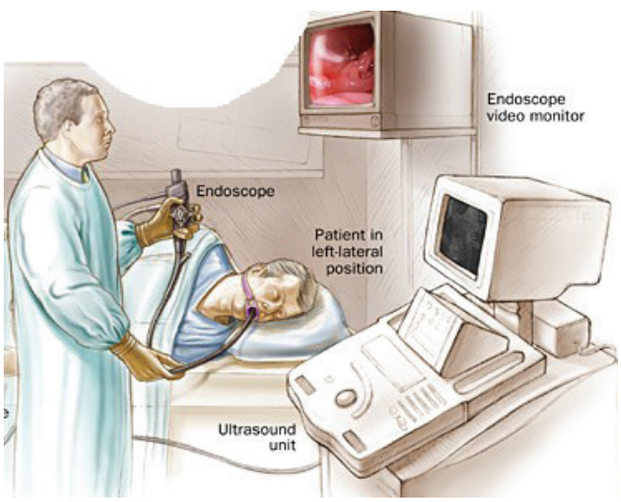

Fig. 2. Endoscopic retrograde cholangiopancreatography.

- Exclusion: patients underwent ERCP and LC but:

+ Had concomitant intrahepatic stones.

+ Post-op diagnosis was malignancy of biliary tract, ampullary or periampullary cancer.

+ Presence of old scar in the middle: choledochotomy, gastrectomy.

Technique (Fig. 2):

- Patients diagnosed with concomitant gallstones and CBD stones are characterised by clinical, biochemical, haematologist and abdominal ultrasonography. Patients could not excluded CBD stones as dilatation of CBD, increasing of direct bilirubinaemia and alkaline phosphatasemia, thus, magnetic resonance imaging (MRI) was required for confirmation and a different diagnosis.

- Endoscopic retrograde cholangiopancreatography (ERCP) [5]:

+ General anaesthesia is used for all patients; the cannula is inserted gently through the mouth into the esophagus, stomach and the duodenum and the ampullar Vater, where the bile duct and pancreatic duct fall into the duodenum.

+ Evaluation of the combined lesions of the esophagus and stomach during the endoscopic examination was possible.

+ The catheter was inserted into the bile in the direction of 11 hours, injecting the contrast to assess the position of CBD obstruction and other lesions such as CBD stones and CBD stenosis.

+ Oddi sphincterotomy: guidewire guided, cutting and haemostatic control of the sphinterotomy was made in the direction from 11 to 1 o'clock.

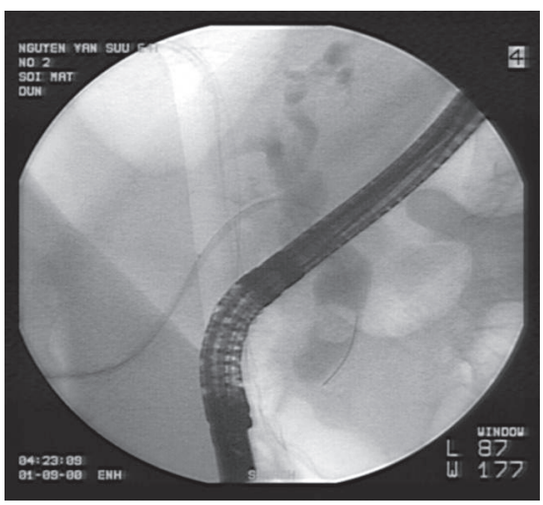

+ Enlarging the papillary opening, extraction stones by the balloon catheter or the basket and placing the stent. The process takes 2-3 times if the stones are large and many in number [5].

- Laparoscopic cholecystectomy:

+ For Single-step (at the same time anaesthesia): after the ERCP, the patient was changed to a Trendelenburg posture, the trocas was inserted to perform the laparoscopic cholecystectomy.

For Separated-step (2 times anaesthesia): after the ERCP and sphincterotomy for remove stones, the patient was returned to the GI Department and the ductal clearance was evaluated by abdominal ultrasonography, bilirubin blood (in the next day). The complications of ERCP were evaluated through blood tests, amylasemia and lipasemia for stable treatment. If remnant stones still existed after the first ERCP, the second or the third ERCP was performed for ductal clearance and separated-step LC.

+ After three times, if ERCP is not ductal clean, it has fail. Patients will be changed to other treatments.

- The length of the hospital stay (LOH) is from the first ERCP to the discharge of the patient from the hospital.

Results

General characteristics of patients

	n=68 (%)
Mean age (min 24; max 90)	52.2±12.5
Male/Female (27/41)	0.7/1
Clinical manifestations	
- Abdominal pain	62 (91.2)
- Jaundice	35 (51.5)
- Biliary infection	15 (22.1)
Direct bilirubin (2.2-165 µmol/l)	27.3±15.6
Abdominal ultrasound findings	
- Quantity of CBD stones (1-5 stones)	1.7±2.1
- Size of CBD stones (min 6 mm; max 20 mm)	12.4±3.2
- Size of gallstones (min 5 mm; max 36 mm)	11.3±6.2
CBD stones characteristics	
- Primary stones	65 (95.6)
- Recurrent stones	3 (4.4)
Concomitant morbidity	
- Biliary infection	15 (22.1)
- Acute pancreatitis	7 (10.3)

Surgical procedures

	ERCP+LC (n=34) (Single-step)	ERCP/LC (n=34) (Separated-step)
ERCP+LC (single-step)	34	-
1ERCP/LC (separated-step)	-	25
2 ERCP/LC	-	7
3 ERCP/LC	-	2
Time of ERCP (mean)	1	1.4±2.5

Results

	Single-step n=34 (%)	Separated-step n=34 (%)	p
Ductal clearance	26 (76.5)	32 (94.1)	0.041
Remnant	8 (23.5)	2 (5.9)	0.041
Complications			
- Bleeding (ERCP)	2 (5.9)	2 (5.9)	-
- Bleeding (LC)	0 (0)	1 (2.9)	0.321
- Duodenal perforation	1 (2.9)	0 (0)	0.321
- Acute pancreatitis	5 (14.7)	3 (8.8)	0.453
- Biliary infection	3 (8.8)	2 (5.9)	0.649
- Injury of the biliary tract (LC)	0 (0)	1 (2.9)	0.321
Conversion	1 (2.9)	1 (2.9)	-
Length of hospital stay (day) (Exclusion of conversion)	6.5±4.3 (n=33)	13.6±2.2 (n=33)	<0.0001

Discussion

Based on our experience, 68 patients underwent endoscopic retrograde cholangiopancreatography combined with laparoscopic cholecystectomy for three years for the treatment of concomitant gallstones and CBD stones.

All patients having concomitant gallstones and CBD stones are not suitable for ERCP to clean CBD stones. However, when it is properly indicated that ERCP is required, this technique can be considered as a 'minimal intervention with maximum efficiency'. For ductal clearance, the advancement of the equipments as well as the experience of the gastrointestinal endoscopist, the patient does not have to undergo a long incision or traditional Kehr drainage and its complications [1].

The mean age in our study was 52.2±12.5 years (min 24, max 90). A.H. Ghazal and M.A. Sorour [6] showed an average of 45.07±11.3 years (27-65), and according to R.

Mallick and K. Rank [7], the mean age in two study groups was 52.1±20.7 years and 49±20.0 years.

Technically, this is a combination of two techniques: endoscopic intervention and laparoscopic surgery. In the early stages of our study, the majority of patients underwent ERCP and LC at the same time anaesthesia. This work is theoretically more beneficial, as patients do not have to suffer the second anaesthesia for LC. However, it is not suitable in reality; the evaluation and monitoring of the complications resulting from ERCP was considerably difficult, easily obscured and hard to distinguish from the complications resulting from LC, such as bleeding, biliary tract injury and other organ damage, during the laparoscopic operation. We observed one case of duodenal perforation following the late single-step ERCP and LC - patients with fever, abdominal fluid and, especially, disadvantages of abdominal X-rays - that could not distinguish free air intraperitoneum from the duodenal perforation or from the pneumo-peritoneal; additionally, this affects early diagnosis.

According to many authors, the safety and feasibility of the technique of ERCP should be based on the criteria for ductal clearance, complications, morbidity and mortality rate that are technically related [4, 8, 9]. The rate of ductal clearance in our study was 85.3% (58/68), which was consistent with the study of J.H. Darrien and K. Connor [9] that showed 84-97% ductal clearance, complications 4-16% and mortality 0-0.8%. Kieu Van Tuan and Tran Huu Vinh [8] reported 97.8-98.2% ductal clearance, no duodenal perforation, mild bleeding or only injection adrenalin of 7.1%. A.H. Ghazal and M.A. Sorour [6] showed 100% ductal clearance and the length of hospital stay as 2.55±0.89 days (2-5). La Van Phuong, et al. [1] showed a mortality rate of 14.3% due to late hospitalisation, hypotension, coagulopathy, renal failure and electrolyte disorder.

R. Mallick and K. Rank [7] evaluated the combination of single-step ERCP and LC (n=80) or separate-step ERCP and LC (n=33). The LOH of the single-step group was significantly lower than the separate-step group (p=0.03); our results were consistent (p<0.0001). However, according to the study by Mallick, et al., the mean cost was not significant (p=0.167): 49,276 $ for the single-step group versus 42,261 $ for the separate-step group.

ERCP is an invasive procedure for the diagnosis and treatment of CBD and pancreatic diseases. According to Ho Van Han and Tran Duy Binh, the rate of complications is 9.8% (pancreatitis 6%, bleeding 1.5%, perforation 1.56%, infection 0.78%) and 1 patient of death due to pancreatitis after ERCP [10]. Therefore, the decision to LC immediately after ERCP at the same time of general anaesthesia (single-step) or later (separate-step) depends on the patient's morbidity, the ductal clearance identified intraoperative as well as the complications. If the patient was suspected of having gastric-duodenal perforation and bleeding during the ERCP procedure, it is absolutely separate-step LC after complications of infection, pancreatitis, bleeding were treated consistently [11].

Conclusions

The rate of ductal clearance in the separate-step group was significantly higher than the single-step group with p=0.041.

The indication of single-step laparoscopic cholecystectomy immediately after ERCP or separate-step surgery should be based on the patient's morbidity, the ductal clearance as well as the prognostic complications of ERCP.

REFERENCES

[1] La Van Phuong (2012), "Results of early endoscopic retrograde cholangiopancreatography (ERCP) in the treatment of Complicated cholangitis at Can Tho polyclinic Central Hospital", *Medicine of Ho Chi Minh city*, **16(3)**, pp.49-53.

[2] Nguyen Kim Tue, Pham Nhu Hiep (1999), *Indication and result evaluation of Endoscopic retrograde cholangiopancreatography (ERCP) and sphincterotomy for canal bile duct stones extraction*, Presentation at 10th Vietnam Surgical Conference, pp.127-132.

[3] R. Kadam, D. Saxena, A.S. Rana, S. Chhabra (2016), "Laparoscopic common bile duct exploration versus ERCP/stenting and cholecystectomy: is a single staged procedure better?", *International Journal of Hepatobiliary and Pancreatic Diseases,* **6**, pp.57-63.

[4] A. Shojaiefard, M. Esmaeilzadeh, A. Ghafouri, and A. Mehrabi (2009), "Various techniques for the surgical treatment of common bile duct stones: a meta review", *Gastroenterology Research and Practice*, ID 840208, 12pp, doi:10.1155/2009/840208.

[5] J. Pohl, D.H.S. Klinik (2012), "Choledocholithiasis - sphincterotomy and stone removal with an extraction balloon", *Video Journal and Encyclopedia of GI Endoscopy,* Germany, doi.org/10.1016/S2212-0971(13)70199-7, pp.445-446.

[6] A.H. Ghazal, M.A. Sorour, M. El-Riwini (2009), "Single-step treatment of gall bladder and bile duct stones: a combined endoscopic-laparoscopic technique", *International Journal of Surgery*, **7**, pp.338-346.

[7] R. Mallick, K. Rank, C. Ronstrom, S.K. Amateau, M. Arain (2016), "Single-session laparoscopic cholecystectomy and ERCP: a valid option for the management of choledocholithiasis", *Gastrointestinal Endoscopy*, **84(4)**, pp.639-645.

[8] Kieu Van Tuan, Tran Huu Vinh (2013), "Treatment of stones bile duct infection by Endoscopic retrograde cholangiopancreatography (ERCP)", *Practical of Medicine,* **893**, pp.147-151.

[9] J.H. Darrien, K. Connor, A. Janeczko, J.J. Casey, and S. Paterson-Brown (2015), "The surgical management of concomitant gallbladder and common bile duct stones", *HPB Surgery*, Edinburgh EH16 4SA, UK, pp.1-6.

[10] Ho Van Han, Tran Duy Binh, Nguyen Van Hai (2010), "Diagnostic and therapeutic Endoscopic retrograde cholangiopancreatography (ERCP) at Gia Dinh Hospital", *Medicine of Ho Chi Minh city*, **14(4)**, pp.67-73.

[11] J. Lu, Y. Cheng, X.Z. Xiong, Y.X. Lin, S.J. Wu, N.S. Cheng (2012), "Two-stage vs single-stage management for concomitant gallstones and common bile duct stones", *World J. Gastroenterol.*, **18(24)**, pp.3156-3166.

Construction of a binary vector for the expression of the *Aspergillus niger McoD* laccase gene in the industrial filamentous fungus *Aspergillus oryzae*

Hanh Dung Thai[1,2], Van-Tuan Tran[1,2*]

[1]*Genomics Unit, National Key Laboratory of Enzyme and Protein Technology, VNU University of Science, Vietnam National University, Hanoi*
[2]*Department of Microbiology, Faculty of Biology, VNU University of Science, Vietnam National University, Hanoi*

Received 2 May 2018; accepted 2 August 2018

Abstract:

The filamentous fungus *Aspergillus oryzae,* also named as the *koji* mold, is a preferred host for enzyme production due to its prominent secretion ability into the culture medium. Fungal laccases are widely used in different industrial processes, especially in removing environmental pollutants. Up till now, little was known about the roles of some laccase genes from the black mold *Aspergillus niger*. The *McoD* laccase gene from *A. niger* includes three exons interrupted by two short introns. The respective coding sequence of the gene is computationally predicted to encode a secreted laccase of 563 amino acids. In this study, a binary vector carrying the *A. niger McoD* gene was successfully constructed for heterologous expression in the edible fungus *A. oryzae*. This vector was transformed into *A. oryzae* using the *Agrobacterium tumefaciens*-mediated transformation method. The transformation efficiency was relatively high in two different auxotrophic *A. oryzae* strains, including RIB40Δ*pyrG* and VS1Δ*pyrG*. All the tested transformants possess in their genomes the construct for expression of the *McoD* laccase gene under control of the strong *A. oryzae amyB* promoter. The selected transformants were examined for the laccase activity using the ABTS substrate. The results showed that in comparison to the wild-type fungal strains, the transgenic strains could oxidise ABTS to form the sea green colour, which can be seen directly on the agar plate.

Keywords: **Agrobacterium tumefaciens-mediated transformation, *Aspergillus oryzae,* binary vector, laccase, recombinant expression.**

Classification number: **3.5**

Introduction

Aspergillus oryzae is a safe filamentous fungus and considered as an excellent microbial host for the biopharmaceutical industry and for the production of recombinant proteins. This fungus has been widely used in the food industry in some Asian countries for thousands of years. Several commercial digestive enzymes such as proteases, lipases and cellulases have been produced in *A. oryzae* [1, 2]. *A. oryzae* is a promising fungal cell factory owing to its ability to secrete large amounts of enzymes into the culture media. Therefore, this fungus has been employed for genetic engineering to produce economically valuable enzymes at the industrial scale [3].

Laccases are widely distributed in higher plants, insects, fungi and bacteria. They form the biggest sub-group within the multicopper oxidase (MCO) family and represent a great potential in biotechnological applications such as pulp delignification, textile dye bleaching, and water or soil detoxification [4, 5]. Laccase (EC 1.10.3.2) is a multicopper blue oxidase that couples the four-electron reduction of oxygen with the oxidation of a broad range of organic substrates including phenols, polyphenols, anilines, and even certain inorganic compounds by a one-electron transfer mechanism [6]. The ability of laccases to catalyse reactions by generating water as the only by-product makes these enzymes the 'green' catalysts in the industry [4, 5]. However, in most fungi, laccases are produced at low levels for commercial purposes. Therefore, cloning of the laccase genes followed by heterologous expression in suitable fungal hosts may provide outstanding enzyme yields [7].

In ascomycetes, MCOs have been much less studied [8].

*Corresponding author: Email: tuantran@vnu.edu.vn

The McoD laccase belongs to the cluster of the ascomycetous laccases that exist in the common filamentous fungi such as *Botrytis cinerea*, *Neurospora crassa*, *Aspergillus niger* and *Aspergillus nidulans* [9]. It is remarkable that limited information is available for the potential of the laccase-encoding *McoD* gene. This is the first time that the *McoD* gene from *A. niger* was transformed and expressed in the safe fungus *A. oryzae* using the *Agrobacterium tumefaciens*-mediated transformation (ATMT) method.

Materials and methods

Microbial strains and plasmids

In this study, *Escherichia coli* DH5α was used as a bacterial host for plasmid propagation, with *Agrobacterium tumefaciens* AGL1 as the tool for fungal transformation and *A. niger* N402 as the DNA donor. Two different auxotrophic strains of *A. oryzae* including VS1Δ*pyrG* and RIB40Δ*pyrG* were employed as the recipients for genetic transformation. The binary vector pEX2B was used as the backbone for constructing the pEX2B-McoD vector. All these materials are listed in Table 1.

Table 1. Microbial strains and plasmids used in this study.

Strains, plasmids	Description	Source
E. coli DH5α	F- *endA1 hsdR17 supE44 thi-1* λ- *recA1 gyrA96 relA1 deoR* Δ(*lacZYA-argF)*-U169 Φ80d*lacZ*ΔM15	[10]
A. tumefaciens AGL1	C58, *recA::bla*, pTiBo542ΔT-DNA, Mop^+, Cb^R	[11]
A. niger N402	The wild-type strain used as DNA donor	[12]
A. oryzae RIB40	The wild-type strain used as a negative control	[13]
A. oryzae VS1	The wild-type strain used as a negative control	[14]
A. oryzae RIB40Δ*pyrG*	The uridine/uracil auxotrophic strain used for genetic transformation	[14]
A. oryzae VS1Δ*pyrG*	The uridine/uracil auxotrophic strain used for genetic transformation	[14]
pEX2B	This plasmid harbours the *A. oryzae pyrG* marker and the *DsRed* gene under control of the *A. oryzae amyB* promoter	[14]
pEX2B-McoD	This plasmid harbours the *A. oryzae pyrG* and the *A. niger McoD* laccase gene under regulation of the *A. oryzae amyB* promoter	This study

Media for cultivation

Potato dextrose agar (PDA) medium (with supplements of 0.1% uracil and 0.1% uridine) was used for cultivating the auxotrophic *A. oryzae* VS1Δ*pyrG* and *A. oryzae* RIB40Δ*pyrG* strains.

M+met medium comprising 0.2% NH_4Cl, 0.1% $(NH_4)_2SO_4$, 0.05% KCl, 0.05% NaCl, 0.1% KH_2PO_4, 0.05% $MgSO_4$, 0.002% $FeSO_4$, 2% glucose, 0.15% methionine and pH 5.5 [15] was used as the selective medium for fungal transformation.

The induction medium (IM) supplemented with 0.05% uracil, 0.05% uridine and 200 µM acetosyringone (AS) was used for co-cultivation between the *Agrobacterium* cells and fungal spores. The liquid IM contains MM salts (2.05 g K_2HPO_4, 1.45 g KH_2PO_4, 0.15 g NaCl, 0.5 g $MgSO_4.7H_2O$, 0.1 g $CaCl_2.6H_2O$, 0.5 g $(NH_4)_2SO_4$, 0.0025 g $FeSO_4.7H_2O$), 40 mM 2-(*N*-morpholino)ethanesulfonic acid (MES), 10 mM glucose and 0.5% (w/v) glycerol. The solid IM contains only 5 mM glucose and 2% agar [16-18].

Preparation of spore suspensions

The VS1Δ*pyrG* or RIB40Δ*pyrG* strain was cultivated on the PDA plate that was supplemented with 0.1% uracil and 0.1% uridine for 3-5 days at 30°C. Sterile distilled water was added to the plate and the spores were released from the fungal layer by scraping the plate surface with a sterile glass spreader. The obtained liquid was filtered using sterile Miracloth (Calbiochem, Germany) and the filtrate was centrifuged at 5000 rpm for 10 min. The spore pellet was washed twice with sterile distilled water prior to being resuspended in sterile distilled water to gain the respective spore suspension. The spore concentration was calculated and adjusted to 10^6 spores/ml using a Thoma counting chamber.

Genomic DNA extraction

The extraction of fungal genomic DNA was performed as previously reported [19]. The obtained genomic DNA samples were dissolved in the TE buffer and treated with 3 µl RNase A (Qiagen, Hilden, Germany) for 30 min at 60°C to remove RNA.

Analysis of the McoD gene from A. niger

The sequence of the *Aspergillus niger McoD* gene

with the accession number An11g03580 was extracted from the *Aspergillus* genome database (http://www.aspergillusgenome.org). The deduced McoD protein was used for the detection of a signal peptide using the SignalP 4.1 Server (http://www.cbs.dtu.dk/services/SignalP) [20]. The conserved domains of McoD were detected by the web tools InterPro (https://www.ebi.ac.uk/interpro) and Pfam (https://pfam.xfam.org). The comparative phylogeny of McoD and its homologues from other filamentous fungi was performed with the MEGA6 software [21] using the neighbour-joining method with 1000 bootstrap replicates.

Construction of the binary vector pEX2B-McoD

The *McoD* gene was amplified from genomic DNA of *A. niger* N402 by PCR using the following primer pair including AnMcoD-F (GGG CTT AAG ATG CAC TTG CAT ACT ATC CTG G) and AnMcoD-R (GGG GAG CTC TTA GAT ACC AGA ATC ATC CTC CTC). To ensure the accuracy of DNA replication by the PCR, Phusion® high-fidelity DNA polymerase (Thermo Scientific, USA) was used. The PCR conditions were as follows: initial denaturation at 94°C for 5 min followed by 35 cycles of denaturation at 94°C for 30s, annealing at 58°C for 30s, and extension at 72°C for 1 min 40s, with a final extension at 72°C for 10 min. The PCR product was purified with Wizard® SV Gel and PCR Clean-Up System (Promega, USA). The purified product was digested with the restriction enzymes *Afl*II and *Sac*I, and ligated into the binary vector pEX2B [14] at the respective restriction enzyme sites to replace the *DsRed* gene. The ligation mixture was then used to transform the competent *E. coli* DH5α cells. The recombinant plasmid was purified using Wizard® Plus SV Minipreps DNA Purification System (Promega, USA) and further confirmed by digestion with *Bam*HI (Thermo Scientific, USA) to indicate the presence of the *McoD* gene.

Genetic transformation of A. oryzae using ATMT method

ATMT transformation was performed as previously described [14, 18]. Briefly, the binary vector pEX2B-McoD was transformed into the *A. tumefaciens* AGL1 cells by electroporation method [22]. A single AGL1 colony carrying pEX2B-McoD was inoculated in a conical flask containing 20 ml of liquid LB (Luria-Bertani) supplemented with kanamycin (100 µg/ml) on a rotary shaker with 200 rpm at 28°C for 17h. The bacterial culture (1 ml) was diluted with the liquid IM (9 ml) containing 200 µM acetosyringone (AS) to obtain an OD_{600} value ranging from 0.2 to 0.3. The diluted culture was further incubated for 6h at 28°C, 200 rpm to reach an OD_{600} value ranging from 0.6 to 0.8. A mixed volume including 100 µl of the induced AGL1 suspension and 100 µl of the *A. oryzae* spore suspension (10^6 spores/ml) was spread onto the 90 mm filter paper (Sartorius, Germany) placed on the IM agar plate supplemented 200 µM AS, 0.05% (w/v) uracil and 0.05% (w/v) uridine. The plate was incubated at 22°C in the dark for 60h. After the co-cultivation period, the filter paper was transferred to the M+met plate containing cefotaxime (300 µg/ml) to eliminate the *Agrobacterium* cells. This plate was incubated at 30°C for 5-7 days until the fungal transformants appeared.

Analysis of fungal transformants

Fungal transformants were purified and examined for mitotic stability by single spore isolation for three successive generations. The purified transformants were then grown for genomic DNA extraction. PCR was employed to confirm the existence of the *A. niger McoD* gene in the *A. oryzae* genome using the specific primer AnMcoD-F/AnMcoD-R. To screen the transformants expressing the *McoD* gene, some obtained transformants were grown on the M+met agar medium containing 2% maltose as the inducer of the *amyB* promoter. After incubating at 37°C for 48h, 4 mM of ABTS (2,2'-azino-bis(3-ethylbenzothiazoline-6-sulphonic acid)) in the McIlvaine buffer (also known as citrate-phosphate buffer, pH 4.6) [23] was dropped directly onto the fungal mycelium. The oxidation of the substrate ABTS by a suitable laccase results in the stable blue/green cation radical $ABTS^{\cdot+}$ [24]. Fungal transformants expressing successfully the *McoD* laccase gene can oxidise ABTS to generate the sea green colour.

Results and discussion

Structural analysis of the A. niger McoD laccase gene

The *McoD* gene indicated by the locus An11g03580 in the *Aspergillus niger* genome database and by the accession number XP_ 001394357 in the GenBank database has a total length of 1806 bp including three exons (881 bp, 483 bp and 328 bp) interrupted by two introns (52 bp and 62 bp). The coding sequence of *McoD* encodes a predicted protein of 563 amino acids with three conserved Cu-oxidase domains

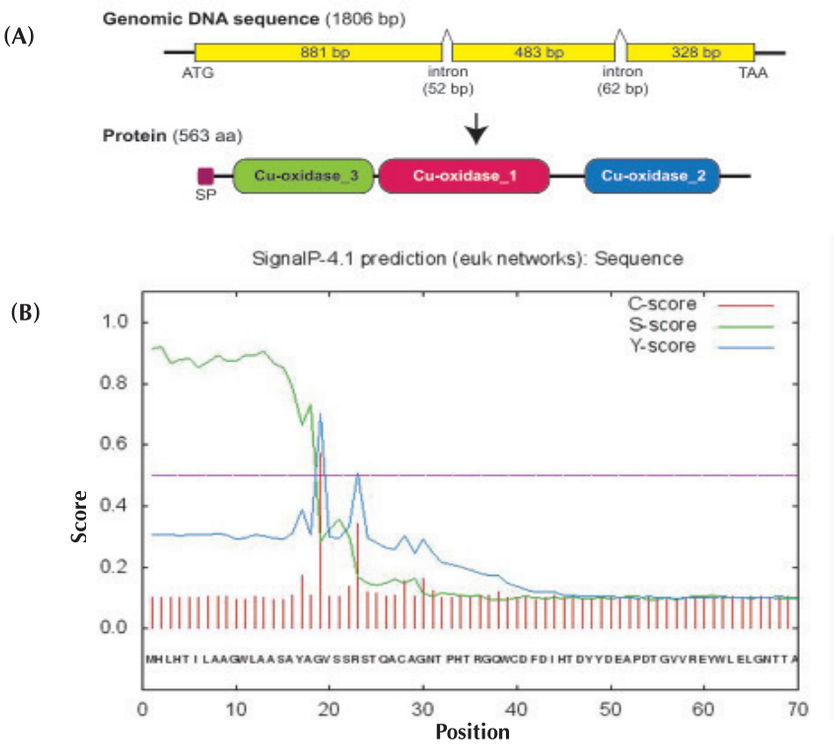

Fig. 1. Structural analysis of the *McoD* gene from *A. niger*. (A) The structure of the *McoD* gene and the respective encoded protein possessing a signal peptide (SP) and typical conserved domains for laccase family. **(B)** The signal peptide of the deduced McoD protein was detected with SignalP 4.1 [20].

(Fig. 1A). The deduced protein sequence is also indicated by the bioinformatics tool SignalP 4.1 to possess a putative signal peptide with the cleavage site between amino acid positions 18 and 19 at the N terminus (Fig. 1B).

In fungi, laccases play different physiological roles during the fungal life cycle. These enzymes display a huge potential for a variety of biotechnological applications due to their broad substrate range [4, 25, 26]. The black mold *A. niger* possesses 16 different genes encoding putative laccases in its genome [9]. Among them, McoD belongs to the group of the ascomycetous laccases. Although McoD is conserved in some other *Aspergillus* species, surprisingly, it does not exist as a homologue in the genome of *A. oryzae* (Fig. 2). Therefore, *A. oryzae* can be used as an excellent host for the heterologous expression of the *McoD* gene, as it appears that there is no activity of the McoD laccase in this filamentous fungus.

Successful construction of a binary vector for expressing the A. niger McoD laccase gene

Based on the respective sequence for *McoD* (An11g03580) from the *A. niger* genome database, this gene was successfully amplified by PCR using the specific primer pair AnMcoD-F/AnMcoD-R. The obtained PCR product was digested with two restriction enzymes, *Afl*II and *Sac*I. This digestion generated the compatible sticky ends enabling the ligation of the DNA insert to the binary vector pEX2B [14], which were also treated with the same enzymes *Afl*II and *Sac*I in order to remove the *DsRed* reporter gene (Fig 3A). The resulting recombinant plasmid pEX2B-McoD (Fig. 3A) was confirmed for the presence of the *McoD* gene by PCR with the specific primer pair AnMcoD-F/AnMcoD-R (data not shown). This plasmid was then purified and further confirmed by digestion with *Bam*HI, which cuts the plasmid at two different sites including one in the *McoD* sequence and the other in the plasmid backbone. The result showed that there were two DNA bands as theoretically calculated with the sizes of 10.56 kb and 1.39 kb appearing on the agarose gel (Fig. 3B). Therefore, we can conclude that the binary vector pEX2B-McoD for expressing the *A. niger McoD* laccase gene under the regulation of the *A. oryzae amyB* promoter was successfully constructed.

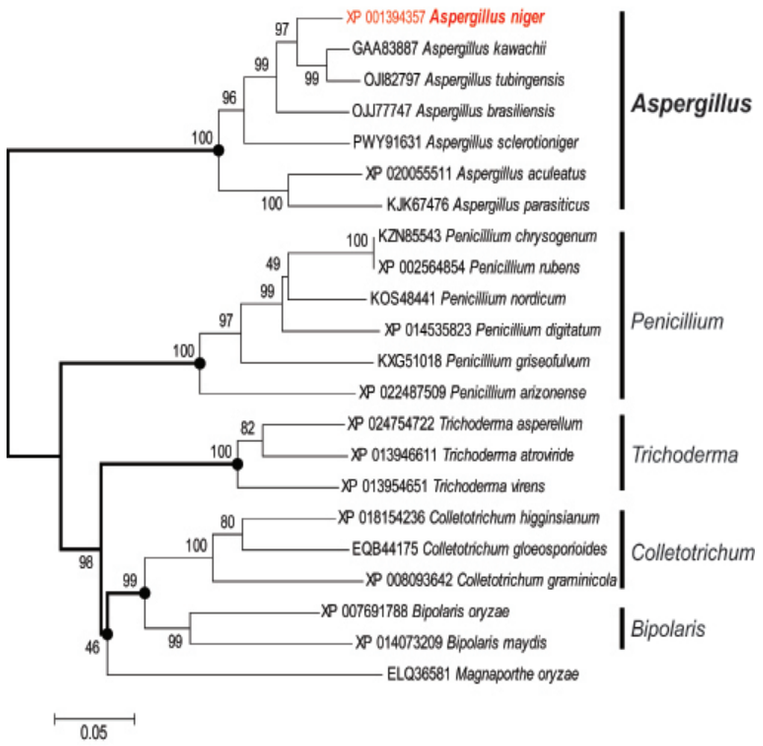

Fig. 2. Phylogenetic analysis of the *McoD* gene from *A. niger* in comparison to its homologues from other filamentous fungi. The phylogenetic tree was constructed with the MEGA6 software [21] using the neighbour-joining method with 1000 bootstrap replicates. The statistical support values at nodes of branches, genetic distance scale bar and the accession numbers from the GenBank database have been indicated.

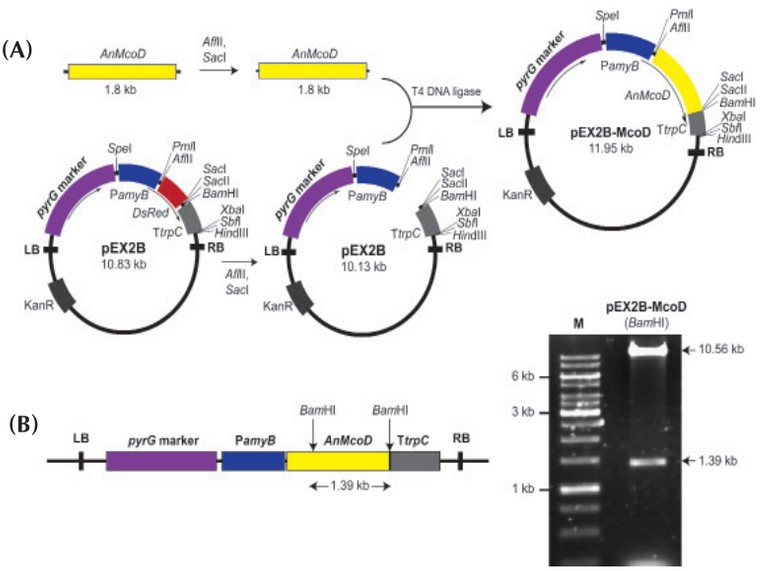

Fig. 3. Construction of the pEX2B-McoD binary vector. (A) The procedure for constructing pEX2B-McoD by replacing the *DsRed* gene in the pEX2B vector with the *A. niger McoD* laccase gene. **(B)** Confirmation of the correctness of pEX2B-McoD by digestion of this plasmid with *Bam*HI.

Successful transformation of A. oryzae using the ATMT method and the pEX2B-McoD vector

The ATMT method has been recently demonstrated to be a powerful tool for the genetic transformation of the filamentous fungus *A. oryzae* based on the uridine/uracil auxotrophy [14]. This method does not use drug resistance markers, and therefore, it is considered as a safe approach for subsequent applications. In this study, the binary pEX2B-McoD was constructed and transformed successfully into the competent *Agrobacterium tumefaciens* AGL1 cells by electroporation. The resulting bacterial colonies were screened for the presence of the plasmid by PCR with the primer pair AnMcoD-F/AnMcoD-R using GoTaq® Green Master Mix (Promega, USA). All of the tested colonies were indicated to carry pEX2B-McoD via the DNA band for *McoD* appearing on the 0.7% agrose gel (data not shown). The steps for fungal transformation using *Agrobacterium tumefaciens* were performed as previously reported [14, 18]. The procedure was summarised in Fig. 4A. During the co-cultivation step, *A. oryzae* spores germinated on the induction medium (IM) were supplemented with 0.05% uracil and 0.05% uridine at 22°C for 60h. Germination of fungal spores could facilitate the transfer and random integration of T-DNA carrying the *McoD* expression cassette and the auxotrophic *pyrG* selection marker from *Agrobacterium* cells into the *A. oryzae* genome. The mechanism of this DNA transfer event has been proved in numerous fungi [27]. The fungal transformants as prototrophic strains were selected on the M+met minimal medium [15], which was supplemented with cefotaxime to eliminate the *Agrobacterium* cells. After 5-7 days, the results showed that on an average, the transformation efficiency reached 6 transformants per plate, which corresponded to a total of 60 transformants per 10^6 spores for the auxotrophic *A. oryzae* VS1Δ*pyrG* strain. Meanwhile, 136±17 transformants per plate corresponded to a total of approximately 1360 transformants per 10^6 spores for the auxotrophic *A. oryzae* RIB40Δ*pyrG* strain (Fig. 4B).

ATMT has been reported to be an effective method for gene targeting in several filamentous fungi with the transformation efficiency up to 100-250 transformants per 10^6 spores [28, 29]. In the previous study, we showed that genetic transformation of the auxotrophic *A. oryzae* strains by the ATMT method using the pEX2B vector resulted in very high transformation efficiencies with 265±13 transformants per 10^6 spores for the auxotrophic VS1Δ*pyrG* strain and 1060±143 transformants per 10^6 spores for the auxotrophic RIB40Δ*pyrG* strain [14]. In this study, using the pEX2B-McoD vector, we also obtained similar results for the transformation efficiencies of the auxotrophic VS1Δ*pyrG* strain and the auxotrophic RIB40Δ*pyrG* strain (Fig. 4B).

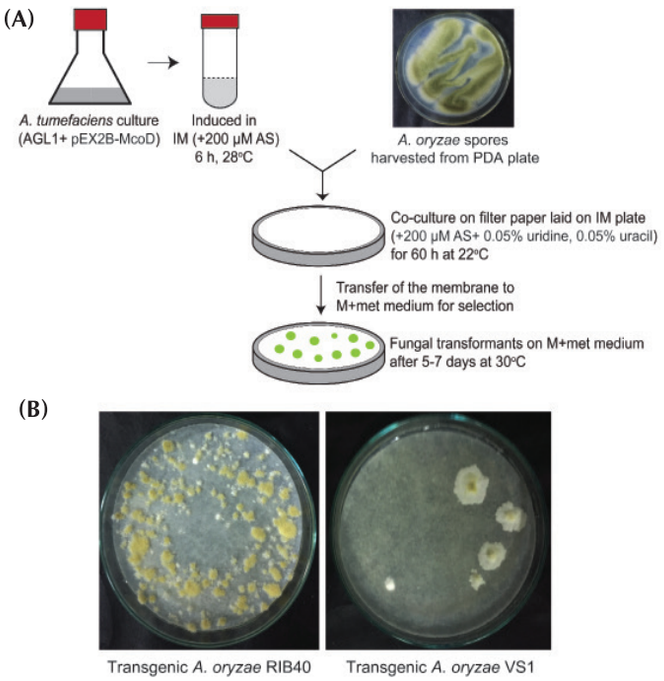

Fig. 4. Genetic transformation of the auxotrophic *A. oryzae* strains using the ATMT method. (A) The detailed ATMT procedure for *A. oryzae* VS1Δ*pyrG* and RIB40Δ*pyrG* with pEX2B-McoD. **(B)** The prototrophic *A. oryzae* transformants grew on the filter papers placed on M+met agar plates after 5 days of incubation at 30°C.

Successful integration of the McoD expression cassette into the A. oryzae genomes

In a recent publication, the overexpression of *McoD* in *A. niger* under the control of the *glaA* promoter could result in a green halo with ABTS oxidation [9]. In the constructed binary vector, *McoD* gene is regulated by the *amyB* promoter from *A. oryzae* RIB40. The *amyB* promoter is responsible for regulating the high-level expression of amylase in *A. oryzae*, and it is induced by starch or maltose [30]. Therefore, to activate the expression of the *McoD* gene under regulation of the *amyB* promoter, the M+met minimal medium was supplemented with 2% maltose as the sole carbon source. The mycelia of the transformants, which were cultivated on M+met (2% maltose) at 37°C for 48h, were tested for the ABTS oxidation ability. The transgenic strains expressing *McoD* in this study showed laccase activity towards ABTS. After treating with the ABTS substrate for 10-15 min, the fungal mycelia of all tested transformants changed to a sea green colour in comparison to the wild-type strains (Fig. 5A). This is a quick assay for screening the potential strains expressing the *McoD* laccase gene. The successful integration of the *McoD* expression cassette into the *A. oryzae* genome in the transformants was confirmed by PCR with the primer pair AnMcoD-F/AnMcoD-R. All of the tested strains were demonstrated to carry the McoD laccase gene with the size of 1.8 kb (Fig. 5B).

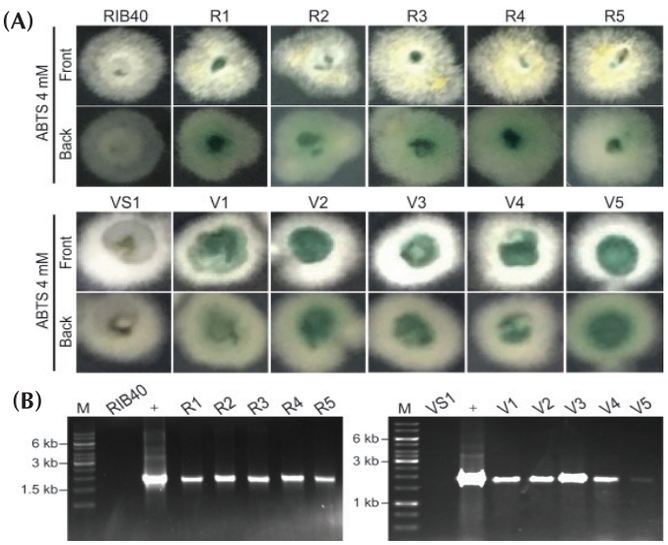

Fig. 5. Confirmation of the *A. oryzae* transformants expressing the *A. niger McoD* laccase gene. (A) Examination of some transformants expressing the *McoD* laccase gene. The selected transformants were grown on M+met (2% maltose as the sole carbon source for activating the *amyB* promoter) at 37°C for 48h. The ABTS solution was used to screen positive transformants by directly placing a drop onto the fungal mycelium. The VS1 and RIB40 wild-type strains were used as negative controls. **(B)** The above-tested transformants were confirmed by PCR for the existence of the *McoD* gene in the genome using the specific primer pair AnMcoD-F/AnMcoD-R. The genomic DNA samples extracted from the VS1 and RIB40 wild-type strains were used as templates for negative controls. The plasmid PEX2B-McoD was used as a template for positive controls.

Laccases from different fungal species may differ in their substrate specificities, and therefore, several substrates should be tested to assess a laccase activity [26]. The *A. oryzae* transformants expressing the *A. niger McoD* gene should be tested by plate activity assays for other substrates such as N, N-dimethyl-p-phenylenediamine sulphate (DMPPDA), 2,6-dimethoxyphenol (DMP) and 4-amino-2,6-dibromophenol/3,5-dimethylaniline (ADBP/DMA) to have more insights in its substrate specificity. A large number of transformants would show laccase activity against one or more than one substrate. According to Tamayo Ramos, et al. the *McoD* gene when overexpressed in *A. niger* showed its laccase activity towards ABTS, ADBP/DMA and DMPPDA, whereas it did not show activity when assayed with DMP [9]. Therefore, further studies need to be performed to examine the *A. oryzae* transformants for oxidation of these substrates by the McoD laccase activity.

Expression of a target gene in a suitable fungal host also depends on gene copy number. One copy of the gene expression cassette was sufficient for its expression, but an increase in copy number had a positive effect on the expression [31]. To identify the copy number of the target gene in a transgenic strain, real-time PCR or Southern hybridisation could be used. Furthermore, in order to determine the expression level of the *McoD* gene in potential *A. oryzae* transformants, the transcription level of the gene should be analysed by using real-time PCR with a gene-specific primer pair or by Northern hybridisation with a gene-specific probe.

Conclusions

In this study, we have succeeded in constructing the binary vector pEX2B-McoD carrying the *McoD* laccase gene from the black mold *A. niger* under the regulation of the strong *amyB* promoter. The ATMT method was employed to successfully transfer the T-DNA containing the *McoD* expression cassette from this binary vector to the genomes of two different auxotrophic *A. oryzae* strains. The *A. oryzae* strains expressing the *A. niger McoD* laccase gene were generated fruitfully by using the ATMT method with the *pyrG* auxotrophic marker. As the obtained transgenic *A. oryzae* strains possess no drug resistance gene, they are safe for exploiting potential applications of the McoD laccase in the future.

ACKNOWLEDGEMENT

We thank the members of the Genomics Unit, National Key Laboratory of Enzyme and Protein Technology (VNU University of Science, Vietnam National University, Hanoi) for their assistance and discussion.

REFERENCES

[1] M. Braaksma, P.J. Punt (2008), "*Aspergillus* as a cell factory for protein production: Controlling protease activity in fungal production", *The Aspergilli: Genomics, Medical Aspects, Biotechnology, and Research Methods*, pp.441-455.

[2] K. Ohnishi, Y. Yoshida, J. Sekiguchi (1994), "Lipase production of *Aspergillus oryzae*", *J. Biosci. Bioeng.*, **77**, pp.490-495.

[3] M. Machida, O. Yamada, K. Gomi (2008), "Genomics of *Aspergillus oryzae*: Learning from the history of koji mold and exploration of its future", *DNA Res.*, **15**, pp.173-183.

[4] V. Faracom, P. Giardina, C. Pezzella, A. Piscitelli, S. Vanhulle, G. Sannia (2010), "Laccases: a never-ending story", *Cell Mol. Life Sci.*, **67**, pp.369-385.

[5] T. Sakurai, K. Kataoka (2007), "Basic and applied features of multicopper oxidases, CueO, bilirubin oxidase, and laccase", *Chem. Rec.*, **7**, pp.220-229.

[6] A. Kunamneni, F.J. Plou, A. Ballesteros, M. Alcalde (2008), "Laccases and their applications: a patent review", *Recent Pat. Biotechnol.*, **2**, pp.10-24.

[7] R.M. Berka, P. Schneider, E.J. Golightly, S.H. Brown, M. Madden, K.M. Brown, T. Halkier, K. Mondorf, F. Xu (1997), "Characterization of the gene encoding an extracellular laccase of *Myceliophthora thermophila* and analysis of the recombinant enzyme expressed in *Aspergillus oryzae*", *Appl. Environ. Microbiol.*, **63(8)**, pp.3151-3157.

[8] J.P. Kallio, C. Gasparetti, M. Andberg, H. Boer, A. Koivula, K. Kruus, J. Rouvinen, N. Hakulinen (2011), "Crystal structure of an ascomycete fungal laccase from *Thielavia arenaria* - common structural features of asco-laccases", *FEBS J.*, **278(13)**, pp.2283-2295.

[9] J.A. Tamayo Ramos, S. Barends, R.M.D. Verhaert, L.H. de Graaff (2011), "The *Aspergillus niger* multicopper oxidase family: analysis and overexpression of laccase-like encoding genes", *Microb. Cell Fact.*, **10**, p.78.

[10] S.G. Grant, J. Jessee, F.R. Bloom, D. Hanahan (1990), "Differential plasmid rescue from transgenic mouse DNAs into *Escherichia coli* methylation-restriction mutants", *Proc. Natl. Acad. Sci. USA*, **87**, pp.4645-4649.

[11] G.R. Lazo, P.A. Stein, R.A. Ludwig (1991), "A DNA transformation-competent *Arabidopsis* genomic library in *Agrobacterium*", *Nat. Biotechnol.*, **9**, pp.963-967.

[12] C.J. Bos, A.J. Debets, K. Swart, A. Huybers, G. Kobus, S.M. Slakhorst (1988), "Genetic analysis and the construction of master strains for assignment of genes to six linkage groups in *Aspergillus niger*", *Curr. Genet.*, **14(5)**, pp.437-443.

[13] M. Machida, K. Asai, M. Sano, T. Tanaka, T. Kumagai, G.

Terai, K. Kusumoto, T. Arima, O. Akita, Y. Kashiwagi, K. Abe, K. Gomi, H. Horiuchi, K. Kitamoto, T. Kobayashi, M. Takeuchi, D.W. Denning, J.E. Galagan, W.C. Nierman, J. Yu, D.B. Archer, J.W. Bennett, D. Bhatnagar, T.E. Cleveland, N.D. Fedorova, O. Gotoh, H. Horikawa, A. Hosoyama, M. Ichinomiya, R. Igarashi, K. Iwashita, P.R. Juvvadi, M. Kato, Y. Kato, T. Kin, A. Kokubun, H. Maeda, N. Maeyama, J. Maruyama, H. Nagasaki, T. Nakajima, K. Oda, K. Okada, I. Paulsen, K. Sakamoto, T. Sawano, M. Takahashi, K. Takase, Y. Terabayashi, J.R. Wortman, O. Yamada, Y. Yamagata, H. Anazawa, Y. Hata, Y. Koide, T. Komori, Y. Koyama, T. Minetoki, S. Suharnan, A. Tanaka, K. Isono, S. Kuhara, N. Ogasawara, H. Kikuchi (2005), "Genome sequencing and analysis of *Aspergillus oryzae*", *Nature*, **438**, pp.1157-1161.

[14] T.K. Nguyen, N.Q. Ho, T.B.X.L. Do, T.D.L. Mai, D.N. Pham, T.T.H. Tran, H.D. Le, Q.H. Nguyen, V.T. Tran (2017), "A new and efficient approach for construction of uridine/uracil auxotrophic mutants in the filamentous fungus *Aspergillus oryzae* using *Agrobacterium tumefaciens*-mediated transformation", *World J. Microbiol. Biotechnol.*, **33**, pp.107.

[15] L. Zhu, J.I. Maruyama, K. Kitamoto (2013), "Further enhanced production of heterologous proteins by double-gene disruption (ΔAosedD ΔAovps10) in a hyper-producing mutant of *Aspergillus oryzae*", *Appl. Microbiol. Biotechnol.*, **97(14)**, pp.6347-6357.

[16] P. Bundock, A. den Dulk-Ras, A. Beijersbergen, P.J. Hooykaas (1995), "Trans-kingdom T-DNA transfer from *Agrobacterium tumefaciens* to *Saccharomyces cerevisiae*", *EMBO J.*, **14**, pp.3206-3214.

[17] E.D. Mullins, X. Chen, P. Romaine, R. Raina, D.M. Geiser, S. Kang (2001), "*Agrobacterium*-mediated transformation of *Fusarium oxysporum*: an efficient tool for insertional mutagenesis and gene transfer", *Phytopathology*, **91**, pp.173-180.

[18] T.K. Nguyen, N.Q. Ho, H.T. Pham, T.N. Phan, V.T. Tran (2016), "The construction and use of versatile binary vectors carrying *pyrG* auxotrophic marker and fluorescent reporter genes for *Agrobacterium*-mediated transformation of *Aspergillus oryzae*", *World J. Microbiol. Biotechnol.*, **32**, p.204.

[19] V.T. Tran, L.T.B.X. Do, K.T. Nguyen, T.X. Vu, N.B. Dao, H.H. Nguyen (2017), "A simple, efficient and universal method for the extraction of genomic DNA from bacteria, yeasts, molds and microalgae suitable for PCR-based applications", *Vietnam Journal of Science, Technology and Engineering*, **59(4)**, pp.66-74.

[20] T.N. Petersen, S. Brunak, G. von Heijne, H. Nielsen (2011), "SignalP 4.0: discriminating signal peptides from transmembrane regions", *Nat. Methods*, **8(10)**, pp.785-786.

[21] K. Tamura, G. Stecher, D. Peterson, A. Filipski, S. Kumar (2013), "MEGA6: Molecular Evolutionary Genetics Analysis version 6.0", *Mol. Biol. Evol.*, **30(12)**, pp.2725-2729.

[22] T.X. Vu, T.T. Ngo, L.T.D. Mai, T.T. Bui, D.H. Le, H.T.V. Bui, H.Q. Nguyen, B.X. Ngo and V.T. Tran (2018), "A highly efficient *Agrobacterium tumefaciens*-mediated transformation system for the postharvest pathogen *Penicillium digitatum* using DsRed and GFP to visualize citrus host colonization", *J. Microbiol. Methods*, **144**, pp.134-144.

[23] X.O. Weenink, P.J. Punt, C.A. van den Hondel, A.F. Ram (2006), "A new method for screening and isolation of hypersecretion mutants in *Aspergillus niger*", *Appl. Microbiol. Biotechnol.*, **69(6)**, pp.711-717.

[24] R. Bourbonnais, M.G. Paice (1990), "Oxidation of non-phenolic substrates: An expanded role for laccase in lignin biodegradation", *FEBS Lett.*, **267**, pp.99-102.

[25] G.J. Mander, H. Wang, E. Bodie, J. Wagner, K. Vienken, C. Vinuesa, C. Foster, A.C. Leeder, G. Allen, V. Hamill (2006), "Use of laccase as a novel, versatile reporter system in filamentous fungi", *Appl. Environ. Microbiol.*, **72**, pp.5020-5026.

[26] J. Yang, W. Li, T.B. Ng, X. Deng, J. Lin, X. Ye (2017), "Laccases: Production, Expression Regulation, and Applications in Pharmaceutical Biodegradation", *Front. Microbiol.*, **8**, pp.832.

[27] P.J.J. Hooykaas, G.P.H. van Heusden, X. Niu, M. Reza Roushan, J. Soltani, X. Zhang and B.J. van der Zaal (2018), "*Agrobacterium*-Mediated Transformation of Yeast and Fungi", *Curr. Top Microbiol. Immunol*., pp.1-26.

[28] M.J.A. de Groot, P. Bundock, P.J.J. Hooykaas, A.G.M. Beijersbergen (1998), "*Agrobacterium tumefaciens*-mediated transformation of flamentous fungi", *Nat. Biotechnol.*, **16**, pp.840-842.

[29] C.B. Michielse, P.J. Hooykaas, C.A. van den Hondel, A.F. Ram (2008), "*Agrobacterium*-mediated transformation of the flamentous fungus *Aspergillus awamori*", *Nat. Protoc.*, **3**, pp.1671-1678.

[30] K. Tsuchiya, S. Tada, K. Gomi, K. Kitamoto, C. Kumagai, G. Tamura (1992), "Deletion analysis of the Taka-amylase A gene promoter using a homologous transformation system in *Aspergillus oryzae*", *Biosci. Biotechnol. Biochem.*, **56(11)**, pp.1849-1853.

[31] M. Li, L. Zhou, M. Liu, Y. Huang, X. Sun, F. Lu (2013), "Construction of an engineering strain producing high yields of α-transglucosidase via *Agrobacterium tumefaciens*-mediated transformation of *Aspergillus niger*", *Biosci. Biotechnol. Biochem.*, **77(9)**, pp.1860-1866.

Synthesis and antibacterial activity of silver/reduced graphene oxide nanocomposites against *Salmonella typhimurium* and *Staphylococcus aureus*

Minh Dat Nguyen[1], Vu Duy Khang Pham[2], Le Phuong Tam Nguyen[1], Minh Nam Hoang[1, 2], Huu Hieu Nguyen[1, 2*]

[1]Faculty of Chemical Engineering, Ho Chi Minh city University of Technology, Vietnam National University, Ho Chi Minh city
[2]Key Laboratory of Chemical Engineering and Petroleum Processing, Ho Chi Minh city University of Technology, Vietnam National University, Ho Chi Minh city

Received 5 March 2018; accepted 4 June 2018

Abstract:

In this study, silver/reduced graphene oxide (Ag/rGO) nanocomposites were synthesized *in situ* using three different mass ratios of silver nitrate and graphene oxide (1:1, 2:1, and 4:1). L-ascorbic acid (LAA) was used as an environment-friendly reducing agent. The characterization of Ag/rGO was investigated using Fourier transform infrared spectroscopy, X-ray diffraction, Raman spectroscopy, and transmission electron microscopy. The investigated results showed that the Ag/rGO nanocomposites were successfully synthesized with silver nanoparticles in the size range of 10-25 nm uniform distribution on rGO sheets. The antibacterial activity of Ag/rGO was tested against Gram-negative (*Salmonella typhimurium)* and Gram-positive (*Staphylococcus aureus*) bacteria using plate colony-counting and broth dilution methods, in comparison with individual rGO and silver nanoparticles. The tested results showed that the Ag/rGO nanocomposite with the $AgNO_3$:GO ratio of 4:1 (Ag/rGO4:1) exhibited the strongest antibacterial activity. The minimal inhibitory concentration values of Ag/rGO4:1 against *Salmonella typhimurium* and *Staphylococcus aureus* were 10 µg/ml and 50 µg/ml, respectively. Hence, the Ag/rGO nanocomposite could be considered as a potential antibacterial agent.

Keywords: **nanocomposite, *Salmonella typhimurium*, silver/reduced graphene oxide, *Staphylococcus aureus*.**

Classification number: **5.2**

Introduction

In spite of the advanced developments in drug discovery and biotechnology, people continue to be affected annually by bacterial infection, making it one of the world's public health concerns. Conventional antibacterial drugs are commonly used to address the problem. However, the overuse of antibiotics and drugs has led to bacterial resistance [1]. Therefore, various antibacterial agents, such as carbon nanotubes, metal oxide nanoparticles [2], graphene-based materials [3], and metal nanoparticles [4], have been studied to resolve the issue.

Graphene oxide (GO) is a two-dimensional material that consists of a single layer of carbon atoms arranged in honeycomb network. Each carbon atom forms three covalent bonds with three other carbon atoms by sp^2 hybridization, creating a hexagonal structure with electron-rich π-π conjugation system [5]. GO was fabricated oxidizing graphite to form graphite oxide (GiO), followed by exfoliation; thus, it contains various oxygenated functional groups on the surface and edges, such as hydroxyl (OH), epoxy (-O-), cacbonyl (-C=O), and carboxylic (-COOH) [6, 7]. Similar to GO, reduced graphene oxide (rGO) is also a two-dimensional material but has few oxygenated functional groups on its basal plane or in its structure. It can be synthesized by the chemical reduction of GO [8, 9]. rGO is applied in many different fields, such as biology [6], nanoelectronics [7], energy storage devices, and water purification [8, 9]. Recently, the antibacterial activity of rGO has been widely researched due to the physical contact between rGO and the bacteria cell wall. rGO sheets with around 1 nm in diameter are capable of both deteriorating bacteria membrane integrity and surrounding the bacteria due to their electron-rich surfaces [2]. However, rGO

*Corresponding author: Email: nhhieubk@hcmut.edu.vn

antibacterial activity is relatively low due to the difficulty of fabricating single-layer rGO sheets and the fact that rGO sheets are easily accumulated. To enhance the antibacterial activity of rGO, metal nanoparticles or metal oxides have been employed to fabricate new nanocomposites. Among these, silver is commonly used owing to its potential antibacterial activity as compared with other metal nanoparticles or metal oxides and because it causes no harm to mammals [10]. AgNPs can easily release silver ions, generating reactive oxygen species (ROS), such as superoxide, hydrogen peroxide, or hydroxyl radicals [11]. Silver ions are capable of interacting with DNA, as DNA mostly contains sulfur and phosphorus, causing DNA replication malfunction and inhibiting bacteria growth [12].

The addition of silver in the fabrication of Ag/rGO leads to certain advantages: (1) It prevent the irreversible agglomerates due to strong π-π stacking tendency between reduced GO sheets; (2) reduces the thickness of rGO sheets; and (3) prevents aggregation of silver nanoparticles as the rGO sheets become substrates [13]. Therefore, the antibacterial activity of new fabricated nanocomposite could be relatively higher in relation to its precursors.

In this work, Ag/rGO nanocomposites were fabricated *in situ* with L-ascorbic (LAA) acid as a green reducing agent. The characterization of Ag/rGO was investigated by Fourier transform infrared spectroscopy (FTIR), X-ray diffraction (XRD), transmission electron microscopy (TEM), and Raman spectroscopy. Gram-negative bacteria, *Salmonella typhimurium* (*S. typhimurium)*, and Gram-positive bacteria, *Staphylococcus aureus* (*S. aureus*), were selected as model strains to study the antibacterial properties of the nanocomposites.

Materials and methods

Materials

Graphite powder (D_h<20 μm) was obtained from Sigma-Aldrich, Germany. Potassium permanganate ($KMnO_4$, 99%), ammoniac (NH_4OH), ethanol (C_2H_5OH, 95%), and L-ascorbic acid ($C_6H_8O_6$, 99.7%) were purchased from ChemSol, Vietnam. Sulfuric acid (H_2SO_4, 98%), phosphoric acid (H_3PO_4, 86%), hydrogen peroxide (H_2O_2, 85%), chlohydric acid (HCl, 36%), silver nitrate ($AgNO_3$, 99.8%), poly (vinylpyrrolidone) (PVP, M_w=10,000), and sodium chloride (NaCl, 99.5%) were purchased from Xilong, China. Mueller-Hinton agar powder (500 g) and Luria-Bertani (LB) powder were purchased from Himedia, India. All chemicals were analytical grade and used as received without performing any further purification.

Synthesis of GO

GO was prepared from graphite powder using the improved Hummers method [14]. 3 g of graphite powder was slowly added to the mixture of 360 ml of H_2SO_4 and 40 ml of H_3PO_4 in a 1,000 ml beaker. Then, 18 g of $KMnO_4$ was added into the mixture, followed by a 30-minute stirring in an ice bath. The mixture was stirred and heated to 50°C for 12h. Then, the mixture was cooled to room temperature and slowly diluted with 500 ml of distilled water. 15 ml of H_2O_2 was added and the colour of the solution changed from brown to yellow. The mixture was centrifuged and washed with HCl, distilled water, and ethanol, respectively, until the pH reached 6. The solid was dried at 50°C for 24h in order to obtain GiO.

GiO was then dispersed in distilled water to form a GO suspension by sonication for 12h.

Synthesis of rGO

The rGO was synthesized by the chemical reducing method [15]. First, 40 ml of LAA (4 mg/ml) was added into 10 ml of GO (4 mg/ml). The mixture was stirred and heated to 95°C for 2.5h. After that, the mixture was cooled to room temperature. The resulting mixture was centrifuged and washed with deionized water and ethanol, respectively, until pH of the wastewater reached 7, and dried at 60°C. The rGO powder was obtained.

Synthesis of silver/ammonia solution ($AgNO_3/NH_3$)

$AgNO_3/NH_3$ was prepared by dissolving 2 g of silver nitrate in 450 ml water, then adding aqueous ammonia solution into the silver nitrate solution under continuous stirring until the brown precipitates disappeared. The mixture was adjusted to a final volume of 500 ml with water. The concentration of $AgNO_3$ obtained in $AgNO_3/NH_3$ solution was about 4 mg/ml.

Synthesis of silver nanoparticles (AgNPs)

AgNPs was synthesized using the chemical reducing method in a PVP environment [16]. First, 32 mg of PVP was dispersed in 10 ml $AgNO_3/NH_3$ (4 mg/ml). Then, 5 ml of LAA (4 mg/ml) was added. The mixture was stirred and heated to 95°C for 2.5h. Thereafter, the solution was cooled to room temperature. The resulting mixture was centrifuged and washed with deionized water and ethanol, respectively, until the pH of the wastewater reached 7, and then it was dried at 60°C. The AgNPs powder was obtained.

Synthesis of Ag/rGO nanocomposites

The Ag/rGO nanocomposites were synthesized using an *in-situ* method, in which both silver nitrate and GO were reduced simultaneously using LAA as a green reducing agent. The nanocomposites prepared from different mass ratio of $AgNO_3$:GO were labelled as Ag/rGO1:1, Ag/rGO2:1, and Ag/rGO4:1.

The $AgNO_3/NH_3$ solution was added into the GO solution. The mixture was sonicated for 20 minutes, after which, LAA was added. The mixture was stirred and heated to 95°C for 2.5h. The resulting mixture was centrifuged and washed with deionized water and ethanol, respectively, until the pH of the wastewater reached 7, and then it was dried at 60°C to obtain Ag/rGO. The volumes of reactants used to prepare corresponding samples are shown in Table 1.

Table 1. The volumes of reactants used to prepare corresponding samples (ml).

Samples	$AgNO_3/NH_3$ (4 mg/ml)	GO (4 mg/ml)	LAA (4 mg/ml)
Ag/rGO1:1	10	10	45
Ag/rGO2:1	10	5	25
Ag/rGO4:1	10	2.5	15

Characterization

The XRD patterns of GO, rGO, and Ag/rGO were studied using XRD D2 Pharser machine (Bruker AXS, Germany) with Cu Kα radiation (λ=0.154 nm). FTIR spectra of GO, rGO, and Ag/rGO were performed by the Tensor 27 FTIR spectrophotometer (Bruker, Germany). The TEM images were obtained using the JEM 1400 microscope (JEOL, Japan) at an acceleration voltage of 100 kV. Raman spectroscopy was obtained by using LabRam HR Evolution (Horiba, Japan) with an excitation wavelength of 632 nm (He-Ne laser).

Antibacterial test

The antibacterial activities of nanocomposite materials and precursors were tested using plate colony-counting method in order to identify the material with the strongest antibacterial potential. The minimal inhibitory concentration (MIC) of the material was determined by dilution. *S. typhimuriu* and *S. aureus* were obtained from Faculty of Biology and Biotechnology, HCMUS and incubated at 37°C in LB.

Plate colony-counting method: antibacterial agents (rGO, AgNPs, and Ag/rGO) were added to 20 ml of the bacterial suspension at a concentration of 200 mg/ml. The mixture was shaken constantly at 37°C for 6h. 0.1 ml of the diluted solution was uniformly spread in the solid medium in the agar plate and incubated at 37°C for 24h. The growth of the bacteria was observed by counting the total number of colonies per dish [13].

Broth dilution method: the antibacterial agents were added to 20 ml of the bacterial suspension at a concentration of 0.19 to 50 mg/l. The mixture was shaken constantly at 37°C for 24h. The resazurin 0.01% indicator was added. The color was blue at normal condition and changed to pink if there was bacterial growth. The MIC was determined using the test tube where the concentration was the lowest and the color of the solution remained blue.

Results and discussion

Characterization

FTIR spectra: the FTIR spectra of GO, rGO, Ag/rGO1:1, Ag/rGO2:1, and Ag/rGO4:1 are presented in Fig. 1. The distinctive diffraction peaks of GO at 3422 cm^{-1}, 1735 cm^{-1}, and 1400 cm^{-1} corresponded to the vibration of carboxylic (C=O), hydroxyl (C-OH), and epoxide (C-O-C), respectively [17]. These results confirmed the existence of oxygen-containing groups in the structure of the GO, indicating that graphite was successfully oxidized to GO. It can be seen from the FTIR spectra of rGO and Ag/rGO that there was a decrease in the intensity of characteristic peaks corresponding to oxygen-containing functional groups. This indicated that GO was reduced to rGO when using LAA as a green reducing agent [18, 19].

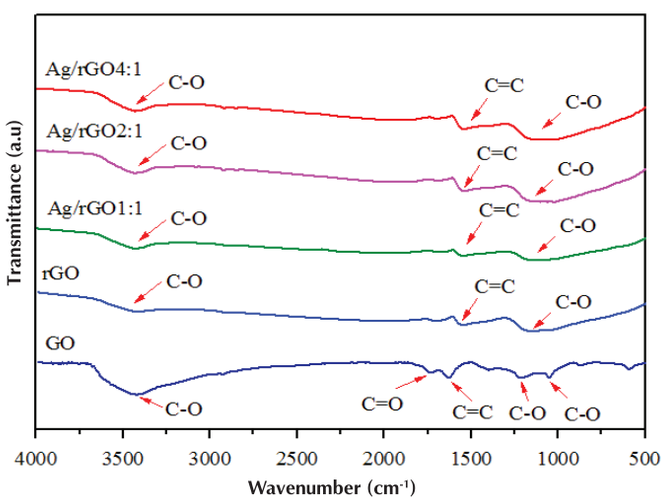

Fig. 1. The FTIR spectra of GO, rGO, Ag/rGO1:1, Ag/rGO2:1, and Ag/rGO4:1.

XRD patterns: the XRD patterns of GO, rGO, and Ag/rGO as shown in Fig. 2. GO exhibited a distinctive diffraction peak at $2\theta=9.6^0$, ascribing to (002) crystallographic plane with interlayer spacing $d_{(002)}=0.902$ nm. In the XRD pattern of rGO, there was no characteristic peak of GO but another peak at $2\theta=26^0$, indicating that GO has been was reduced successfully into rGO. The disappearance of the diffraction peak of GO can also be observed in the XRD patterns of Ag/rGO1:1, Ag/rGO2:1, and Ag/rGO4:1 fabricated materials. In addition, the distinctive diffraction peaks of silver nanoparticles can be clearly observed from the XRD patterns of Ag/rGO1:1, Ag/rGO2:1, and Ag/rGO4:1 at 2θ values of 38^0, 44^0, 64^0, and 77^0 ascribing to the crystallographic plane (111), (200), (220), and (311), respectively. These results confirmed the existence of silver in the structure of the Ag/rGO nanocomposites [20]. Besides, the disappearance of the characteristic peak of GO at $2\theta=26^0$ proved that the nanoparticles enhanced the interlayer spacing between rGO sheets.

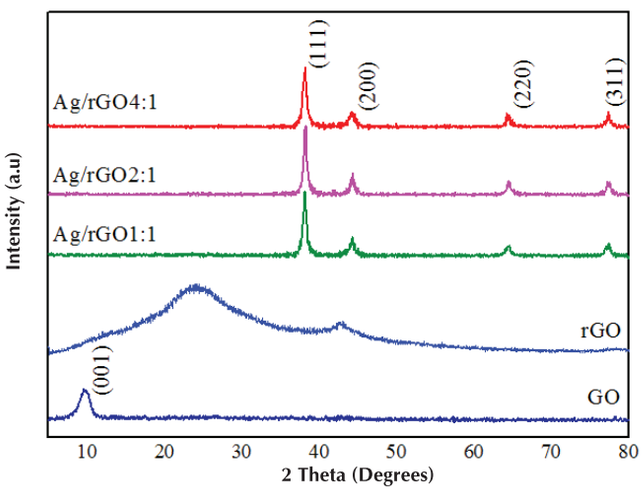

Fig. 2. XRD patterns of GO, rGO, Ag/rGO1:1, Ag/rGO2:1, and Ag/rGO4:1.

Raman spectroscopy: Raman spectra of GO, rGO, Ag/rGO1:1, Ag/rGO2:1, and Ag/rGO4:1 are presented in Fig. 3. G-band and D-band were approximately in the range of 1320-1335 cm^{-1} and 1585-1610 cm^{-1}, respectively [21]. The D-band is related to the disordered carbon and the G-band is associated with the in-plane stretching vibration of sp^2 C-C bonds [22]. The intensity ratio of the D-band and G-band (I_D/I_G) is referred to the structural imperfection of graphene-based materials. As shown in Fig. 4, the I_D/I_G ratios of GO and rGO were 1.05 and 1.19, respectively. These results showed that rGO had more defects than GO, indicating that GO was been reduced to rGO [21]. According to Fig. 4, the I_D/I_G ratios of Ag/rGO1:1, Ag/rGO2:1, and Ag/rGO4:1 were 1.20, 1.24, and 1.24, respectively, which were similar to that of rGO. This indicated that rGO was formed in the solution of silver ions during the fabrication of Ag/rGO.

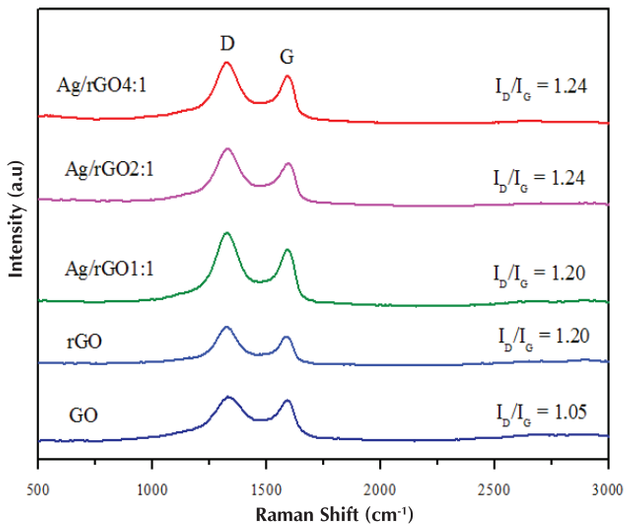

Fig. 3. Raman spectra of GO, rGO, Ag/rGO1:1, Ag/rGO2:1, and Ag/rGO4:1.

TEM images: TEM images of rGO, AgNPs, and Ag/rGO nanocomposites with different mass ratios of $AgNO_3$:GO are shown in Fig. 4. The light-gray thin films were rGO sheets [in Figs. 4(A, C, and E)] while black particles were silver nanoparticles. The results showed that with the presence of silver nanoparticles in the structure of rGO, there was also enhancement in the interlayer spacing between rGO sheets, which was indicated by the planar in Figs. 4(C, E), which was lighter than that in Fig. 4A. In Fig. 4B, the silver nanoparticles synthesized in PVP had the size range of 50 to 60 nm. Under the same synthesis conditions, upon replacing PVP with GO solutions, the silver nanoparticles synthesized and the size ranged from 15 to 25 nm, as shown in Figs. 4(C, E). The results were consistent with that of the previous study, as given in Table 2. This difference could be explained by the fact that rGO had high specific surface area along with many activated sites, which located the silver nanoparticles and prevented aggregation. The TEM images also showed that upon increasing the amount of $AgNO_3$, the amount of silver nanoparticles increased as well [17, 23].

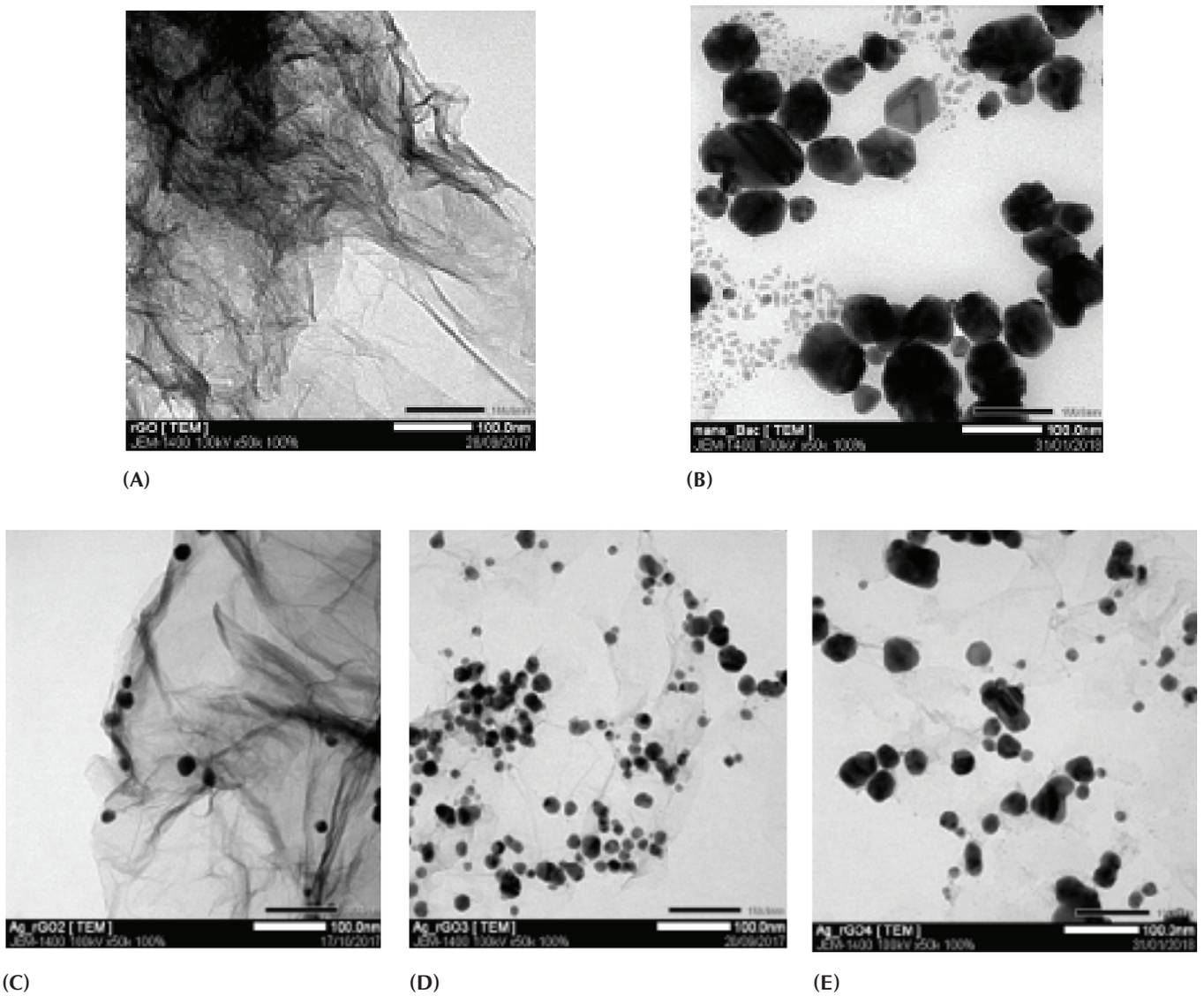

(A) (B)

(C) (D) (E)

Fig. 4. TEM images of (A) rGO, (B) AgNPs, (C) Ag/rGO1:1, (D) Ag/rGO2:1, and (E) Ag/rGO4:1.

Table 2. The size of AgNPs (nm).

Materials	Size	References
Ag/rGO	15-25	Present work
AgNPs	50-60	Present work
Ag/rGO	20-50	[13]
Ag/GO	5-25	[23]
Ag/GO	22	[24]
AgNPs/PVP	69	[25]

Antibacterial activity evaluation

Antibacterial activity of fabricated materials: the antibacterial activities of rGO, AgNPs, and Ag/rGO nanocomposites with different mass ratios of $AgNO_3$:GO were evaluated by applying the plate colony-counting method. The antibacterial activity of each material depends on the number of colonies in each plate. The higher the number of colony in each plate, the lower the antibacterial activity of the sample was. The antibacterial activities of rGO, AgNPs, and Ag/rGO nanocomposites against *S. aureus* and *S. typhimurium* are presented in Fig. 5. The results showed that the materials showed higher antibacterial

activity against *S. typhimurium* rather than *S. aureus*. This could be explained by the fact that the cell wall of *S. aureus* was thicker than that of *S. typhimurium*; and hence, generated radicals could break the cell wall and decompose the inner parts of the cell. Among the tested materials, the Ag/rGO4:1 nanocomposite exhibited the strongest antibacterial potential owing to the highest amount of silver in Ag/rGO4:1. On the other hand, in the AgNPs sample, the large size of silver nanoparticles and the fact that they were covered by PVP resulted in the limitation of releasing silver ions.

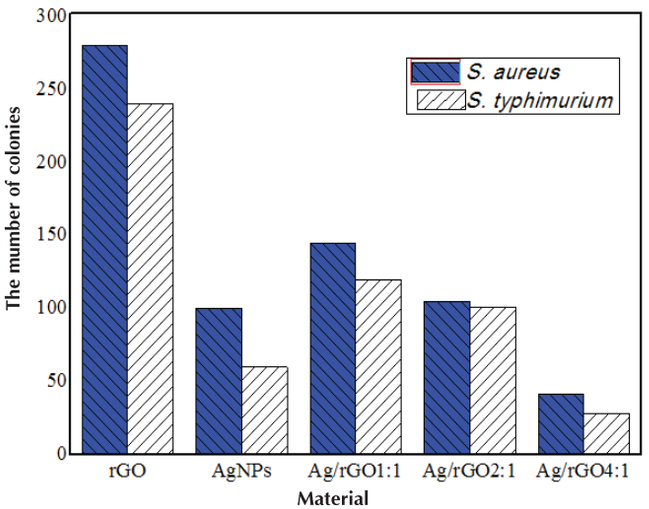

Fig. 5. The number of colonies of *S. aureus* and *S. typhimurium* in the presence of GO, rGO, Ag/rGO1:1, Ag/rGO2:1 and Ag/rGO4:1.

MIC value: the MIC value of Ag/rGO4:1 was determined using the broth dilution method, as shown in Fig. 6. According to this, the MIC values of Ag/rGO4:1 against *S. typhimuriu* and *S. aureus* were 10 mg/l and 50 mg/l, respectively. The higher MIC against *S. typhimurium* rather than *S. aureus* showed that *S. typhimurium* was more easily inhibited than *S. aureus.*

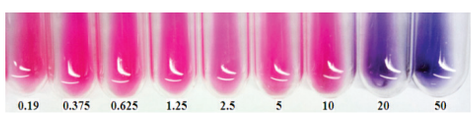

(A)

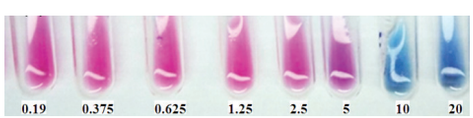

(B)

Fig. 6. Experiment to determine MIC of Ag/rGO4:1 against (A) *S. aureus* and *(B) S. Typhimuriu.*

Conclusions

The analysis results pertaining to XRD, FTIR, Raman, and TEM showed that Ag/rGO nanocomposites was fabricated successfully *in situ*. The silver nanoparticles in the size range of 10-25 nm were decorated uniformly on rGO sheets. The antibacterial test showed that the fabricated Ag/rGO had a strong antibacterial potential. Upon using more silver nitrate, the amount of silver nanoparticles increased, and hence, the antibacterial activity was enhanced. The Ag/rGO nanocomposites exhibited the strongest antibacterial activity, with the MIC value against *S. typhimuriu* and *S. aureus* being 10 mg/l and 50 mg/l, respectively. Therefore, it can be concluded that the fabricated Ag/rGO nanocomposite has great potential in antibacterial field.

REFERENCES

[1] L. Rizzello, P.P. Pompa (2014), "Nanosilver-based antibacterial drugs and devices: Mechanisms, methodological drawbacks, and guidelines", *Chem. Soc. Rev.*, **43**, pp.1501-1518.

[2] Shaobin Liu, Tingying Helen Zeng, Mario Hofmann, Ehdi Burcombe, Jun Wei, Rongrong Jiang, Jing Kong, Yuan Chen (2011), "Antibacterial Activity of Graphite, Graphite Oxide, Graphene Oxide, and Reduced Graphene Oxide: Membrane and Oxidative Stress", *ACS Nano*, **5(9)**, pp.6971-6980.

[3] Yong-WookBaek, Youn-JooAn (2011), "Microbial toxicity of metal oxide nanoparticles (CuO, NiO, ZnO, and Sb_2O_3) to Escherichia coli, Bacillus subtilis, and Streptococcus aureus", *Science of the Total Environment*, **409(8)**, pp.1603-1608.

[4] P.K. Vemula, P.M Ajayan, G. John A. Kumar (2008), "Silver-nanoparticles-embedded antimicrobial paints based on vegetable oil", *Nat. Mater.*, **7**, pp.236-241.

[5] S. Stankovich, D.A. Dikin, Geoffrey H.B. Dommett, Kevin M. Kohlhaas, Eric J. Zimney, Eric A. Stach, Richard D. Piner, SonBinh T. Nguyen, Rodney S. Ruoff (2006), "Graphene-based composite materials", *Nature*, **442**, pp.282-286.

[6] A.K Geim, S.V Morozov, E.M Hill, P. Blake, M.I Katsnelson, K.S Novoselov, F. Schedin (2007), "Detection of individual gas molecules adsorbed on graphene", *Nature Mater.*, **6**, pp.652-655.

[7] D.A Areshkin and C.T White (2007), "Building blocks for integrated graphene circuits", *Nano Lett.*, **7**, pp.3253-3259.

[8] P. Jain, T. Pradeep (2005), "Potential of silver nanoparticle-coated polyurethane foam as an antibacterial water filter", *Biotechnology and Bioengineering*, **90(1)**, pp.59-63.

[9] Dankovich (2011), "Bactericidal paper impregnated with silver nanoparticles for point-of-use water treatment", *Environ. Sci. Technol.*, **45(5)**, pp.1992-1998.

[10] S.W. Chook, C.H. Chia, S. Zakaria, and M.K. Ayob (2012), "Silver nanoparticles - graphene oxide nanocomposite for antibacterial purpose", *Advanced Material Research*, **364**, pp.439-443.

[11] Yang Li, Wen Zhang, Junfeng Niu, Yongsheng Chen (2013),

"Surface-coating-dependent dissolution, aggregation, and reactive oxygen species (ROS) generation of silver nanoparticles under different irradiation conditions", *Environ. Sci. Technol.*, **47(18)**, pp.10293-10301.

[12] David D. Evanoff Jr., George Chumanov (2005), "Synthesis and optical properties of silver nanoparticles and arrays", *Chem. Phys. Chem.,* **6(7)**, p.1221.

[13] Gu Danxia, Chang Xueting, Zhai Xinxin, Sun Shibin, Li Zhongliang, Liu Tao, Dong Lihua, Yin Yansheng (2016), "Efficient synthesis of silver-reduced graphene oxide composites with prolonged antibacterial effects", *Ceramics International*, **42(8)**, pp.9769-9778.

[14] Daniela C. Marcano, Dmitry V. Kosynkin, Jacob M. Berlin, Alexander Sinitskii, Zhengzong Sun, Alexander Slesarev, Lawrence B. Alemany, Wei Lu, James M. Tour (2010), "Improved synthesis of graphene oxide", *ACS Nano,* **4(8)**, pp.4806-4814.

[15] K.K.H. De Silva, H.H. Huang, R.K. Joshi, M. Yoshimura (2017), "Chemical reduction of graphene oxide using green reductants", *Carbon*, **119**, pp.190-199.

[16] Quang Huy Tran, Van Quy Nguyen, Anh Tuan Le (2013), "Silver nanoparticles: synthesis, properties, toxicology, applications and perspectives", *Adv. Nat. Sci.: Nanosci. Nanotechnol.*, **4**, p.033001.

[17] Jinlin Lu, Yanhong Li, Shengli Li, and San Ping Jiang (2016), "Self-assembled platinum nanoparticles on sulfonic acid-grafted graphene as effective electrocatalysts for methanol oxidation in direct methanol fuel cells", *Scientific Reports*, **6**, p.21530.

[18] Henan Zhang, Deon Hines, and Daniel L. Akins (2014), "Synthesis of a nanocomposite composed of reduced graphene oxide and gold nanoparticles", *Dalton Trans.*, **43**, pp.2670-2675.

[19] Tarko FentawEmiru and Delele WorkuAyele (2017), "Controlled synthesis, characterization and reduction of graphene oxide: A convenient method for large scale production", *Egyptian Journal of Basic and Applied Sciences*, **4(1)**, pp.74-79.

[20] Balwinder Kaur, Thangarasu Pandiyan, Biswarup Satpati, and Rajendra Srivastava (2013), "Simultaneous and sensitive determination of ascorbic acid, dopamine, uric acid, and tryptophan with silver nanoparticles-decorated reduced graphene oxide modified electrode", *Colloids and Surfaces B: Biointerfaces*, **111**, pp.97-106.

[21] J. Zhang, H. Yang, G. Shen, P. Cheng, and J. Zhang (2010), "Reduction of graphene oxide via L-ascorbic acid", *Chemical Communications*, **46(7**), pp.1112-1114.

[22] M. Zainy (2012), "Simple and scalable preparation of reduced graphene oxide-silver nanocomposites via rapid thermal treatment", *Materials Letters*, **89**, pp.180-183.

[23] Manash R. Das, Rupak K. Sarma, Ratul Saikia, Vinayak S. Kale, Manjusha V. Shelke, Pinaki Sengupta (2011), "Synthesis of silver nanoparticles in an aqueous suspension of graphene oxide sheets and its antimicrobial activity", *Colloids and Surfaces B: Biointerfaces*, **83**, pp.16-22.

[24] Wei Shao, Xiufeng Liu, Huihua Min, Guanghui Dong, Qingyuan Feng, Songlin Zuo (2015), "Preparation, characterization, and antibacterial activity of silver nanoparticle-decorated graphene oxide nanocomposite", *ACS Appl. Mater. Interfaces*, **7(12)**, pp.6966-6973.

[25] RasmusFoldbjerg, PingOlesen, MadsHougaard, Duy Anh Dang, Hans JürgenHoffmann, HermanAutrup (2009), "PVP-coated silver nanoparticles and silver ions induce reactive oxygen species, apoptosis and necrosis in THP-1 monocytes", *Toxicology Letters*, **190(2)**, pp.156-162.

Energy development in Vietnam's Mekong river delta: a 'green' or 'grey' outlook?

Le Anh Tuan*

Research Institute for Climate Change - Can Tho University (DRAGON ins.)

Received 27 February 2018; accepted 1 June 2018

Abstract:

The Vietnamese Mekong river delta (MD) is recognised as the biggest agriculture and aquaculture region of Vietnam. The MD plays an important role in ensuring food security for the country. The MD also has many sensitive ecosystems reliant on the ecology of the Mekong river basin. However, during the last decade, many electricity generation plants, both renewable and non-renewable power projects, have been built and some will be built in the near future in the MD. These energy plants' construction and operation may prove to be a challenge to the national energy strategy.

This paper is a monograph review of two sides of energy sector industrialisation in the MD with a focus on 'green' and 'grey' socio-economic development (as 'xanh' and 'xám' in Vietnamese respectively). 'Green' energy is understood as the electricity generated from inexhaustible sources and known as renewable energy. It emits fewer greenhouse gases and causes less harm to habitats in comparison to traditional fossil fuels and hydropower. 'Grey' energy is another word for non-renewable energy or polluting energy, which can have negative effects on human health, environment, and climate. This paper finds that the MD's energy development plans at present might not be as 'green' as expected, due to more 'grey' power plans in the planning pipeline. This paper also considers an outlook on energy prices and impacts on long-term sustainable development of the MD.

Keywords: **air pollution, energy sector, green or grey, Mekong river delta, sustainable development.**

Classification number: **6.1**

Background

The MD of Vietnam is located between 8-11° latitude and 104-106° longitude, belonging to a monsoonal humid subtropical climate zone of South East Asia Region (Fig. 1). Since it lies in the most downstream portion of the Mekong river basin before entering the East Sea via seven river mouths, the topography of the MD is very low and flat. The MD's average land elevation is less than 1.5 meter above the mean sea level. The MD climatic regime is dominated by two seasons: the dry season, from December to April and the rainy season, from May to November. Annual rainfall is substantial in all provinces, ranging from 1,600 (the North-West areas) to 2,200 millimetres (the South-East coastal areas), with humidity averaging 85% throughout the year. More than 85% of the precipitation in the MD, within 100 to 110 rainy days, occurs during the monsoon season. Because the MD has strong solar radiation potential, the average daily temperatures in the MD are rather high - varying between 25-29°C with monthly average temperatures invariant throughout the year. In the dry season, the MD receives a lot of solar radiation resulting in a very high surface land temperature (Fig. 1). The absolute minimum/maximum temperatures in the MD rarely exceed 15/39°C. In general, weather and river flows' characteristics support very favourable conditions for agriculture and aquaculture development of the MD when compared with other regions in Vietnam. The MD is drawn on a rich endowment of biomass to achieve the highest levels of agriculture - aquaculture - mangrove forest production in the nation [1].

*Email: latuan@ctu.edu.vn

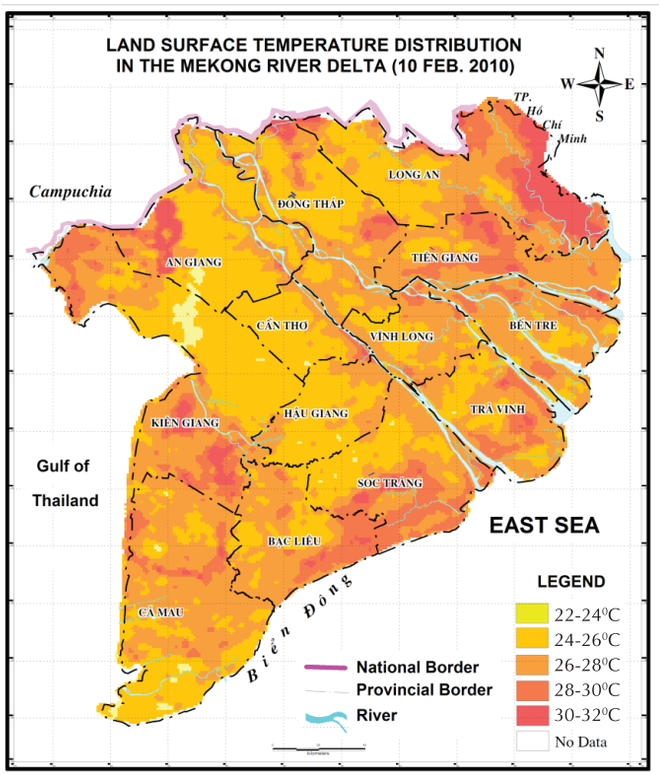

Fig. 1. Map of the MD's land surface temperature distribution treated by using MODIS satellite image on 10 Feb. 2010 [2].

Power development policies in Vietnam

On 17th June, 2010, the Law on Economical and Efficient Use of Energy was promulgated by the National Assembly [3]. The main purpose of this Law is to provide economic and efficient use of energy; policies and measures to promote economic and efficient use of energy; and to outline the rights, obligations and responsibilities of organisations, households and individuals for economic and efficient use of energy. One year later, the National Master Plan for Power Development for the period of 2011-2020 with the vision for 2030 (called shortly PDP VII) was approved by the Vietnamese Government in Decision 1208/QĐ-TTg [4]. In March 2016, the Prime Minister approved the revision of the National Power Development Master Plan for the period of 2011-2020, vision for 2030 with main target to satisfy the country's electricity demand and to meet the objectives of national socio-economic development with an average GDP growth of about 7.0% per year through the period 2016-2030. According to the PDP VII Revised, the electricity generation mix for 2013-2030 is demonstrated in Fig. 2. The development of renewable energy sources for electricity production will increase from 3.7% of total electricity production in 2013 to 10.7% by 2030. However, coal thermal power distribution for the country from 19.8% in 2013 will rise up to 58.2% in 2030, while hydropower as a primary electricity source will fall down from 42% to 12.4% during the period 2013-2030. The plan discusses how Vietnam will apply nuclear power generation for electricity with 5.7%, but the country's current plans for nuclear power generation have been put on hold indefinitely.

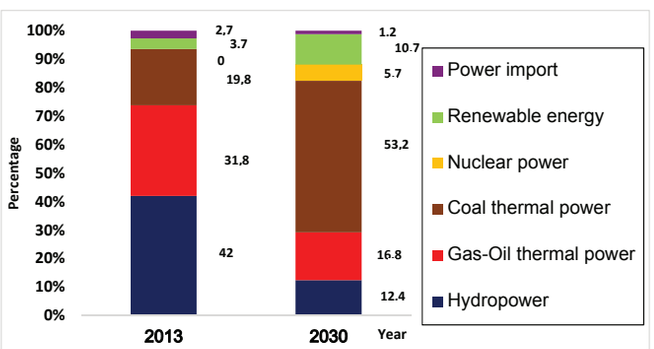

Fig. 2. Energy structure distribution in percentage in 2013 and 2030 (Graphic drawing by Le Anh Tuan from data source in PDP VII Revised).

Environmental concepts on energy sector: 'green' or 'grey'

Green energy (or 'xanh' in Vietnamese) comes from natural sources such as sunlight, wind, rain, tides, plants, algae and geothermal heat. These energy resources are renewable, meaning they can be naturally replenished [5]. Green energy sources have significantly lower carbon footprints when compared to other energy generation sources. Renewable and nuclear sources are near-zero carbon generation sources [6].

Traditionally and predominantly, many countries have burned fossil fuels as coal, oil, gas or combustible fuels as solid-waste or biomass in thermal power plants for electricity production. Fossil fuels are exploited by either mining or drilling deep into the earth and sea, often in ecologically sensitive locations. Almost all thermal power plants produce pollutants such as greenhouse gases (carbon dioxide, water vapor) and acid gas emissions (sulphur dioxide and nitrogen oxide) as a by-product, contributing to global warming phenomenon and to climate change. Gaining access to fossil fuels typically requires either mining or drilling deep into the earth. Coal-thermal plants are favourable to build because coal is inexpensive, plentiful, relatively easy to transport, and easy to purchase in the

global market [7]. In 2012, coal was responsible for 72% of electricity-sector emissions [6]. Coal and other fossil fuel burning power plants are environmental polluters. They are known as 'grey' energy (or 'xám' in Vietnamese) and can have negative effects on human health, environment, and climate. Even the most efficient coal plants generate twice as much carbon pollution as gas-fired power plants and over 20-80 times more than renewable energy systems.

Since the late 19th century up to the present, hydropower has been a popular source for generating electricity in America, Europe and Asian countries. Although hydropower is considered, by many, as a renewable energy, most hydropower plants are built with large reservoirs-dams, which block rivers. This can have significantly negative social and environmental impacts. Additionally, hydropower is associated with deforestation for reservoir building, which may emit more greenhouse gas concentration in the atmosphere. So, a large-scale hydropower plant is possible to rank as a term of grey energy. Officially in Vietnam, large-scale hydropower plants are not labelled as a form of renewable energy.

Energy power development in the MD

Green energy development

As part of the Power Development Master Plan VII released in July 2011, the country will give priority to developing renewable energy sources. The rate of renewable power is planned to account for 4.5% by 2020 and 6% in 2030. However, the revised Power Development Master Plan VII released in March 2016 adjusted those rates upward. In PDP VII, power from renewable energy is estimated at 4.5% by 2020 and 6.0% by 2030, compared with the system's total power output. The estimated capacity by 2020 shall be at 5.6% and 10.7% by 2030.

In 2013, the total installed capacity of renewable energy was approximately 1,800 MW, accounting for 5.6% of total installed capacity and approximately 3.8% of total power production. In the recent years, the share of power produced from renewable energy is increasing primarily through small hydropower development (installed capacity less than 30 MW). Thus, the actual share of renewable energy in the power mix has reached its set target seven years earlier than expected in PDP VII. With the current trends related to renewable energy technologies and cost reductions, promoting additional contributions of renewable energy to meet Vietnam's future power demand is a promising opportunity.

The MD has approximately 700 km long coast lines facing the East Sea and the Gulf of Thailand, the Delta is advantageously positioned to receive wind streams from the sea. The potential of wind energy in Tra Vinh, Soc Trang and Bac Lieu coastal lines at the height of 80 m above the coastal land surface, with the average wind speed reaching the range of 5.57-6.0 m/s is presented in Fig. 3. According to [8], Cong Ly Construction-Trade Tourism Limited Company has invested in an installation of 52 wind turbines each having a 1.6 MW capacity, for a total capacity of 83.2 MW in Bac Lieu province. The Bac Lieu wind farm will have a gross annual electricity output of 335.2 GW hours at full operational capacity. This power plant reduces 143,761 tCO_2 emissions on average per year and 1,006,328 tCO_2 over the first crediting period [9]. The project's third phase will reach a total wind power capacity of up to 300 MW by 2030 as expected.

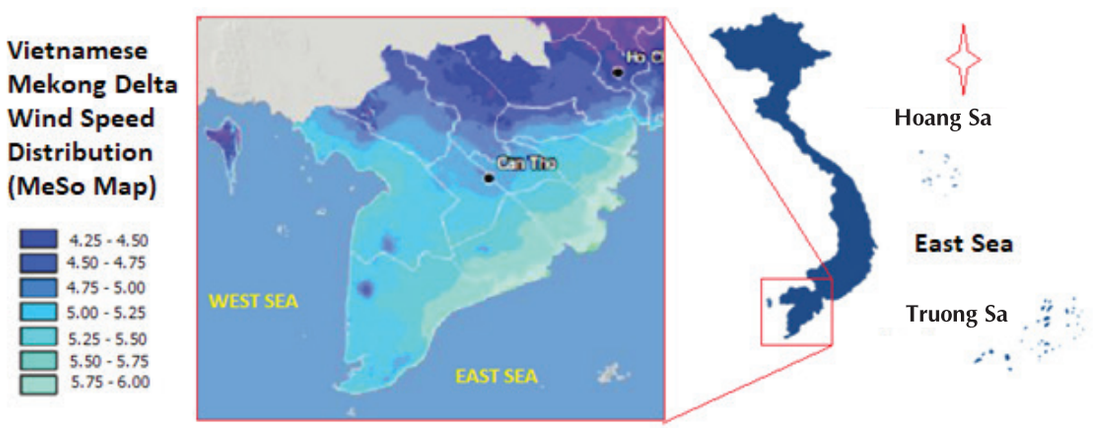

Fig. 3. Wind speed (m/s) distribution map in the MD based on the Meso Map simulation [10].

It is estimated that the entire MD receives about 2,000-2,600 sunshine hours per year. Can Tho, a central city in the MD, receives around 2,300±200 sunshine hours per year (equivalent of 6.300 MJ/m^2 per year), corresponding to more or less 2,000 kWh/m^2 per year [1]. Aisma, et al. [11] have reported that the South of Vietnam (including the East South and the West South Region) has a maximum regional solar photovoltaic (PV) resource potentials up to 535 GW. Based on 2014 statistical data for rice production [12], the MD produced nearly 5 million tons of rice husk taken from 20% of 24.7 million tons of harvested rice grain. Furthermore, about 26 million tons of rice straw is produced annually [13]. Assuming that a half of provincial rice husk amounts from paddy milling stations are used to make rice husk charcoal briquettes, the MD can also produce approximately 1.1 Million Kcal per year for heating value or equivalent of 265,160 KJ per year.

Grey energy from burning fossil fuels

According to the Revised Power Development Plan VII to respond to the increasing power demand in the MD, the government plans to build 13 additional new coal-thermal power plants taking the existing total to 14 by 2030. See Table 1 and Fig. 4 for a list of coal fired power plants. With 14 coal thermal plants equivalent to estimated approximate 110.34 billion kWh power produced annually by 2030, the MD will become Vietnam's top region for coal power production. These 14 coal-fired thermal power plants will increase the total capacity of Vietnam's power generation 15 times by 2030 (Table 2).

The amount of coal used for generating power from those plants will also increase to 15 times higher than the current amount. While pollution control equipment can reduce toxic air emissions, they only eliminate a portion of pollution. Instead, they transfer much of the toxic air pollutants to liquid and solid waste streams. Oftentimes, companies and governments' priorities profit public health concerns and thus a full suite of available pollution control equipment is not installed. In these cases, toxic pollution still goes into the air, leading to premature deaths and increased rates of diseases. Moreover, according to international experiences, coal power has the highest portion of water consumption among energy generation processes. Coal plants consume vast amounts of water for cooling and steam production. A typical 1,000 MW coal plant uses enough water in one

Table 1. List of coal-fired power plants in the MD [14].

No	Names of coal thermal plants	Total capacity (MW)	Coal sources	Locations	Water used (Mil. m^3/day)
1	Duyen Hai I	1,200	Quang Ninh	Tra Vinh	16.5
2	Duyen Hai II	1,200	Import		
3	Duyen Hai III	1,200	Quang Ninh		
4	Duyen Hai IV extended	660	Import		
5	Song Hau I	1,200	Import	Hau Giang	12.4
6	Song Hau II	2,000	Import		
7	Long Phu I	1,200	Import	Soc Trang	16.7
8	Long Phu II	1,320	Import		
9	Long Phu III	1,800	Import		
10	Long An I	1,200	Import	Long An	10.8
11	Long An II	1,600	Import		
12	Tan Phuoc I	1,200	Import	Tien Giang	9.3
13	Tan Phuoc II	1,200	Import		
14	Bac Lieu	1,200	Import	Bac Lieu	4.6

Table 2. Key figures about coal-fired power plants in the MD.

Key figures	2016	2030	Comparison
Number of plants	1	14	14 times higher
Installed capacity	1,245 MW	18,390 MW	15 times higher
Annual power production output	7.47 billion kWh/year	110.34 billion kWh/year	15 times increased
Coal fuel consumption	3.36 million tons/year	49.7 million tons/year	15 times higher
Coal ash	1.1 million tons/year	16.6 million tons/year if using coal from Quang Ninh mines	15 times higher
Water demand	5.38 million m^3/day	79.44 million m^3/day	15 times higher
CO_2 emission	6.7 million tons CO_2	99.3 million tons CO_2	15 times higher

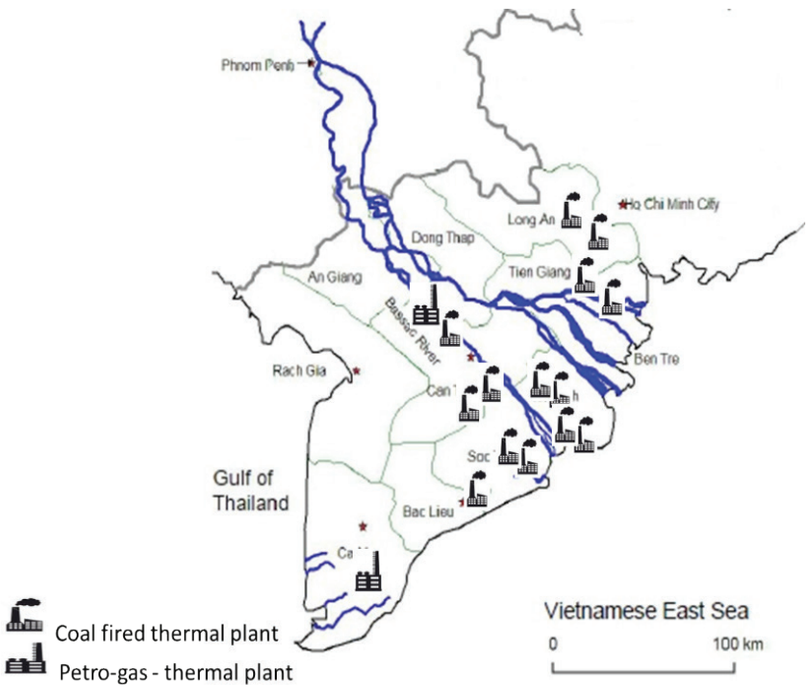

Fig. 4. Location map of proposed thermal power plants in the South-West of the Hau river (Bassac) area.

year to meet the basic water needs of 500,000 people. The operation of coal power plants in the MD in the near future will likely add another layer of threat for water resources in this region, especially during the dry season. Technology to capture and store carbon dioxide is expensive and largely unproven.

Discussion

The application of renewable power generation such as wind, solar and biomass energy in the MD will contribute to a sustainable green revolution. Although initial installation costs for these renewable energy sources are rather high compared to hydro and thermal electricity, these renewables provide virtually no additional environmental pollution impacts and fit well within the Clean Development Mechanism's expectations. However, the cost of renewable energy scoping and operation will decrease rapidly over time. According to the International Renewable Energy Agency (IRENA) [15], costs of most renewable energy generation has fallen below the price range of fossil fuel generation. Solar photovoltaic (PV) is most competitive. Solar PV module prices in 2014 were around 75% in comparison with prices from 2009. Between 2010 and 2014, the total installed costs of utility-scale PV systems have fallen by 29% to 65%, depending on the region. The Levelised Cost of Energy (LCOE)[1] of utility-scale solar PV has fallen by half in four years. The most competitive utility-scale solar PV projects are now regularly delivering electricity for just $0.08/kWh without financial support, compared to a range of $0.045 to $0.14/kWh for fossil fuel power plants. LCOE cost of electricity generated from biogas, geothermal, and hydropower have remained unchanged since 2010. Onshore wind is also an increasingly competitive energy source. In

[1]According to IRENA (2014), the LCOE of a given technology is the ratio of lifetime costs to lifetime electricity generation, both of which are discounted back to a common year using a discount rate that reflects the average cost of capital.

addition to the reduction in installation costs, technology improvement has contributed to the decreasing LCOE. Some wind projects with a preferable location can have the price of $0.05/kWh without financial support.

Under the national electricity generation development program, coal-run thermal power will take up 60% of the country's total electricity output. The policy of building 14 coal fired thermal power plants, if fully or partially implemented, will subject the MD to a number of risks for sustainable development. The burning of coal emits hazardous air pollutants that can spread for hundreds of kilometres throughout the MD. Exposure to these pollutants can damage people's cardiovascular, respiratory and nervous systems, increasing the risk of lung cancer, stroke, heart disease, chronic respiratory diseases and lethal respiratory infections. Children, the elderly, pregnant women, and people with already compromised health will suffer most. The emission of sulfates and nitrates also leads to acid rain, which damages streams, forests, crops and soils. It is noticed that coal as fossil fuel source for Duyen Hai I and Duyen Hai III thermal power plants is mainly exploited from anthracite reserves in Quang Ninh province but these reserves are expected to deplete by 2030. Other coal-fired power plants in the MD will have to import coal from Australia or Indonesia.

In Vietnam, according to Decision 37/2011/QD-TTg [16], the buyer must purchase 100% of wind power production at 7.8 US Cent/kWh. The investor can enjoy preferential loans and tax reductions or fee exemptions. However, according to some experts, with the current level of incentives, investors still suffer heavy losses. With such mechanisms, wind power cannot be developed as expected. With the target of increasing the total wind power capacity from the current 52 MW to around 1,000 MW by 2020 and 6,200 MW by 2030, the share from wind power will account for 0.7% in 2020 to 2.4% in 2030. However, progress is very difficult to achieve without changing current mechanisms.

Regarding biomass, Decision 24/2014/QD-TTg [17] decided that biomass energy will be sold at 5.8 US Cent/kWh. Investors also enjoy advantages in capital and tax exemptions similar to wind power. There are 41 sugar mills in Vietnam using bagasse to produce self-service electricity with a capacity of about 150 MW. It is said that to build a plant of biomass power from bagasse, tariffs need to be at least 8 US Cent/kWh because bagasse power plant requires about $750,000 to $1 million/MW of installed capacity. Thus, expectations regarding the tariff of domestic biomass power at 8-9 US Cent/kWh over the next three to five years seem to be impossible. Therefore, it is necessary to have more support for the feed-in tariff from the Government.

In term of solar power, there has not been any mechanism to encourage the development of solar power so far, specifically in remote and off-grid areas. Currently, the Government is ordering the MOIT to complete the mechanism for grid-connected solar power, including energy market sharing quota mechanism and long term stable electricity price frameworks. Besides, the Government should consider to provide financial support for effective combined renewable energy sources models as well as to exempt renewable energy production and circulation taxes as one of the climate change mitigation solutions of Vietnam.

Conclusions

Based on scientific evidences and discussion, it is important for the government to issue new policies, which will remove barriers of renewable energy development. Using more renewable energy and reducing the share of coal-fired power means reducing greenhouse emissions and ensuring energy security, which is believed to be the best method for current electrical systems in Vietnam.

REFERENCES

[1] Le Anh Tuan (2016), "An overview of the renewable energy potentials in the Mekong River Delta, Vietnam", *Can Tho University Journal of Science*, Special issue: Renewable Energy, pp.70-79.

[2] Huynh Thi Thu Huong, Vo Quang Minh, Le Anh Tuan (2013), *Using remote sensing MODIS data for monitoring the effects of drought and flood to rice farming system changes in the Mekong Delta*, PhD student's special report, Can Tho University, Vietnam, available access from web-link: https://gs.ctu.edu.vn/luan-an/toan-van-luan-an-ncs/106-toan-van-luan-an-tien-si-cua-ncs-huynh-thi-thu-huong-chuyen-nganh-moi-truong-dat-va-nuoc-khoa-2010.html.

[3] National Assembly (2010), *Law on Economical and Efficient Use of Energy*, Decision No. 50/2010/QH12 dated June 17th, 2010, available access from web-link: https://thuvienphapluat.vn/van-ban/Tai-nguyen-Moi-truong/Law-No-50-2010-QH12-on-economical-and-efficient-use-of-energy-113380.aspx.

[4] Prime Minister (2011), *National Master Plan for Power Development for the period of 2011-2020 with the vision to 2030*, Decision 1208/QD-TTg dated July 21st, 2011, available access from web-link: http://gizenergy.org.vn/media/app/media/PDF-Docs/Legal-Documents/PDP%207%20revised%20Decision%20428-QD-TTg%20dated%2018%20March%202016-ENG.pdf .

[5] Rogers Stephani (2012), *What is green energy*? available access from web-link: http://www.mnn.com/earth-matters/energy/stories/what-is-green-energy.

[6] T. Lindeman, T. Mellnik, and W. Englund (2015), *As appetite for electricity soars, the world keeps turning to coal*, The Washington Post, Section, Oct. 12, 2015.

[7] Jorge Ribas, and Julio Negron (2015), *Why the world still uses coal*, The Washington Post, Video Channels: WORLD, October 16, 2015.

[8] Black and Veatch (2014), *Environmental and social impact assessment addendum for Cong Ly wind power plant phase 2*, B&V Project No. 185014, Draft ver. on 9 Oct. 2014.

[9] UNFCCC/CCNUCC (2012), *Project design document form for CDM project activities (F-CDM-PDD)*, Project Design Document, CDM - Executive Board, 40p.

[10] MOIT, True Wind Solutions, and World Bank (2010), *Wind resource Atlas of Vietnam*, available access from web-link: https://esmap.org/sites/default/files/esmap-files/MOIT_Vietnam_Wind_Atlas_Report_18Mar2011.pdf.

[11] V. Aisma, D. Nina, and T. Mikael (2017), *Renewable energy scenarios for Vietnam*. Technical report published by Ea Energy Analyses and Danish Energy Agency, available access from web-link: http://www.ea-energianalyse.dk/reports/1639_ technical_report_vietnam_energy_outlook_2017.pdf.

[12] GSO (2015), *Vietnam General Statistical Data in 2015*, available access from web-link: https://www.gso.gov.vn/default.aspx?tabid=717.

[13] N.H. Diep, K. Sakanishi, N. Nakagoshi, S. Fujimoto, T. Minowa (2015), "Potential for rice straw ethanol production in the Mekong Delta, Vietnam", *Renewable Energy*, **74**, pp.456-463.

[14] GIZ (2016), *Vietnam Power Development Plan for the period 2011-2020: Highlights of the PDP 7 revised*, available access from web-link: http://gizenergy.org.vn/media/app/media/legal%20documents/GIZ_PDP%207%20rev_Mar%202016_Highlights_IS.pdf.

[15] IRENA (2014), *Renewable power generation costs in 2014. Executive summary*, available access from web-link: http://www.irena.org/DocumentDownloads/ Publications/IRENA_RE_Power_Costs_Summary.pdf.

[16] Prime Minister (2011), *Decision No. 37/2011/QD-TTg of on the mechanism supporting the development of wind power project in Vietnam*, available access from web-link: http://hethongphapluatvietnam.com/decision-no-37-2011-qd-ttg-of-on-the-mechanism-supporting-the-development-of-wind-power-project-in-vietnam.html.

[17] Prime Minister (2014), *Decision No. 24/2014/QD-TTg dated March 24, 2014, on support mechanism for development of biomass power projects in Vietnam*, available access from web-link: http://hethongphapluatvietnam.com/decision-no-24-2014-qd-ttg-dated-march-24-2014-on-support-mechanism-for-development-of-biomass-power-projects-in-vietnam.html.

New records of genus *Volvariella* (Pluteaceae) from Cuc Phuong National Park

Huyen Thanh Le*, Ngoc Thi Chu

Hanoi University of Resources and Environment

Received 23 March 2018; accepted 25 June 2018

Abstract:

Cuc Phuong National Park is a natural reserve located in Ninh Binh, Hoa Binh and Thanh Hoa provinces. Cuc Phuong is Vietnam's oldest National Park and also is one of the most important sites for biodiversity in Vietnam. Little is known about the diversity of macrofungi in this special area. This paper presents the collecting process of fungal samples and the identification and description of some fungal species belonging to the genus *Volvariella* (Pluteaceae) based on the morphological characteristics in Cuc Phuong National Park, Ninh Binh province. This study identified 5 species including *Volvariella murinella, Volvariella gloiocephala, Volvariella volvaceae, Volvariella taylorii,* and *Volvariella pusilla*. Interestingly, of them, 4 macrofungus species were first recorded at this National Park.

Keywords: **Cuc Phuong National Park, mushroom, new records, Pluteaceae, *Volvariella.***

Classification number: **6.1**

Introduction

Volvariella is a large genus belonging to the family Pluteaceae, order Agaricales, Hymenomycetidae, Eubasidiomycetes, Basidiomycotina and Eumycota [1]. Most of the *Volvariella* species possess some morphological characteristics such as a volva at the bottom of the stipe, none annulus, none pink gills, none free lamellae, not attached to the stipe, spore print pinkish or brownish, pink spores thin-walled to somewhat thick-walled and growing on porous soils or on wood. However, some *Amanita* species are also superficially similar to *Volvariella*, and therefore, they are easily recognised as *Amanita.*

Volvariella species are best known as valuable foods. Many of them are natural nutrient sources rich in proteins, amino acids, minerals and vitamins A, B, C, D, E, etc. In addition, some species have medicinal value. At present, some species are being studied for the processing or extraction of bioactive ingredients for the production of drugs that support the treatment of many diseases.

Materials and method

Morphological description

This study is based on samples collected during the period 2016-2017. The materials are deposited at the Faculty of Environment, Hanoi University of Natural Resources and Environment (Vietnam).

Macromorphological features are all based on fresh materials and all aspects of size, shape, colour and colour changes, texture, odour and taste are documented [2]. Features of both young and old fruit bodies were recorded. The colour was described in daylight using terms and notations in a colour guide by Kornerup and Wanscher (1978) [3].

Micromorphological characteristics were documented from the analyses of dried materials. Spores were observed for measurements and drawings; all other structures were observed in 2-5% KOH or Congo-red.

Microscopy technique:

Add 3 small drops of distilled water to the microscope slide, and then cut 3 small pieces of mushroom in the pileus, lamella and stipe. Then, put them on each drop of water. Use a razor blade to chop the samples. Cover them with the lamen and then press lightly.

Observe specimen at the lens of x 4, x 10 and x 40. Then, add a drop of immersion oil on the specimen on the glass at a lens of x 100.

(Note: when glassing at the lens of x 100, only return to observe at the lens of x 4 and x 100).

Microscopic data need to be determined:

**Corresponding author: Email: lthuyen@hunre.edu.vn.*

Spore (at lamella): size, shape, colour and structure (thick or thin, having internal substance or not, internal substance is coloured or colourless, there is a pillar layer between 2 layers or not); **Basidia** (at lamella): size, shape, number of horns, colour and structure (thick or thin, internal substance is coloured or colourless); **Cystidia** (at lamella): size, shape, density, colour and structure (thick or thin, internal substance is colour or colourless); **Pileipellis** (at pileus) and **Stipitipellis** (at stipe): size, shape, having branches or not, having partitions or not, structure of pileipellis (thick or thin, internal substance is coloured or colourless); Clamp connection, if present.

The approach of fungal identification

All the species were identified from *Volvariella* according to taxonomy by Ahlawat, et al. (2010) [4], Dutta, et al. (2011) [5], A. Justo and M.L. Castro (2010) [6] and Seok Soon-Ja, et al. (2002) [2].

The taxonomy of the species was described, and the illustrations were then compared with the species checklist in Vietnam by Tam Kiet Trinh (2011, 2014) [7, 8] and Van Mao Tran (2005) [9].

Results and discussion

Key to species of Volvariella from Cuc Phuong National Park

1. The largest spores being more than 11 µm long; the cap spread out, thick, white or brownish grey, rugged and brownish grey top of cap ……...*V. gloiocephala.*

2. Growing on humus soil ……..…..3

2'. Growing on soil in the coniferous forest ……4

3. The diameter of the cap being about 5-10 cm, blackish brown, grey, volva externally date white or brownish grey ……... *V. volvacea.*

3'. Unclear volva, just roughly, white …… *V. murinella.*

4. Cone-shaped or umbonatae cap. White, dry, smooth surface. Small cap less than 5 cm, volva grey to pale brownish grey ……..…….. *V. pusilla.*

4'. Cap with whitish, greyish to pale brownish grey hairs, cap dry and wrinkled…… *V. taylorii.*

1. *Volvariella murinella* (Quél.) M.M. Moser, in Gams, Kl. Krypt.-Fl. Mitteleuropa - Die Blätter- und Baupilze (Agaricales und Gastromycetes) (Stuttgart) 2: 110 (1953).

Syn: *Volvaria murinella* Quél., Compt. Rend. Assoc. Franç. Avancem. Sci. 11: 391 (1883) - *Volvariella murinella* (Quél.) M.M. Moser ex Dennis, P.D. Orton & Hora, Trans. Br. mycol. Soc. 43(2): 167 (1960) (see in Figs. 1-3).

Fig. 1. *Volvariella murinella.*

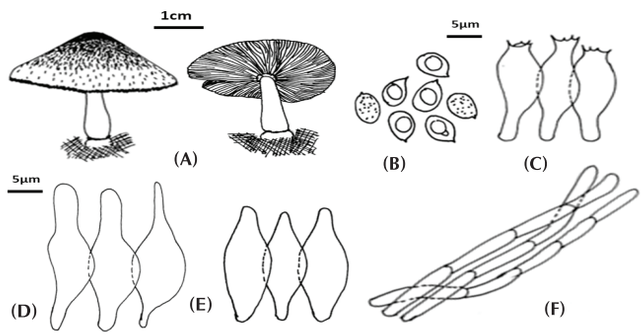

Fig. 2. Microscopic characteristics of *Volvariella murinella.* **(A)** Pileus, **(B)** Spore, **(C)** Basidia, **(D)** Cheilocystidia, **(E)** Pleurocystidia, **(F)** Pileipellis.

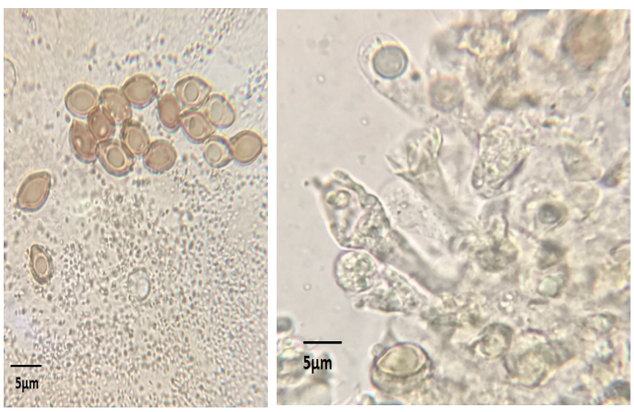

Fig. 3. Microscopic images of *Volvariella murinella.*

Pileus 3-6 cm wide, cone when young and umbonatae when mature, surface with greyish to pale brownish, smooth, clear hairs, edge white, unclear, easy to separate when expanded. Context thick, spongy, soft, white to pinkish. Lamellae free, subcrowded to crowded, at first white then becoming pinkish, spacing about 0.7-1 mm,

breadth 0.2-0.4 mm and the number of series is 3. Pink spore prints. Stipe 3-10 cm long, 0.5-1.5 wide, cylindric to subcylindric, expanded at the bottom, white or brown, roughly and unclear volva at the base. Spores 4.8-5.6 x 4.9-6.6 µm, ellipsoid. Basidia 19-25 x 6-7 µm, clavate shaped and 4-spored. Cheilocystidia with size from 45-65 x 8-15 µm, clavate, subfusiform or ventricose lageniform. Size of pleurocystidia from 20-30 x 10-15 µm, clavate. Pileipellis is a cutis made up of shortcelled hyphae.

Sign: CN27.17-20/7/2017 - Hoa Mac lake - 20°14'52"N - 105°29'38"E; M131.17 - 8/6/2017 - Hoa Mac lake - 20°21'42"N - 105°39'50"E, Cuc Phuong National Park, Ninh Binh.

Edibility: unknown.

Habitat: terrestrial, on porous soils, high humidity.

Comments: when comparing our specimens collected from Cuc Phuong National Park to *Volvariella murinella* of T. Boekhout (1986) [10], it was noted that they have some similar features of morphology and microscopy as follows: pileus in float shape - convex, brown-grey, fade to the outside, visible fuzz on the surface; pink-white stipe; spore in ellipse shape; cheilocystidia in the rhombus shape- fusoid; Pleurocystidia in the bottle shape. Compared to T. Boekhout (1986), the morphological characters of our specimens are clearer and consistent with the documentation of, for instance, basidia, pileipellis. According to T. Boekhout (1986), *Volvariella murinella* grow on moist soil or sandy soil, under trees with a large canopy and appears in the local area.

Comparing our specimens with *Volvariella murinella* of Dong Anh Tran (2013) [11], it was noted that there are some similar features such as: shape of pileus, size of pileus, and gills; the most similar feature according to Dong Anh Tran (2013) is unclear volva only slightly rising. This paper has described the morphology as well as the microscopy more clearly and fully of cheilocystidia, pleurocystidia, pileipellis and some external morphological features of species.

2. *Volvariella volvacea* (Bull.) Sing. in Lilloa 22: 401, ('1949') 1951 var. volvacea.

Syn: *Agaricus volvaceus* Bull., Herb. France: pl. 262. 1786; *Agaricus volvaceus* Bull: Fr., Syst. mycol. 1: 278. 1821; *Volvaria volvaceus* (Bull.: Fr.) Kumm., Fuhr. Pilzk.: 99. 1871; *Volvariopsis volvacea* (Bull.: Fr.) Murrill in N. Amer. Fl. 10: 144. 1917; *Agaricus virgatus* Tent. Disp. meth. Fung.; 66. 1797; *Volvaria virgata* (Pers.) Quél. in Mém. Soc. Émul. Montbéliard, sér. II, 5: 344. 1873 (Champ. Jura Vosges 2) (see in Figs. 4-6).

Fig. 4. *Volvariella volvacea.*

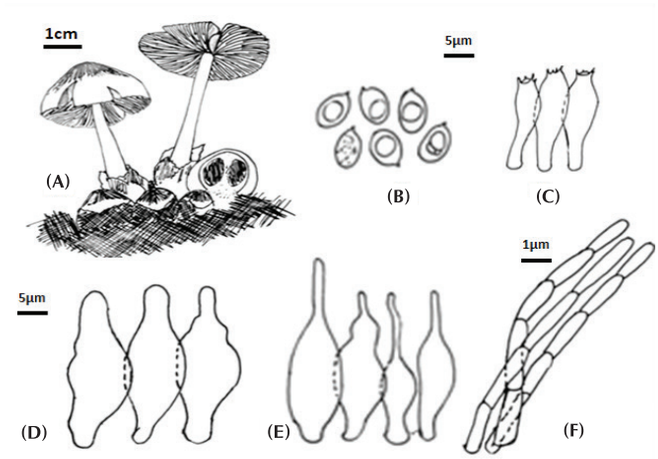

Fig. 5. Microscopic characteristics of *Volvariella volvacea.* (A) Pileus, **(B)** Spores, **(C)** Basidia, **(D)** Cheilocystidia, **(E)** Pleurocystidia, **(F)** Pileipellis.

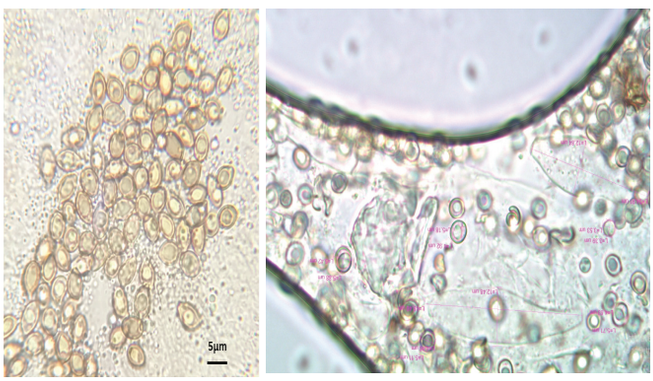

Fig. 6. Microscopic images of *Volvariella volvacea.*

Pileus 2.5-5 cm, ellipse-shaped with young specimens, expanded development to convex or broadly conic, flat, dry, hairs spread out uniformly, greyish, blackish brown or nearly black when young. Context soft, solid, spongy,

white to pale brownish. Lamellae free from the stem, white when young and becoming pink when they mature, close or nearly crowded, spacing about 0.5-1 mm, breadth 0.2-0.4 mm. Pink spore prints. Stipe 3-7 cm long, 0.5-1 cm wide, cylindrical shape, expanded at the bottom, a volva at the base; dry; whitish or brownish; silky, volva is brownish grey to nearly black above and whitish below. Odour likes moist straw. Taste sweetish. Spores 4.6-5.8 x 7-8.5 µm; ellipsoid to elongate or somewhat ovoid. Pleurocystidia 25-30 x 10-15 µm and cheilocystidia 40-58 x 10-12 µm, variously shaped but mostly fusoid-ventricose or clavate. Pileipellis a cutis made up of shortcelled hyphae.

Edibility: edible, high nutritional value.

Habitat: terrestrial or gregarious on porous soils, high humidity, hot and humid time in summer.

Sign: CN33.17 - 20/7/2017 - Hoa Mac lake - 20°15'24"N - 105°32'54"E; CN34.17 - 20/7/2017 - Hoa Mac lake - 20°16'43"N - 105°33'30"E, Cuc Phuong National Park, Ninh Binh.

Comments: comparing this to the research of Dong Anh Tran (2013) [11], it was noted that there are some similar features in morphology, such as: at first, toadstool in the egg shape, as mature pileus in cone shape, convex at the top and flat expanding on both sides; smooth surface, smooth white grey yarns, black mushroom top; odour are soft, sweet and slightly sour, stipe is smooth and white, volva is calyx, dark grey or ash grey; basidia is the mace shape with 4 horns. Compared to *Volvariella volvacea* of Dong Anh Tran (2013), I have described the morphology as well as the microscopy of the CN33.17 sample more clearly and fully. According to Dong Anh Tran (2013), *Volvariella volvacea* appears in the North provinces mainly from April to November and Southern delta all year. Compared to the research by Seok Soon-Ja, et al. (2002), the CN33.17 sample collected from Cuc Phuong National Park has many similar features in microscopy, such as spores, basidia, cheilocystidia, pleurocystidia and pileipeillis. However, our specimens have not yet described the fibre system such as stipitipellis and the structure of the fibre system of volva.

Compared to M. Kuo (2008) [12], our specimens also has some similarities with the *Volvariella volvacea* species, such as toadstool has the egg shape at early ages, pileus has the cone shape with slightly convex top as mature, or the pileus enlarges almost flat, dry surface, grey colour and white or brown stalk. Compared to the microscopy with *Volvariella volvacea* of M. Kuo (2008), our specimen also has some similar characteristics such as the shape of spores, cheilocystidia, pleurocystidia and pileipellis. However, M. Kuo (2008) did not characterise the morphology of basidia. According to M. Kuo (2008), *Volvariella volvacea* grows in clusters, in woody forests, greenhouses, flower gardens, composting piles and similar locations all year depending on the climate, but they often grow in the summer and are widely distributed in North America, more commonly in the Eastern Great Plains. Thus, our specimens were collected in Cuc Phuong National Park and have many same morphological and morphological characteristics with *Volvariella volvacea* of Seok Soon-Ja, et al. (2002), Dong Anh Tran (2013) and M. Kuo (2008). As a result, we recognise that our samples belong to the species *Volvariella volvacea*.

3. *Volvariella gloiocephala* (DC.) Boekhout & Enderle, Beiträge zur Kenntnis der Pilze Mitteleuropas 2: 78 (1986) (see Figs. 7-9).

Syn: *Agaricus gloiocephalus* DC. in DC. & Lam., Fl. franc. 6: 52. 1815; *Agaricus gloiocephalus* DC.: Fr., Syst. Mycol. 1: 278. 1821; Volvaria gloiocephala (DC.: Fr.) Gillet, Hyménomycètes: 388. 1876; *Volvaria speciosa* var. *gloiocephala* (DC.: Fr.) R. Heim in Rey. Mycol. 1, Suppl.: 89. 1936; *Volvariella speciosa* var. *gloiocephala* (DC.: Fr.) Sing. in Lilloa 22: 401. ('1949') 1951; *Volvariella speciosa* f. *gloiocephala* (DC.: Fr.) Konr, & M., Ic. sel. Fung. 6: 52. 1924; *Volvariella speciosa* f. *gloiocephala* (DC.: Fr.) Court. in Bull. Soc. mycol. Nord. 34: 16. 1984; *Amanita speciosa* Fr., Observ. mycol. 2: 1. 1818; *Agaricus speciosus* (Fr.) Fr.: Fr., Syst. mycol. 1: 278. 1821; *Volvaria speciosa* (Fr.: Fr.) Kumm., Führ. Pilzk.: 99. 1871; *Volvariella speciosa* (Fr.: Fr.) Sing. in Lilloa 22: 401. ('1949') 1951; *Agaricus emendatior* Berk. & M. A. Curtis, in Ann Mag. nat. Hist., ser. III, 4: 288. 1859.

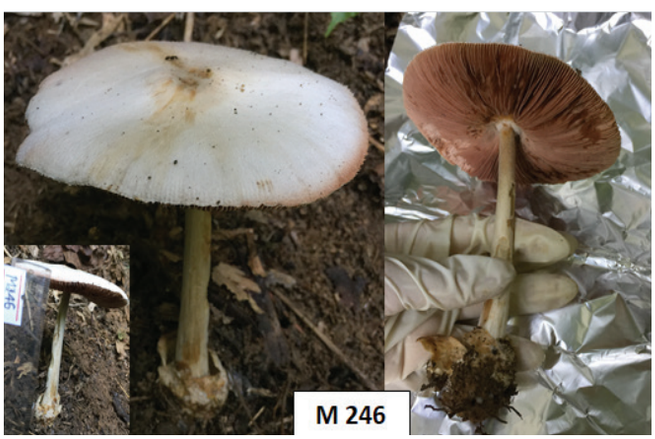

Fig. 7. *Volvariella gloiocephala.*

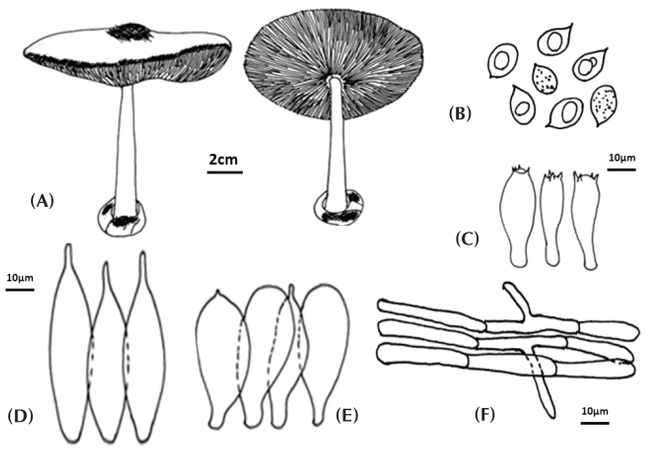

Fig. 8. Microscopic characteristics of *Volvariella gloiocephala.* **(A)** Pileus, **(B)** Spores, **(C)** Basidia, **(D)** Cheilocystidia, **(E)** Pleurocystidia, **(F)** Pileipellis.

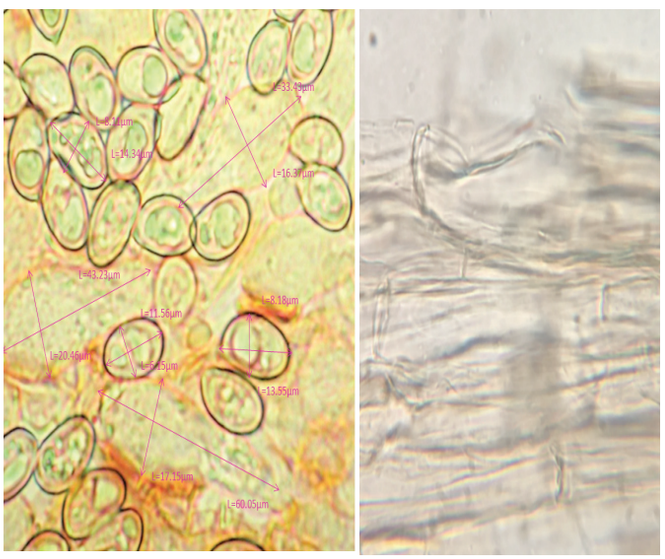

Fig. 9. Microscopic images of *Volvariella gloiocephala.*

Pileus 5-13 cm, void when young, becoming somewhat campanulate to convex or umbonatae, dry, surface with white and smooth hairs, greyish or brownish top of pileus. Context flesh, soft, spongy, thin, white. Lamellae free, subcrowded to crowded, edge fimbriate, white when young and then becoming brownish-pink, spacing 0.5-1 mm, breadth about 0.2-0.3 mm. Pink spore prints. Stipe 8-12 long, 1-1.5 thick, white to pale brownish, cylindric to subcylindric, expanded at the bottom and glabrous. Sack-like volva which may be prominent, white. Spores 11-14 x 6-8 µm, ovoid or elipsoid. Basidia 30-35 x 10-14 µm, 4-spored. Pleurocystidia 30-50 x 15-25 µm subcylindric to fusoid at times with knob at the apex or not. Cheilocystidia 50-75 x 15-25 µm, fusoid with, the neck enlarged or slender, clavate at times with long neck. Pileipellis consist of gelatinous hyphae, branched.

Edibility: edible.

Habitat: terrestrial on porous soils, high humidity.

Sign: M246.17 - 8/8/2017 - Antediluvian cave - 20°20’22”N - 105°37’46”E; M247.17 - 8/7/2017 - Antediluvian cave - 20°20’23”N - 105°37’48”E, Cuc Phuong National Park, Ninh Binh.

Comments: compared to the research of Seok Soon-Ja, et al. (2002) [2], the M246 sample collected from Cuc Phuong National Park has many similar features such as the Pileus is large, oval-shaped, slightly convex at the top, as they mature, it becomes almost flat (umbonate), it is covered with fine white fuzz, has light brown, darker mushrooms edges, slightly dry surface, the pileus meat is thin, white and soft; lamella are freely lined up closely and is pink brown as they mature; the stalk is cylinderical, white and expanded to the bottom; the spores are egg-shaped and the basidia is mace-shaped with four horns; the pleurocystidia is fusoid-shaped with a knob at the apex; the cheilocystidia is oval. Mostly, the M246 sample has the similar morphological and morphological characteristics compared to the *Volvariella gloicephala* species from Vietnam. According to Seok Soon-Ja, et al. (2002), the *Volvariella gloiocephala* species is edible, distributed shingly on humus areas, especially in shiitake plantations.

Compared to M. Kuo (2008) [12], the M246 sample also has similarities with the *Volvariella gloicephala* species such as: size of pileus, shape of pileus, colour, lamella, stipe, spore, cheilocystidia and pleurocystidia. However, M. Kuo (2008) did not clearly describe the surface of pileus, the substance in context, the substance in stipe, lamella, basidia and pileipellis. According to M. Kuo (2008), the *Volvariella gloiocephala* species is edible and distributed individually in gardens, lawns and firewood, mainly in the forest and grows primarily in the North in spring and in southern California in the winter, and is widely distributed in North America.

Based on the morphological and microscopic characteristics of the *Volvariella gloiocephala* species observed by Seok Soon-Ja, et al. (2002), M. Kuo (2008), it is noted that our specimen (M246.17) has many similarities with them. Therefore, I identify that the specimen M246.17 belongs to the *Vovariella gloiocephala* species.

4. *Volvariella taylorii* (Berk. & Broome) Singer [as ‘taylori’], Lilloa 22: 401 (1951).

Syn: *Agaricus taylorii* Berk. & Broome [as ‘taylori’], Ann. Mag. nat. Hist., Ser.2 13: 398 (1854) - *Volvaria taylorii* (Berk. & Broome) Gillet [as ‘taylori’], Hyménomycètes (Alençon): 386 (1876) (see Figs. 10-12).

Fig. 10. ***Volvariella taylorii.***

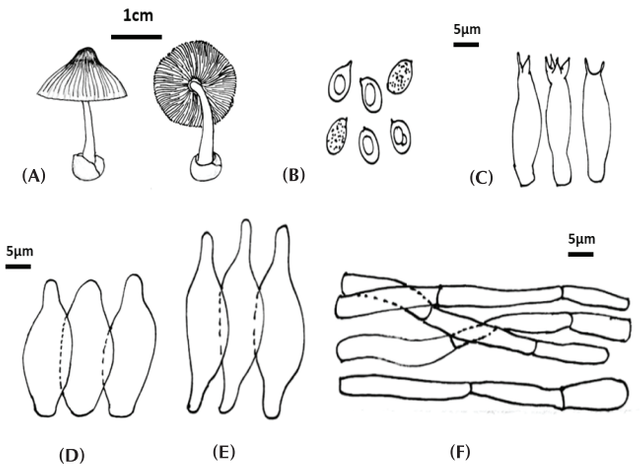

Fig. 11. Microscopic characteristics of *Volvariella taylorii.* **(A)** Pileus, **(B)** Spores, **(C)** Basidia, **(D)** Pleurocystidia, **(E)** Cheilocystidia, **(F)** Pileipellis.

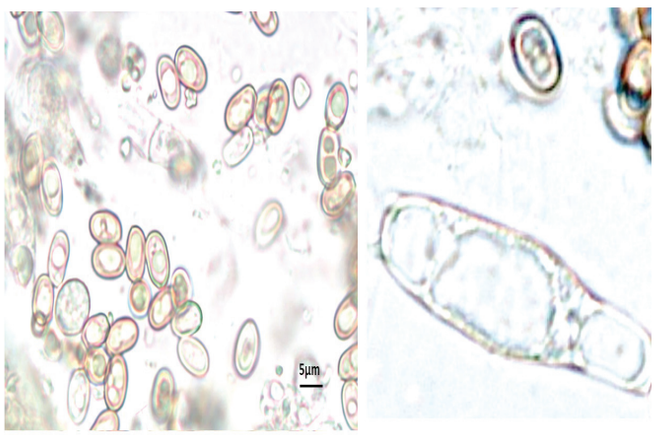

Fig. 12. Microscopic images of *Volvariella taylorii.*

Pileus 1-2 cm when young and 2-5 when mature, convex after expanding to nearly flat, dry, finely hairy; greyish to brownish grey, the margin not lined, white. Context white, soft, spongy; the thickness in pileus about 1 mm when young and 2-3 mm when mature. Free lamellae and not attached to stipe; whitish becoming pink, close or almost distant, spacing 0.5-1 mm, breadth 0.2-0.3 mm, the number of series is 3 lamellulae. Pink spore prints. Stipe 2.5-6 cm long; 2-5 mm thick, white, thickened downward, glabrous, but somewhat pilose at the base; smooth, finely hairy, grey or brownish volva. Spores 4.8-6 x 4.5-5.2 µm, ellipsoid, thick-walled. Basidia 20-25 x 7-10 µm, normal, 2-4-spored, rarely 2-spored. Pleurocystidia 25-30 x 10-15 µm, fusoid-ventricose, sublageniform, ventricose, thin-walled. Cheilocystidia 35-50 x 10-20 µm, fusoid-ventricose, clavate with obtuse or narrow neck, thin-walled, abundant. The Pileipellis has a size of about 35~360 x 11~14.0 µm, has cylindric hyphae and is thin-walled. The Pileipellis is composed of cylindric hyphae with clamp connection.

Edibility: edible.

Habitat: terrestrial on porous soils, high humidity, in dense forest.

Sign: M106.17 - 8/7/2017 - Center of Cuc Phuong National Park - 20°22'35"N - 105°40'41"E; M108.17 - 8/7/2017 - Center of Cuc Phuong National Park - 20°22'30"N - 105°40'39"E.

Comments: comparing the M106.17 collected from Cuc Phuong National Park, Ninh Binh to *Vovariella taylorii* of Dong Anh Tran (2013) [11], there are some similarities: pileus is convex-shaped or wide hemisphere, fine fuzz, the color of grey to slightly grey, the edge of mushroom is incomplete, the diameter is 2-5 cm; the stalk is 3-6 cm, a bulge in the root, the color is white, smooth, calyx-shaped; the spore is egg-shaped or ellipse-shaped; the basidia is rhombus-shaped; it grows on land. Compared to Dong Anh Tran (2013), our specimen described the morphology as well as the microscopy more clearly and fully described the microscopic characters such as cheilocystidia, pleurocystidia, pileipellis and other morphological features.

Comparing our species to the *Vovariella taylorri* species by Seok Soon-Ja, et al. (2002) [2], there are many similarities in the toadstool morphology, colour and microscopy with *Vovariella taylorri* species such as spores, basidia, cheilocystidia, pleurocystidia and pileipellis. Additionally, Seok Soon-Ja, et al. (2002) clearly described the living environment of species growing singly on humus soil, mainly in the Shiitake forest.

Thus, compared to *Volvariella taylorii* of Dong Anh Tran (2013) and Seok Soon-Ja, et al. (2002), it is noted that there are many similar morphological and morphological characteristics. As a result, we identified that the M106.17 sample collected is a *Vovariella taylorii* species.

5. *Volvariella pusilla* (Pers.) Singer, Lilloa 22: 401 (1951).

Syn: *Amanita pusilla* Pers., Observ. mycol. (Lipsiae) 2: 36 (1800) - *Agaricus parvulus* Weinm., Hym. à Gast. Imp. Ross. Obs. (Petropoli): 238 (1836) - *Volvaria parvula* (Weinm.) P. Kumm., Führ. Pilzk. (Zwickau): 99 (1871) - *Volvaria pusilla* (Pers.) Lloyd, Mycol. Writ. 1(4): 31 (1899) (see Figs. 13-15).

Fig. 13. *Volvariella pusilla.*

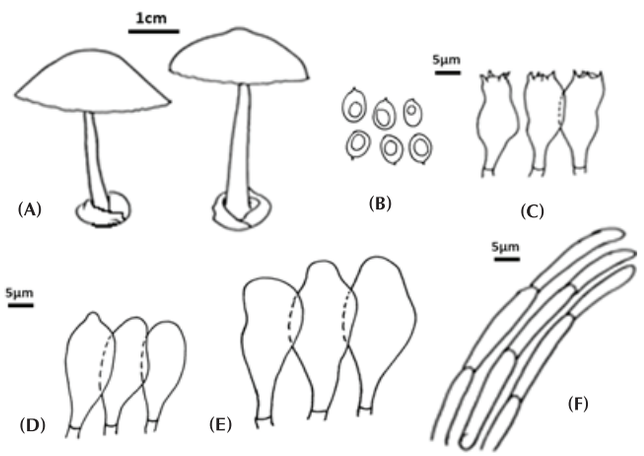

Fig. 14. Microscopic characteristics of *Volvariella pusilla.* **(A)** Pileus, **(B)** Spores, **(C)** Basidia, **(D)** Pleurocystidia, **(E)** Cheilocystidia, **(F)** Pileipellis.

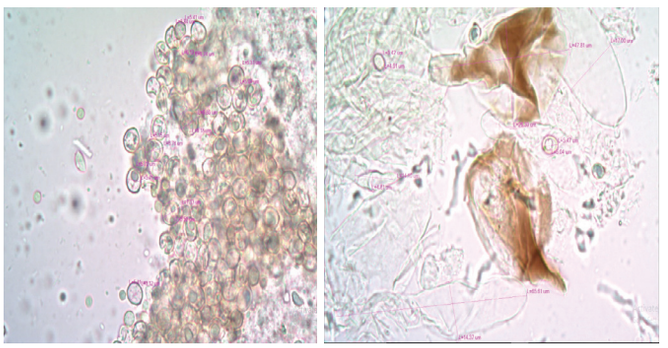

Fig. 15. Microscopic images of *Volvariella pusilla.*

Pileus 1-4 cm, convex to broadly convex to nearly flat, white, the margin lined, slightly sticky when fresh but soon dry, slightly wrinkled when old. Lamellae free from the stem; sub-crowded to crowded, at first, white and then becomes pinkish, spacing about 0.7-0.9 mm. Pink spore prints. Stipe 6-8 cm long, 0.3-0.6 cm thick, cylinder, dry, white, smooth, the base encased in a thick, white to greyish, volva white or brownish, may be buried. Spores 5-7 x 4.5-5.5 µm, ellipsoid. Pleurocystidia 20-30 x 10-15 µm and cheilocystidia 3-50 x 15-25 µm, mostly clavate. Pileipellis composed of cylindric hyphae with clamp connection.

Edibility: unknown.

Habitat: terrestrial on porous soils, high humidity, mostly on grass.

Sign: M185.17 - 15/5/2017 - Hoa Mac lake - 20°15'40"N - 105°33'39"E; M186.17 - 15/5/2017 - Hoa Mac lake - 20°15'42"N - 105°33'22"E; M187.17 - 15/5/2017 - Hoa Mac lake - 20°15'32"N - 105°33'18"E; M188.17 - 15/5/2017 - Hoa Mac lake - 20°16'41"N - 105°32'44"E; M189.17 - 15/5/2017 - Hoa Mac lake - 20°16'42"N - 105°32'43"E, Cuc Phuong National Park, Vietnam.

Comments: comparing specimens (M185.17-M189.17) collected from Cuc Phuong National Park - Ninh Binh to *Volvariella pusilla* of Dong Anh Tran (2013) [11], there are some similarities observed between them: the shape of toadstool, white or slightly brown colour at the top and edge; lamella; stipe is smooth, dried and white; the spores shape. In this paper, we clearly examine some morphology characters as well as the microscopy and fully provide the data of basidia, pleurocystidia, cheilocystidia and pileipellis. According to Dong Anh Tran (2015), *Volvariella pusilla* grows on humus land.

Compared to the *Volvariella pusilla* species in the research by Seok Soon-Ja, et al. (2002) [2], there are many similarities such as size of pileus and stipes, surface of pileus, colour, shape of spores, shape of basidia, pleurocystidia and cheilocystidia và pileipellis. Thus, based on the notes

on *Volvariella pusilla* by Dong Anh Tran (2013) and Seok Soon-Ja, et al. (2002), there are many similar morphological and morphological characteristics of the species *Volvariella pusilla* (Figs. 14, 15).

Conclusions

During the research, based on the morphology described species, we found 5 species described for Cuc Phuong National Park, Ninh Binh province, including *Volvariella murinella, Volvariella gloiocephala, Volvariella volvaceae, Volvariella taylorii* and *Volvariella pusilla.* Additionally, the number of species grows in the lower area. Although, sometimes, there is a strong morphological resemblance of the Vietnam species to the European species and Korean species, there is no co-specificity. Moreover, Cuc Phuong National Park is a place with high biodiversity in general and large mushrooms in particular. It requires further research as well as an establishment of the official list.

ACKNOWLEDGEMENTS

Our group would like to thank the Hanoi University of Natural Resources and Environment for their support for this research. Furthermore, we would like to thank the Faculty of Environment for allowing us to conduct this study in the Faculty of Environment.

REFERENCES

[1] P.M Kirk, P.F Cannon, D.W Minter, J.A Stalpers (2008), *Dictionary of Fungi (10th Ed.)*, Wallingford, United Kingdom: CAB International, 671pp.

[2] Seok Soon-Ja, Kim Yang-Sup, Weon Hang-Yeon, Lee Kang-Hyo, Park Ki Moon, Min Kyong-Hee and Yoo Kwan-Hee (2002), "Taxonomic Study on Volvariella in Korea", *Mycobiology,* **30(4)**, pp.183-192.

[3] A. Kornerup and J.H. Wanscher (1978), *Methuen Handbook of Colour*, London, Eyre Methuen, UK, 252pp.

[4] O.P. Ahlawat, Pardeep Gupta, Shwet Kamal, B.L. Dhar (2010), "Variability in intra-specific and monosporous isolates of Volvariella volvacea based on enzyme activity, ITS and RAPD", *Indian J. Microbiol.,* **50(2),** pp.192-198.

[5] A.K. Dutta, P. Pradhan, A. Roy, K. Acharya (2011), "Volvariella of West Bengal, India I", *Researcher,* **3(6),** pp.13-17.

[6] A. Justo, M.L. Castro (2010), "An annotated checklist of Volvariella in the Ibe rian Peninsula and Balearic Islands", *Mycotaxon*, **112**, pp.271-273.

[7] Trinh Tam Kiet (2011), *Large Mushrooms in Vietnam*, **Vol. 1** (second edition), Natural Science and Technology Publishers (in Vietnamese).

[8] Trinh Tam Kiet, et al. (2014), *List of mushrooms in Vietnam*, Agricultural Publishers, Hanoi (in Vietnamese).

[9] Van Mao Tran (2005), *Mushrooms in Cuc Phuong*, Agricultural Publishers, Hanoi (in Vietnamese).

[10] T. Boekhout (1986), *Small, saprophylic Volvariella species in the Netherlands, Persoonia,* **13**, part 2, pp.197-211

[11] Dong Anh Tran (2013), "Researching the species composition and biology characteristics of some representatives belongs to Pluteaceae canopy mushroom in some main ecological areas in Vietnam", *Scientific Conference,* Vietnam Academy of Agriculture, Hanoi (in Vietnamese).

[12] Michael Kuo (2008), *The Genus Volvariella*, Retrieved from the Mushroom Expert.Com (Website: http://www.mushroomexpert.com).

A study of seasonal rainfall in Vietnam at the end of 21st century according to the Non-Hydrostatic Regional Climate Model

Mau Nguyen-Dang[1*], Truong Nguyen-Minh[2], Hidetaka SASAKI[3], Izuru TAKAYABU[3]

[1]Vietnam Institute of Meteorology, Hydrology and Climate change
[2]Hanoi University of Science, Hanoi, Vietnam,
[3]Meteorological Research Institute, Tsukuba, Japan

Received 6 May 2018; accepted 13 August 2018

Abstract:

This article presents analyses of changes in the seasonal characteristics of the far future climate (2080-2099) across Vietnam as projected by the Non-Hydrostatic Regional Climate Model (NHRCM) in terms of the RCP 8.5 (Representative Concentration Pathways 8.5) scenario. The results show significant changes in seasonal rainfall in Vietnam compared with the 1982-2003 baseline period. Specifically, the June-August rainfall is projected to increase in South Central (SCVN), Central Highlands (CHVN), and South Vietnam (SVN), but to decrease by approximately 50% in North Central (NCVN) and off the Central coast. In the September-November season, the NHRCM detects an increase in rainfall of about 50% in North Vietnam (NVN) and CHVN. The increase and decrease in rainfall are due to the convergence and divergence of moisture flux that might be associated with the westward expansion of the Northwestern Pacific High Pressure in the far future.

Keywords: **geopotential height, moisture flux, NHRCM model, rainfall, 850 hPa winds.**

Classification number: **6.2**

Introduction

Rainy season in Vietnam

During the Asian summer monsoon, the main winds in the lower atmospheric layers (from the above ground to 500 hPa) are from the south-west, and from the north-east in the higher atmospheric layers (above the 500 hPa atmospheric layer) [1]. The summer monsoon circulation shifts north-eastwards from the southern hemisphere (north of Australia), crossing the equation in the Indian Ocean, to Vietnam. The positive activity of the summer monsoon circulation brings substantial moisture from the warm Indian Ocean to generate the rainy season across Vietnam. However, much of the variability of the summer monsoon and its weather events are due to the reasons listed below.

1) Variability of large-scale circulations

Figure 1 shows the Asian-Pacific summer monsoon regions. The Asia-Pacific region is divided into three summer monsoon systems: India, East Asia, and the Pacific Northwest [2]. According to Fig. 1, Vietnam is located in the interaction region of the Asia-Pacific summer monsoon systems. As a result, the variability of the summer monsoon and its weather events across Vietnam clearly depends on the variability of these Asian-Pacific summer monsoon regions.

During the summer months, the wind and airstream flowing near the ground are south-west to south and south or south-east to north. The air flow prevailing in Vietnam is equatorial and tropical, originating in the southern hemisphere and the tropical sea as well as the North Pacific high pressure [1]. In addition, during the pre-onset and summer, westerly winds originating in the South Asian low pressure [1] and the extratropical region [3] also effect NVN.

*Corresponding author: Email: mau.imhen@gmail.com

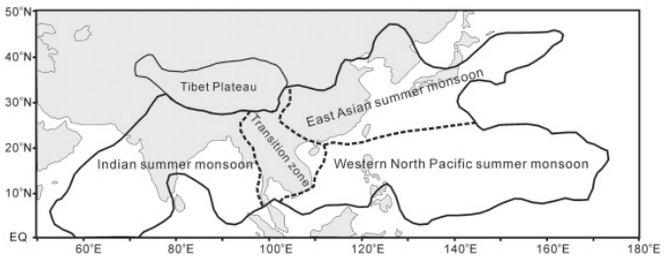

Fig. 1. The three summer monsoon regions of the Asian-Pacific summer monsoon: Indian summer monsoon (ISM), East Asian summer monsoon (EASM), West North Pacific summer monsoon (NWPSM) [2].

2) Variability of El Niño Southern Oscillation (ENSO)

The ENSO is the major factor causing variability in the summer monsoon in Vietnam [1-3]. In Vietnam, the onset date of summer monsoon and its rainy season is later in the El Niño phase and earlier in the La Niña phase [4, 5]. In most of the climatic regions of Vietnam, the total rainfall in the summer monsoon is below normal in the El Niño phase and above normal in the La Niña phase.

3) Local-scale factors

Figure 2 shows that Vietnam is a part of Southeast Asia and is bordered by the Western Pacific to the east, China to the north, and Cambodia and Laos to the west. Topography plays an important role in variability of the monsoon [1]. During the summer monsoon, the mountains in Western Vietnam, especially Truong Son, and in Laos cause a Foehn effect, changing the humid and hot characteristics of the wind from the Bay of Bengal and causing the very hot and dry weather event in the Central region (CVN). A Foehn wind is also referred to as a hot-dry west wind, or Laos wind, that often occurs in NVN and the CVN.

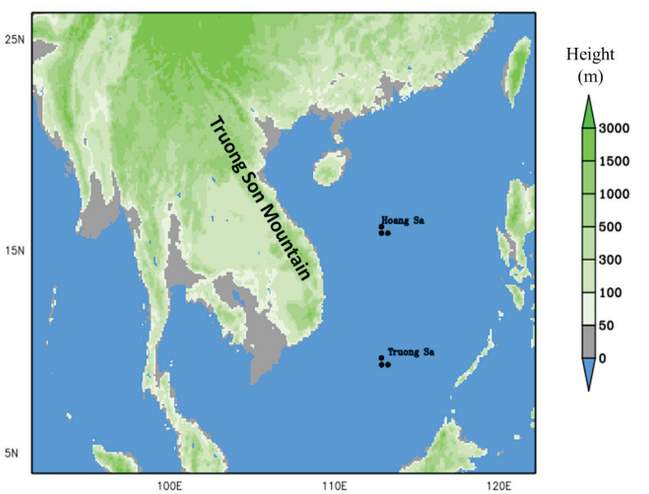

Fig. 2. The terrain map of Vietnam derived from terrain of NHRCM model.

Due to topography, a depression, the 'Bac Bo depression', is formed above the northern Indochinese Peninsula. It primarily causes hot weather over mountainous areas in NVN and Laos. This depression is a region of wind convergence. It causes the wind to change direction from south-west to south-east, blowing over the Gulf of Tonkin and heading towards the north of Vietnam (it often occurs in the northeast and Red River Delta). Due to characteristics of geography, territory, and topography, monsoon circulation in Vietnam is typical, complex, and difficult to forecast.

4) The rainy season and the mesoscale factor

As result of the abovementioned factors, the climate in Vietnam varies significantly, especially the rainfall during the rainy season. In general, the climate in Vietnam is divided into rainy and dry seasons.

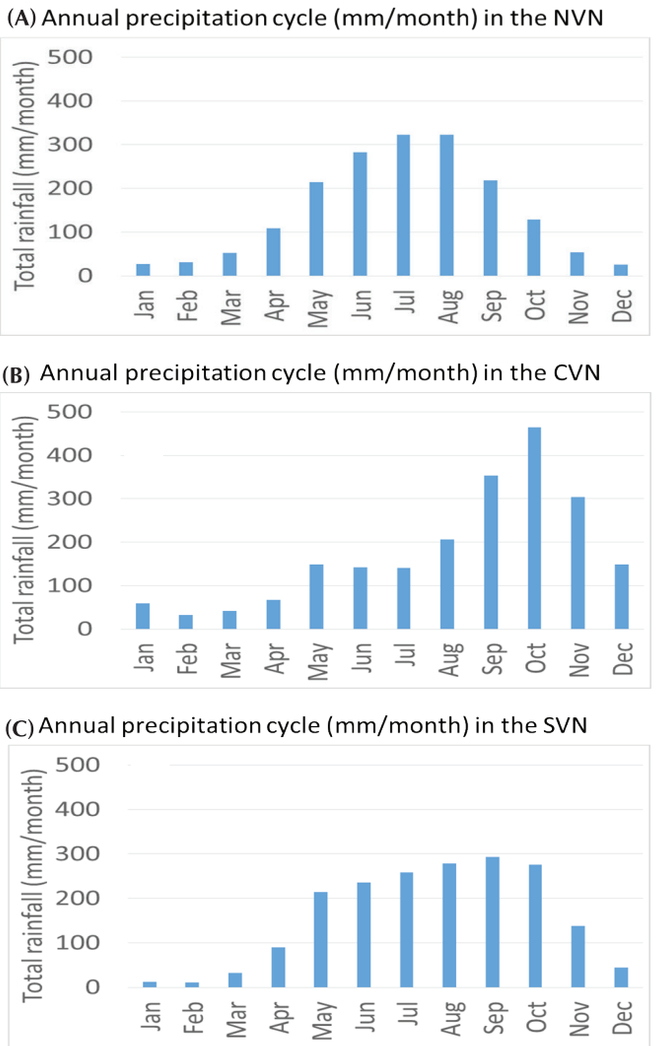

Fig. 3. Annual precipitation cycle in NVN (A), CVN (B), and SVN (C) calculated from observed data from 150 stations, 1961-2014.

Figure 3 shows that the rainy season is from May to November in NVN, CHVN, and SVN; and from September to December in CVN. The rainy season is driven by the summer monsoon in NVN, CHVN, and SVN. However, the rainy season in NCVM and SCVN is driven by cold fronts and tropical cyclones (TCs) [1]. The peak duration of the rainy season is similar to the peak duration of TCs in the East Vietnam Sea, with the two to three TCs per month. The peak duration of the rainy season in CVN is close to the high frequency of TCs and cold fronts.

Projection of seasonal rainfall

The global climate system is expected to undergo significant changes in the future in terms of the greenhouse gas (GHG) scenarios. By the end of the 21st century, the global average temperature will increase by 4°C compared to the baseline scenario of RCP 8.5 [6]. RCP8.5 is a so-called 'baseline' scenario that does not include any specific climate mitigation target. The greenhouse gas emissions and concentrations in this scenario increase considerably over time, leading to a radiative forcing of 8.5 W/m^2 at the end of the century. Projections show that the summer monsoon is expected to be stronger. These projections also show the earlier onset and latter withdrawal date, which will lead to a longer rainy season [6]. In recent years, many studies have mentioned the impact of the increase of GHG concentration on summer monsoon variability. However, very high uncertainty projections in terms of scenarios for summer monsoon variability are found in the studies. According to projections, the general trend is that summer monsoon rainfall is expected to increase with global warming [6-8]. The extreme rainfall events caused by heavy rains are expected to increase in the ISM region [9].

In Vietnam, climate projection studies have been considered in some research [10-12]. The projections for changes in the summer monsoon and its rainfall have been considered by using the PRECIS (Providing REgional Climates for Impacts Studies) [13] and CCAM (Conformal Cubic Atmospheric Model) models [12].

In this study, we focus on the assessment of the rainy season and the amount of rain. In particular, changes in seasonal rainfall in Vietnam by the end of 21st century are investigated using the NHRCM to simulate climate in the baseline period (1982-2003) and to project the far future climate (2080-2099) in terms of the RCP 8.5 scenario. In the next section, data and model configuration are presented. The results and conclusion are presented in the below section.

Data and analysis

The 850 hPa winds from CFSR (Climate Forecast System Reanalysis) of the NCEP (National Centers for Environmental Prediction) [14] are used to validate 850 hPa wind simulations.

The daily gridded precipitation of the Asian Precipitation Highly-Resolved Observational Data Integration towards Evaluation (Aphrodite) [15] is used to validate distributions of simulated rainfall over the entire domain.

The NHRCM used in this study is the extended version of the Non-Hydrostatic Model (NHM), in which the soil model is replaced by MRI (Meteorological Research Institute)-Simple Biosphere model [16], and lateral boundary conditions are replaced by spectral nudging boundary conditions. A detailed description of the NHRCM can be found in K. Saito, et al. (2006) [17]. The model is able to simulate the regional climate and dynamically downscale from Atmospheric General Circulation Model (AGCM) outputs for the Japan [18, 19] and Vietnam [20] regions.

The model domain covers a region of about 85°E -130°E and 5°S-35°N, with a 10 km horizontal grid spacing and 40 vertical levels. The initial and boundary conditions for the NHRCM are the MRI-AGCM3.2 outputs with a 20 km horizontal grid spacing, supplied by the SOUSEI Programme.

Results and discussion

In this section, we examine seasonal characteristics and compare the changes predicted by the 2080-2099 projections with the 1982-2003 simulations, focusing on main rainy months of June-August (JJA) and September-November (SON).

850 hPa Winds Simulations

The JJA 850 hPa wind averages for the period 1982-2003 are shown in Figure 4A for CFSR, and in Figure 6A for NHRCM's simulation. The Figure 4A shows the development of the south-west winds in the 850 hPa layer during summer monsoon season. The significant feature is that the south-west wind will cover most of the Indochina Peninsula and then extend over the eastern Philippines. The monsoon trough occurs due to the development of the south-west winds and its axis crosses NVN in the north-west-south-east direction.

A comparison of Fig. 6A with Fig. 4A shows that the development of the south-west winds and monsoon trough

are well simulated by the NHRCM model. However, the monsoon trough in the simulation and intensity of the south-west winds (Fig. 6A) are stronger than in the CFSR (Fig. 4A). In addition, the meridional winds simulated (Fig. 6A) are weaker in intensity in the northern East Vietnam sea than they are in the CFSR (Fig. 4A).

Figure 4B shows the SON 850 hPa wind averages for the period1982-2003 from CFSR data and the corresponding NHRCM winds (Fig. 7A). In Figure 4B, the east winds are in the northern area and the west winds in the southern area. The comparison shows that the NHRCM model simulates stronger east winds (Fig. 7A) than does CFSR (Fig. 4A). However, the model shows weaker west winds (Fig. 8A) in the southern area than does the CFSR (Fig. 4B).

These comparisons show that the NHRCM model well captures the JJA and SON circulations. However, the wind speed and monsoon trough during the JJA season is stronger than in CFSR. In addition, the wind speed during SON season is weaker than in CFSR.

Rainfall simulations

Figure 5 shows the mean of JJA and SON rainfall averaged during 1982-2003 calculated from the Aphrodite data and the corresponding NHRCM rainfall is shown in the Fig. 6A and Fig. 7A, respectively.

The comparison of Fig. 5A with Fig. 6A indicates that the spatial distribution of JJA rainfall simulation is quite similar to that of Aphrodite. However, there is a quite clear difference in the JJA rainfall, which is higher in the simulation than in Aphrodite. The clearest error in simulation of JJA rainfall can be found in the area to the west of the Truong Son mountains. In addition, an underestimation in rainfall simulation can be found in southern CVN. These results show that the NHRCM model overestimates the rainfall due to summer monsoon, and underestimates rainfall due to Foehn wind effects.

Results in Fig. 5B and Fig. 8A show that the spatial distribution of SON rainfall in the NHRCM model is similar to that of Aphrodite. However, the rainfall simulation is higher than that of Aphrodite, especially in NCVN.

Generally, the JJA and SON simulations have the same spatial distribution as that of Aphrodite. However, the model tends to capture the higher rainfall due to JJA and SON monsoon circulations. Additionally, the lower rainfall due to Foehn wind effects on the eastern side of the Truong Son mountains during JJA season is simulated.

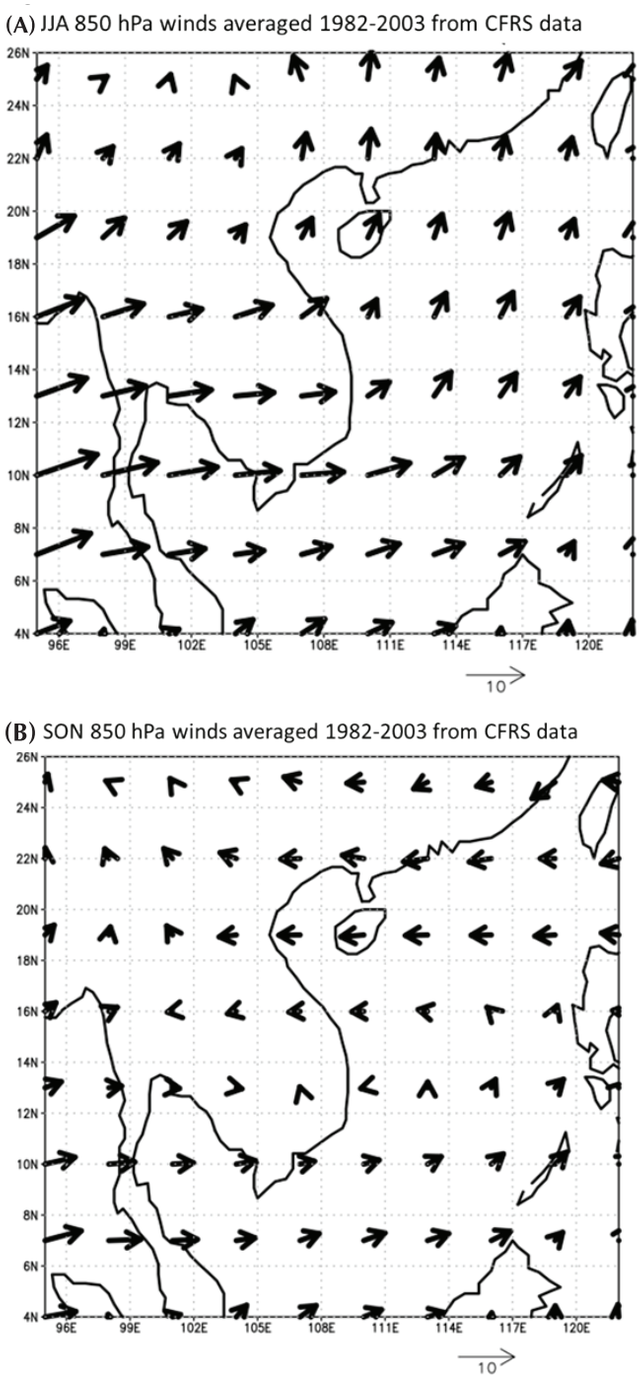

Fig. 4. CFSR mean 850 hPa winds, 1982-2003 (m/s): (A) JJA and (B) SON.

Seasonal rainfall projection for the end of 21st century (far future)

Figure 6 shows the 850 hPa winds and daily rainfall in JJA at present and in the far future climate, simulated and projected by the NHRCM model. It can clearly be seen that the south-westerly summer monsoon prevails in Southeast Asia and the East Sea of Vietnam. Heavy rainfall belts

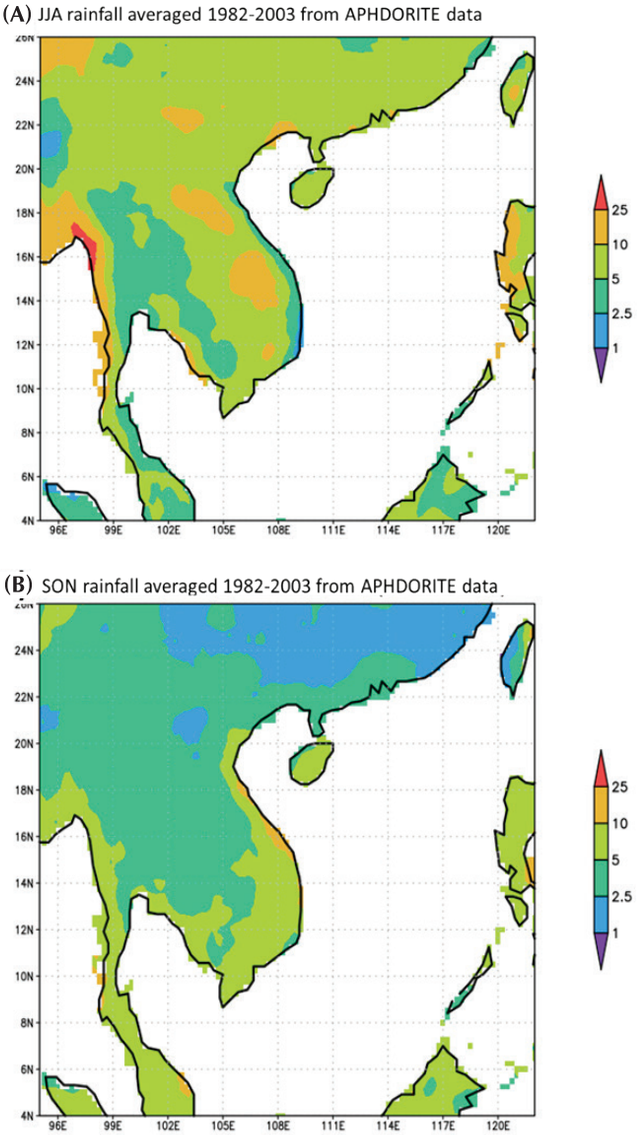

Fig. 5. (A) JJA rainfall (mm/day) and (B) SON rainfall (mm/day), 1982-2003, from Aphrodite.

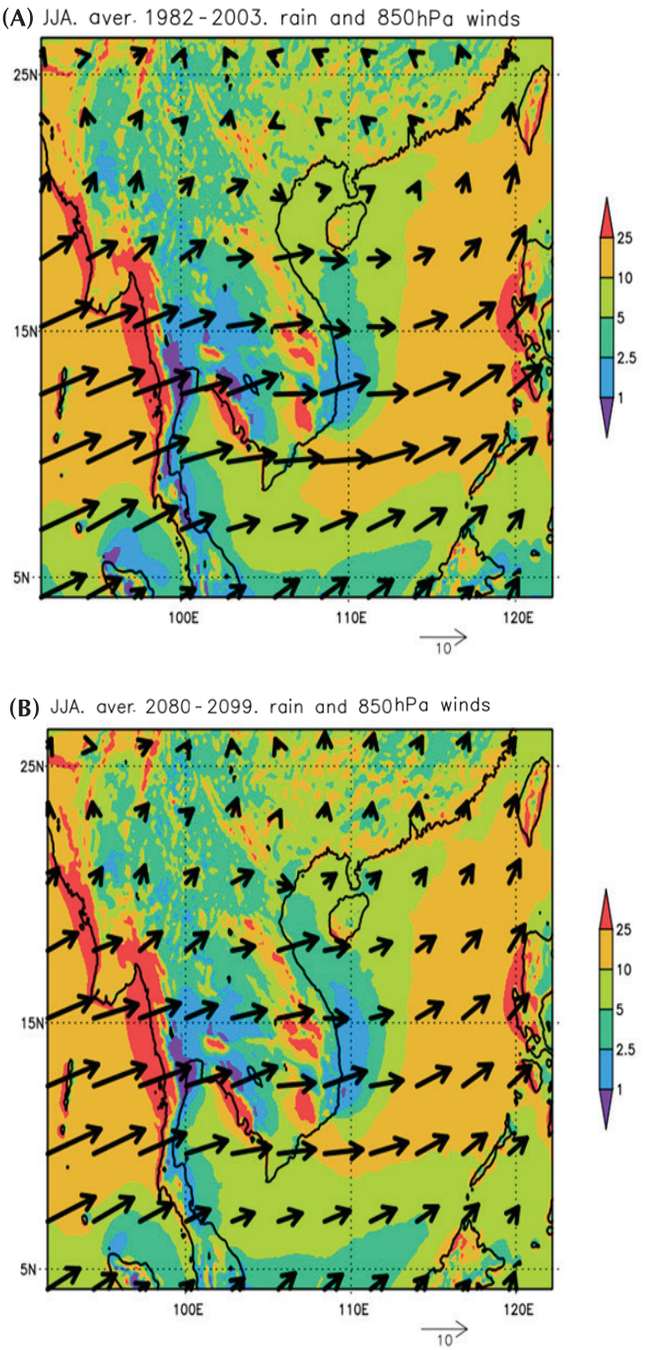

Fig. 6. JJA rainfall (mm/day) and 850 hPa winds (m/s) from NHRCM for (A) 1982-2003 and (B) 2080-2099.

are found along the western coast of Thailand, Cambodia, and along the border between Laos and Vietnam, where a mountain range located (also refer to Kieu-Thi, et al., 2016). There is a small area of the South-Central coastal region where upwelling with low sea-surface temperature is often observed.

The SON pattern is presented in Fig. 7. A heavy rainfall belt is located on the windward side of the mountain range that blocks easterly winds to the North of 15°N (i.e., the trade winds) from the tropical Western Pacific. A cyclonic circulation dominates over the East Sea of Vietnam that seems to weaken in far future (Fig. 7B).

Distributions of changes in 850 hPa winds and rainfall in JJA and SON between far future and the baseline period are shown in Fig. 8. During JJA season in 2080-2099, rainfall should increase by about 40% compared to the baseline rainfall in SCVN, CHVN, and SVN. However, a considerable decrease in rainfall can be found in NCVN.

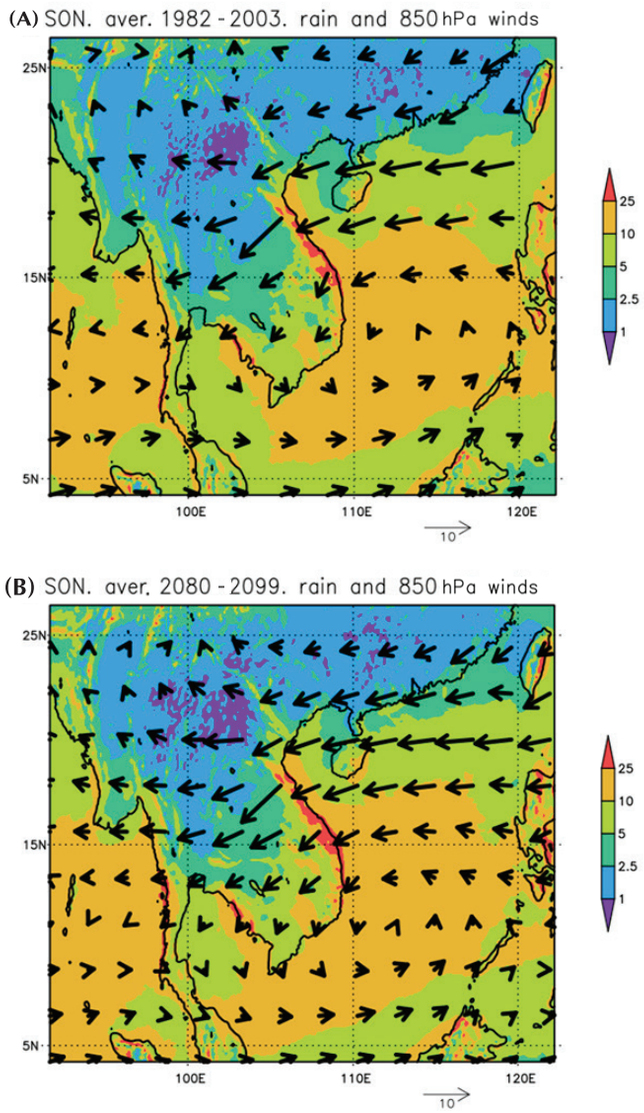

Fig. 7. Same as Fig. 6 but for SON values.

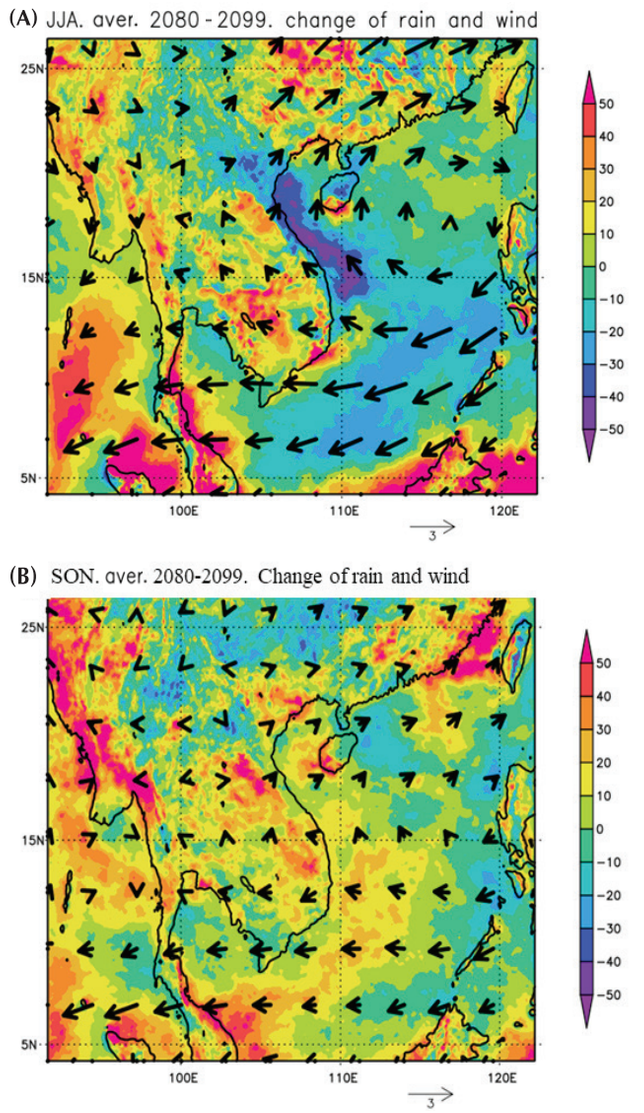

Fig. 8. Changes in 850 hPa winds and total rainfall (%) in JJA (A) and SON (B) for the 1982-2003 and 2080-2099 periods.

850 hPa wind anomalies describe an anticyclonic circulation over the East Sea of Vietnam that is expected to modify moisture flow toward sub-regions of Vietnam in the summer months (Fig. 8A).

During SON season, the NHRCM model shows an increase in 2080-2099 rainfall over most of the country compared to the baseline. The most noticeable increase is of approximately 50% in NVN and CHVN (Fig. 8B). An anticyclonic circulation anomaly is also found over the East Sea of Vietnam; however, it is much weaker than that in JJA.

To explore the reasons for the changes in 850 hPa winds and rainfall mentioned above, we calculated the changes in 850 hPa geopotential height (GHT) and 850-500 hPa vertically integrated moisture flux (IMF) in the far future compared to the baseline period. In general, GHT increases in the entire domain in the far-future climate (Fig. 9). However, Fig. 9A indicates a strong positive anomaly over the East Sea of Vietnam in JJA that helps explain the anticyclonic anomaly mentioned above. IMF is expected to diverge off the CVN coast but converge in SCVN, CHVN, and SVN (Fig. 9), where rainfall increases and decreases, respectively.

Similar to the JJA case, a positive GHT anomaly is also observed over the East Sea of Vietnam in SON, but it is weaker than that in JJA. This means that the Northwestern Pacific Subtropical High (NPH) will be stronger over this sea area in the far future. Due to the westward expansion of NPH

toward the East Vietnam Sea, IMF is expected to increase in inland Vietnam. Convergence of IMF will probably to occur in NVN and CHVN where rainfall increases. The strongest IMF is found to the south of 15°N from the tropical Western Pacific towards the Bay of Bengal.

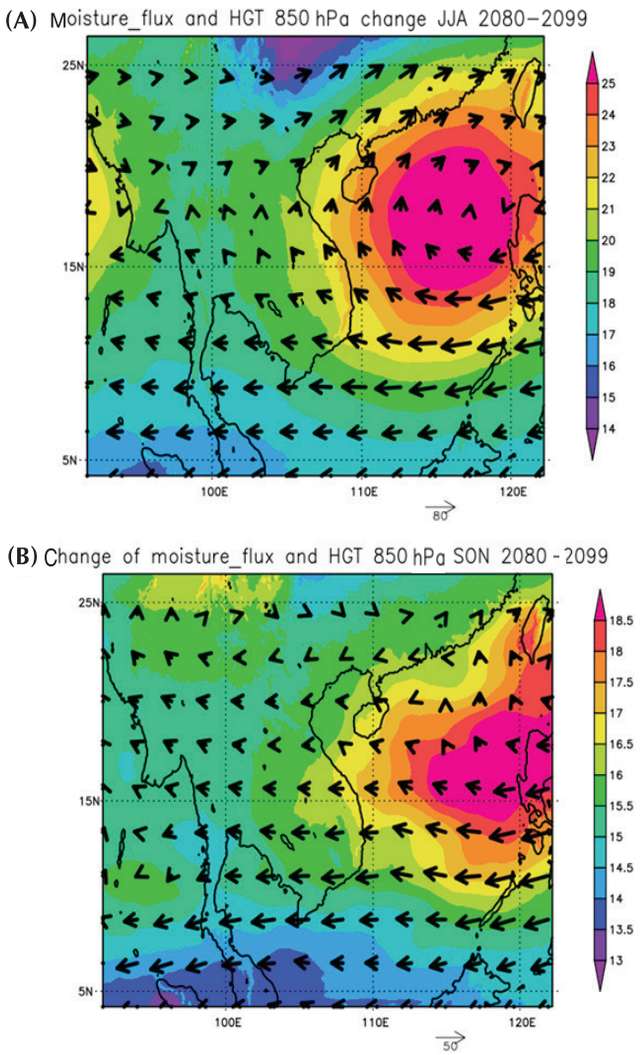

Fig. 9. Same as Fig. 8 but for 850 hPa GHT (m) and 850-500 hPa IMF (kg/kg/m/s).

Conclusions

Using the RCP8.5 emission scenario, the NHRCM model indicates clear changes in seasonal characteristics over the Vietnam region by the end of the 21st century compared to the present climate. Rainfall and 850 hPa wind patterns in the 2080-2099 period are similar to those of the 1982-2003 period, illustrating the influences of the south-westerly summer monsoon and NPH. Rainfall is projected to increase to about 40% in SCVN, CHVN, and SVN; however, it decreases to 50% in NCVN and off the CVN coast due to the projected IMF divergence. Conversely, the rainfall increase may be owing to stronger moisture flux convergence. For the SON season, rainfall is projected to increase to 50% in NVN and CHVN compared to the present climate. This increase in rainfall can be explained by the stronger NPH that will bring more moisture towards inland Vietnam in the far future.

ACKNOWLEDGEMENTS

This work was conducted with the co-operation of Development of Basic Technology for Risk Information on Climate Change, supported by the SOUSEI Programme of the Ministry of Education, Culture, Sports, Science, and Technology of Japan. The authors thank the Ministry of Land, Infrastructure, Transport, and Tourism for funding travel expenses between Vietnam and Japan.

REFERENCES

[1] N.D. Ngu and N.T. Hieu (2004), *Climate and Climate Resources in Vietnam,* Agricultural publisher, Hanoi.

[2] B. Wang, LinHo (2002), "Rainy season of the Asian-Pacific summer monsoon", *Journal of Climate,* **15**, pp.386-398.

[3] B. Wang, LinHo, Zhang, Yongsheng, M.-M. Lu (2004), "Definition of South China Sea monsoon onset and commencement of the East Asia summer monsoon", *Journal of Climate,* **17(4)**, pp.699-710, DOI:10.1175/2932.1.

[4] N.D. Ngu, et al. (2003), *Impact of ENSO on weather, climate, environment and socio-economic in Vietnam*, Final report of the national project.

[5] N.T.H. Thuan (2008), *Impact of ENSO on summer monsoon and rainfall in the South Vietnam*, PhD thesis, Vietnam Institute of Meteorology, Hydrology and Climate change.

[6] IPCC (2013), *IPCC fifth assessment report: climate change 2013 - The physical science basis*, Cambridge University Press, Cambridge, UK, 1535pp.

[7] R.H. Kripalani, A. Kulkarni, S.S. Sabade (2003), "Indian monsoon variability in a global warming scenario", *Nat. Hazards,* **29**, pp.189-206.

[8] P.C. Hsu, T. Li, J.J. Luo, H. Murakami, A. Kitoh and M. Zhao (2012), "Increase of global monsoon area and precipitation under global warming: a robust signal?", *Geophysical Research Letters,* **39(6)**, DOI: https://doi.org/10.1029/2012GL051037.

[9] Menon, A. Levermann, J. Schewe, J. Lehmann and K. Frieler (2013), "Consistent increase in Indian monsoon rainfall and its variability across CMIP-5 models", *Earth Syst. Dynam.,* **4**, pp.287-300.

[10] Ministry of Natural Resources and Environment (MONRE, 2016), *Climate change and sea level rise scenarios for Vietnam*, Vietnam Publishing House of Natural Resources, Environment and Cartography.

[11] N.V. Hiep, et al. (2015), *Climate change and sea level rise scenarios for Vietnam*, National project, Funded by Vietnamese Government.

[12] J.J. Katzfey, J.L. McGregor and R. Suppiah (2014), *High-Resolution Climate Projections for Vietnam: Technical Report,* CSIRO, Australia, 266pp.

[13] N.D. Mau, N.V. Thang, M.V. Khiem (2017), "Variability of the Vietnam summer monsoon for the 21st century: Projection of PRECIS model under RCP4.5 and RCP8.5 scenarios", *Journal of Climate Change Science,* **4**, pp.25-33.

[14] National Centers for Atmospheric Research Staff (Eds) (2016), *The Climate Data Guide: Climate Forecast System Reanalysis (CFSR),* Last modified 05 Jul retrieved from https://climatedataguide.ucar.edu/climate-data/climate-forecast-system-reanalysis-cfsr.

[15] National Center for Atmospheric Research Staff (Eds) (2017), *The Climate Data Guide: APHRODITE: Asian Precipitation - Highly-Resolved Observational Data Integration Towards Evaluation of Water Resources*, Last modified 27 Feb, retrieved from https://climatedataguide.ucar.edu/climate-data/aphrodite-asian-precipitation-highly-resolved-observational-data-integration-towards.

[16] M. Hirai, T. Sakashita, H. Kitagawa, T. Tsuyuki, M. Hosaka, and M. Oh'izumi (2007), "Development and validation of a new land surface model for JMA's operational global model using the CEOP observation dataset", *J. Meteor. Soc.*, pp.1-24.

[17] K. Saito, T. Fujita, Y. Yamada, J. Ishida, Y. Kumagai, K. Aranami, S. Ohmori, R. Nagasawa, S. Kumagai, C. Muroi, T. Kato, H. Eito, and Y. Yamazaki (2006), "The operational JMA nonhydrostatic mesoscale model", *Mon. Wea. Rev.,* **134**, pp.1266-1298.

[18] A. Kitoh, T. Ose, K. Kurihara, S. Kusunoki, M. Sugi, and KAKUSHIN Team-3 Modeling Group (2009), "Projection of changes in future weather extremes using super-high-resolution global and regional atmospheric models in the KAKUSHIN Program: Results of preliminary experiments", *Hydrol. Res. Lett.,* **3**, pp.49-53.

[19] H. Sasaki, K. Kurihara, A. Murata, M. Hanafusa, and M. Oh'izumi (2013), "Future changes of snow depth in a non-hydrostatic regional climate model with bias correction", *SOLA,* **9**, pp.5-8.

[20] Kieu-Thi X., H. Vu-Thanh, T. Nguyen-Minh, D. Le, L. Nguyen-Manh, I. Takayabu, H. Sasaki, and A. Kitoh (2016), "Rainfall and tropical cyclone activity over Vietnam simulated and projected by the non-hydrostatic regional climate model", *J. Meteor. Soc. Japan,* pp.135-150, doi:10.2151/jmsj.2015-057.

Vietnam Journal of Science, Technology and Engineering (VJSTE): Manuscript Template

General Instructions on using this template and submitting a manuscript to VJSTE: Thank you for preparing a manuscript for submission to VJSTE. Using this template, or following the guidelines below, will help us in processing your paper. Our goal is to be able to identify each section of your manuscript so that we can accurately record the title, authors, abstract, etc. and also be able to enrich it by including reference links and an accurate layout.

You can submit your paper at http://vietnamscience.vn

So that we can identify the parts of your paper, and even if you do not use our template, please begin each section with the specific key words listed below. Please do not use paragraph breaks in the title, author list, or abstract.

Title

Authors

Affiliations

Abstract

One Sentence Summary

Main Text

Acknowledgements

References

Several of these headings are optional, for example, not all papers will include a one-sentence summary, figures or tables.

Please use the .docx format (all version after Word 2007).

More specific formatting instructions are provided in the actual template, which follows.

Title: How to Format a Science Paper (replace with your real title)

Authors: The author list should be one single paragraph (no breaks). Authors should be listed by first name or initial followed by last name and separated by commas. Use superscript numbers to link affiliations, and symbols *†‡ for author notes. For example, X. Jones[1]*, P. Smith[1,2]

Affiliations:

[1]Affiliations should be preceded by superscript numbers corresponding to the author list, and each affiliation should end with a period.

[2]Each affiliation should be a separate paragraph.

*Correspondence to: include the email addresses or telephone number of the corresponding author(s). Please use the asterisk (*) symbol for the corresponding author information.

Abstract: The abstract should be about 100-150 words, and organized in this structure: An opening sentence that sets the question that you address and is comprehensible to the general reader, background content specific to this study, results, and a concluding sentence. It should be one paragraph only.

One Sentence Summary: A brief summary of the main result of your paper, without excessive jargon and less than 150 characters.

Main Text: In general, this should include a brief (1-2 paragraph) introduction, followed by a statement of the specific scope of the study, followed by results and then interpretations. Please avoid statements of future work or claims of priority, and avoid repeating the conclusions at the end.

All of the Figures and Tables should be cited in order (which should be cited as, for example, figure S1, and table S1). You can include page breaks if you would like to place the figures within the text.

Subheads: These can be included in Research Articles or Reviews and should be brief.

Equations can be included. We do not recommend using the native Word 2007, 2008, 2010 or 2011 equation editor. This can in some cases produce less reliable MathML, the online markup language we use, which may result in display errors. Instead, use the legacy equation editor in word (Insert menu; select insert object; select word equation) or use Mathtype (recommended). If you enter equations in simple LaTeX, check that they will convert accurately (Word 2007 and higher can convert simple LaTeX equations).

Fig. #: (Begin each figure caption with a label, "**Fig. 1.**" for example, as a new paragraph.).

Fig. 1. The figure caption should begin with an overall descriptive statement of the figure followed by additional text. They should be immediately after each figure. Figure parts are indicated with capital letters (**A**). If you prefer, you can place both the actual figures and captions logically through the text near where they are cited rather than at the end of the file (but not both). If a paragraph in the main text begins with the name of a figure, write out "Figure" in full (e.g., <para>"Figure 1 shows….").

Fig. 2. You can place graphics above each equation as part of this file.

Table #: (Begin each table caption with a label "**Table 1.**", etc.) as a new paragraph.

Table 1. Start this caption with a short description of your table. Format tables using the Word Table commands and structures. Do not create tables using spaces or tabs characters.

Acknowledgments: The acknowledgments should include a statement about where the data reported in the paper are presented, archived, or available. If in an archive, include the accession number or a placeholder for it. Please also include relevant funding information such as grant numbers and funding agencies. You can also include a statement of author contributions here. The acknowledgements can be multiple paragraphs.

References:

References should be cited in bracket with a number [1]. Multiple reference citations are separated by commas [2, 3] or if a series, dashes [4-6].

References are listed in numerical order, and in the same order in which they are cited in text. The reference list should include all and only those references you have cited in the text. The reference list appears at the end of the paper.

Please include the above heading "References".

Please do not mix in references with explanatory notes.

The reference consist of: Family name(s) and initials of all authors (year of publication), "Titles of journal articles" (optional), *Title of journal, book or other publication*, **volume(number)**, page numbers.

Example of a reference list:

[1] T. Binzoni, T.S. Leung, D. Boggett, D.T. Delpy (2002), "A new near infrared laser-Doppler flowmeter for deep tissue perfusion monitoring", *MAGMA*, **14,** pp.74-75.

[2] T. Binzoni, T.S. Leung, D. Boggett, D.T. Delpy (2003), "Non-invasive laser Doppler perfusion measurements of large tissue volumes and human skeletal muscle blood RMS velocity", *Phys. Med. Biol.*, **48(1)**, pp.2527-2549.

ISSN 2525-2461

Vietnam Journal of Science, Technology and Engineering

SEPTEMBER 2018 • VOL.60 NUMBER 3

EDITORIAL OFFICE

113 Tran Duy Hung Str., Cau Giay Dist., Hanoi

Tel: (84.24) 39436793; Fax: (84.24) 39436794

Email: khcnvn@most.gov.vn

Website: vietnamscience.vn

PUBLICATION LICENCE

No.1153/GP-BTTTT 26th July 2011
No.2528/GP-BTTTT 26th December 2012
No.592/GP-BTTTT 28th December 2016